



University of
Stavanger

Faculty of Science and Technology

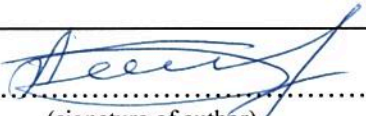
MASTER'S THESIS

Study programme/specialisation: Petroleum
Geosciences Engineering

Spring semester, 2017

Open

Author: Adelya Bilalova


.....
(signature of author)

Faculty supervisor:

Arild Buland

Rock physics models for Cenozoic siliciclastic sediments in the North Sea

Credits: 30

Keywords:

Johan Sverdrup field
Utsira High
the North Sea
shallow unconsolidated sandstones
rock physics models for shale and sand

Number of pages: 220

+ supplemental material/other: USB flash-
drive

Stavanger, June 30th 2017

Table of Contents

Acknowledgements	5
List of acronyms and log names	7
List of symbols	11
Abstract	13
1. Introduction	15
1.1. Johan Sverdrup field	15
1.2. Greenberg and Castagna empirical model	16
1.3. Failure of Greenberg and Castagna empirical model	18
1.4. Objectives of the thesis	20
2. Geological setting	21
2.1. Tectonic setting	21
2.2. Stratigraphy	24
2.2.1. The Hordaland Group - Grid Formation	25
2.2.2. The Hordaland Group - Skade Formation	25
2.2.3. The Nordland Group - Utsira Formation	26
2.3. A lower bound for unconsolidated sands	27
2.3.1. Temperature data	27
2.3.2. Porosity data	29
3. Derivation of shale models constrained by small to moderate differential pressures based on laboratory measurements	33
3.1. Origin and description of laboratory data	33
3.2. Principle of models selection	34
3.3. Modeling of compressional velocity in a smectite/kaolinite/brine system with varying differential pressure	35
3.3.1. Second order polynomial model	35
3.3.2. Power model	38
3.4. Modeling of compressional velocity in a kaolinite/silt/brine system with varying differential pressure	43
3.4.1. Second order polynomial model	43
3.4.2. Power model	46
3.5. Modeling of shear wave velocity in a smectite/kaolinite/brine system with varying differential pressure	49
3.5.1. Second order polynomial model	49
3.5.2. Power model	52
3.6. Modeling of shear wave velocity in a kaolinite/silt/brine system with varying differential pressure	56
3.6.1. Second order polynomial model	56
3.6.2. Power model	59
3.7. Summary of shale models	62
4. Derivation of unconsolidated sand models based on lab measurements	63
4.1. Principle of laboratory data selection	63
4.1.1. Comparison of Zimmer's data with Bhuiyan's and Holt's data	63
4.1.2. Description of Bhuiyan and Holt's data	64
4.1.3. Organization of laboratory data	64
4.2. Rock physics models for sandstone	65
4.2.1. Theoretical basics	65
4.2.1.1. Gassmann's relations	65
4.2.1.2. Murphy's relations	68
4.2.1.3. Biot's relations	68
4.2.1.4. Geertsma-Smit approximations of Biot's relations	72
4.2.1.5. Mavko - Jizba squirt relations	73
4.3. Sandstone models based on laboratory data	74
4.3.1. First and second load models	74
4.3.2. Velocity models based on the first and second dry loads	81
5. Establishment of a well database for Cenozoic sediments in twelve wells of the Johan Sverdrup field	87
5.1. How were the wells selected	87

5.2. Basic calculation before logs editing	87
5.3. Editing of well logs	87
5.3.1. Editing of gamma-ray logs	88
5.3.2. Editing of deep resistivity logs	88
5.3.3. Editing of soic logs	89
5.3.3.1. Editing of compressional slowness logs	89
5.3.3.2. Editing of shear slowness logs	92
5.3.4. Editing of density logs	93
5.4. Main calculation done on well logs	96
6. Sonic modeling from well logs	100
6.1. Motivation for two sonic models	100
6.2. The first models for compressional and shear wave velocities - optimization is based on all wells	102
6.2.1. The first model for compressional wave velocity	102
6.2.2. The first model for shear wave velocity	104
6.3. Consistency of the seabed velocities	107
6.4. The second models for compressional and shear wave velocities – optimization is based on all wells	107
6.4.1. The second model for compressional wave velocity	107
6.4.2. The second model for shear wave velocity	108
6.5. The first models for compressional and shear wave velocities - optimization is based on every well	109
6.5.1. The first model for compressional wave velocity	109
6.5.2. The first model for shear wave velocity	110
6.6. The second models for compressional and shear wave velocities – optimization is based on every wells	111
6.6.1. The second model for compressional wave velocity	111
6.6.2. The second model for shear wave velocity	112
6.7. Comparison of the first and second sonic models based on optimization for all wells simultaneously and well by well	113
6.8. QC and removal outliers	117
6.9. Are the standard Greenberg and Castagna relations are optimal for any depth?	120
7. Discussion of results and conclusions	129
8. Suggestions for the future work	133
Faust Revisited – A Shallow Modification of the Faust Empirical Relationship Between Sonic Slowness and Resistivity	136
References	141
Appendix A. Fitting clay models from data	145
A1. Vp fitting	146
A1.1. Polynomial models for Vp fitting in a smectite/kaolinite/brine system	146
A1.2. Power models for Vp fitting in a smectite/kaolinite/brine system	149
A1.3. Second order polynomial models for Vp fitting in a kaolinite/silt/brine system	152
A1.4. Power models for Vp fitting in a kaolinite/silt/brine system	154
A2. Vs fitting	156
A2.1. Polynomial models for Vs fitting in a smectite/kaolinite/brine system	156
A2.2. Power models for Vs fitting in a smectite/kaolinite/brine system	159
A2.3. Polynomial models for Vs fitting in a kaolinite/silt/brine system	162
A2.4. Power models for Vs fitting in a kaolinite/silt/brine system	164
A3. Summary of second order polynomial models	166
Appendix B. Programming codes applied in the thesis	167
B.1. Coppen’s code for the brine velocity calculation	167
B.2. Batzle -Wang’s code for the brine velocity calculation	167
B3. Batzle -Wang’s code for the brine density calculation	168
B4. Biot - Geertsma’s code for velocities prediction	169
Appendix C. CPI plots displaying editing and main calculations that were done on well logs	173
Appendix D. CPI plots showing DT and DTS calculated based on the first and second sonic models for the Utsira, Skade and Grid formations - optimization is based on all wells	189
Appendix E. CPI plots showing DT and DTS calculated based on the first and second sonic models for the Utsira, Skade and Grid formations – optimization is based on every well	206

Acknowledgements

My greatest gratitude goes to my adviser Inge H.A. Pettersen for his constant advice, patience, encouragement and support in my achievement of this goal. Your help gave me a better understanding how to use new software, how to apply programming in the thesis. I would not have been able to work independently without your guidance. Thank you for always being available for questions and helpful discussions. You have at all the times made me feel welcome and your kind attitude always kept spirits high.

I would like also to thank my supervisor Arild Buland for his help and assistance during my work on the thesis.

I acknowledge Aker BP ASA, Lundin Norway AS, Maersk Oil Norway AS, Petoro AS, and Statoil AS for approving the use of well data for my thesis. Honorable mentions go to Statoil company also for the possibility of finishing my thesis within the company.

I thank Nazmul Mondol, Knut Bjoerlykke, Jens Jahren, Kaare Hoeeg, Mohammad Bhuyian and Rune Holt for the providing an access to laboratory data that were used in the thesis for shale and sand modeling.

I am grateful to the university's professors for their essential and timely help.

Lastly, I would like to thank my family and friends for their significant support and belief in me during my working on the thesis.

List of acronyms and log names

BHT

bottomhole temperature

BS

log name for a bit size

CALI

log name for caliper curve

DT

log name for compressional slowness

DT_12WELLS_1ST_SAND

calculated compressional slowness curve based on the first velocity model
for sand including all wells simultaneously in the optimization

DT_12WELLS_1ST_SHALE

calculated compressional slowness curve based on the first velocity model
for shale including all wells simultaneously in the optimization

DT_12WELLS_2ND_SAND

calculated compressional slowness curve based on the second velocity model
for sand including all wells simultaneously in the optimization

DT_12WELLS_2ND_SHALE

calculated compressional slowness curve based on the second velocity model
for shale including all wells simultaneously in the optimization

DT_1ST_*_SAND

calculated compressional slowness curve based on the first velocity model
for sand in the well with a name *, e.g. DT_1ST_2_12_SAND
calculated compressional slowness curve based on the first velocity model
for sand in the well 16/2-12

DT_1ST_*_SHALE

calculated compressional slowness curve based on the first velocity model
for shale in the well with a name *

DT_2ND_*_SAND

calculated compressional slowness curve based on the second velocity model
for sand in the well with a name *

DT_2ND_*_SHALE

calculated compressional slowness curve based on the second velocity model
for shale in the well with a name *

DT_FAUST

log name for compressional slowness curve calculated based on Faust equation

DT_FINAL

log name for the final edited compressional slowness curve

DT_FLAG

flag for the compressional slowness curve

DT_SHALLOW_FAUST

log name for compressional slowness curve calculated based on the modified Faust equation for shallow part

DTS

log name for shear slowness

DTS_12WELLS_1ST_SAND

calculated shear slowness curve based on the first velocity model for sand including all wells simultaneously in the optimization

DTS_12WELLS_1ST_SHALE

calculated shear slowness curve based on the first velocity model for shale including all wells simultaneously in the optimization

DTS_12WELLS_2ND_SAND

calculated shear slowness curve based on the second velocity model for sand including all wells simultaneously in the optimization

DTS_12WELLS_2ND_SHALE

calculated shear slowness curve based on the second velocity model for shale including all wells simultaneously in the optimization

DTS_1ST_*_SAND

calculated shear slowness curve based on the first velocity model for sand in the well with a name *

DTS_1ST_*_SHALE

calculated shear slowness curve based on the first velocity model for shale in the well with a name *

DTS_2ND_*_SAND

calculated shear slowness curve based on the second velocity model for sand in the well with a name *

DTS_2ND_*_SHALE

calculated shear slowness curve based on the second velocity model
for shale in the well with a name *

DTS_FINAL

log name for the final edited shear slowness curve

DTS_FLAG

flag for the shear slowness curve

DTS_SYNT

log name for the synthetic shear slowness curve

GR

log name for gamma-ray

GR_FINAL

log name for the final edited gamma-ray curve

GR_FLAG

flag for the gamma-ray log

GRMAX

maximum of gamma-ray log

GRMIN

minimum of gamma-ray log

KB

kelly bushing

NPD

Norwegian Petroleum Directorate

NPHI

log name for neutron curve

PHIT

log name for the total porosity

PRESS_DIFF

log name for the differential pressure

PRESS_HYDRO

log name for the hydrostatic pressure

PRESS_OB

log name for the overburden pressure

PSU

practical salinity unit (Wikipedia)

QC

quality control

RDEP

log name for the deep resistivity

RDEP_FINAL

log name for the final edited deep resistivity curve

RDEP_FLAG

flag for the deep resistivity log

RHOB

log name for density

RHOB_FINAL

log name for the final edited density curve

RHOB_FLAG

flag for the density log

RHOB_SYNT

log name for the synthetic density curve

TVD

true vertical depth

TVDML

true vertical depth mud line

TVDSS

true vertical depth subsea

V_CLAY

log name for clay volume curve

WD

water depth

List of symbols

Latin expressions

a – a pore-size parameter or a constant in Archie equation

a_{ij} – an empirical regression coefficients

$bei(\zeta)$ – an imaginary part of the Kelvin function

$ber(\zeta)$ – a real part of the Kelvin function

D – depth measured relative to Kelly bushing

Dsb – depth of seabed

f – frequency

f_c – a reference frequency

$F(\zeta)$ – the viscodynamic operator

g – acceleration due to gravity

G_{dry} – the effective shear modulus of the rock skeleton

G_{sat} – the effective shear modulus of the rock with a pore fluid

G_{uf} – the effective high-frequency, unrelaxed, wet-frame shear modulus

i – imaginary number

J_n – Bessel function of order n

k – the absolute permeability of the rock

K_{dry} – bulk modulus of the rock skeleton

$K_{dry-hiP}$ – the effective bulk modulus of dry rock at very high pressure

K_{fl} – bulk modulus of the fluid

K_s – bulk modulus of the solid material

K_{sat} – bulk modulus of the rock with a pore fluid

K_{uf} – the effective high-frequency, unrelaxed, wet-frame bulk modulus

L – a number of monomineralic lithologic constituent

N_i – an order of polynomial for constituent I

P_0 – datum pressure (pressure at the surface)

R_w – resistivity of the water

S – salinity

T – temperature

V_{silt} – relative volume fraction of silt

V_{smec} – relative volume fraction of smectite

V_p – compressional wave velocity
 V_{p_b} – the compressional velocity of the brine at seabed
 $V_{p_{dry}}$ – compressional wave velocity of the rock skeleton
 $V_{p_{sat}}$ – compressional wave velocity of the rock with a pore fluid
 $V_{p_{\infty}}$ – the Biot high-frequency limiting compressional wave velocity
 V_{p_0} – the Biot-Gassmann low-frequency limiting compressional wave velocity
 V_s – shear wave velocity
 V_{s_b} – the shear wave velocity of the brine at seabed
 $V_{s_{dry}}$ – shear wave velocity of the rock skeleton
 $V_{s_{sat}}$ – shear wave velocity of the rock with a pore fluid
 $V_{s_{\infty}}$ – the Biot high-frequency limiting shear wave velocity
 X_i – a volume fractions of lithological constituents

Greek expressions

α – tortuosity parameter
 η – viscosity
 ν – Poisson's ratio
 ρ – bulk density
 ρ_{dry} – density of the rock skeleton
 ρ_{fl} – density of the fluid
 ρ_{ma} – density of the rock matrix
 ρ_s – density of the solid material
 ρ_{sat} – density of the rock with a pore fluid
 $\rho(z)$ – density of the overlying rock at depth z
 σ – differential (effective) pressure
 φ – porosity
 φ_{soft} – the soft porosity is the amount of porosity that closes at high pressure
 ω – the angular frequency of the plane wave

Abstract

The Norwegian North Sea is a huge and mature hydrocarbon province which has been mapped extensively since the discovery of oil and gas in the late 1960s. There is a numerous amount of data that is available for companies work and various studies. It is an area of multidisciplinary interest, such as, geology, geochemistry, geophysics or petrophysics. However, some investigations of the area are vague, challenging and remain open. In particular, the questions related to prediction of seismic velocities of shallow sediments in the Utsira High in the North Sea.

High pore pressure predominantly associated with shallow unconsolidated sediments presents a significant hazard during drilling and completion of offshore wells. Hence, defining overpressured intervals before drilling not only diminishes drilling hazards but also reduces drilling cost. The correct rock physics model can be a key element in predicting overpressure.

The standard Greenberg and Castagna rock physics model showing the empirical relationship between compressional and shear wave velocities has been applied for unconsolidated shallow sediments in the North Sea. Observation from a particular well in the Johan Sverdrup field is shown to indicate that this model works for deeper formations, but seems not to be valid for shallow sediments. One possible reason for this could be a low effective pressure appropriate to their environment. Therefore, in the thesis we aimed to define proper rock physics models for Cenozoic siliciclastic sediments in the North Sea based on laboratory data and well logging models.

The laboratory data analysis motivated for a power model as the best model for sonic modeling on well logs. Testing of the power models for V_p and V_s did not give proper results on well logging data. Thus, inspired by Faust we derived second sonic models for V_p and V_s prediction. We found that resistivity is an essential parameter that should be included to the models. Furthermore, we realized that models should be estimated in every well separately. The comparison of our sonic models with the standard Greenberg and Castagna empirical model showed that our derived models behave appropriately in the shallow formations up to the depth around 1100 m TVDML where the standard Greenberg and Castagna empirical model breaks down. This is the depth that we got using porosity trend together with Murphy's porosity boundary between unconsolidated and consolidated sand which is equal roughly to 35%. Consequently, we can claim that our final sonic models are correct for unconsolidated siliciclastic sediments.

1. Introduction

This Chapter represents the general information about study area of the thesis which is the Johan Sverdrup field as well as the result of previous observations and main goals of the thesis. The Chapter is based on the references: (Joerstad, 2012), (Wesenlund & Karlsen, 2016), (NPD) and (Greenberg & Castagna, 1992).

1.1. Johan Sverdrup field

The Johan Sverdrup field is located on the southern Utsira High in the Norwegian North Sea, is the 5th largest discovery on the Norwegian Continental Shelf (Figure 1.1.1). It is defined as a combined structural trap (hanging wall fault) and stratigraphic trap. It covers approximately 200 km² and it is considered to play an essential role for the years in the Norwegian petroleum industry (Joerstad, 2012).

The discovery of the Johan Sverdrup field came as a surprise since the North Sea is a mature offshore region. As well 16/3-2 drilled in 1976 by Norsk Hydro Produksjon AS proved dry, little faith was given for later drilling on the Utsira High. However, Lundin Petroleum AS drilled well 16/1-8 on the Luno prospect on the southern Utsira High in 2007 leading to the discovery of the Edvard Grieg field. Further interest and confidence on the southern Utsira High gave rise to the Avaldsnes prospect further east. The Avaldsnes prospect was subsequently drilled in 2010 by well 16/2-6, which in combination with several other delineation and appraisal wells have discovered and quantified the Johan Sverdrup field. The production of the field is expected to last for 50 years (Wesenlund & Karlsen, 2016).

The Figure 1.1.1 below shows the location of the Johan Sverdrup field with the wells considered in the thesis. The map was modified by the author of the thesis by adding the location of wells from the Fact Pages of NPD (NPD).

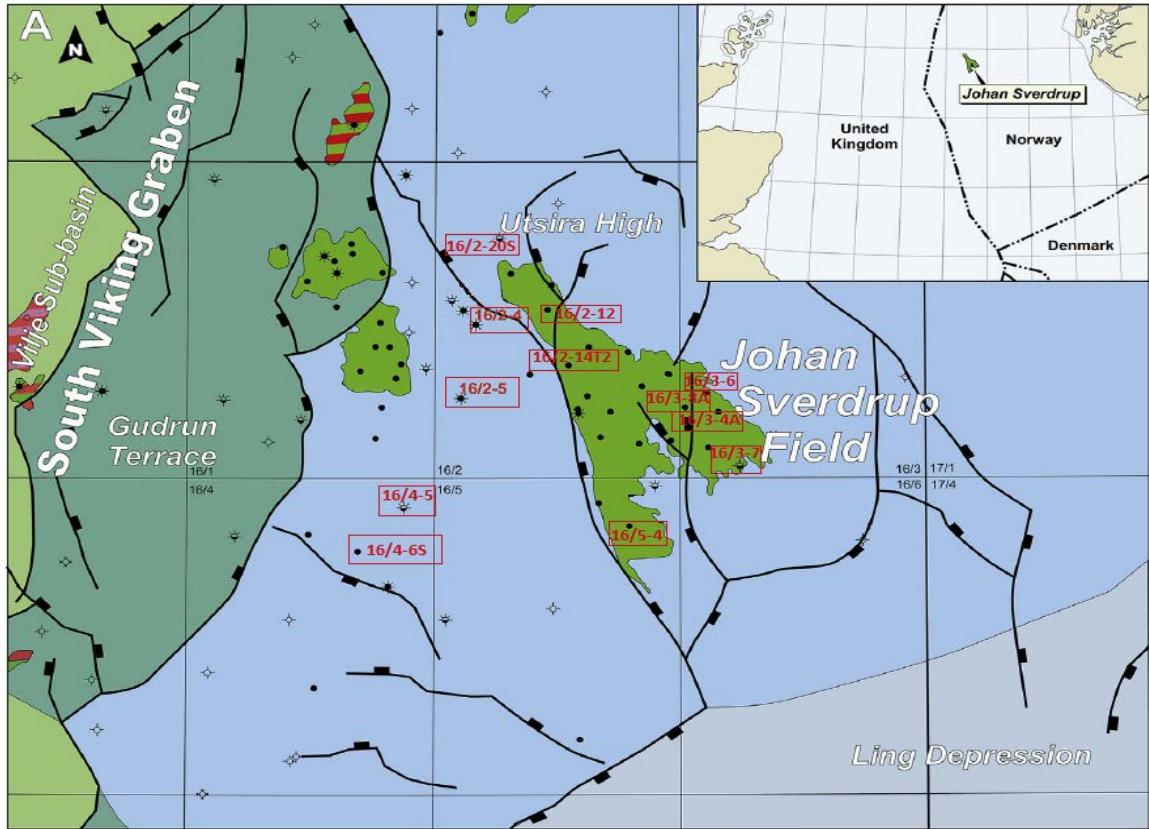


Figure 1.1.1. Location map of the southern part of the Utsira High and surrounding area with key wells considered in the thesis.

In the thesis we are going to work with twelve particular wells that lay within the Utsira High, mainly in the Johan Sverdrup field (Figure 1.1.1).

1.2. Greenberg and Castagna empirical model

Physical properties of shallow unconsolidated formations are distinguishable from most reservoir and seal rocks studied for petroleum exploration because these materials are located next to the transition zone between rocks and sediment (Huffman & Castagna, 2001). Due to overpressure shallow unconsolidated sediments can provoke hazards for successful exploration and production of hydrocarbons. Rock models involving relationship between differential pressure and V_p/V_s ratio could be the key tool in predicting overpressured intervals. However, for shallow unconsolidated rocks compressional and shear wave velocities are difficult to determine due to the uncemented nature of these rocks.

Previous studies of shallow unconsolidated sediments have been based on the usage of empirical relations between compressional and shear wave velocities predicted by Greenberg and Castagna. The developed general method allows to define shear wave velocity in porous rocks if reliable compressional wave velocity and pure (monomineralic) lithology in brine-filled rocks are available (Greenberg & Castagna, 1992):

$$V_s = \frac{1}{2} \left\{ \left[\sum_{i=1}^L X_i \sum_{j=0}^{N_i} a_{ij} V_p^j \right] + \left[\sum_{i=1}^L X_i \left(\sum_{j=0}^{N_i} a_{ij} V_p^j \right)^{-1} \right]^{-1} \right\},$$

where $\sum_{i=1}^L X_i = 1$; L is a number of monomineralic lithologic constituent; X_i is a volume fractions of lithological constituents; a_{ij} is an empirical regression coefficients; N_i is an order of polynomial for constituent I ; V_p and V_s are compressional and shear velocities (km/s) in composite brine-saturated rock.

Table 1.2.1.

Representative regression coefficients for shear wave velocity (km/s) versus compressional wave velocity (km/s) in pure porous lithologies: $V_s = a_{i2}V_p^2 + a_{i1}V_p + a_{i0}$ (Greenberg & Castagna, 1992).

Lithology	a_{i2}	a_{i1}	a_{i0}
Sandstone	0	0.80416	-0.85588
Limestone	-0.05508	1.01677	-1.03049
Dolomite	0	0.58321	-0.07775
Shale	0	0.76969	-0.86735

The trends showing compressional wave velocity versus shear wave velocity for different lithologies based on Greenberg and Castagna empirical model is shown in the Figure 1.2.1.

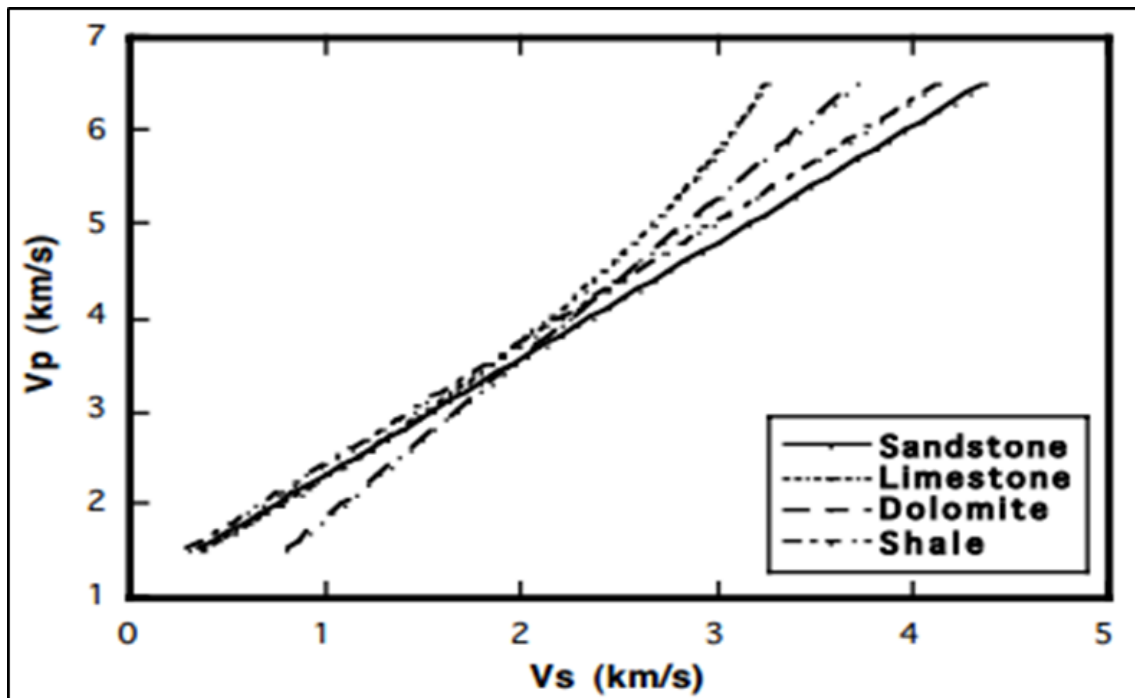


Figure 1.2.1. Greenberg and Castagna model (Greenberg & Castagna, 1992).

1.3. Failure of Greenberg and Castagna empirical model

The Greenberg and Castagna empirical model is successfully used by many industrial companies. In particular, it was applied in the well 16/3-6 for constructing standard petrophysical templates in Geolog program. Both Figures 1.3.1 and 1.3.2 include two cross-plots: the image A represents V_p/V_s ratio versus acoustic impedance where sonic velocities were calculated based on sonic logs. The image B shows V_p/V_s ratio versus acoustic impedance where shear wave velocity was determined based on Greenberg and Castagna model. The cross-plots in the Figure 1.3.1 are related to the depth 992-1712 meters, while the cross-plots in the Figure 1.3.2 were done for the depth 780-882 meters. One can see that both trends in the Figure 1.3.1 have similar behaviour and they have the same lithological distribution. In contrast, the trends for more shallow formations differ from each other demonstrating a divergent lithology which can be noticed in the Figure 1.3.2. Moreover, reflection coefficients in the Figure 1.3.1 are visibly more distinguishable than in the Figure 1.3.2, in the latter one they are almost flat and practically identical.

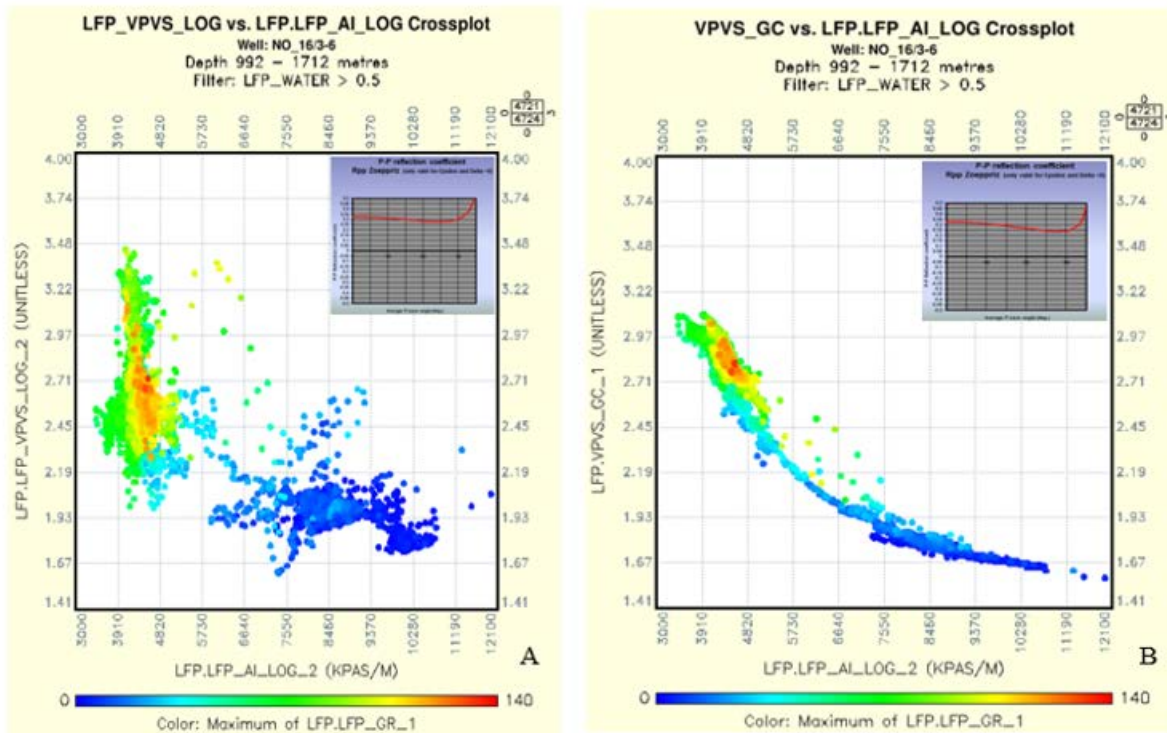


Figure 1.3.1. Cross-plots showing Vp/Vs ratio versus acoustic impedance at the depth 992-1712 meters. A. Vp/Vs were derived from the sonic logs. B. Vs was determined from the standard Greenberg and Castagna model.

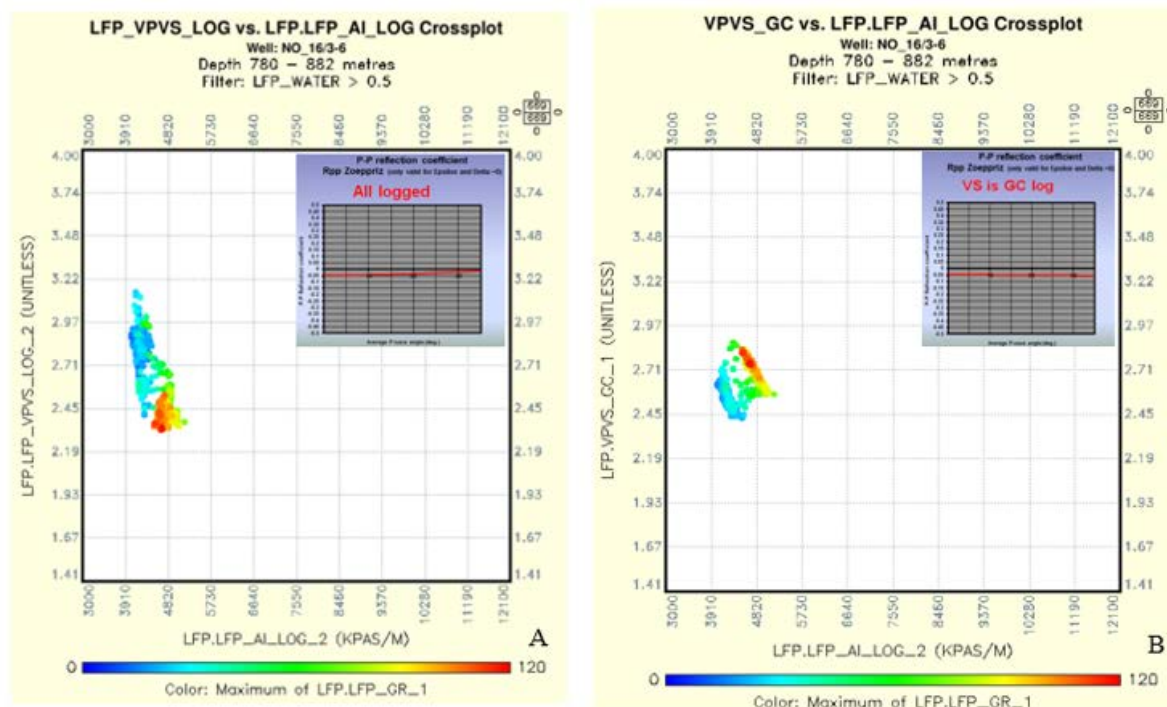


Figure 1.3.2. Cross-plots showing Vp/Vs ratio versus acoustic impedance at the depth 780-882 meters. A. Vp/Vs were derived from the sonic logs. B. Vs was determined from the standard Greenberg and Castagna model.

The investigation of this well allowed us to suggest that the standard Greenberg and Castagna empirical model applies only for deeper formations. Further, this example suggests also that an alternative to the Greenberg and Castagna model is needed in the shallow formations.

1.4. Objectives of the thesis

In the thesis we mainly aim to determine rock physics models that would be relevant for shallow unconsolidated sediments. We are going to work with both laboratory and well logging data in order to derive models for shale and sand. Furthermore, we will test our models for shallow unconsolidated formations for twelve wells in the Johan Sverdrup field and compare them with the standard Greenberg and Castagna empirical model. We hope that our obtained models will be of a practical use for the future studying of the area.

2. Geological setting

This Chapter is dedicated to the tectonical, geological and stratigraphical features of the area of our interest – the south Viking Graben at the Utsira High. The main source of information is Norwegian Petroleum Directorate (NPD).

2.1. Tectonic setting

The flooded North Sea palaeorift system forms a minor epicontinental basin confined by the Shetland Platform to the west and the Norwegian mainland to the east (Figure 2.1.1). The N-S-trending Viking-Central Graben has a length of approximately 1000 km and a width that varies between 25 and 100 km (Ziegler, 1992).

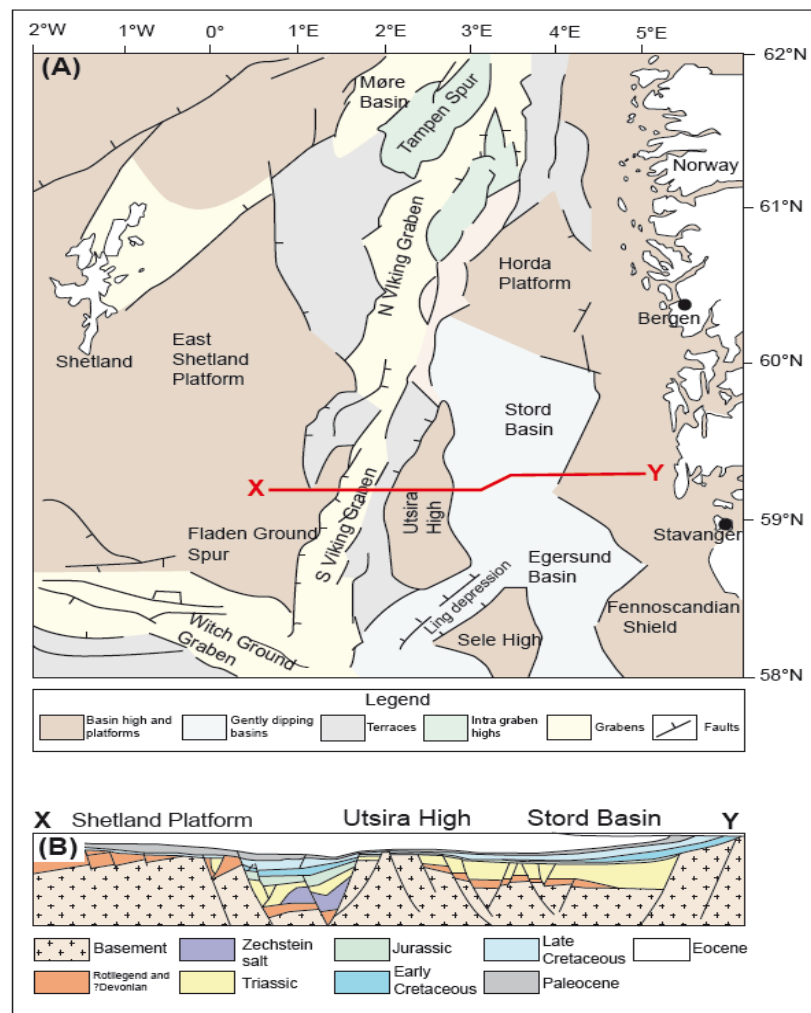


Figure 2.1.1. A. Regional map of the North Sea area (modified from Gregersen, Michelsen, & Sørensen, 1997) with cross-section marked X-Y. B. Cross-section (X-Y) of the South Viking Graben (modified from Ziegler, 1992).

The North Sea basin is composed of several major Mesozoic grabens and highs (Gregersen et al., 1997). The Viking Graben is an example of the intracratonic basin (Figure 2.1.1) located on the continental crust in the North Sea (Faleide, Bjørlykke, & Gabrielsen, 2015). The initial necessary condition to form sedimentary successions in the intracratonic basin is a crustal thinning due to extension followed by subsidence as a result of an isostatic equilibrium compensation and sediment loading (Faleide et al., 2015). The Viking Graben rift system was affected by two extensional events which are dated to be of Permian-Triassic and Late Jurassic-Early Cretaceous age (Gabrielsen, Færseth, Steel, Idil, & Kløvjøn, 1990). The latter extensional setting resulted in rotated fault blocks of Jurassic age which were the main objectives for hydrocarbon accumulation. The rift system is bounded to the west by the East Shetland Platform and the Oeygarden Fault Zone to the east (Figure 2.1.1).

The Permian-Triassic and Late Jurassic-Early Cretaceous rift episodes are superimposed onto the Caledonian suture (Faleide et al., 2015). The Caledonian basement encountered by wells in the North Sea includes intrusive igneous rocks and/or low- to high-grade metamorphic rocks (Gautier, 2005). The Caledonian plate movement altered from subduction to strike-slip tectonic setting in Late Devonian between Greenland and Fennoscandia which later terminated in the transition from Devonian to Carboniferous. The strike-slip setting was followed by diverging plate movement in Early Carboniferous till the present day. Late Carboniferous rifting reveals in the Oslo Graben, as well as Permian-Triassic and Late Jurassic-Early Cretaceous. The final continental break-up accompanied by onset of sea-floor spreading took a place in the earliest Eocene time (Faleide et al., 2015).

The Utsira High is one of the intrabasinal structural highs forming the eastern flank of the southern Viking Graben. It is bounded to the east and north by the Stord basin and to the south by the Ling depression (Figure 1.1.1). The southern part of the Utsira High is referred to as the Haugaland high, while the Augland graben separates the main Utsira High from the Avaldnes high to the east (Figure 2.1.2) (Riber, Dypvik, & Senile, 2015).

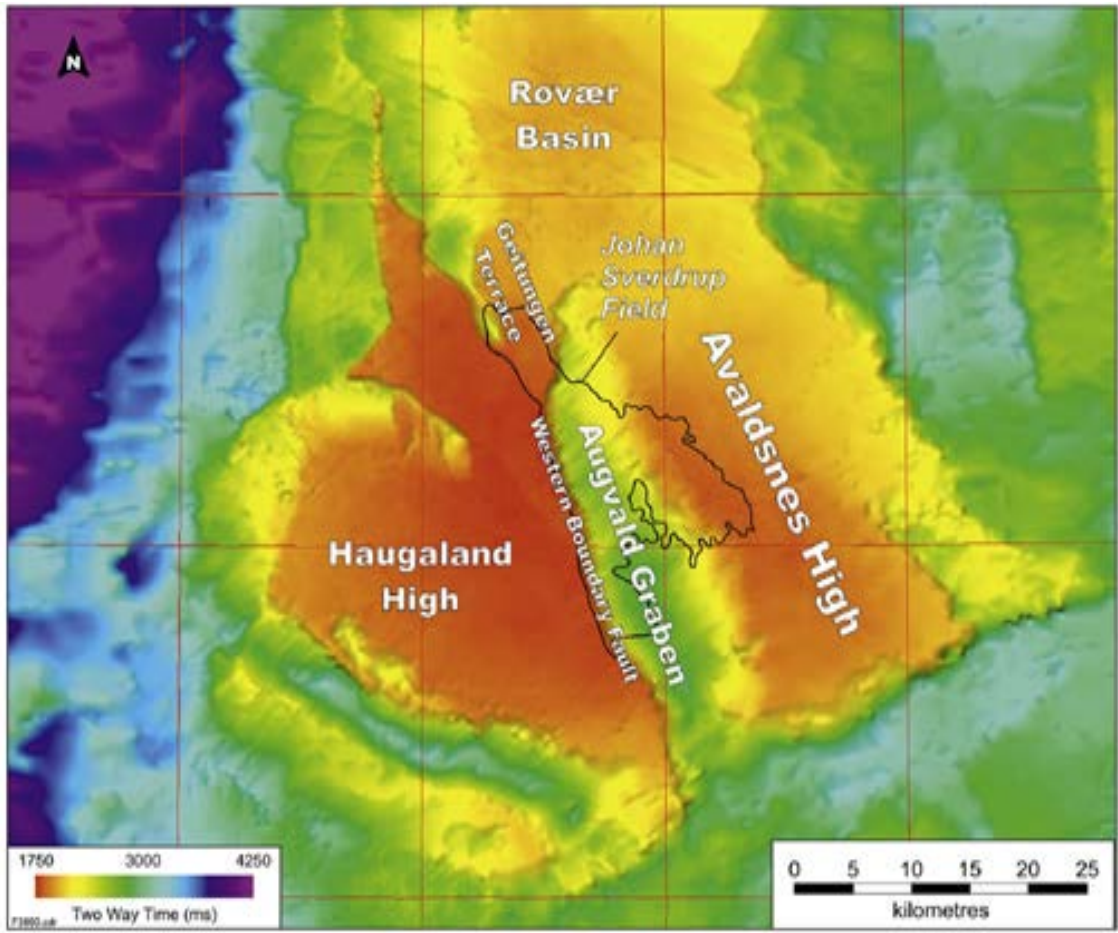


Figure 2.1.2. Top Basement Two-Way-Time structure map with additional structural subdivision (Olsen, Briedis, & Renshaw, 2017).

2.2. Stratigraphy

The general stratigraphic chart of the southern Viking Graben and the Utsira High is presented in the Figure 2.2.1.

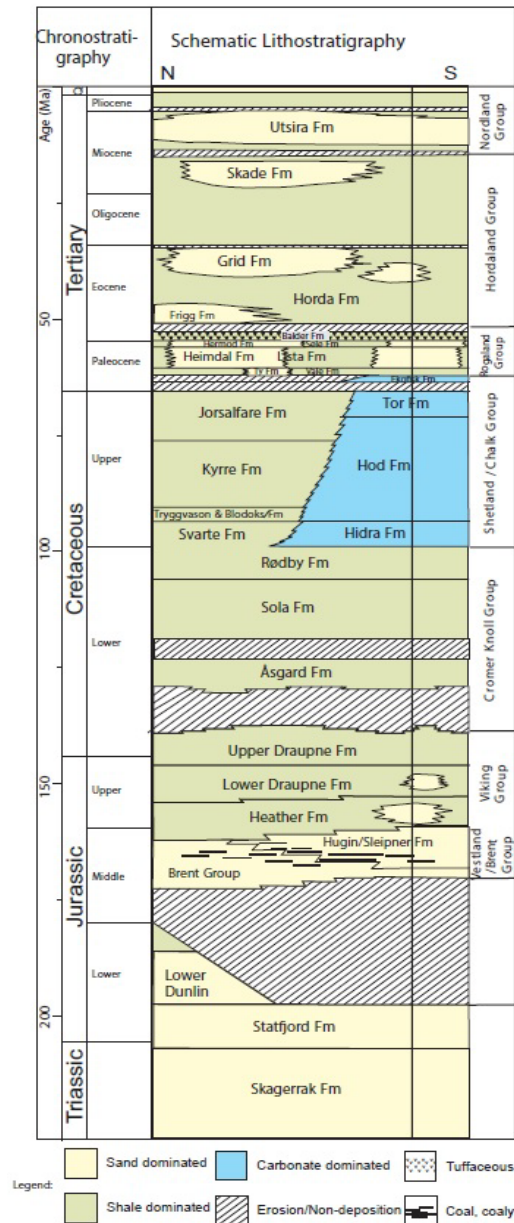


Figure 2.2.1. General stratigraphic chart of the Southern Viking Graben and the Utsira High (Justwan, Dahl, & Isaksen, 2006).

As the thesis is related to the rock physics models of the Cenozoic sediments, thus, our area of the interest is in the shallow part – from sea bed to the top of the Shetland. The most upper part of the stratigraphic chart shows three sand dominated formations the Grid, Skade and Utsira Formations we are interested in the thesis.

2.2.1. The Hordaland Group - Grid Formation

Middle to Upper Eocene

The Grid Formation of the Hordaland Group consists of a series of sand-bodies probably sourced from the East Shetland Platform and located in the Viking Graben between 58°30'N and approximately 60°30'N. The thickness in the typical well is 370 m. The formation thins eastward. There is a considerable difference in thickness north and south. To the north the thickness is less than 200 m and to the south nearly 400 m. This is due to the fact that sand deposition started earlier in the south. Due to soft sediment deformation, there may be poor connectivity between individual sand bodies, and some sands may be interpreted as injectites. The deposition of the formation took place in an open marine environment during regression (NPD).

2.2.2. The Hordaland Group - Skade Formation

Eocene to Middle Miocene

The Skade Formation of the Hordaland Group together with the Eir (informal) and Utsira Formations and the Upper Pliocene sands of the Nordland Group form the outer part of a large deltaic system with its source area on the East Shetland Platform. The proximal parts of this system are mainly located in the UK sector, and these deposits are named the Hutton sand (informal). In the Norwegian sector, sands belonging to the system are the Miocene–Lower Pliocene Skade, Eir (informal) Utsira Formations, and Upper Pliocene sands of the Nordland Group (no formal name) (NPD).

The Skade Formation, Lower Miocene, consists of marine sandstones (mainly turbidites) deposited over a large area of the Viking Graben. The maximum thickness exceeds 300m and decreases rapidly towards the east where the sands shale out or terminate towards large shale diapirs (Figure 2.2.2.1) (NPD).

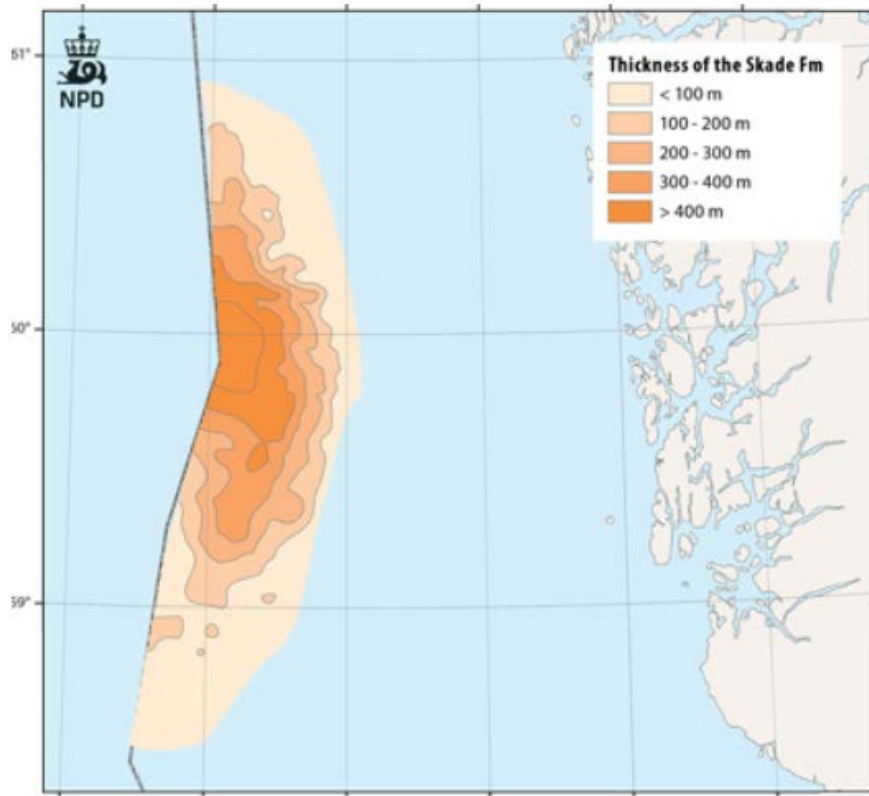


Figure 2.2.2.1. Thickness of the Skade Formation (NPD).

2.2.3. The Nordland Group - Utsira Formation

Uppermost Middle Miocene to Quaternary

The Utsira Formation of the Nordland Group (uppermost Middle Miocene to Quaternary) consists of marine sandstones with source area mainly to the west. The maximum thickness exceeds 300 m (Figure 2.2.3.1). The sands of the Utsira Fm display a complex architecture and the elongated sand body extends some 450 km N-S and 90 km E-W. The northern and southern parts consist mainly of large mounded sand systems. In the middle part the deposits are thinner, and in the northernmost part (Tampen area) they consist of thin beds of glauconitic sands (NPD).

Upper Pliocene deltaic sand deposits overlie the Utsira Formation and Eir formation (informal) with a hiatus. We regard the Upper Pliocene sand as a part of the large Utsira-Skade aquifer system. The Upper Pliocene sand has previously often been assigned to the Utsira Formation. The top of the sand is found at about 150 m below the sea floor in the Norwegian sector. Seismic data indicates that the latest active progradation of these sands took place

towards the north-east in the Tampen area, where their distal parts interfinger with glacial sediments derived from Scandinavia (NPD).

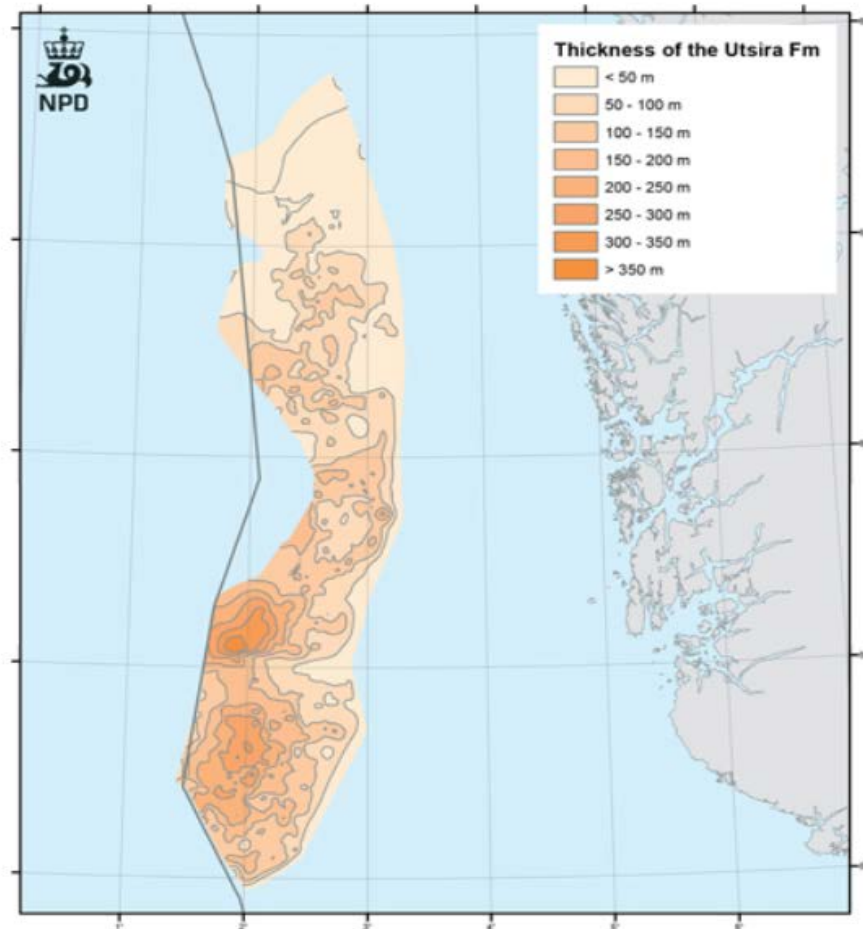


Figure 2.2.3.1. Thickness of the Utsira Formation (NPD).

2.3. A lower bound for unconsolidated sands

2.3.1. Temperature data

In sedimentary basins a mechanical compaction dominates in the shallow part down to the temperature of about 80-100°C depending on the geothermal gradient (Bjørlykke, 2010).

A temperature model that was built for considered wells allows to estimate the depth at which the mechanical compaction changes to cementation. The data for the model is presented in the Table 2.3.1.1 The values of bottomhole temperature (BHT), kelly bushing (KB), true vertical depth (TVD) and water depth (WD) and were taken from Fact Pages of Norwegian Petroleum Directorate (NPD). Since we are working with siliciclastic shallow sediments we are interested in formations that lay till top of the Shetland where there is contrast change in

lithology. The values of top of the Shetland were taken from completion logs. True vertical depth subsea and true vertical depth mud line (TVDSS and TVDML accordingly) were calculated based on the formulas:

$$TVDSS = TVD - KB$$

$$TVDML = TVDSS - WD$$

Seabed was calculated as follows:

$$KB + WD$$

The temperature in the water depth bed assumed to be equal to 4°C. The temperature model shows the temperature values in the bottom of the well versus the true vertical depth mud line (Figure 2.3.1.1).

Table 2.3.1.1.

Basic depth and temperature values for wells under consideration.

Well	BHT (°C)	KB (m)	TVD (m)	WD (m)	TVDSS (m)	TVDML (m)	Seabed (m)	Top of the Shetland (m)
16/2-4	91	48	2000.00	113	1952.00	1839.00	161	1708
16/2-5	90	49.2	2373.00	109	2323.80	2214.80	158.2	1756.5
16/2-12	87	22	2067.00	115	2045.00	1930.00	137	1671.5
16/2-14 T2	85	22	1982.00	113	1960.00	1847.00	135	1567
16/2-20 S	91	30	2098.00	109.5	2068.00	1958.50	140.1	1899.5
16/3-4 A	88.1	25	1958.60	117	1933.60	1816.60	141.5	1570
16/3-6	86.2	25	2050.00	117	2025.00	1908.00	142	1500
16/3-7	89	25	2100.00	116.5	2075.00	1958.50	141.5	1452
16/3-8 A	89.3	25	2053.00	116	2028.00	1912.00	141	1569.5
16/4-5	84	26	2019.80	104	1993.80	1889.80	130	1780
16/4-6 S	85	25	2213.00	100.5	2188.00	2087.50	125.5	1915
16/5-4	90	25	2100.00	108	2075.00	1967.00	133	1486.5

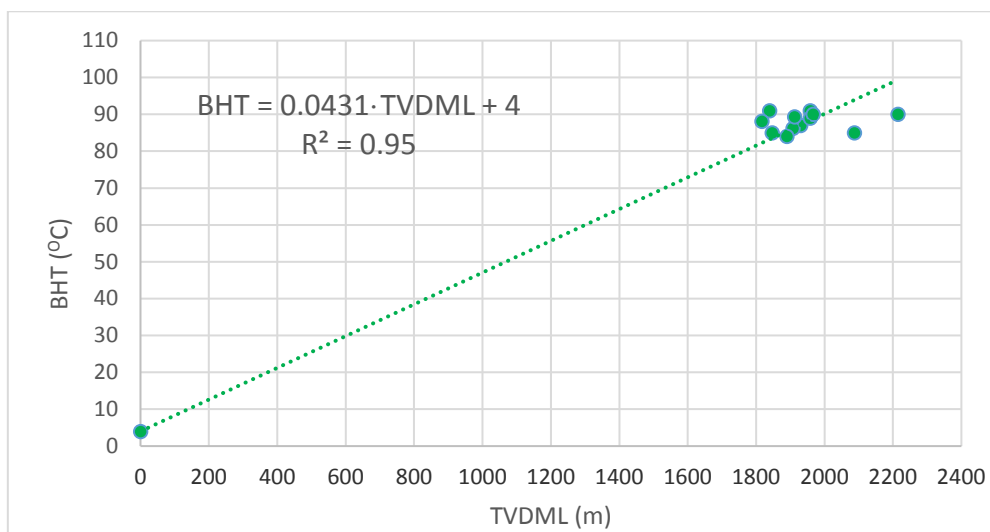


Figure 2.3.1.1. BHT (°C) versus TVDML (m).

Based on our temperature model and considering the average temperature to be equal to 90°C we can make a suggestion that the diagenesis starts at about 2000 m burial depth. So, we can say that cementation will take place at the depth greater than 2000 m where the sandstone would be become stiffer and consolidated.

2.3.2. Porosity data

We also estimated a burial depth based on porosity data. We considered two models: linear and exponential. Linear trends of porosity versus true vertical depth mud line for sand and shale are presented in the Figure 2.3.2.1 A and B.

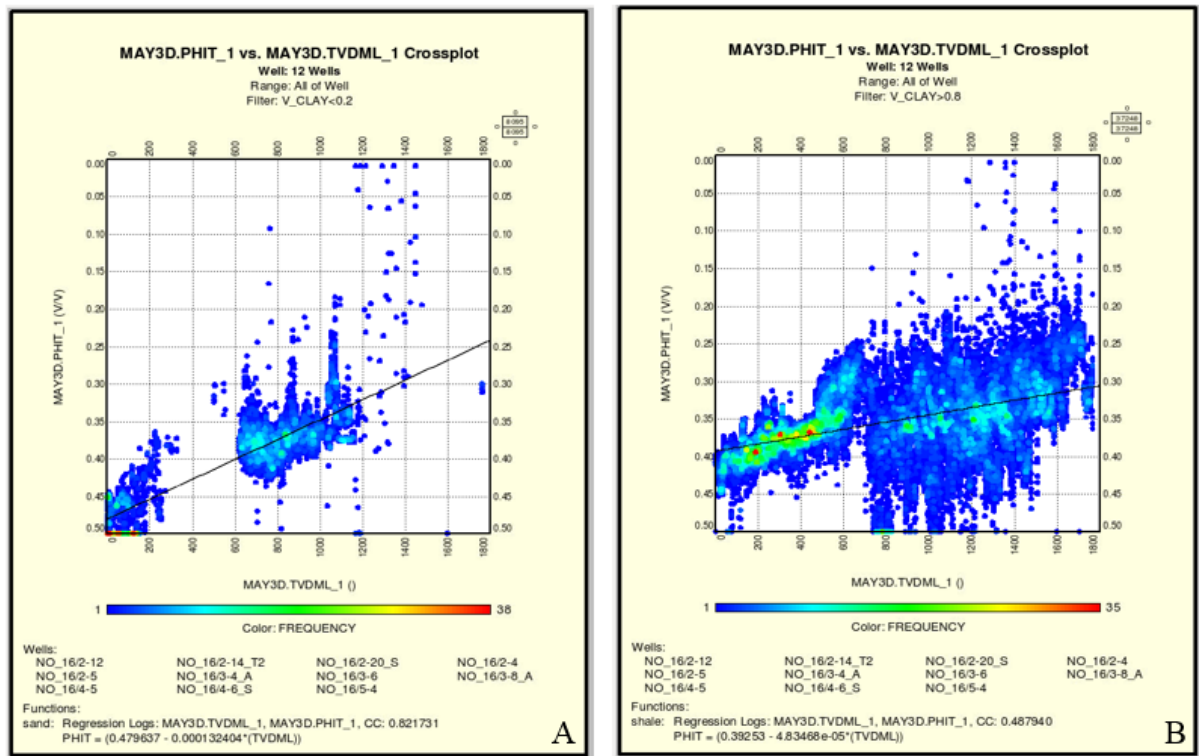


Figure 2.3.2.1. Linear model for porosity including all considered wells: A. For sand. B. For shale.

Murphy in his work suggested that porosity of unconsolidated sand is about 35% and could be even higher (Murphy, Reischer, & Hsu, 1993). Taking this value into account we can assume the depth of the shallow unconsolidated part to be equal to approximately 1100 m according to both linear trends for sand and shale. However, the linear trends for porosity seem to be not so appropriate because one can notice a slight curvature of the trends close to sea bed. Therefore, we considered an exponential model as well. We made cross-plots showing

logarithm of porosity versus true vertical depth mud line for sand shale for all considered wells (Figure 2.3.2.2). Exponential model of porosity as function of depth was initially suggested by Athy (Athy, 1930), as well as the model found use further in laboratory studies of clay (Mondol, Bjørlykke, Jahren, & Høeg, 2007). Investigation of our data showed that exponential model has a better fit than linear one. The trends of porosity are different for sand and shale (Figure 2.3.2.2). The crossing point of these two lines in the Figure 2.3.2.3 coincides with the depth which is about 1100 m as well. Up to this value deposition takes place, at higher depths deposition alters to packing (crushing) (Avseth, Flesche, & Van Wijngaarden, 2003).

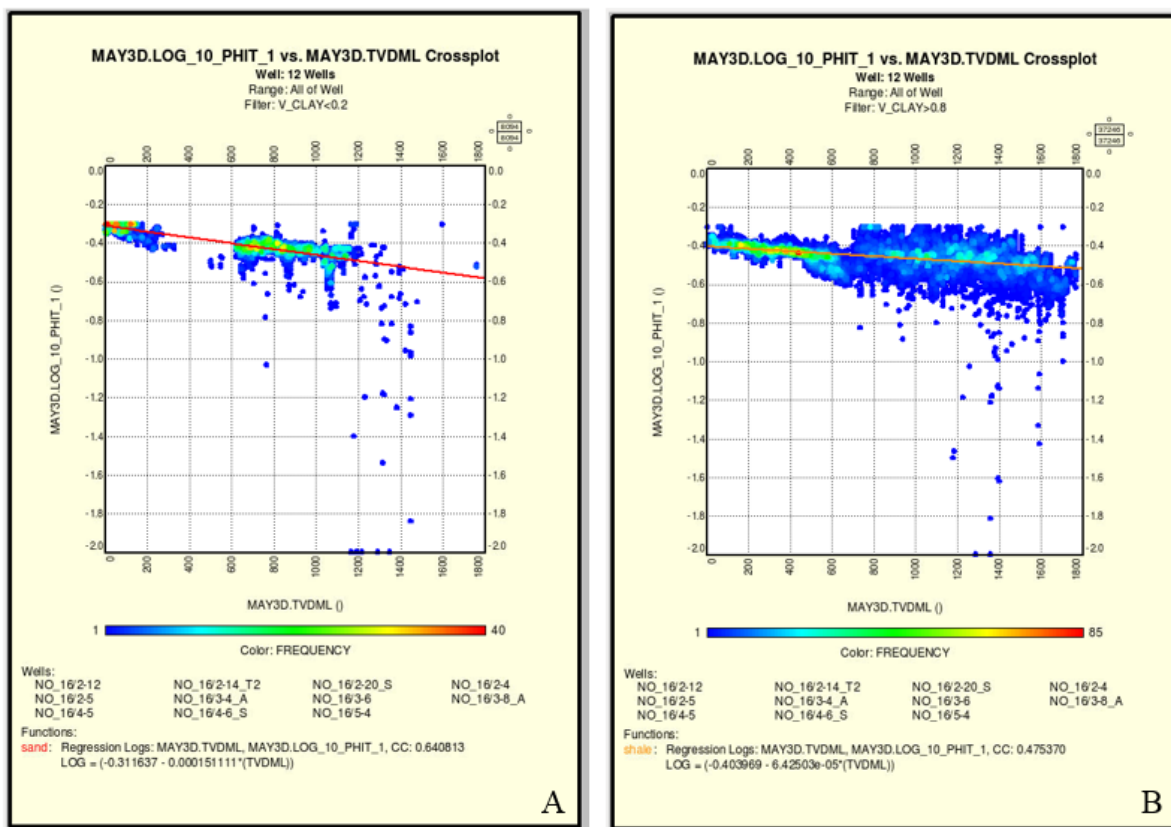


Figure 2.3.2.2. Exponential model for porosity including all considered wells: A. For sand. B. for shale.

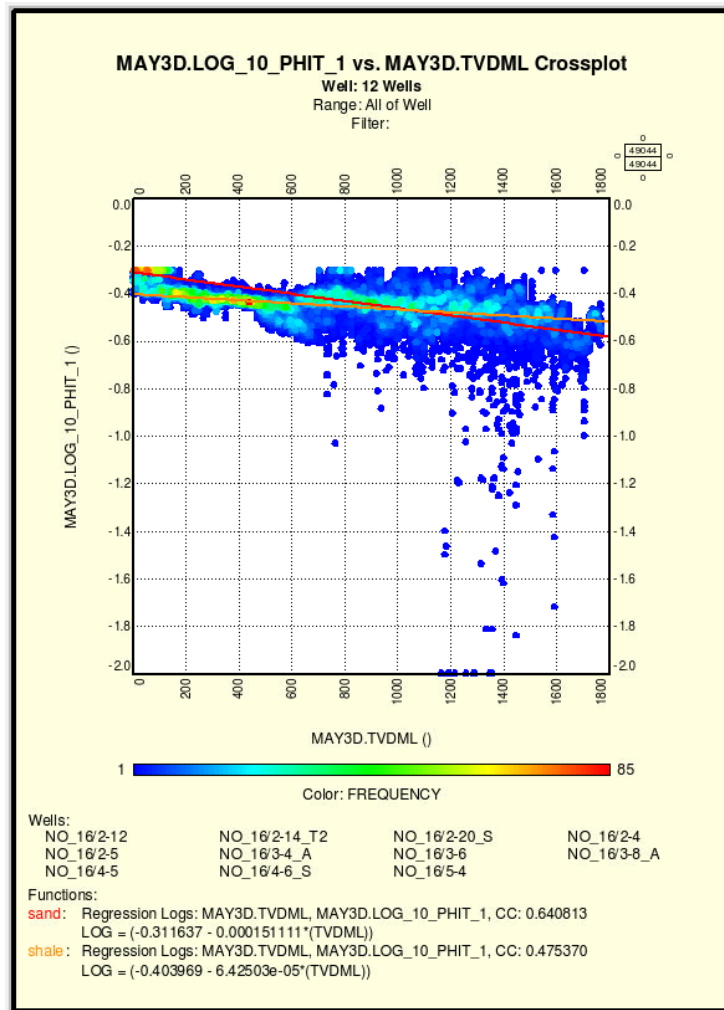


Figure 2.3.2.3. Exponential models for porosity for both sand and shale including all considered wells.

Resuming all of the above, based on the temperature data we got a higher value of burial depth. However, since porosity models are more restrictive and assuming Murphy's model to be correct, we concluded that in our case shallow unconsolidated sediments lay roughly up to 1100 m.

3. Derivation of shale models constrained by small to moderate differential pressures based on laboratory measurements

This Chapter presents the shale models that were derived based on laboratory data analysis. The main reference for this section is (Mondol et al., 2007). It should be mentioned that we considered second order polynomial and power models for laboratory sonic velocities modeling. The former models were constructed in order to define compressional and shear wave velocities values at seabed. The latter models were determined as the most reliable for our case.

We assumed for simplicity that V_p and V_s velocities in shale have an isotropic behavior. This is clearly an approximation as textural properties of shales are more exactly described by an oriental distribution function (Sayers, 1999). Thus, our results here should be considered as experimental average behavior of sonic velocities.

3.1. Origin and description of laboratory data

The source of the laboratory data of clay mineral aggregates are previous observations that were done by H. Mondol, K. Bjoerlykke, J. Jahren and K. Hoeg (Mondol et al., 2007). Their work included dry and brine-saturated clay aggregates ranging from pure smectite to pure kaolinite. Experiments were conducted by increasing vertical effective stress up to 50MPa. The laboratory analysis showed the changing of such physical properties as acoustic velocities, porosity, density. A set of 12 synthetic samples (6 dry and 6 brine saturated) were prepared in the laboratory by mixing known amounts of smectite and kaolinite. All experiments were performed at room temperature which was between 19 and 21°C. The salinity of the fluid in experiments was about 34000 ppm (Mondol et al., 2007).

For the shale modeling part we used brine saturated clay minerals. Since there are two aggregates in the experiments – pure smectite and pure kaolinite, in the thesis we chose two clay systems: smectite/kaolinite/brine and kaolinite/silt/brine ones. These systems were organized based on different relative volume fractions of kaolinite, smectite and silt. The final database was done based on the laboratory experiments mentioned above. It represents the collection of the clay fractions, effective pressure, salinity, porosity, density, compressional and shear wave velocities values. Moreover, it shows a grain size for a certain clay type. Here is a short example how the data look like.

Sources													
Mondol et al. 2007										"Experimental mechanical compaction of clay mineral aggregates—Changes in physical properties of mudstones during burial"		Marine and Petroleum Geology 24 (2007), pp 289 - 311	
Kaolinite (vol frac)	Smectite (vol frac)	Silt (vol frac)	Brine sal (ppm)	Ov (MPa)	Vp (dry) (m/s)	Vp (sat) (m/s)	Vs (dry) (m/s)	Vs (sat) (m/s)	Density gm/cc	Porosity (v/v)	Grain size (µm)	Frequency (MHz)	Source
1	0	0	34000	1,043		1363,544		368,161	2,056	0,41427			Mondol et al. 2007
1	0	0	34000	5,048		1563,094		466,964	2,223	0,31942			Mondol et al. 2007
1	0	0	34000	10,04		1688,784		554,748	2,315	0,26668			Mondol et al. 2007
1	0	0	34000	15,083		1780,105		625,536	2,379	0,23096			Mondol et al. 2007
1	0	0	34000	19,875		1858,757		689,727	2,424	0,20509			Mondol et al. 2007
1	0	0	34000	24,892		1923,848		732,265	2,462	0,18355			Mondol et al. 2007
1	0	0	34000	30,312		1983,087		771,382	2,497	0,16383			Mondol et al. 2007
1	0	0	34000	35,153		2042,129		807,187	2,524	0,14831			Mondol et al. 2007

Figure 3.1.1. Example of clay data from the supplementary materials.

The full clay data can be found in the supplementary materials in the USB flash-drive attached to the printed version of the thesis. It involves not only clay but also marine sediments, sand and glass-bead data. However, for the thesis the most critical are shale and sand values.

3.2. Principle of models selection

The shale modeling was done based on laboratory data of shale mentioned in the section above. According to the clay values for the compressional as well as shear wave velocities modeling we chose the simplest non-linear equations that behave nice when the effective pressure approaches to zero limit. Thus, the logarithmic model is not appropriate in this case. Taking into account it, we used the second order polynomial model as the initial model for both compressional and shear wave velocities against varying differential pressure. This model is described by the following similar equations:

$$Vp = A \cdot \sigma^2 + B \cdot \sigma + C,$$

where Vp is compressional wave velocity, σ is effective pressure and A, B, C are coefficients of the equation.

$$Vs = A' \cdot \sigma^2 + B' \cdot \sigma + C',$$

where Vs is shear wave velocity and A', B', C' are coefficients of the equation.

The power models for compressional and shear wave velocities modeling were selected like a second option as well. These models are described by the following equations:

$$Vp = Vp_b + A'' \cdot \sigma^{B''},$$

where Vp_b is compressional wave velocity of the brine at seabed and A'', B'' are coefficients of the equation.

$$Vs = Vs_b + A''' \cdot \sigma^{B'''},$$

where Vs_b is shear wave velocity of the brine at seabed and A''', B''' are coefficients of the equation.

The equations of the second order polynomial and power models were applied for both considered clay systems – smectite/kaolinite/brine and kaolinite/silt/brine ones.

The derived models are presented Sections further. The models include error bars for both V_p and V_s velocities. The error in the velocity measurements at most pressures above 1 or 2 MPa is generally less than 2% for the compressional wave velocities and 4% for the shear wave velocities (Zimmer, 2004).

A deviation of the first points in the polynomial and power models can be explained by the small values of the effective pressure. However, both models lie in the range of the error bars. We also made plots of the parameters A, B,C, V_{pb} and V_{sb} as functions of smectite and silt volume. It was essential in order to represent the final shale models in relations with relative smectite and silt volume.

We used different colors for the models for V_p and V_s in order to distinguish the type of the model and type of velocity. The different colors for the parameters A, B,C, V_{pb} and V_{sb} were applied to highlight the difference in values between clay systems.

3.3. Modeling of compressional velocity in a smectite/kaolinite/brine system with varying differential pressure

3.3.1. Second order polynomial model

The values of the compressional velocity polynomial models for different relative volume fractions of clay in a smectite/kaolinite/brine system are presented in the Table 3.3.1.1.

Table 3.3.1.1.

Results of fitting of laboratory data of V_p to the second order polynomial model in a smectite/kaolinite/brine system.

Relative smectite volume	Relative kaolinite volume	A	B	C	R^2
0	1	-0.261	28.2	1390	0.987
0.2	0.8	-0.248	27.9	1420	0.981
0.4	0.6	-0.204	23.7	1380	0.988
0.6	0.4	-0.214	23.9	1530	0.992
0.8	0.2	-0.188	19.9	1450	0.989
1	0	-0.169	17.6	1510	0.991

The Figure 3.3.1.1 represents compressional wave velocity values against effective pressure in the second order polynomial model.

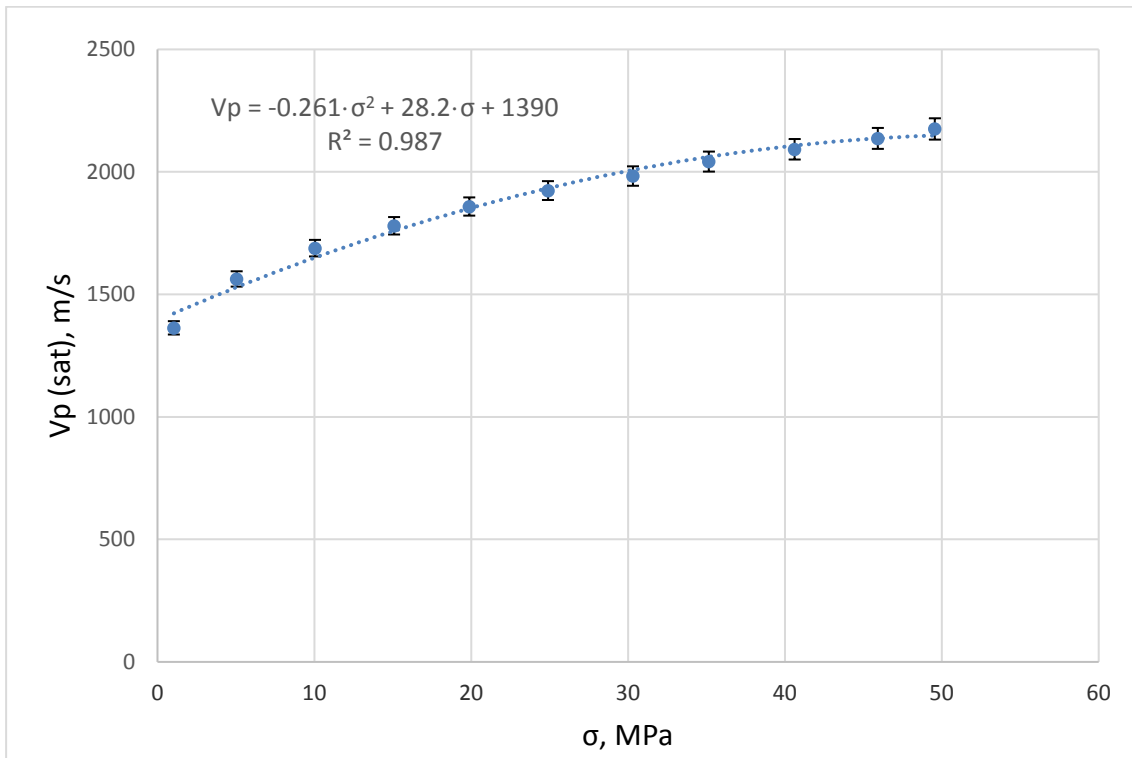


Figure 3.3.1.1. Second order polynomial model for Vp fitting when relative volume fraction of kaolinite is 1 and relative volume fraction of smectite is 0.

The second order polynomial models for Vp fitting for other clay composition in a smectite/kaolinite/brine system are similar and they are presented in the section A1.1 of Appendix A.

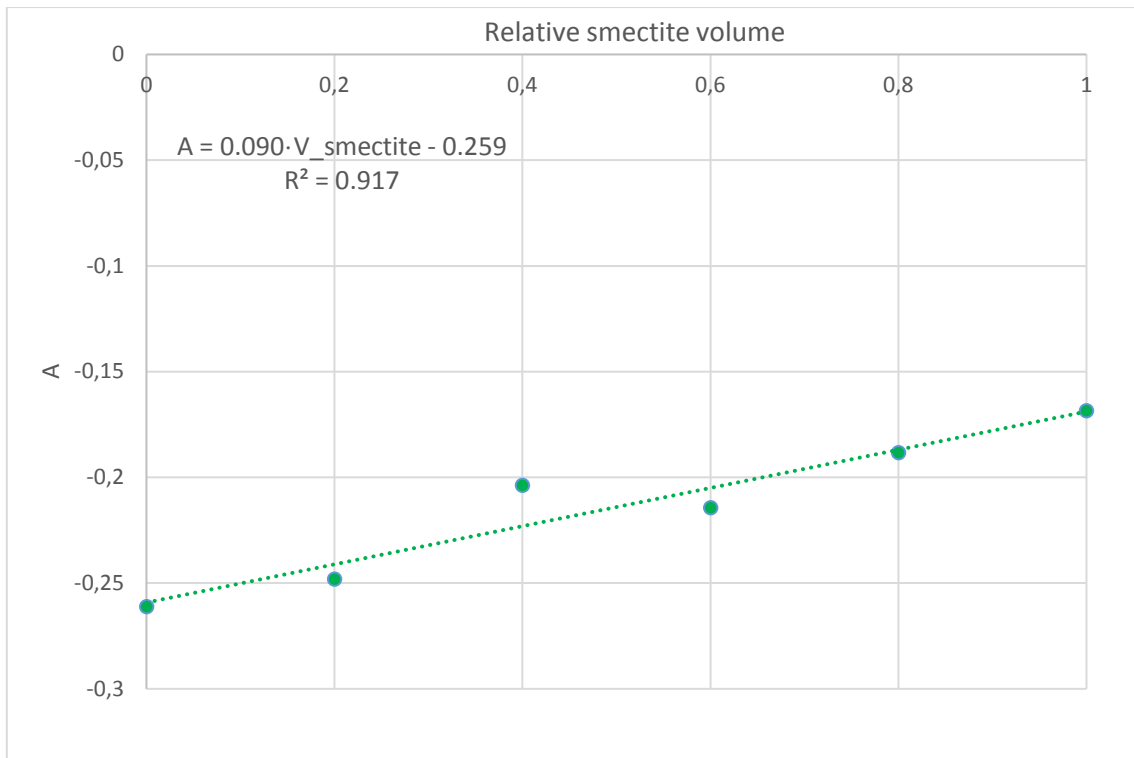


Figure 3.3.1.2. A versus relative smectite volume.

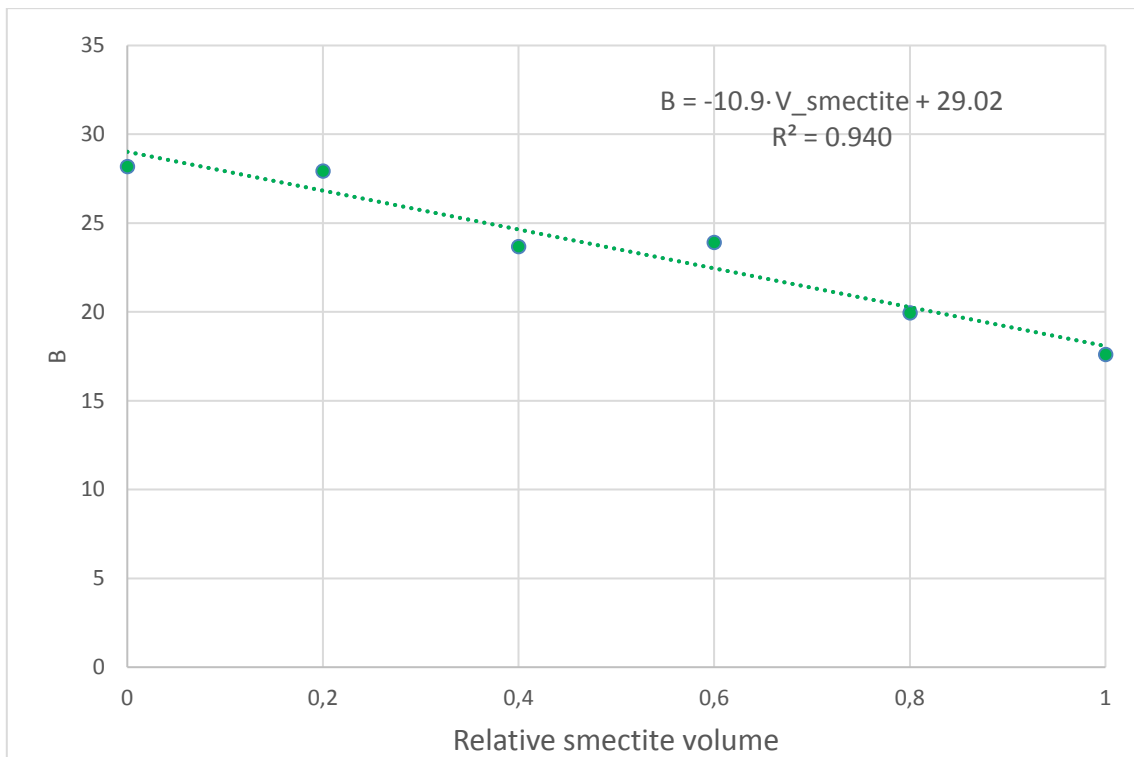


Figure 3.3.1.3. B versus relative smectite volume.

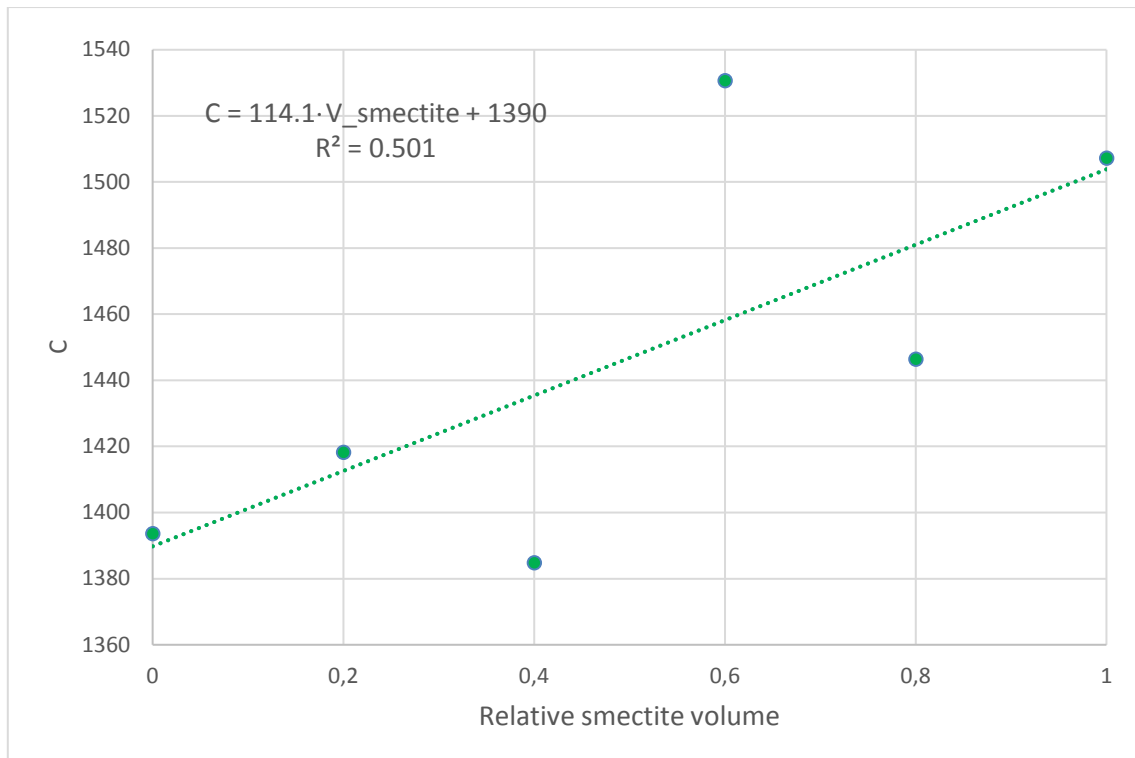


Figure 3.3.1.4. C versus relative smectite volume

The trends in the Figures 3.3.1.2, 3.3.1.3 and 3.3.1.4 show the linear behavior of the parameters A, B, C respectively as functions of the relative smectite volume.

3.3.2. Power model

Polynomial models that were considered above could be the first option of velocities modeling. However, they have some limitations. Notice first of all that $A < 0$ leading to a concave parabola. In particular, when differential pressure is sufficiently large (distant from seabed) then the velocity decreases with increasing differential pressure. This behavior is clearly not physically correct.

Power models were considered as the second possibility of the modeling. Power models were constructed taking into consideration the boundary condition. Compressional velocity of the brine at the seabed (water boundary) was taken as the lowest boundary for the power modeling of compressional velocities against differential pressure. We applied a programming code based on Coppens's (Coppens, 1981), Batzle-Wang's (Batzle & Wang, 1992) models in order to calculate the compressional velocity of the brine at seabed. The codes can be found in the Sections B1 and B2 of the Appendix B. We made calculation of the compressional wave velocity at the seabed for all 12 wells. The values are listed in Table 3.3.2.1.

Table 3.3.2.1.

Compressional wave velocity at seabed for 12 wells based on Batzle-Wang and Coppens modules.

Well	P (Bar)	P (MPa)	V_Coppens (m/s)	V_Batzle-Wang (m/s)	Difference (m/s)	Difference (%)
16/2-12	11.7	1.17	1468.39	1465.86	2.53	0.17
16/2-14_T2	11.5	1.15	1468.36	1465.83	2.53	0.17
16/2-20S	11.2	1.12	1468.31	1465.79	2.52	0.17
16/2-4	11.6	1.16	1468.36	1465.85	2.51	0.17
16/2-5	11.1	1.11	1468.29	1465.77	2.52	0.17
16/3-4A	11.8	1.18	1468.42	1465.88	2.54	0.17
16/3-6	11.9	1.19	1468.42	1465.89	2.53	0.17
16/3-7	11.8	1.18	1468.42	1465.88	2.54	0.17
16/3-8A	11.8	1.18	1468.41	1465.88	2.53	0.17
16/4-5	10.6	1.06	1468.21	1465.70	2.52	0.17
16/4-6S	10.2	1.02	1468.15	1465.64	2.52	0.17
16/5-4	10.9	1.09	1468.28	1465.74	2.54	0.17

It can be seen that values of the compressional velocity at the seabed based on both modules are approximately the same. We should then expect that our models of V_p do not deviate too much from 1470m/s.

The V_{pb} values for the power modeling were defined using the polynomial models for each volume fraction of clay: V_{pb} is equal to C coefficient for zero differential pressure. However, values of V_{pb} that are much lower than the brine water value were replaced with the latter one (such that the V_{pb} values must be close to the brine water velocity value or be higher but strictly not less).

A and B values were obtained after constructing the plots $V_p - V_{pb}$ (difference between experimental values of V_p and the compressional wave velocity of the brine at seabed) against differential pressure. The negative difference between V_p and V_{pb} for particular cases was considered as the most uncertain and it was excluded from the trends.

The values of the power models for V_p fitting for different relative volume fractions of clay for a smectite/kaolinite/brine system are presented in the Table 3.3.2.1.

Table 3.3.2.1.

Results of fitting of laboratory data of V_p to the power model in a smectite/kaolinite/brine system.

Relative smectite volume	Relative kaolinite volume	A	B	V_{pb}
0	1	28.2	0.846	1470
0.2	0.8	69.001	0.631	1420
0.4	0.6	15.9	0.957	1470
0.6	0.4	46.8	0.698	1530
0.8	0.2	41.5	0.673	1450
1	0	31.1	0.756	1470

The Figure 3.3.2.1 represents a power model of the compressional wave velocity V_p versus differential pressure for the certain relative volume fractions of clay.

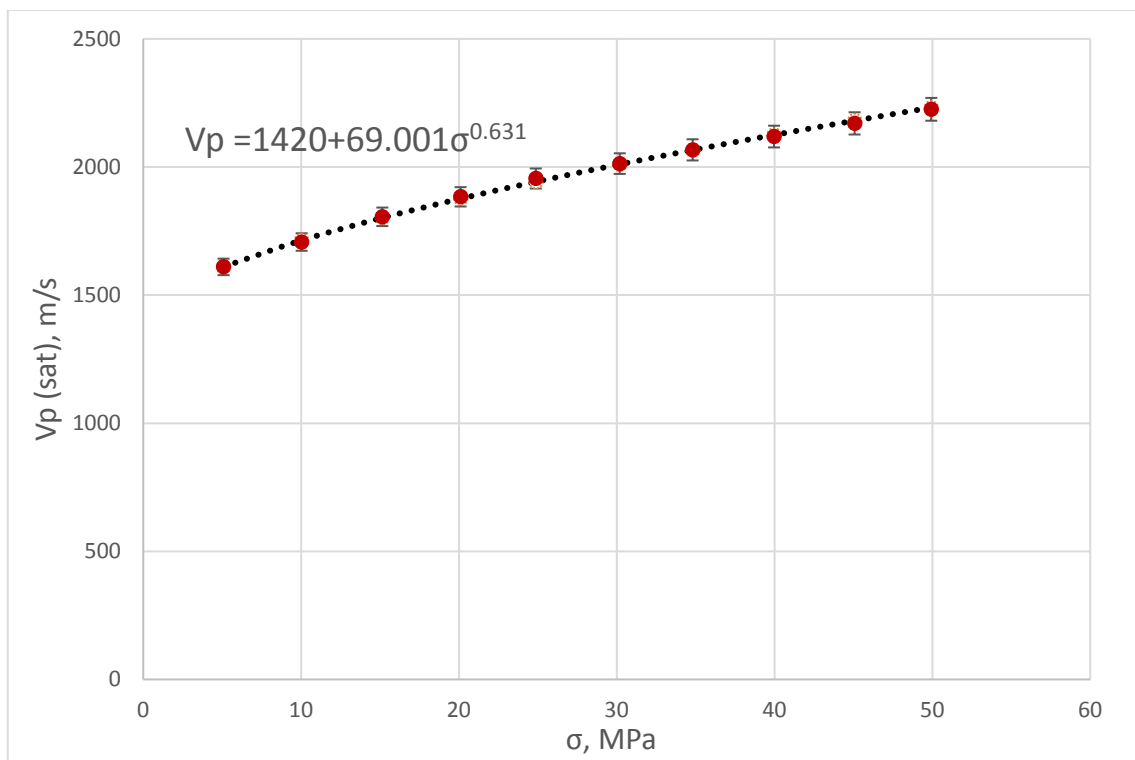


Figure 3.3.2.1. Power model for V_p fitting when relative volume of kaolinite is 0.8 and relative volume of smectite is 0.2.

The power models for V_p fitting for other clay compositions in a smectite/kaolinite/brine system are similar and they are presented in the Section A1.2 of Appendix A.

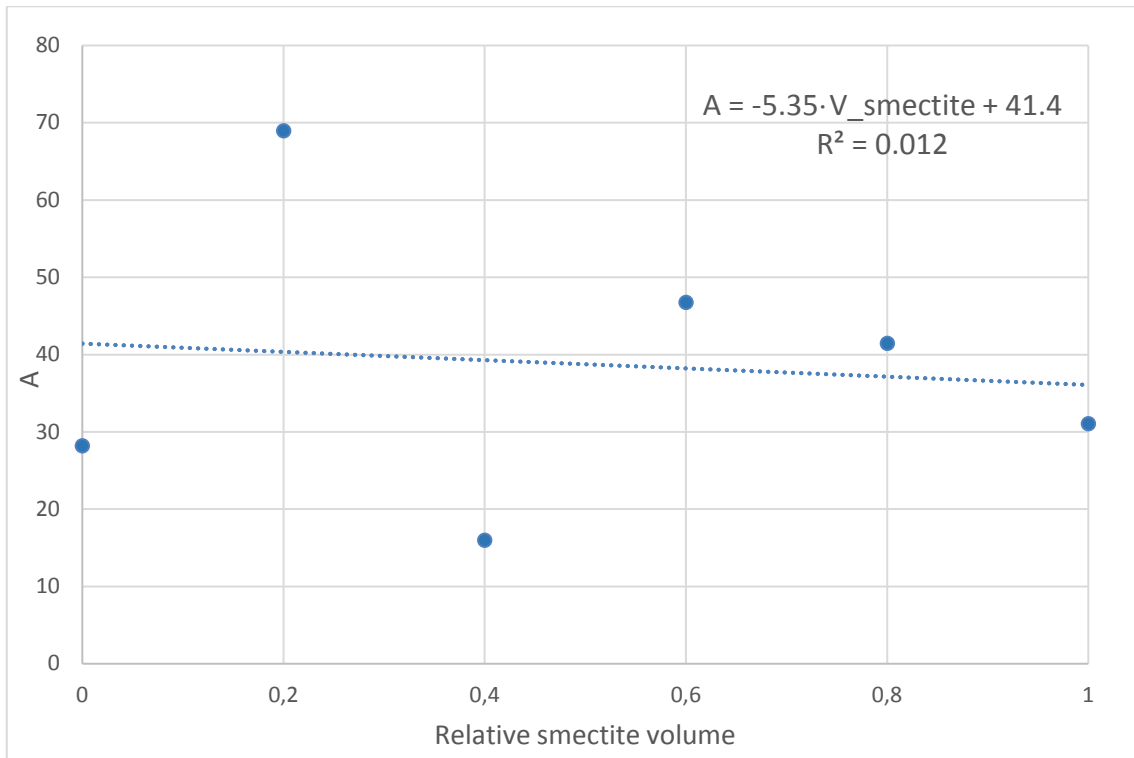


Figure 3.3.2.2. A versus relative smectite volume including outliers

Figure 3.3.2.2. shows the behavior of the parameter A as a function of the relative smectite volume. It can be noticed that two points in the graph look like outliers. Hence, they were neglected from the trend.

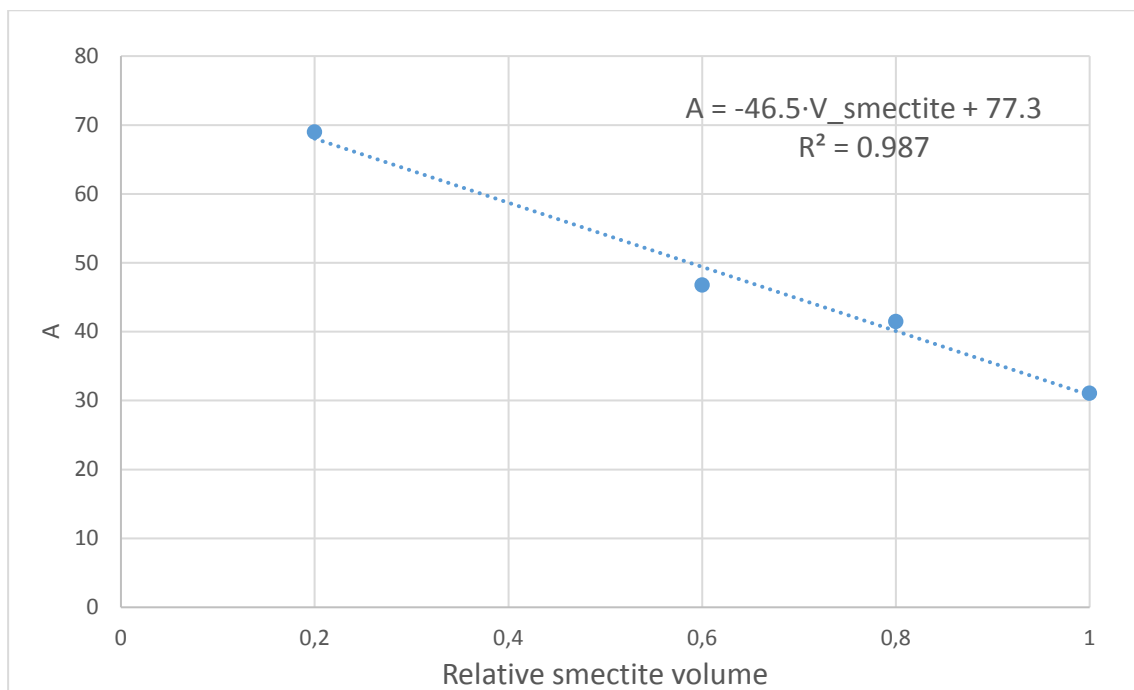


Figure 3.3.2.3. A versus smectite volume without outliers.

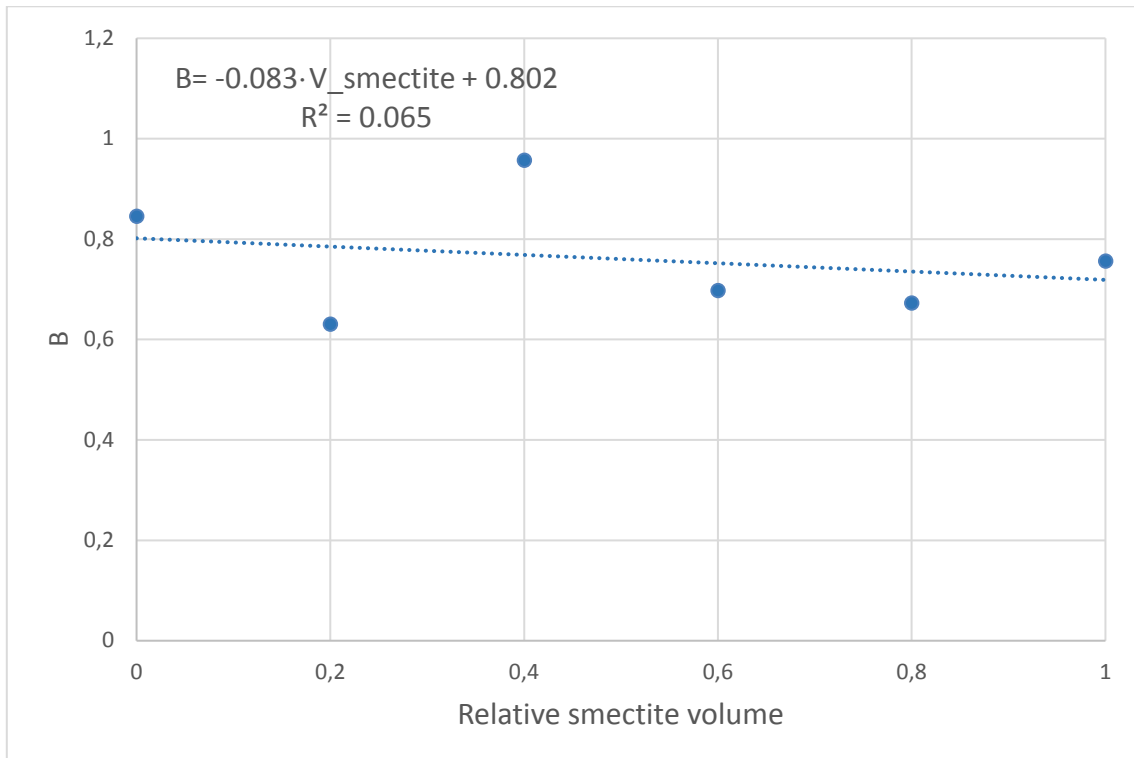


Figure 3.3.2.4. B versus relative smectite volume.

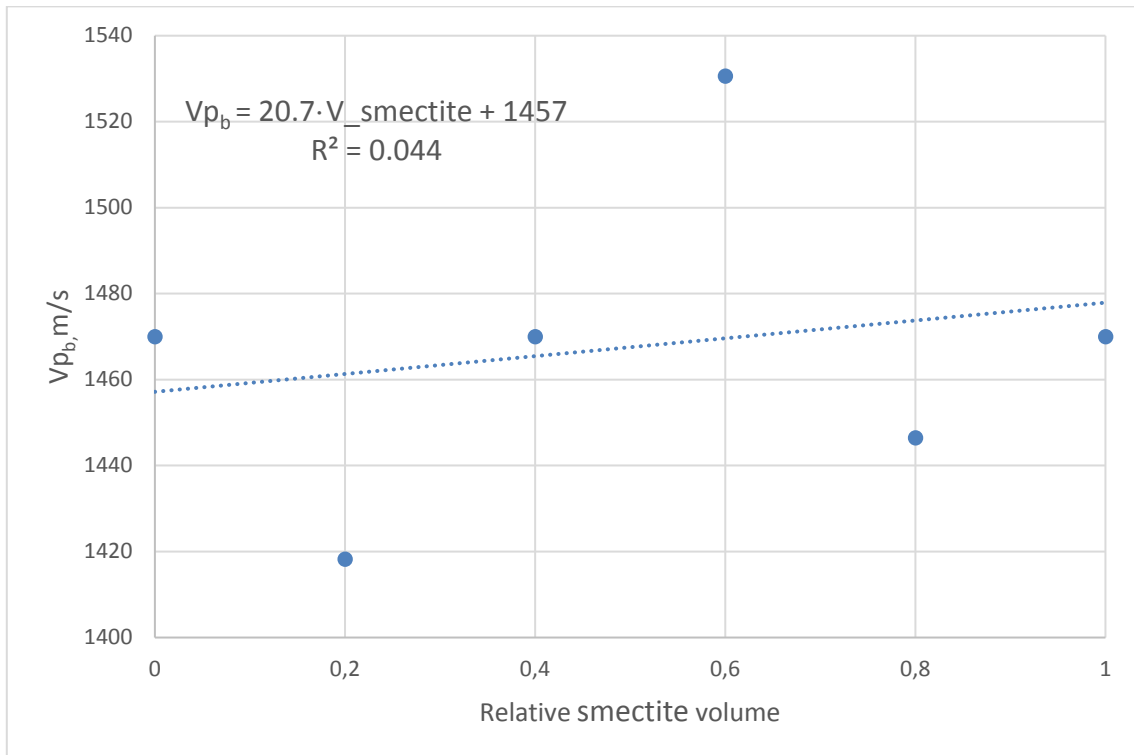


Figure 3.3.2.5. Vp_b versus relative smectite volume including outliers.

Similarly to the parameter A, the V_{p_b} versus relative smectite volume has two points that can be considered as deviation from the trend. Thus, they were excluded from it.

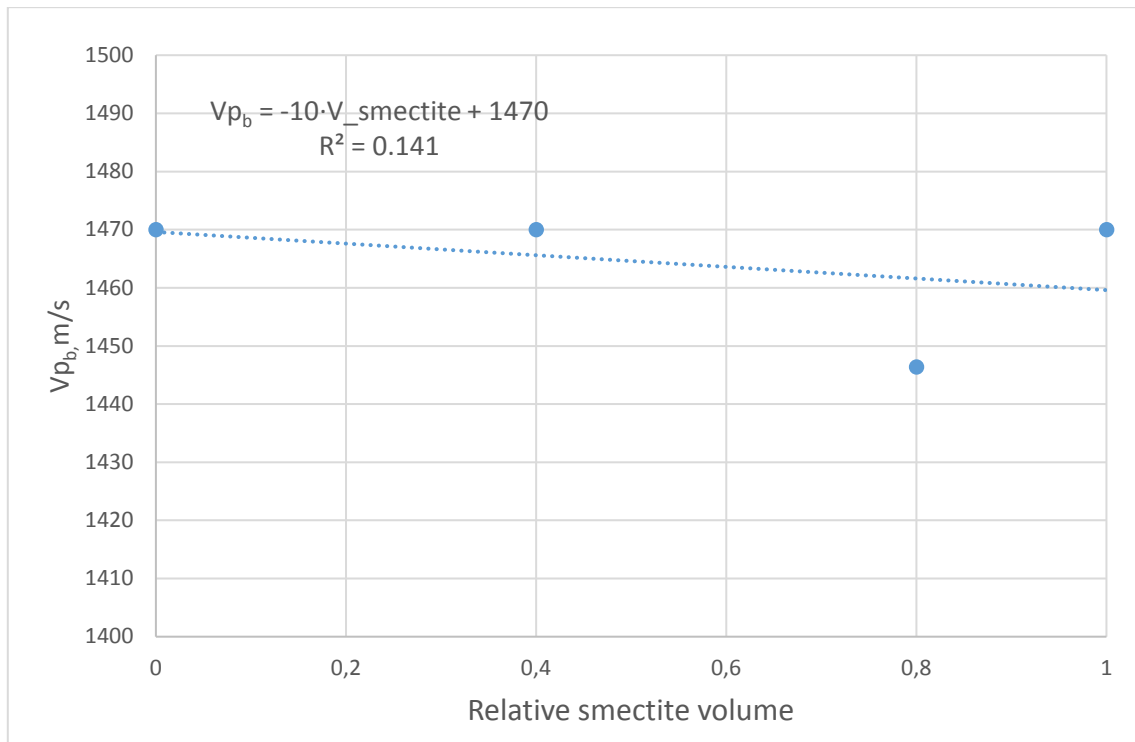


Figure 3.3.2.6. V_{p_b} versus relative smectite volume without outliers.

3.4. Modeling of compressional velocity in a kaolinite/silt/brine system with varying differential pressure

3.4.1. Second order polynomial model

The values of the second order polynomial models for V_p fitting for different relative volume fractions of clay in a kaolinite/silt/brine system are presented in the table 3.4.1.1.

Table 3.4.1.1.

Results of fitting of laboratory data of V_p to the second order polynomial model in a kaolinite/silt/brine system.

Relative silt volume	Relative kaolinite volume	A	B	C	R^2
1	0	-0.144	20.7	1420	0.999
0.75	0.25	-0.389	41.3	1500	0.984
0.5	0.5	-0.495	48.2	1320	0.969
0.25	0.75	-0.478	45.7	1320	0.973

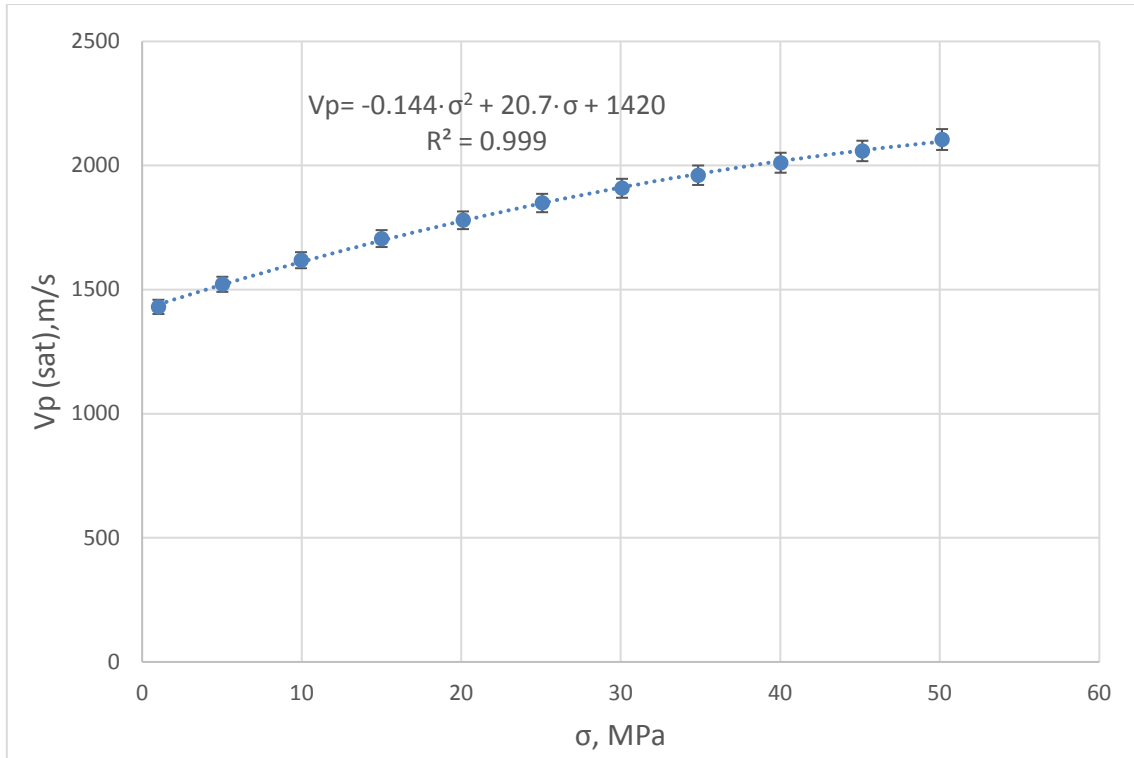


Figure 3.4.1.1. Second order polynomial model for V_p fitting when relative volume fraction of kaolinite is 0 and relative volume fraction of silt is 1.0.

The second order polynomial models for V_p fitting for other clay composition in a kaolinite/silt/brine system are represented in the Section A1.3 of Appendix A.

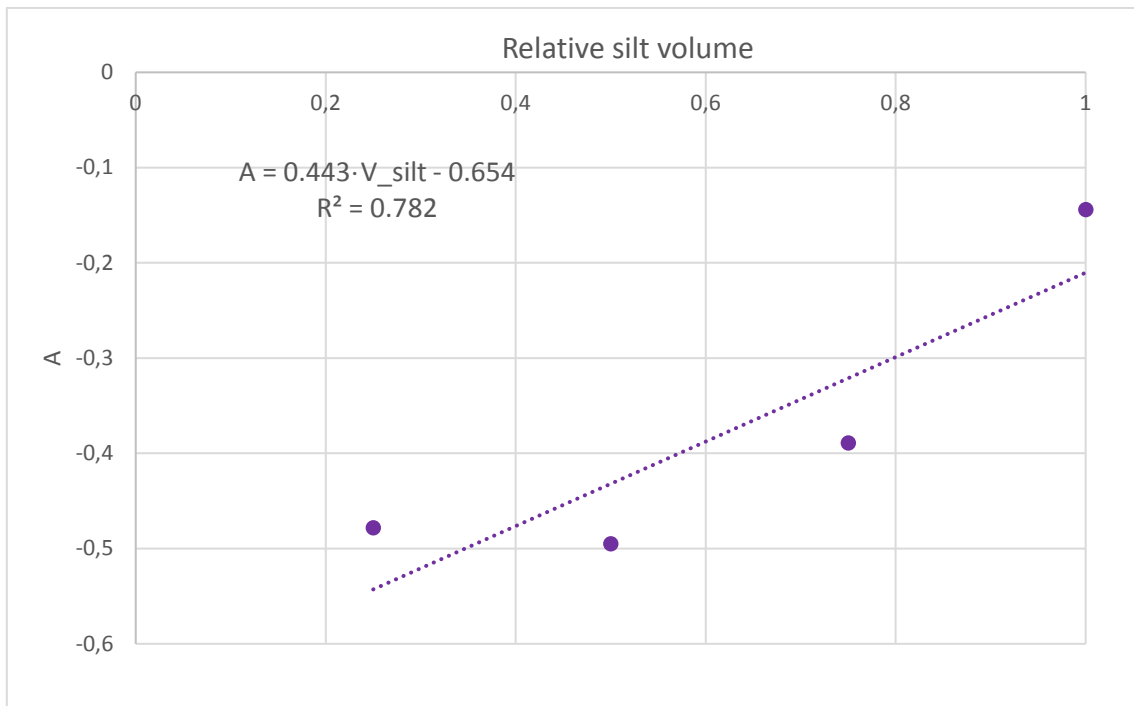


Figure 3.4.1.2. A versus relative silt volume

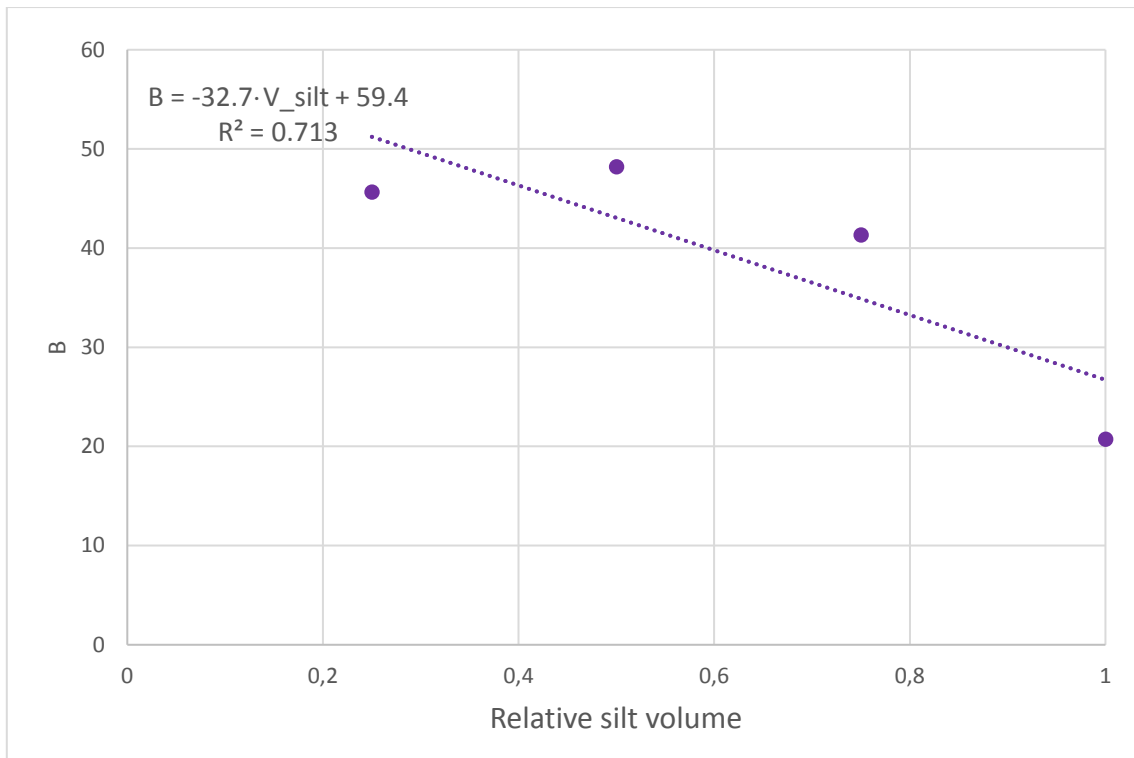


Figure 3.4.1.3. B versus relative silt volume.

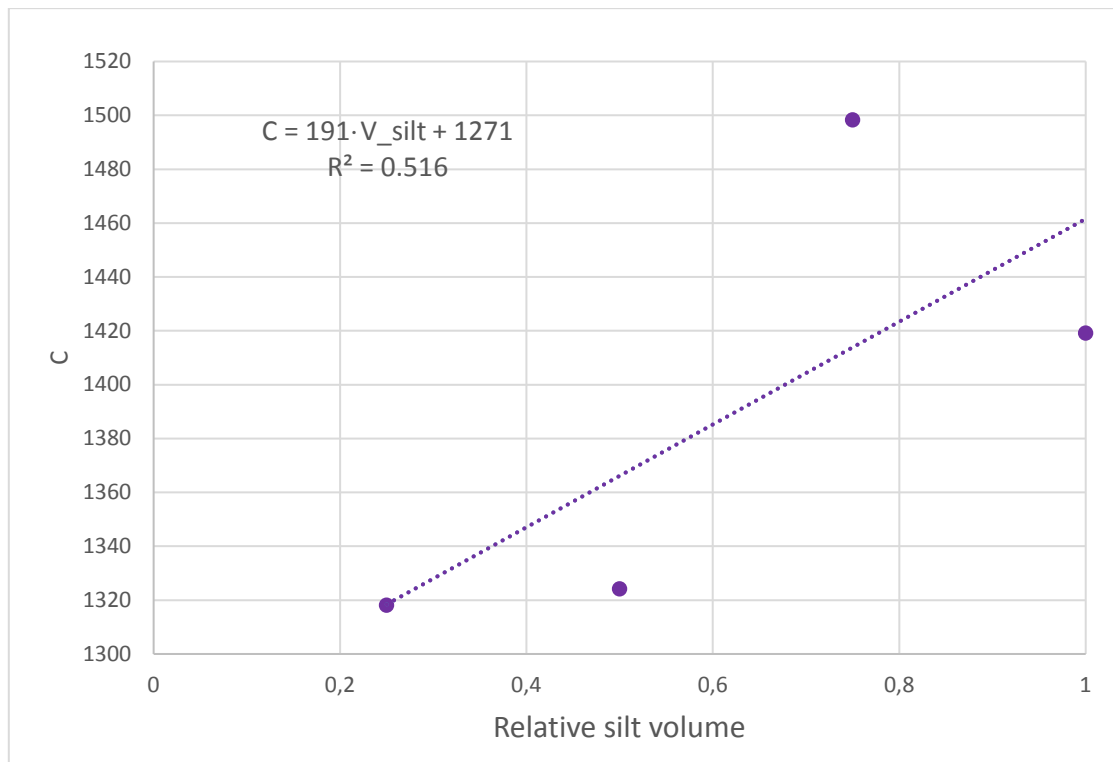


Figure 3.4.1.4. C versus relative silt volume.

The parameters A, B and C versus relative silt volume in the Figures 3.4.1.2, 3.4.1.3 and 3.4.1.4 have a linear behavior.

3.4.2. Power model

The values of the power models for V_p fitting for different clay compositions in a kaolinite/silt/brine system are presented in the Table 3.4.2.1.

Table 3.4.2.1.

Result of fitting of laboratory data of V_p to the power model in a kaolinite/silt/brine system.

Relative silt volume	Relative kaolinite volume	A	B	V_{pb}
1	0	15.2	1.020	1420
0.75	0.25	100.82	0.626	1500
0.5	0.5	54.8	0.785	1470
0.25	0.75	47.2	0.805	1470

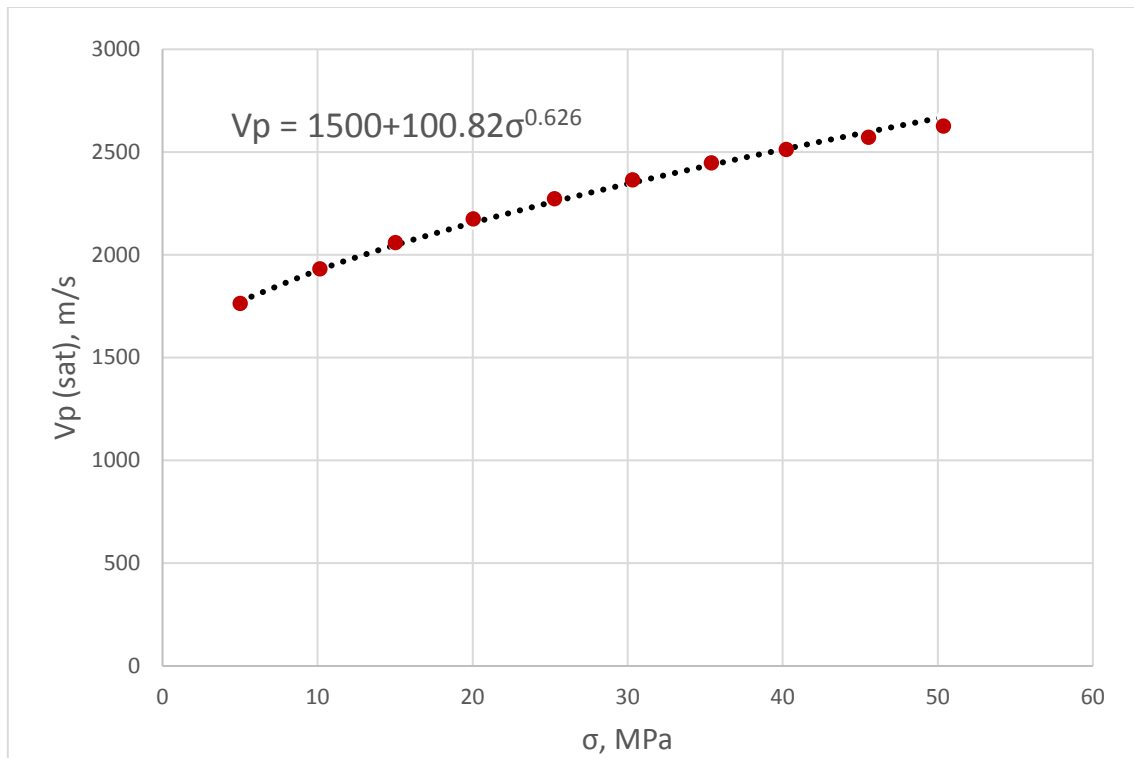


Figure 3.4.2.1. Power model for V_p fitting when relative volume fraction of kaolinite is 0.25 and relative volume fraction of silt is 0.75.

The power models for V_p fitting for other relative volume fractions of clay in a kaolinite/silt/brine system are presented in the Section A1.4 of Appendix A.

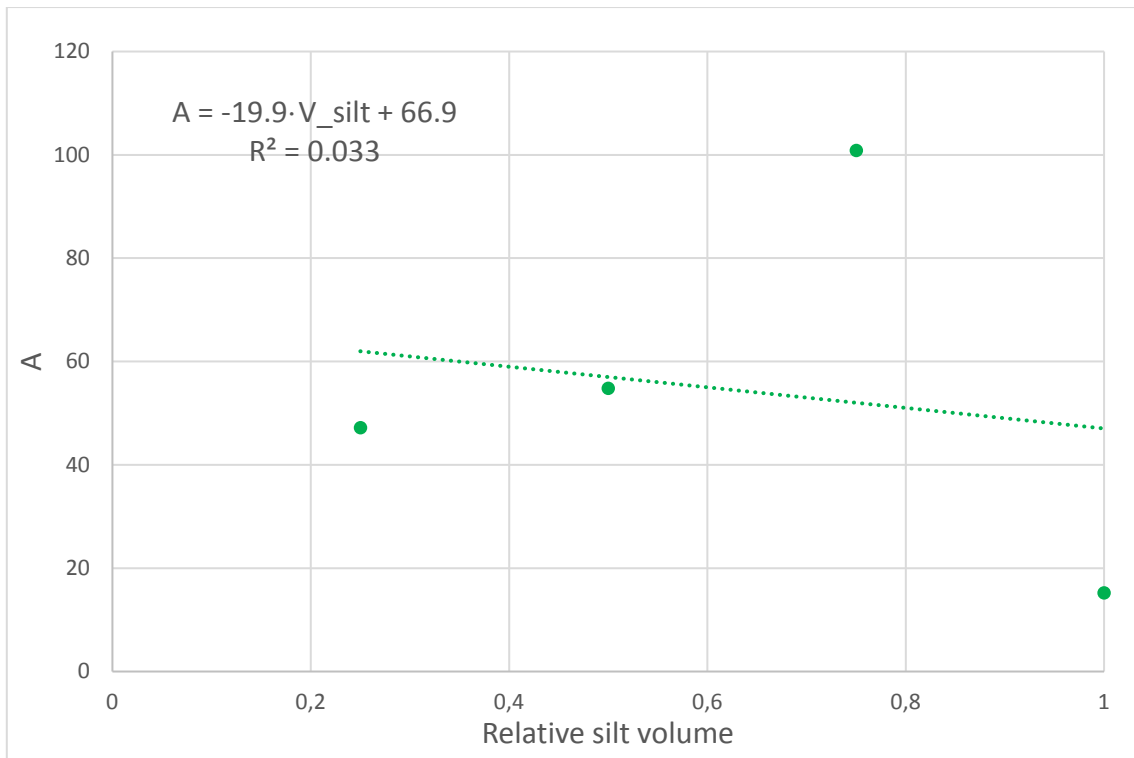


Figure 3.4.2.2. A versus relative silt volume including an outlier.

There is one point in the Figure 3.4.2.2 which looks like an outlier. We omitted this point from the trend.

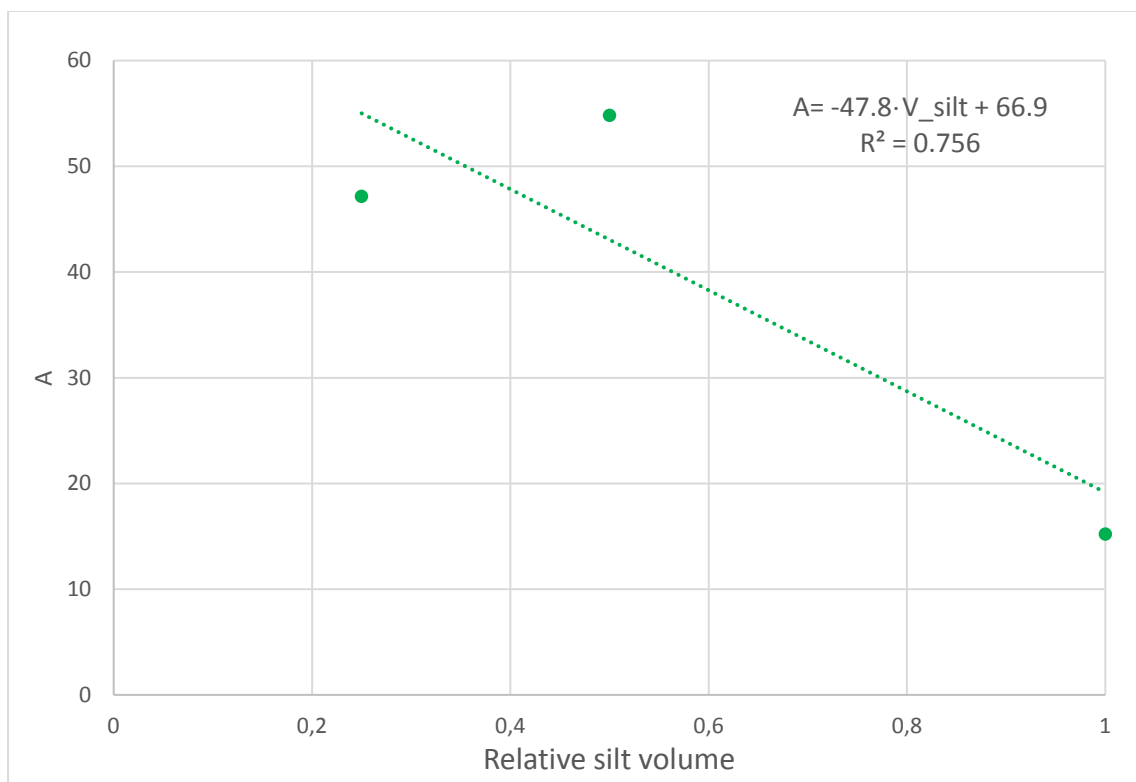


Figure 3.4.2.3. A versus relative silt volume without an outlier.

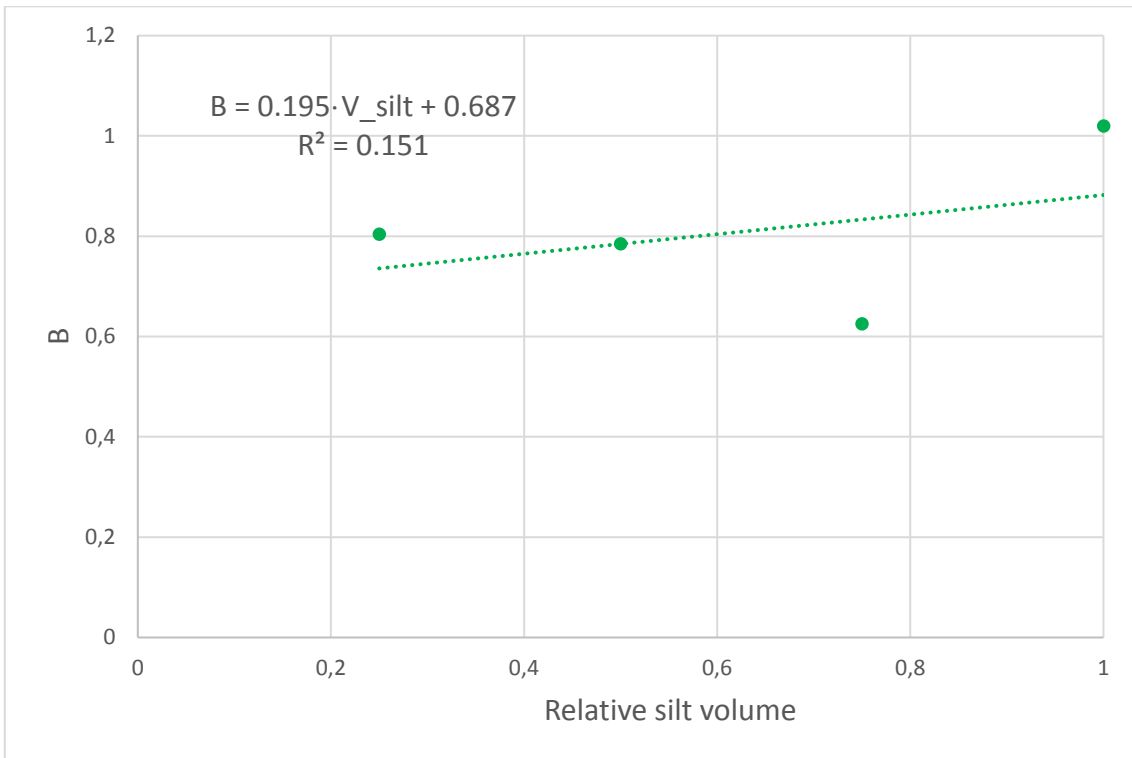


Figure 3.4.2.4. B versus relative silt volume.

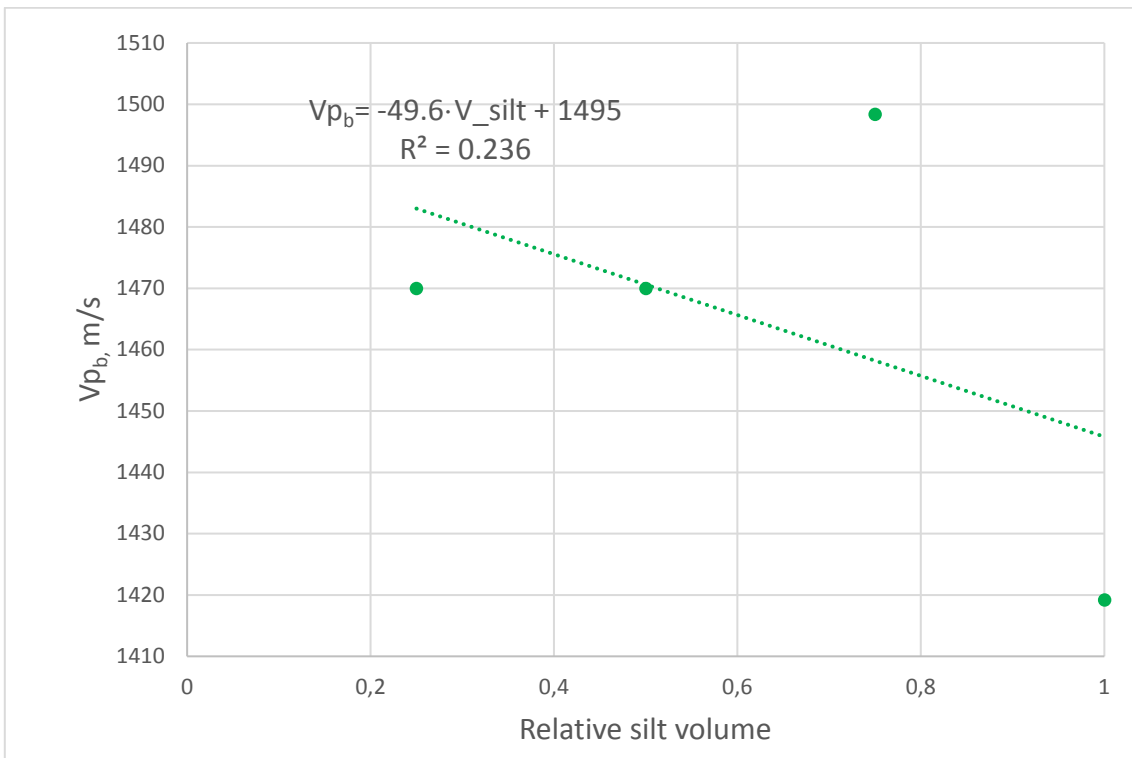


Figure 3.4.2.5. V_{p_b} versus relative silt volume including an outlier.

In the Figure 3.4.2.5. one point visibly deviates from the whole trend and, thus, it was neglected as well.

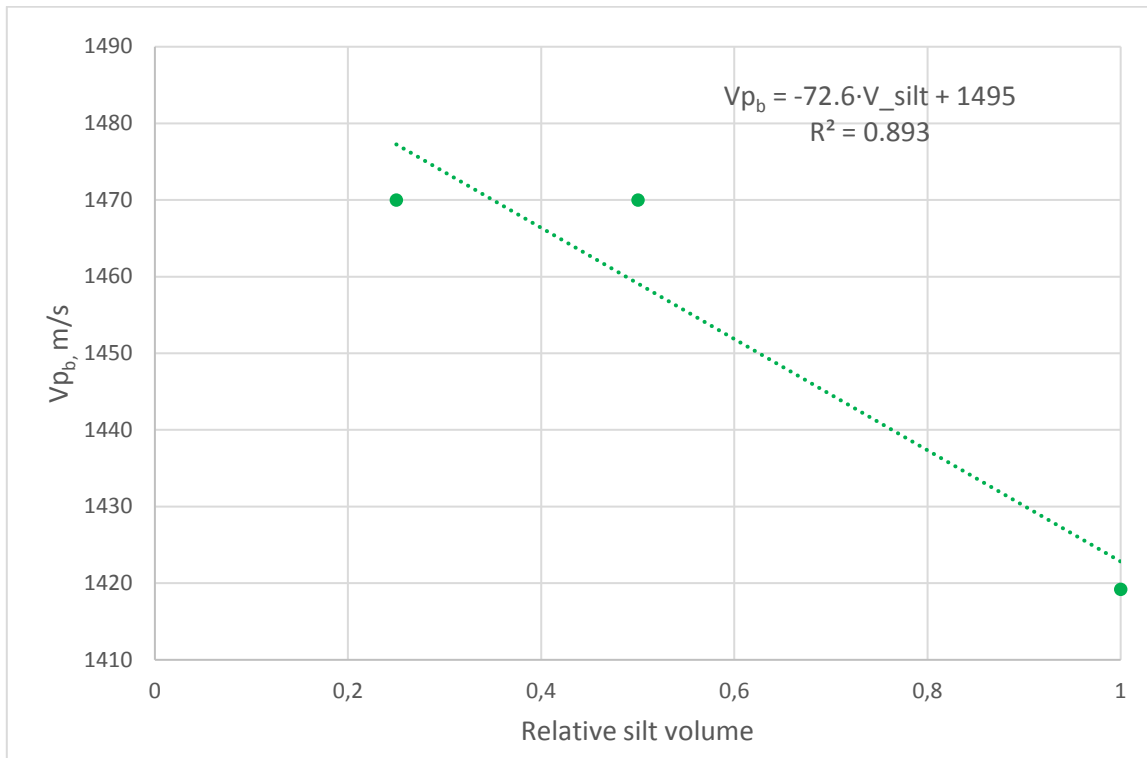


Figure 3.4.2.6. Vp_b versus relative silt volume without an outlier.

3.5. Modeling of shear wave velocity in a smectite/kaolinite/brine system with varying differential pressure

3.5.1. Second order polynomial model

The second order polynomial models for shear wave velocity have a similar behavior as for compressional wave velocities.

The values of the shear wave velocity of second order polynomial models for various relative volume fractions of clay in a smectite/kaolinite/brine system are presented in the Table 3.5.1.1.

Table 3.5.1.1.

Results of fitting of laboratory data of V_s to the second order polynomial model in a smectite/kaolinite/brine system.

Relative smectite volume	Relative kaolinite volume	A	B	C	R ²
0	1	-0.172	18.9	369	0.995
0.2	0.8	-0.152	17.6	395	0.996
0.4	0.6	-0.127	15.2	374	0.997
0.6	0.4	-0.119	15.04	384	0.999
0.8	0.2	-0.103	13.3	324	0.994
1	0	-0.0675	8.81	313	0.996

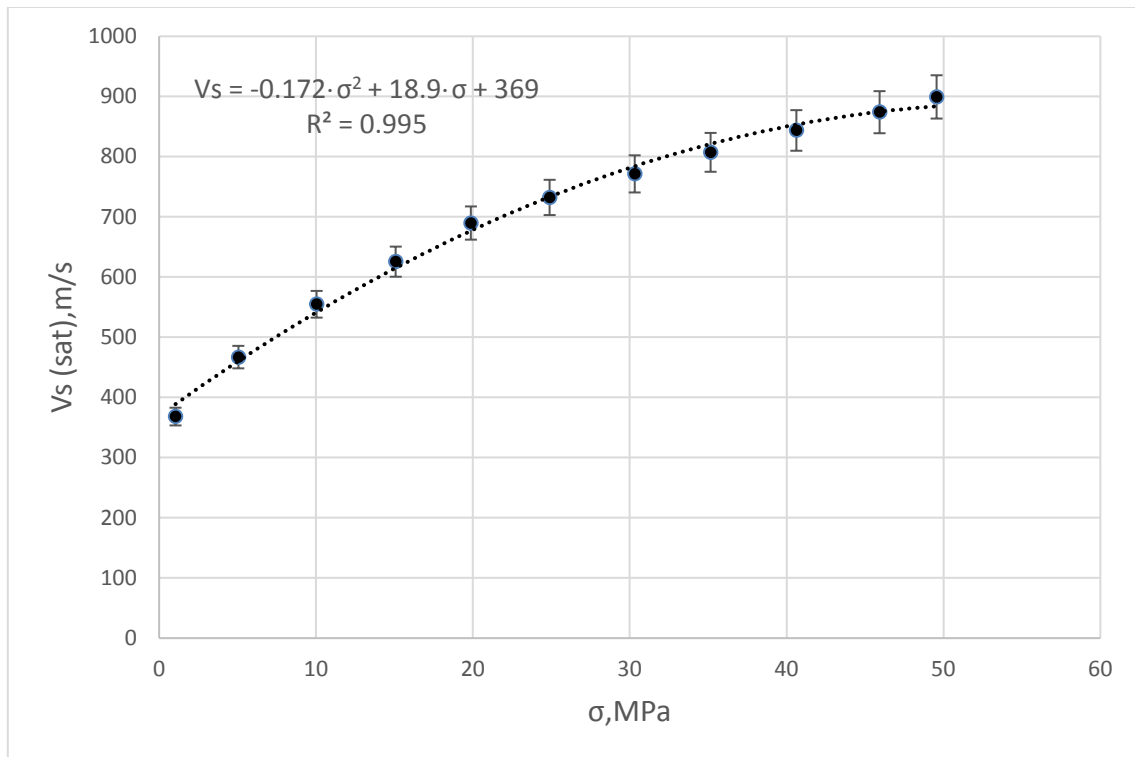


Figure 3.5.1.1. Second order polynomial model for V_s fitting when relative volume fraction of kaolinite is 1 and relative volume fraction of smectite is 0.

The second order polynomial models for V_s fitting for other clay composition in a smectite/kaolinite/brine system are listed in the Section A2.1 of Appendix A.

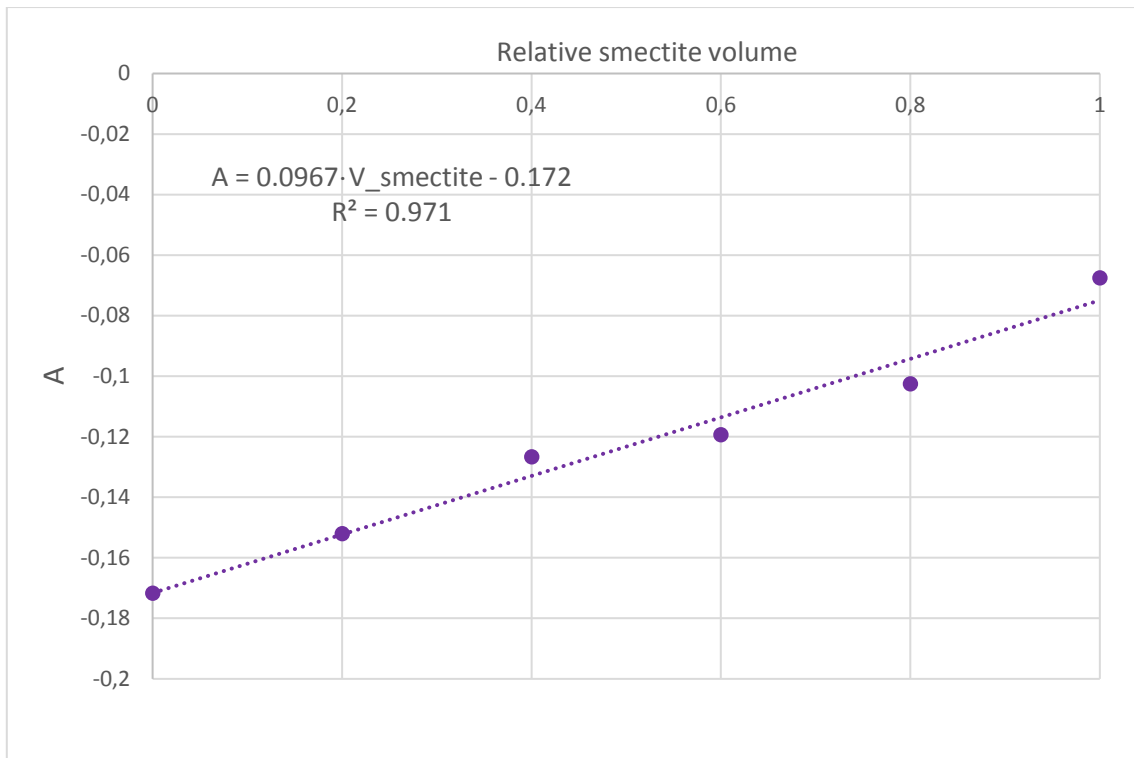


Figure 3.5.1.2. A versus relative smectite volume.

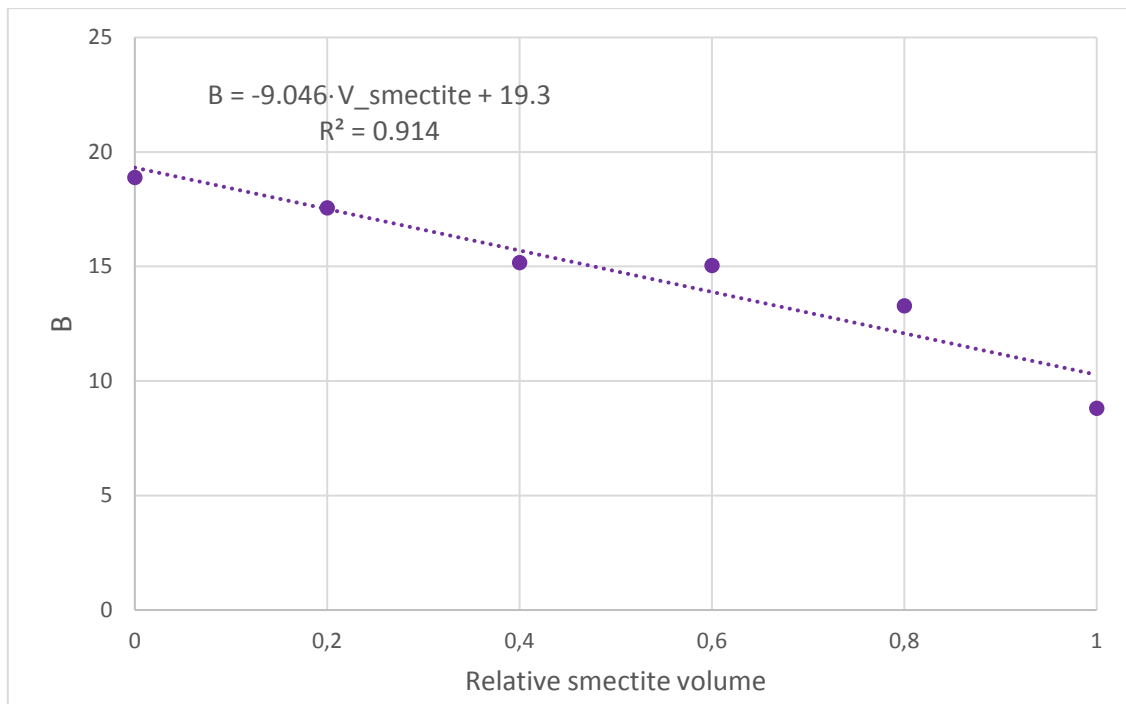


Figure 3.5.1.3. B versus relative smectite volume.

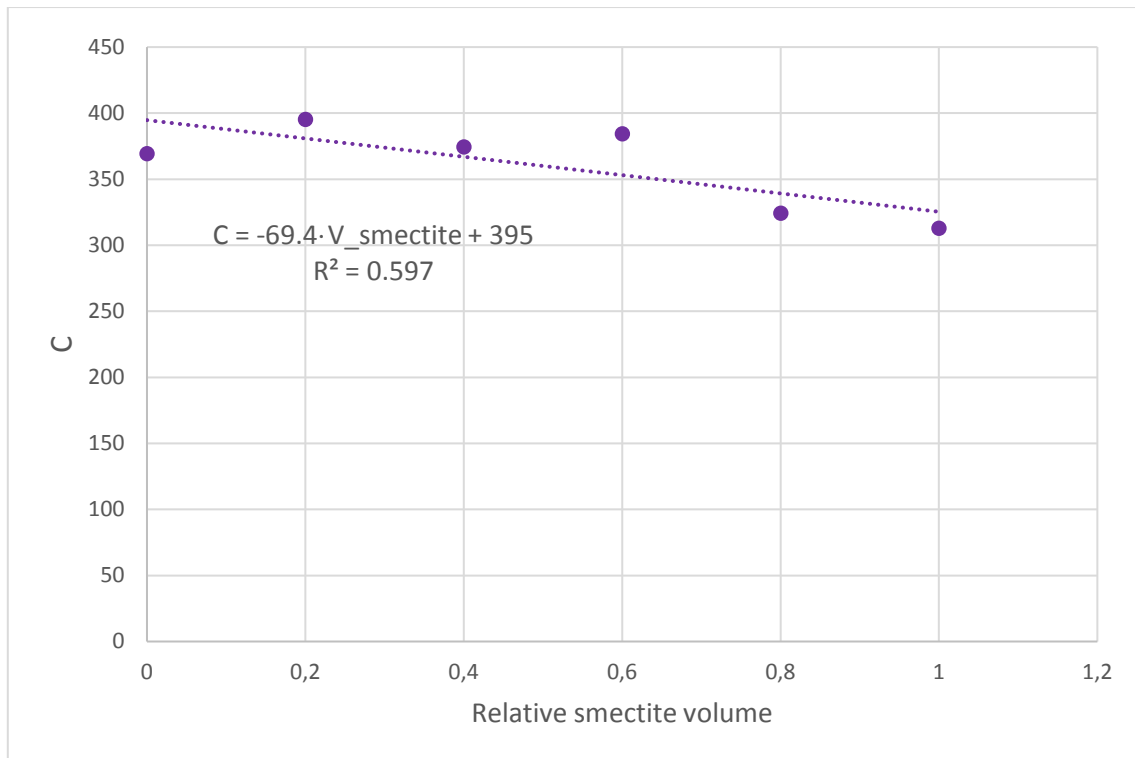


Figure 3.5.1.4. C versus relative smectite volume.

In Figures 3.5.1.2, 3.5.1.3 and 3.5.1.4 the parameters A, B and C as functions of smectite volume have a linear trend similarly to the trends obtained from Vp models.

3.5.2. Power model

Power models for Vs fitting are similar to the power models for the compressional wave velocity. They also follow the boundary condition described earlier.

It is known that shear wave velocity does not propagate in fluids, in particular, in sea water. Hence, there is no particular lowest limit of the shear wave velocity of the brine in this case. V_{sb} was chosen for each clay composition type based on the second order polynomial models: V_{sb} is equal to C coefficient for zero differential pressure. A and B values were obtained after constructing the plots $V_s - V_{sb}$ (difference between experimental values of Vs and the shear wave velocity of the brine at seabed) against differential pressure. The negative difference between Vs and V_{sb} for certain points was excluded from the trends.

The values of the shear-wave velocity power models for Vs fitting in a smectite/kaolinite/brine system are given in the Table 3.5.2.1.

Table 3.5.2.1.

Results of fitting of laboratory data of V_s to the power model in a smectite/kaolinite/brine system.

Relative smectite volume	Relative kaolinite volume	A	B	V_{Sb}
0	1	34.09	0.719	369
0.2	0.8	34.6	0.699	395
0.4	0.6	8.99	1.068	374
0.6	0.4	16.5	0.885	384
0.8	0.2	21.7	0.769	324
1	0	16.4	0.731	313

The power model below shows the shear wave velocity against the differential pressure for the one particular case when relative volume fraction of kaolinite constitutes 1 and relative volume fraction of smectite is zero.

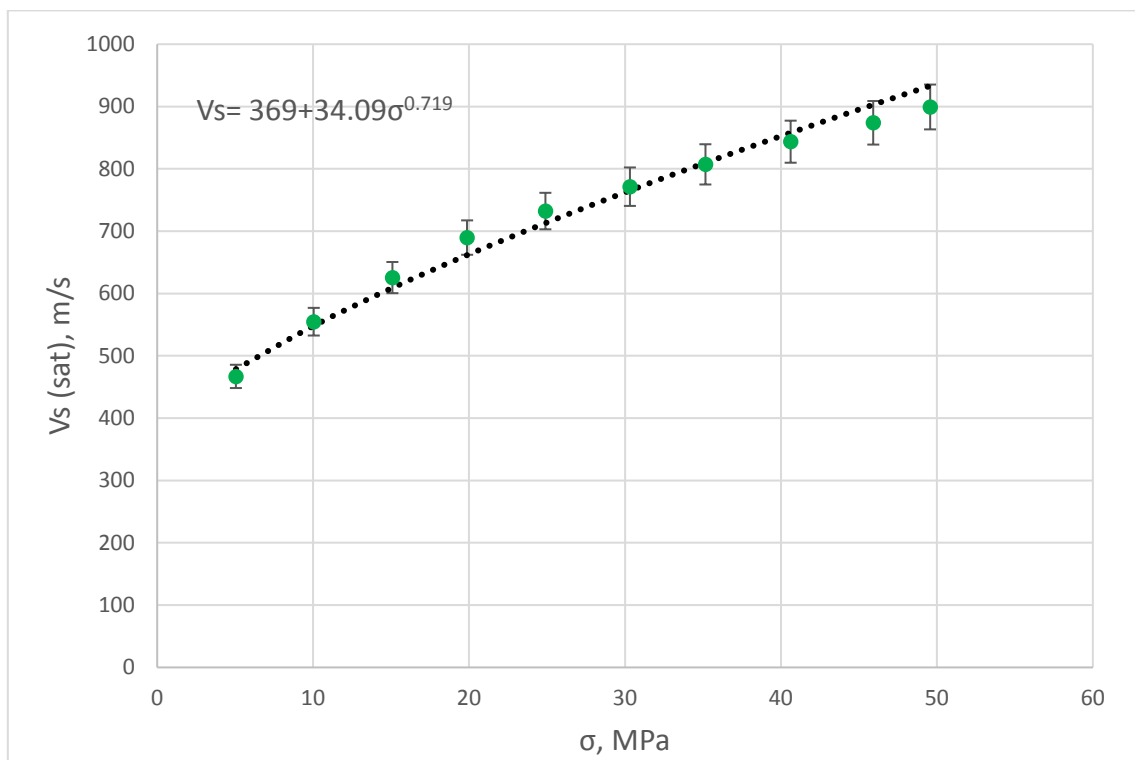


Figure 3.5.2.1. Power model for V_s fitting when relative volume fraction of kaolinite is 1 and relative volume fraction of smectite is 0.

The power models for Vs fitting for other clay composition in a smectite/kaolinite/brine system are comparable to the model above and they are presented in the Section A2.2 of Appendix A.

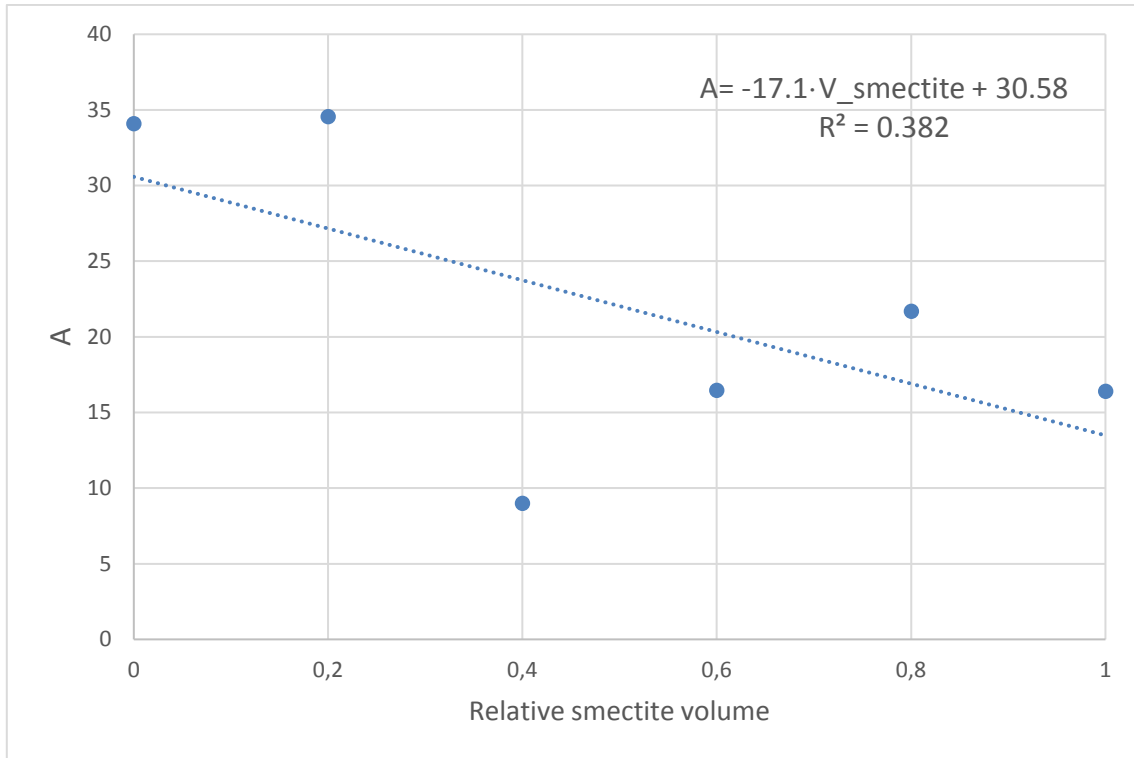


Figure 3.5.2.2. A versus relative smectite volume including an outlier.

One point in the Figure 3.5.2.2 could be considered as an outlier. Hence, it was excluded from the trend.

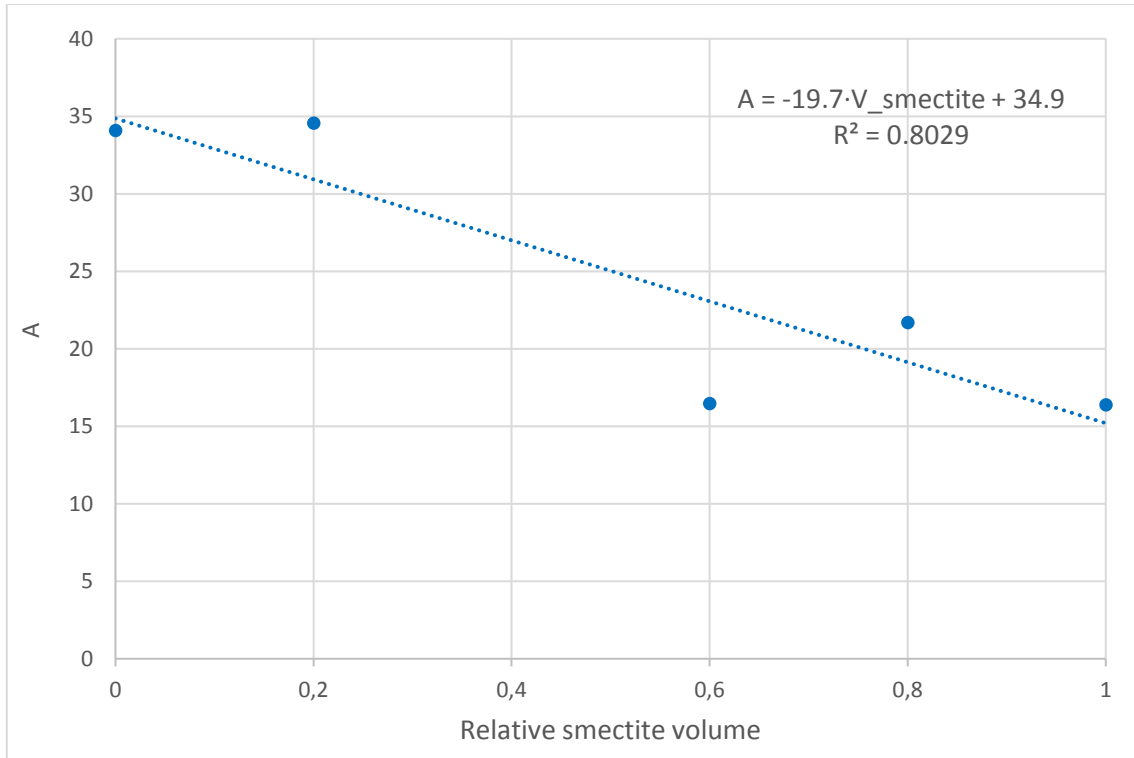


Figure 3.5.2.3. A versus relative smectite volume without an outlier.

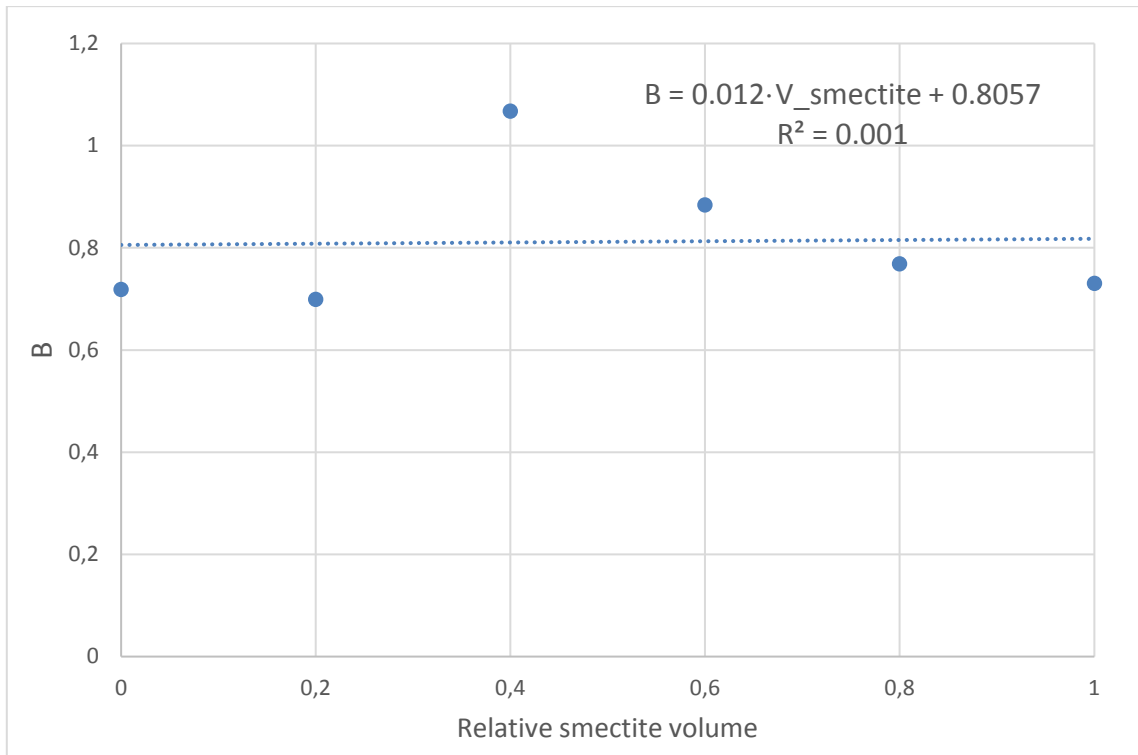


Figure 3.5.2.4. B versus relative smectite volume.

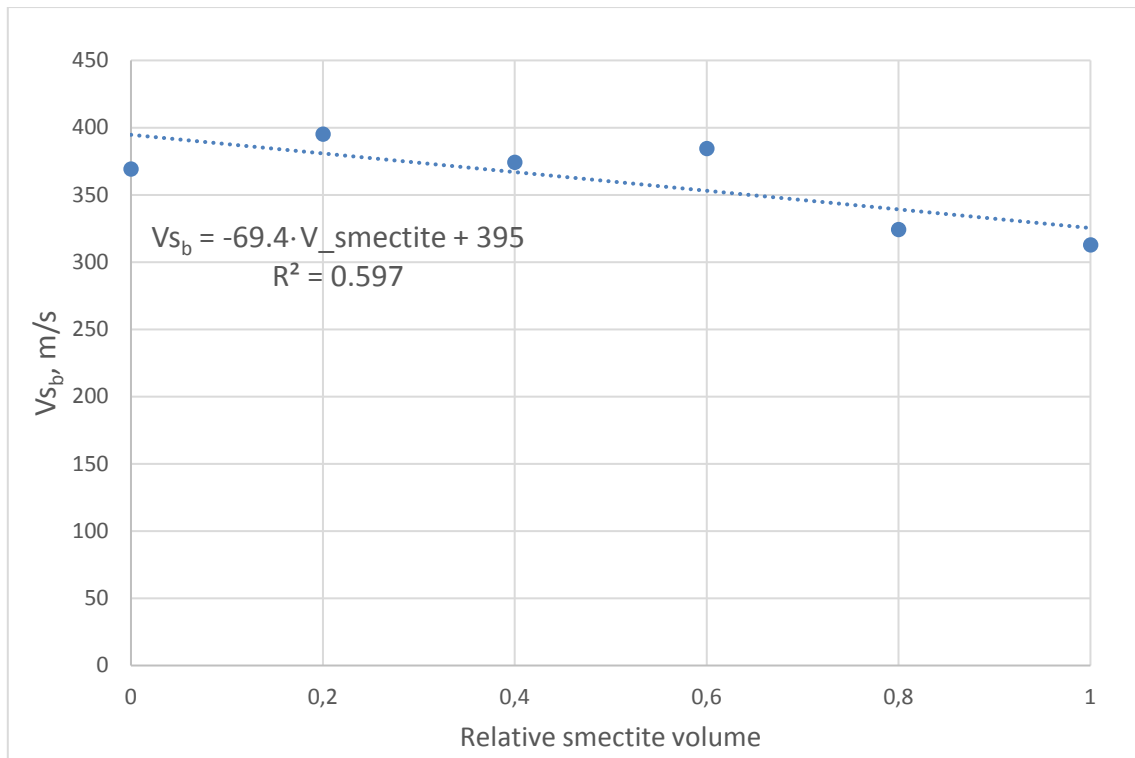


Figure 3.5.2.5. V_{s_b} versus relative smectite volume.

We did not change the trends for parameters B and V_{s_b} as functions of relative smectite volume in the Figures 3.5.2.4 and 3.5.2.5, because we think there are no points in these graphs which deviate significantly from the trends.

3.6. Modeling of shear wave velocity in a kaolinite/silt/brine system with varying differential pressure

3.6.1. Second order polynomial model

The values of the second order polynomial models for V_s fitting for different clay composition in a kaolinite/silt/brine system are presented in the Table 3.6.1.1.

Table 3.6.1.1.

Results of fitting of laboratory data of V_s to the second order polynomial model in a kaolinite/silt/brine system.

Relative silt volume	Relative kaolinite volume	A	B	C	R ²
1	0	-0.1301	15.9	305.7	0.998
0.75	0.25	-0.251	27.7	379	0.993
0.5	0.5	-0.281	29.3	334	0.987
0.25	0.75	-0.229	25.4	311	0.993

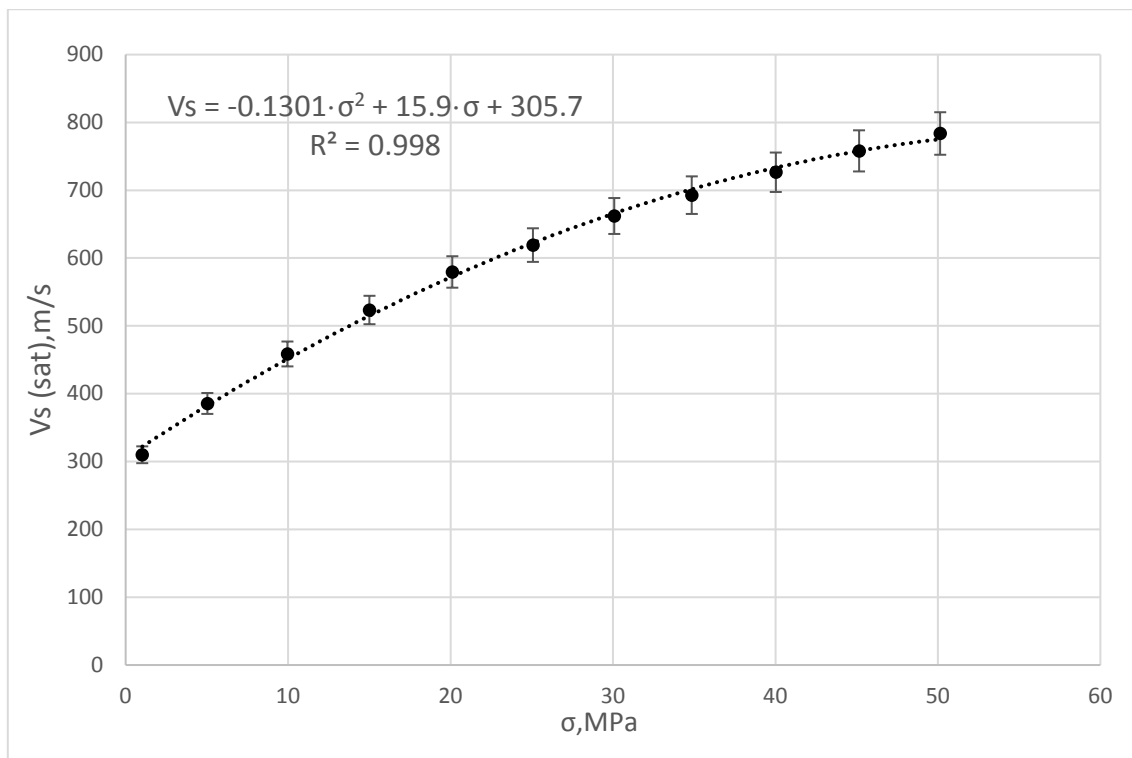


Figure 3.6.1.1. Second order polynomial model for V_s fitting when relative volume fraction of kaolinite is 0 and relative volume fraction of silt is 1.0

The second order polynomial models for other relative volume fractions of clay in a kaolinite/silt/brine system are similar to the model above and they are presented in the Section A2.3 of Appendix A.

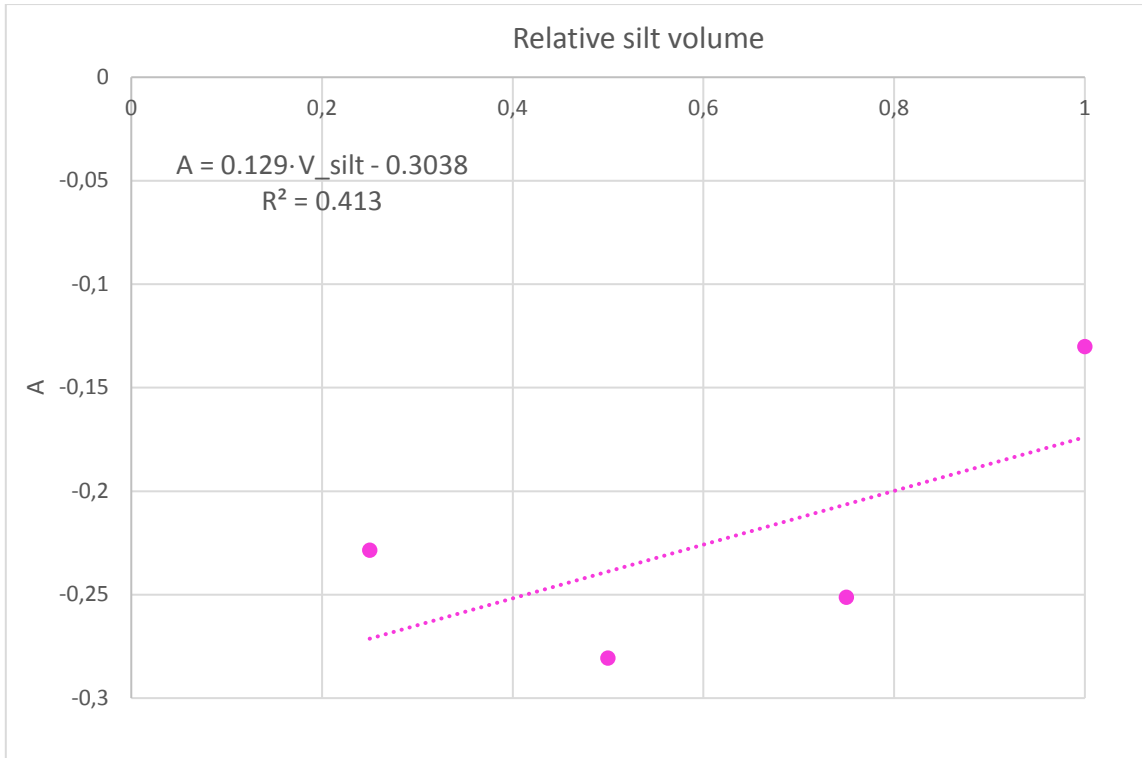


Figure 3.6.1.2. A versus relative silt volume.

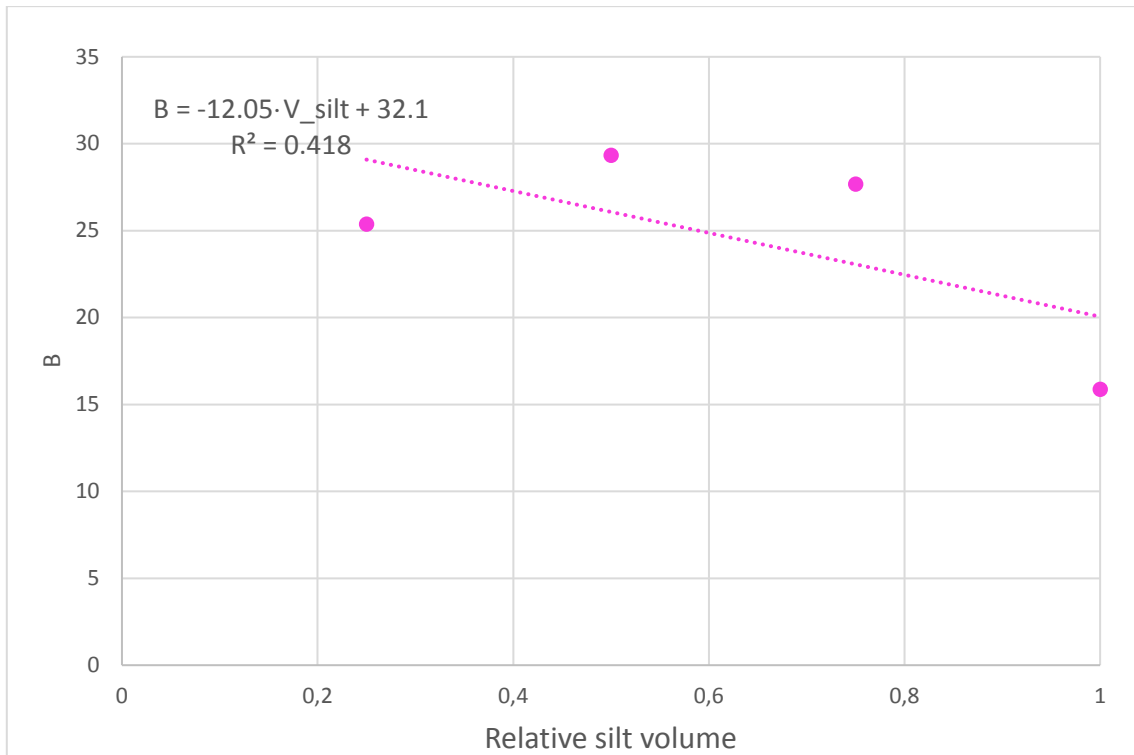


Figure 3.6.1.3. B versus relative silt volume.

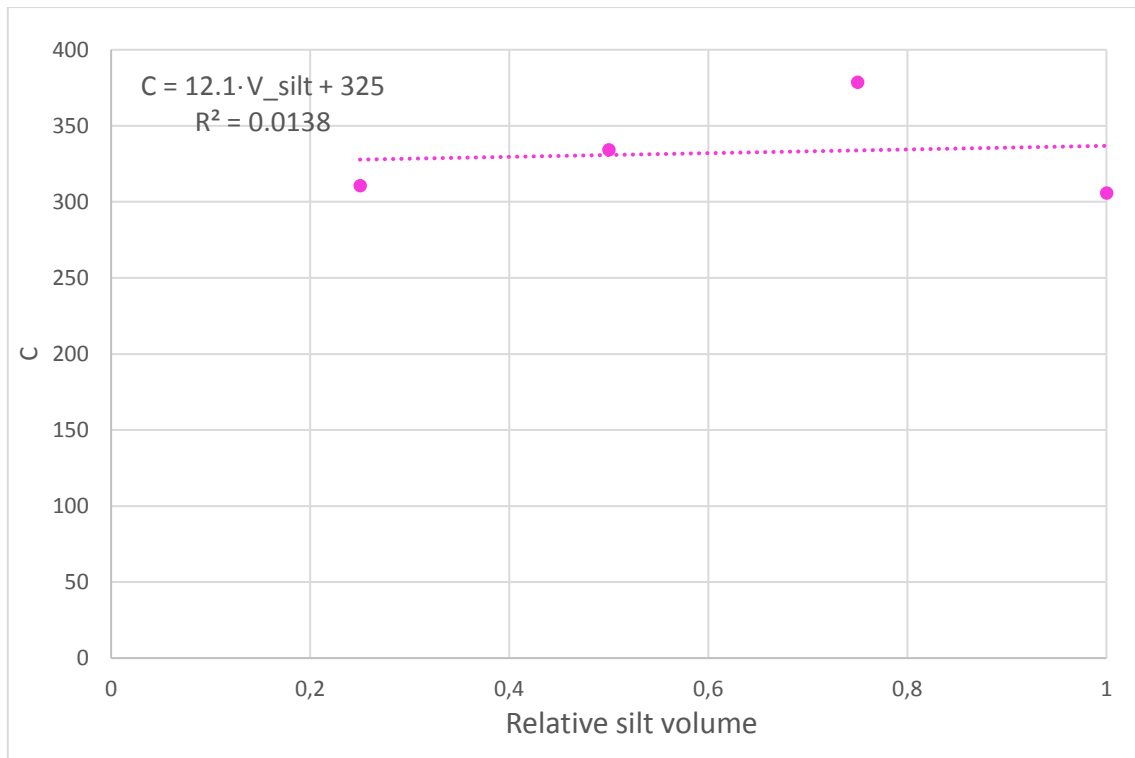


Figure 3.6.1.4. C versus relative silt volume.

Figures 3.6.1.2, 3.6.1.3 and 3.6.1.4 show the linear behavior of the parameters A, B and C as functions of the silt volume.

3.6.2. Power model

The values of the power models for shear wave velocity fitting for various relative volume fractions of clay in a kaolinite/silt/brine system are presented in the Table 3.6.2.1.

Table 3.6.2.1.

Results of fitting of laboratory data of V_s to the power model in a kaolinite/silt/brine system.

Relative silt volume	Relative kaolinite volume	A	B	V_{Sb}
1	0	7.32	1.15	305.7
0.75	0.25	50.48	0.716	379
0.5	0.5	61.8	0.667	334
0.25	0.75	48.3	0.7055	311

The power model showing the shear wave velocity against the differential pressure for the one particular relative volume fraction of clay is shown below in the Figure 3.6.2.1.

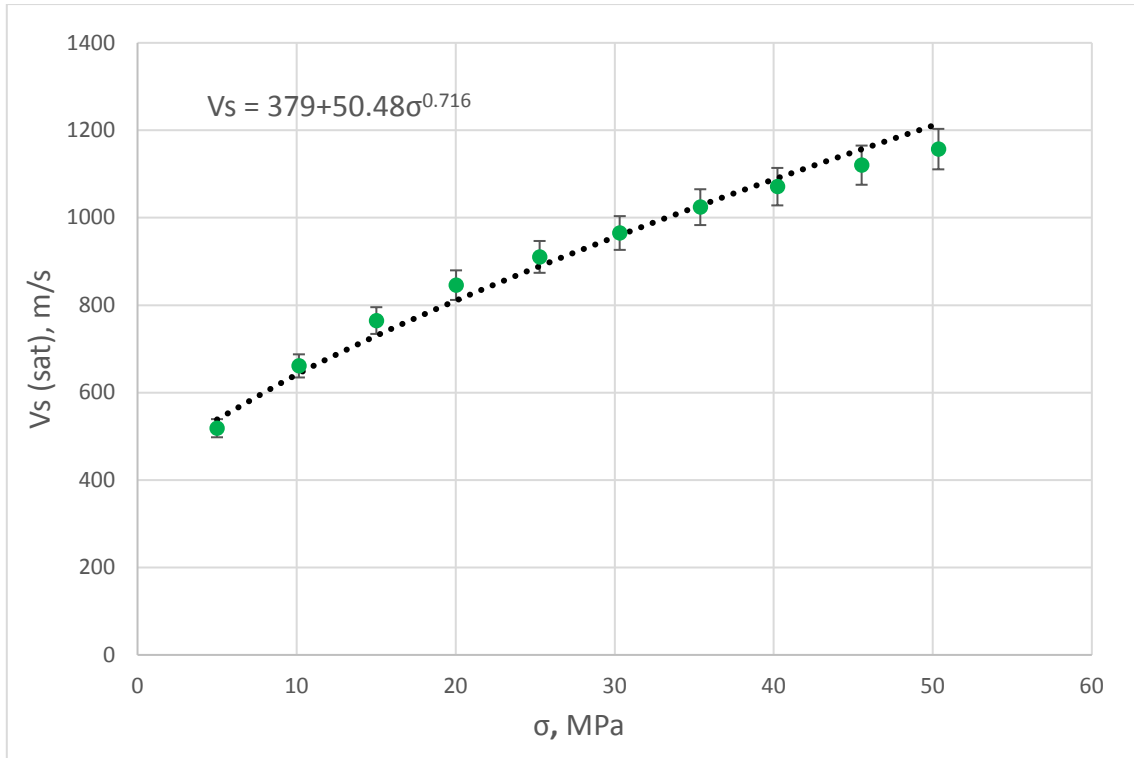


Figure 3.6.2.1. Power model for V_s fitting when relative volume fraction of kaolinite is 0.25 and relative volume fraction of silt is 0.75.

The power models for V_s fitting for other clay composition are similar to the model above and they are demonstrated in the Section A2.4 of Appendix A.

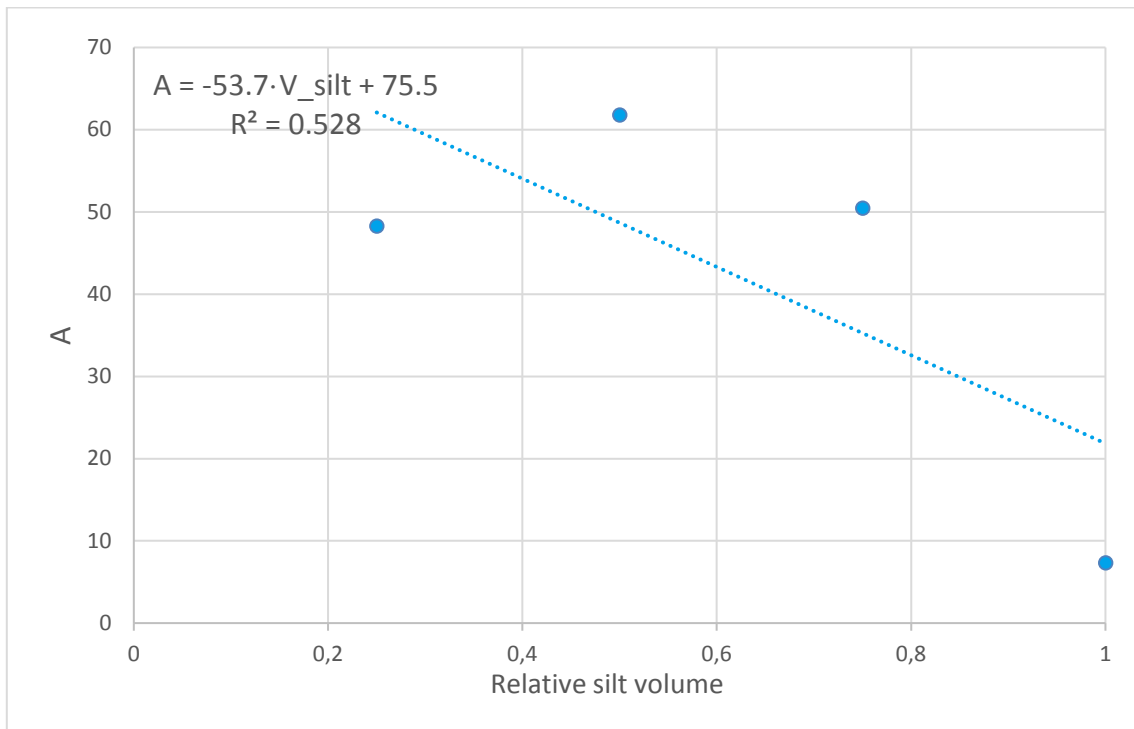


Figure 3.6.2.2. A versus relative silt volume.

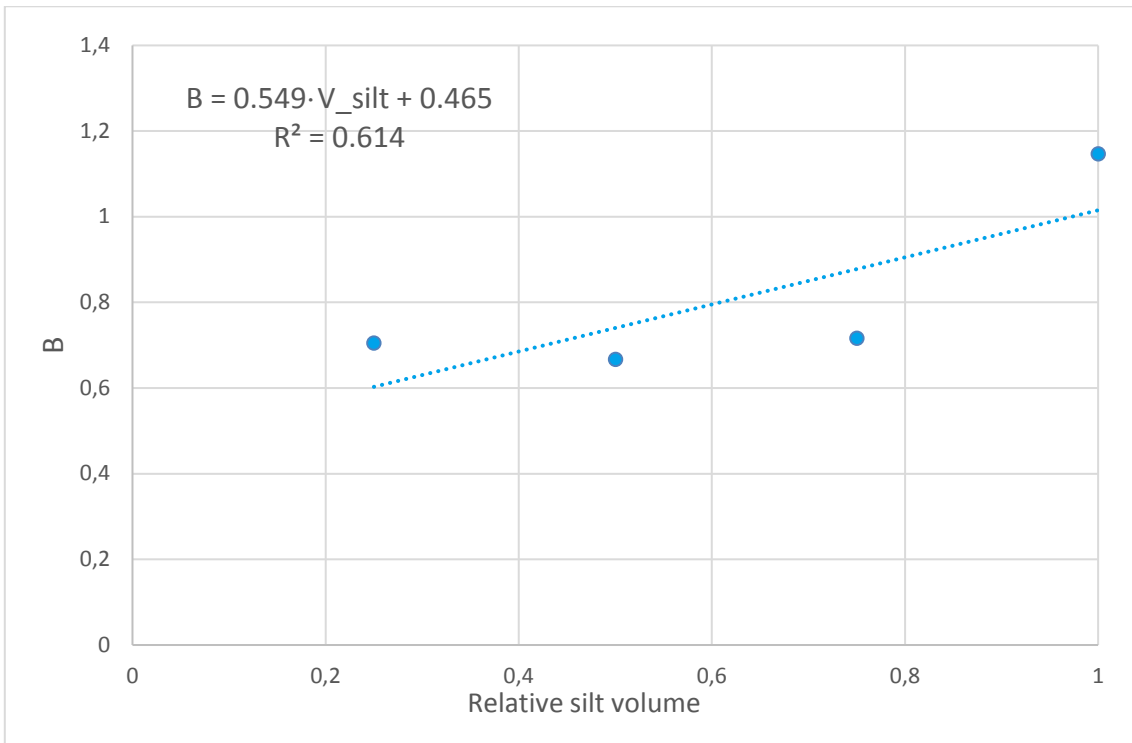


Figure 3.6.2.3. B versus relative silt volume

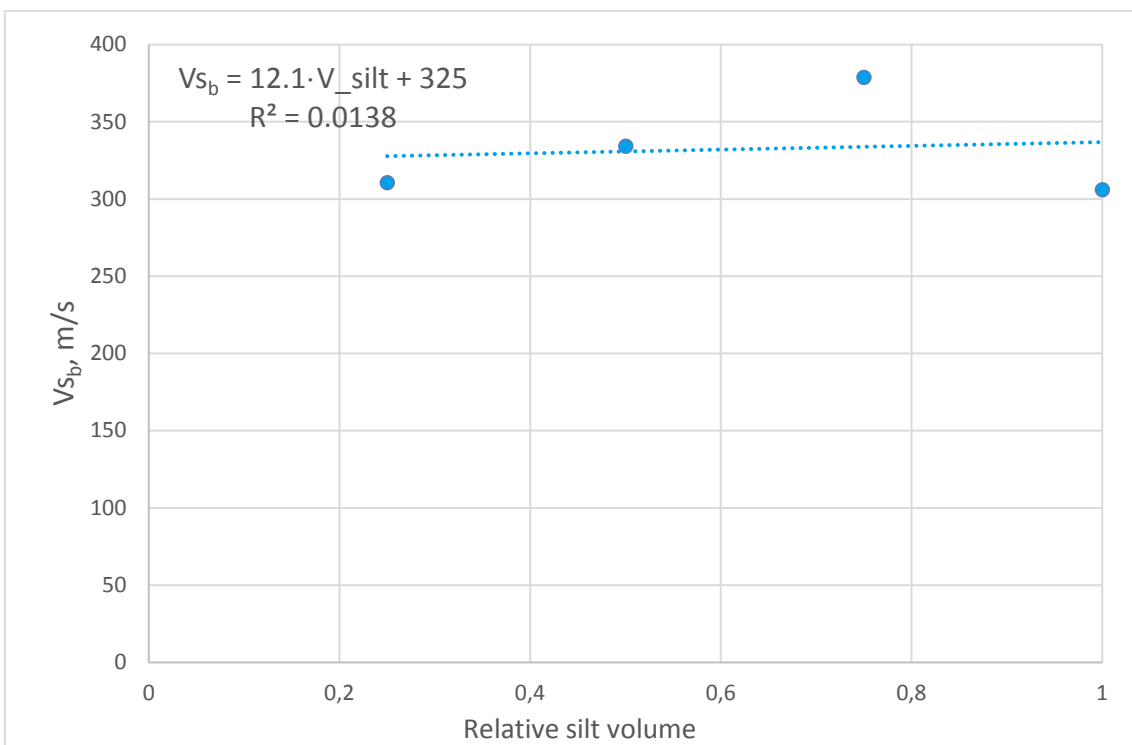


Figure 3.6.2.4. V_{s_b} versus relative silt volume

The trends in the Figures 3.6.2.2, 3.6.2.3 and 3.6.2.4 have a linear character.

3.7. Summary of shale models

Both second order polynomial and power models were considered within laboratory data analysis of shale. It showed that a second order polynomial model in our case does not have a good behavior with high values of differential pressure – it decreases which is physically incorrect. The model should constantly follow the asymptote line or increase moderately with a trend. Power model satisfies this condition. Thus, we assumed that the power model is more reliable model than the polynomial one. In addition, previous studies also suppose that a power model is reasonable for modeling of compressional and shear wave velocities, in particular, for unconsolidated sand and glass-beads (Domenico, 1977).

For completeness the summary of second order polynomial models we included in the Section A3 of Appendix A. In this Section we presented the summary of power models that are essential for further modeling.

Assuming a power model for the smectite/kaolinite/brine systems we get sonic velocities

$$V_p = (-10 \cdot V_{smec} + 1470) + (-46.5 \cdot V_{smec} + 77.3) \cdot \sigma^{(-0.0828 \cdot V_{smec} + 0.8016)} \text{ and}$$
$$V_s = (-69.4 \cdot V_{smec} + 395) + (-19.7 \cdot V_{smec} + 34.9) \cdot \sigma^{(0.012 \cdot V_{smec} + 0.8057)},$$

Whereas for the kaolinite/silt/brine system the sonic velocities in the power model are

$$V_p = (-72.6 \cdot V_{silt} + 1495) + (-47.8 \cdot V_{silt} + 66.9) \cdot \sigma^{(0.195 \cdot V_{silt} + 0.687)} \text{ and}$$
$$V_s = (12.1 \cdot V_{silt} + 325) + (-53.7 \cdot V_{silt} + 75.5) \cdot \sigma^{(0.549 \cdot V_{silt} + 0.465)}.$$

4. Derivation of unconsolidated sand models based on laboratory measurements

This section describes the laboratory data of unconsolidated sand used in the modeling. Moreover, the Chapter covers theoretical bases of the most essential rock physics models for unconsolidated sand based on laboratory data. There are Gassmann's, Biot's and Mavko-Jizba squirt relations. In addition, we also take into account Murphy's equations as well as Biot-Geertsma and Geertsma-Smit approximations of Biot's relations. We will present some mathematical calculations, as well as our derived models for bulk and shear modulus of dry skeleton as well as sonic velocity models of a saturated rock based on the theoretical relations and our obtained models for K_{dry} and G_{dry} . The main reference in the Chapter 4 is (Mavko, Mukerji, & Dvorkin, 2009).

4.1. Principle of laboratory data selection

4.1.1. Comparison of Zimmer's data with Bhuiyan's and Holt's data

Laboratory data for the sand modeling are represented in the supplementary materials in the USB flash drive which is attached to the printed version of the thesis. The database was created based on the previous studies of unconsolidated sand.

According to the database it can be noticed that the most recent laboratory analysis of the sand was done by Zimmer (Zimmer, 2004) as well as Bhuiyan and Holt (Bhuiyan & Holt, 2016). Zimmer in his work (Zimmer, 2004) presented the values of the observation of five different types of sands-the Galveston Beach, Gulf of Mexico, Merritt, Pomponio Beach and Santa Cruz Aggregate ones. Bhuiyan and Holt described their laboratory experiments of two unconsolidated sands -the Ottawa and Columbia sands with a high porosity and different grain sizes (Bhuiyan & Holt, 2016). From innovative point of view, Zimmer's, Bhuiyan and Holt's works cover the most up-to-date studies of unconsolidated sands. Zimmer's investigations of the sand are more extended since he studied more types of sand. However, it can be noticed that there is a missing of quite many values in the Zimmer's measurements and the latter don't include grain size characteristic. In contrast, Bhuiyan and Holt's data are more full. Moreover, the grain size parameter was taken into account in their observation of the unconsolidated sand. Thus, Bhuiyan and Holt's data were prioritized and selected for the sand modeling in the thesis.

4.1.2. Description of Bhuiyan and Holt's data

M. Bhuyain and R.Holt in their article did not present the values of their laboratory experiment. After a special request M. Bhuiyan sent a database with raw values of the laboratory studies. It can be found in the supplementary materials in the USB flash drive which is attached to the printed version of the thesis. These raw values include measurements of the differential pressure, porosity, density, compressional and shear wave velocities of two types of sand – the Ottawa and Columbia. Each type has five different grain sizes. The Ottawa sand has the following grain size variations: 450 μm , 450-355 μm , 355-230 μm , 230 μm and unsorted, while the Columbia sand is characterized by the following grain sizes: 550 μm , 450-355 μm , 355-230 μm , 230-180 μm and unsorted. Ottawa sand has a subrounded to rounded grain shape with a variation of the porosity from 36.4 to 37.5%. Columbia sand has a subangular shape of the grains with the porosity range from 39.8 to 43.8 % (Bhuiyan & Holt, 2016). The laboratory measurements of the sand included two loading-unloading cycles performed in dry condition and one fluid saturated cycle excluding the Ottawa unsorted sand where one can see two dry and two saturated loads. In order to stay consistent, the second saturated load of the Ottawa unsorted sand was not considered in the modeling part. Furthermore, the measurements of shear-wave velocities of the 355-230 μm grain sized Ottawa sand lack of values within the first dry loading. Hence, this particular grain size of the Ottawa sand was omitted in the modeling as well.

The raw database was processed by averaging of the same values of all measured parameters – differential pressure, porosity, density, V_p and V_s velocities. Averaging was done separately for two dry and one saturated loading cycles for each type of sand.

4.1.3. Organization of laboratory data

The collection of the data, in particular for sand modeling, includes the values of the following essential parameters – differential pressure, water saturation, compressional and shear wave velocities, density, porosity, grain size, frequency and uniformity coefficient. It can be seen that laboratory data of sand modeling includes a quite wide range of values from different sources.

Here is an example how the laboratory data of sand are organized.

Sources												
Domenico 1977	"Elastic properties of unconsolidated porous sand reservoirs"										Geophysics, Vol 42, No 7, P 1339 - 1368	
Prasad 1988	"Experimental and theoretical considerations of attenuation and velocity interactions with physical parameters in sands"										Ph. D. thesis, Christian-Albrechts-Universität	
Prasad 2002	"Acoustic measurements in unconsolidated sands at low effective pressure and overpressure detection"										Geophysics, Vol. 67, No. 2, Mar-Apr 2002, P405-412	
Yin 1992	"Acoustic velocity and attenuation of rocks. Isotropy, intrinsic anisotropy, and stress induced anisotropy"										Ph.D. thesis, Stanford University	
Zimmer 2003	"Seismic Velocities in Unconsolidated sands. Measurements of pressure, sorting, and compaction effects"										Ph.D. thesis, Stanford University	
Bhuiyan, Holt 2016	"Variation of shear and compressional wave modulus upon saturation for pure pre-compacted sands"										Geophys. J. Int. (2016) 206, 487-500	
Quantities												
C												
D60/D10 uniformity coefficient												
Brine sal (ppm)	Pd (MPa)	SWT (v/v)	Vp (m/s)	Vs (m/s)	Density gm/cc	Porosity (v/v)	Grain size (µm)	C	Frequency for Vp (MHz)	Frequency for Vs (MHz)	Source	Comments
0.2	0	481	302	1.708	0.3444				0.15	0.15	Zimmer 2003	Santa Cruz Aggregate, Sa 35% Small
0.1	0	444	236	1.704	0.346				0.15	0.15	Zimmer 2003	Santa Cruz Aggregate, Sa 35% Small
0.05	0			1.699	0.3479				0.15	0.15	Zimmer 2003	Santa Cruz Aggregate, Sa 35% Small
0	0			1.682	0.3544				0.15	0.15	Zimmer 2003	Santa Cruz Aggregate, Sa 35% Small
0.7	0	762	506	1.682	0.3654	450			0.5	0.13	Bhuiyan,Holt,2016	Ottawa sand
1.3	0	806	482	1.683	0.3651	450			0.5	0.13	Bhuiyan,Holt,2016	Ottawa sand
2.0	0	891	535	1.686	0.3639	450			0.5	0.13	Bhuiyan,Holt,2016	Ottawa sand
2.6	0	915	545	1.686	0.3638	450			0.5	0.13	Bhuiyan,Holt,2016	Ottawa sand
3.2	0	939	553	1.685	0.3642	450			0.5	0.13	Bhuiyan,Holt,2016	Ottawa sand
3.3	0	970	581	1.689	0.3626	450			0.5	0.13	Bhuiyan,Holt,2016	Ottawa sand
3.9	0	984	587	1.688	0.3630	450			0.5	0.13	Bhuiyan,Holt,2016	Ottawa sand
4.5	0	999	594	1.687	0.3634	450			0.5	0.13	Bhuiyan,Holt,2016	Ottawa sand
4.6	0	1024	617	1.691	0.3620	450			0.5	0.13	Bhuiyan,Holt,2016	Ottawa sand
5.1	0	1023	612	1.688	0.3630	450			0.5	0.13	Bhuiyan,Holt,2016	Ottawa sand
5.2	0	1045	631	1.691	0.3618	450			0.5	0.13	Bhuiyan,Holt,2016	Ottawa sand
5.8	0	1048	635	1.690	0.3622	450			0.5	0.13	Bhuiyan,Holt,2016	Ottawa sand
6.4	0	1076	656	1.692	0.3617	450			0.5	0.13	Bhuiyan,Holt,2016	Ottawa sand
7.0	0	1084	662	1.691	0.3618	450			0.5	0.13	Bhuiyan,Holt,2016	Ottawa sand

Figure 4.1.3.1. Example of sand data from supplementary materials.

4.2. Rock physics models for sandstone

4.2.1. Theoretical basics

4.2.1.1. Gassmann's relations

In the geophysical literature there are many theories of wave propagation in porous media. Gassmann's equation is used to predict velocities in porous media with mixed fluids like water-gas or water-oil. When the seismic wave passes through a porous saturated rock the pore pressure tries to resist the compression of the seismic wave. The resistance of the volumetric compression is called the bulk modulus – K (Aljarrah, 2009). Gassmann's equation predicts the resulting increase in effective bulk modulus of the rock with a pore fluid. Gassmann's equation relate such parameters as porosity, the bulk modulus of the mineral matrix, the bulk modulus of the rock frame, and the bulk modulus of the pore fluids to the saturated bulk modulus of the same rock. This is shown in the following equations (Gassmann, 1951):

$$\frac{K_{sat}}{K_s - K_{sat}} = \frac{K_{dry}}{K_s - K_{dry}} + \frac{K_{fl}}{\varphi \cdot (K_s - K_{fl})} \quad (1),$$

$$K_{sat} = K_{dry} + \frac{\left(1 - \frac{K_{dry}}{K_s}\right)^2}{\frac{\varphi}{K_{fl}} + \frac{(1 - \varphi)}{K_s} - \frac{K_{dry}}{K_s^2}} \quad (2),$$

$$G_{dry} = G_{sat} \quad (3),$$

where K_{dry} is the effective bulk modulus of porous rock frame or skeleton, K_{sat} is the effective bulk modulus of the rock with a pore fluid, K_s is the bulk modulus of the mineral material making up rock, K_{fl} is the effective bulk modulus of pore fluid, φ is porosity, G_{dry} is the effective shear modulus of porous rock frame or skeleton and G_{sat} is the effective shear modulus of the rock with a pore fluid.

Equations (1) and (2) are the same but in a different algebraic order.

Murphy suggested a velocity form of Gassmann's relations (Murphy, Schwartz, & Hornby, 1991):

$$\rho_{sat} V_{p_{sat}}^2 = K_p + K_{dry} + \frac{4}{3} G \quad (4)$$

$$\rho_{sat} V_{s_{sat}}^2 = G \quad (5),$$

where

$$K_p = \frac{\left(1 - \frac{K_{dry}}{K_s}\right)^2}{\frac{\varphi}{K_{fl}} + \frac{(1 - \varphi)}{K_s} - \frac{K_{dry}}{K_s^2}}$$

and ρ_{sat} is the density of the saturated rock, $V_{p_{sat}}$ is a compressional wave velocity of the saturated rock, $V_{s_{sat}}$ is a shear wave velocity of the saturated rock and $G_{dry} = G_{sat} = G$.

Gassmann's equation implicates the following essential assumptions.

Frequency

The equation is valid only at sufficiently low frequencies such that the induced pore pressures are equilibrated throughout the pore space. This means there is enough time for the pore fluid to flow and eliminate wave-induced pore-pressure gradients. Hence, Gassmann's relation works best for very low-frequency in-situ seismic data (<100Hz) and may perform less well as frequencies increase toward sonic logging ($\approx 10^4$ Hz) and laboratory ultrasonic measurements ($\approx 10^6$ Hz) (Mavko, Mukerji, & Dvorkin, 2009, p. 273).

Symmetry of rock

Gassmann's theory assumes that the rock is isotropic and homogeneous physically meaning that the rock has the same physical properties in all directions.

Pores connectivity

All pores within the rock are connected. This means that the rock has a high porosity and there are no isolated pores in the rock. Most of rocks follow this assumption, especially unconsolidated rocks with a high porosity and permeability. Velocities measured at high frequencies like sonic logs or laboratory measurements usually are higher than those calculated with Gassmann's equations.

Rock system

The rock system is closed meaning that there is no fluid flow in or out of the surface of the rock. There are no physical or chemical reactions between solids and fluids.

Viscosity

The fluids that fill the pores have a zero viscosity. Similarly to the assumption (3) this is relate to the wavelength in order to highlight that a pressure equilibrium of pore fluid will be complete. High viscosity fluids are not easy to equilibrate. As a matter of fact, most of fluids have a finite viscosity most of waves have a finite wavelengths. There is a significant difference in bulk and shear moduli between fluids and solids and according to the previous reasons a relative motion between fluids and solids will appear, hence, waves are dispersive. This explains why laboratory velocity measurements are higher than those calculated using Gassmann's equations at a high water saturation (Aljarrah, 2009).

Dry effect

Laboratory measurements on very dry rocks such as those prepared in a vacuum oven are sometimes too dry. Several researchers have found that the first few percent of fluid saturation added to an extremely dry rock will lower the frame moduli possibly as a result of disrupting surface forces acting on the pore surfaces. Hence, in order to avoid the artifacts of ultra-dry rocks it is often recommended to use a slightly wet or moist rock modulus as the "dry-rock" modulus in Gassmann's relations (Mavko et al., 2009, p. 274).

Geometry of rock

Gassmann's theory considers also that the shear modulus is not affected by pore fluid, there is no assumption for a pore geometry as well.

4.2.1.2. Murphy's relations

William Murphy devoted his laboratory studies of pure quartz sand (with $\text{SiO}_2 \geq 0.98$) to assessing of porosity, compressional and shear-wave velocities for full gas and full water saturation. These data were measured using a standard ultrasonic technique at high effective pressures, approximately 50 MPa (Murphy, Reischer, & Hsu, 1993).

The frame moduli which were calculated from the gas saturated velocities demonstrated a significantly clean dependence on porosity which empirically looks as follow (Murphy et al., 1993):

$$K_{dry} = \begin{cases} 38.18[1 - 3.39\varphi + 1.95\varphi^2] & \varphi \leq 0.35 \\ \exp[-62.6\varphi + 22.58] & \varphi > 0.35 \end{cases} \quad (1)$$

and

$$G_{dry} = \begin{cases} 42.65[1 - 3.48\varphi + 2.19\varphi^2] & \varphi \leq 0.35 \\ \exp[-62.69\varphi + 22.73] & \varphi > 0.35 \end{cases} \quad (2)$$

These moduli were measured by varying the effective pressure on an unconsolidated sand from 50 to 5 MPa.

4.2.1.3. Biot's relations

Biot derived theoretical formulas for predicting the frequency-dependent velocities of saturated rocks in terms of the dry-rock properties. His formulation incorporates some of the mechanisms of viscous and inertial interaction between the pore fluid and the mineral matrix of the rock. The low-frequency limiting velocities are the same as those predicted by Gassmann's relations. The high-frequency limiting velocities $V_{p\infty}$ and $V_{s\infty}$ are given by (Biot, 1956):

$$V_{p\infty}(fast, slow) = \left\{ \frac{\Delta \pm [\Delta^2 - 4(\rho_{11}\rho_{22} - \rho_{12}^2)(PR - Q^2)]^{\frac{1}{2}}}{2(\rho_{11}\rho_{22} - \rho_{12}^2)} \right\}^{\frac{1}{2}} \quad (1)$$

$$V_{S\infty} = \left(\frac{G_{dry}}{\rho - \varphi \cdot \rho_{fl} \cdot \alpha^{-1}} \right)^{1/2} \quad (2),$$

where

$$\Delta = P\rho_{22} + R\rho_{11} - 2Q\rho_{12}$$

$$P = \frac{(1 - \varphi) \left(1 - \varphi - \frac{K_{dry}}{K_s} \right) K_s + \varphi K_s K_{dry} / K_{fl}}{1 - \varphi - \frac{K_{dry}}{K_s} + \varphi K_s / K_{fl}} + \frac{4}{3} G_{dry}$$

$$Q = \frac{\left(1 - \varphi - \frac{K_{dry}}{K_s} \right) \varphi K_s}{1 - \varphi - \frac{K_{dry}}{K_s} + \varphi K_s / K_{fl}}$$

$$R = \frac{\varphi^2 K_s}{1 - \varphi - \frac{K_{dry}}{K_s} + \varphi K_s / K_{fl}}$$

$$\rho_{11} = (1 - \varphi)\rho_s - (1 - \alpha)\varphi\rho_{fl}$$

$$\rho_{22} = \alpha\varphi\rho_{fl}$$

$$\rho_{12} = (1 - \alpha)\varphi\rho_{fl}$$

$$\rho = \rho_s(1 - \varphi) + \rho_{fl}\varphi,$$

where K_{dry} and G_{dry} are the effective bulk and shear moduli of the rock frame respectively – either the dry-frame moduli or the high-frequency, K_s is the bulk modulus of the mineral material making up the rock, K_{fl} is the effective bulk modulus of the pore fluid, φ is the porosity, ρ_s is the mineral density, ρ_{fl} is the fluid density and α is the tortuosity parameter which is always greater than or equal to 1.

The two solutions give above for the high-frequency limiting P-wave velocity designated by \pm correspond to the “fast” and “slow” waves. The fast wave is the compressional body-wave most easily observed in the laboratory and the field and it corresponds to overall fluid and solid motions that are in phase. The slow wave is a highly dissipative wave in which the overall solid and fluid motions are out of phase.

The complete frequency dependence can be obtained from the roots of the dispersion relations (Biot, 1956):

$$\begin{vmatrix} \frac{H}{Vp^2} - \rho & \rho_{fl} - C/Vp^2 \\ C & q - M/Vp^2 \end{vmatrix} = 0$$

$$\begin{vmatrix} \rho - \frac{G_{dry}}{V_s^2} & \rho_{fl} \\ \rho_{fl} & q \end{vmatrix} = 0$$

The complex roots are:

$$\frac{1}{V_p^2} = \frac{-(Hq + M\rho - 2C\rho_{fl}) \pm \sqrt{(Hq + M\rho - 2C\rho_{fl})^2 - 4(C^2 - MH)(\rho_{fl}^2 - \rho q)}}{2(C^2 - MH)} \quad (3)$$

$$\frac{1}{V_s^2} = \frac{q\rho - \rho_{fl}^2}{qG_{dry}} \quad (4)$$

The real and imaginary parts of the roots give the velocity and the attenuation respectively. Again, the two solutions correspond to the fast and slow P-waves. The various terms are

$$H = K_{dry} + \frac{4}{3}G_{dry} + \frac{(K_s - K_{dry})^2}{(D - K_{dry})}$$

$$C = \frac{(K_s - K_{dry})K_s}{(D - K_{dry})}$$

$$M = \frac{K_s^2}{(D - K_{dry})}$$

$$D = K_s \left[1 + \varphi \left(\frac{K_s}{K_{fl}} - 1 \right) \right]$$

$$\rho = (1 - \varphi)\rho_s + \varphi\rho_{fl}$$

$$q = \frac{\alpha\rho_{fl}}{\varphi} - \frac{i\eta F(\zeta)}{\omega k},$$

where η is the viscosity of the pore fluid, k is the absolute permeability of the rock and ω is the angular frequency of the plane wave.

The viscodynamic operator $F(\zeta)$ incorporates the frequency dependence of viscous drag and is defined by

$$F(\zeta) = \frac{1}{4} \left(\frac{\zeta T(\zeta)}{1 + \frac{2iT(\zeta)}{\zeta}} \right)$$

$$T(\zeta) = \frac{ber'(\zeta) + ibei'(\zeta)}{ber(\zeta) + ibei(\zeta)} = \frac{e^{\frac{i3\pi}{4}} J_1(\zeta e^{-\frac{i\pi}{4}})}{J_0(\zeta e^{-\frac{i\pi}{4}})}$$

$$\zeta = \left(\frac{\omega}{\omega_r}\right)^{1/2} = \left(\frac{\omega a^2 \rho_{fl}}{\eta}\right)^{1/2},$$

where $ber(\cdot)$ and $bei(\cdot)$ are real and imaginary parts of the Kelvin function respectively, $J_n(\cdot)$ is a Bessel function of order n and a is the pore-size parameter.

The pore-size parameter a depends on both the dimensions and the shape of the pore space. Stoll found that values between 1/6 and 1/7 of the mean grain diameter gave good agreement with experimental data (Stoll, 1974).

At very low frequencies $F(\zeta) \rightarrow 1$ and at very high frequencies (large ζ) the asymptotic values are $T(\zeta) \rightarrow (1+i)/\sqrt{2}$ and $F(\zeta) \rightarrow (k/4)(1+i)/\sqrt{2}$.

The reference frequency f_c which determines the low-frequency range, $f \ll f_c$, and the high-frequency range, $f \gg f_c$, is given by

$$f_c = \frac{\varphi \eta}{2\pi \rho_{fl} k}$$

One interpretation of this relation is that it is the frequency where viscous forces acting on the pore fluid approximately equal the inertial forces acting on it. In the high-frequency limit the fluid motion is dominated by inertial effects and in the low-frequency limit the fluid motion is dominated by viscous effects.

As it was mentioned above, Biot's theory predicts the existence of a slow highly attenuated P-wave in addition to the usual fast P- and S-waves. The slow P-wave has been observed in the laboratory and it is sometimes invoked to explain diffusional loss mechanisms.

4.2.1.4. Geertsma-Smit approximations of Biot's relations

Biot's theoretical formulas predict the frequency-dependent velocities of saturated rocks in terms of the dry rock properties. Low- and middle- frequency approximations of his relations can be expressed as (Geertsma & Smit, 1961):

$$V_p^2 = \frac{V_{p\infty}^4 + V_{p0}^4 \left(\frac{f_c}{f}\right)^2}{V_{p\infty}^2 + V_{p0}^2 \left(\frac{f_c}{f}\right)^2},$$

where V_p is the frequency dependent compressional wave velocity of saturated rock, V_{p0} is the Biot - Gassmann low - frequency limiting compressional wave velocity, $V_{p\infty}$ is the Biot high-frequency limiting compressional wave velocity, f is the frequency and f_c is Biot's reference frequency.

The use of the Geertsma - Smit approximations can be used for the following:

- estimating saturated rock velocities from dry rock velocities and
- estimating the frequency dependence of velocities.

The use of the Geertsma - Smit approximations presented above requires the following assumptions:

- mathematical approximations are valid at moderate-to-low seismic frequencies, so that $f < f_c$. This generally means moderate-to-low permeabilities but it is in this range of permeabilities that squirt dispersion may dominate the Biot effect;
- the rock is isotropic;
- all minerals making up the rock have the same bulk and shear moduli;
- fluid - bearing rock is completely saturated.

4.2.1.5. Mavko - Jizba squirt relations

The *squirt* or *local flow* model suggests that the fluctuating stresses in a rock caused by a passing seismic wave induce pore-pressure gradients at virtually all scales of pore-space heterogeneity - particularly on the scale of individual grains and pores. These gradients impact the viscoelastic behavior of the rock, at high frequencies when the gradients are unrelaxed all elastic moduli will be stiffer than at low frequencies when the gradients are relaxed. Mavko and Jizba derived simple theoretical formulas for predicting the very high-frequency moduli of saturated rocks in terms of the pressure dependence of dry rocks. The prediction is made in two steps: first, the squirt effect is incorporated as high-frequency “wet-frame moduli” K_{uf} and G_{uf} which are derived from the normal dry moduli as (Mavko & Jizba, 1991):

$$\frac{1}{K_{uf}} \approx \frac{1}{K_{dry-hiP}} + \left(\frac{1}{K_{fl}} - \frac{1}{K_s} \right) \varphi_{soft}$$

$$\left(\frac{1}{G_{uf}} - \frac{1}{G_{dry}} \right) = \frac{4}{15} \left(\frac{1}{K_{uf}} - \frac{1}{K_{dry}} \right),$$

where K_{uf} is the effective high-frequency, unrelaxed, wet-frame bulk modulus, K_{dry} is the effective bulk modulus of the rock skeleton, $K_{dry-hiP}$ is the effective bulk modulus of dry rock at very high pressure, K_s is the bulk modulus of the mineral making up the rock, K_{fl} is the effective bulk modulus of the pore fluid, φ_{soft} is the soft porosity – the amount of porosity that closes at high pressure. G_{uf} is the effective high-frequency, unrelaxed, wet-frame shear modulus and G_{dry} is the effective shear modulus of the rock skeleton.

These frame moduli are then substituted into Gassmann’s or Biot’s relations to incorporate the remaining fluid-saturation effects.

The Mavko-Jizba squirt relations can be used to calculate high-frequency saturated rock velocities from dry rock velocities.

The use of the Mavko-Jizba squirt relations requires the following assumptions:

- high seismic frequencies that are ideally suited for ultrasonic laboratory measurements are assumed. In-situ seismic velocities generally will have neither squirt nor Biot dispersion and should be described using Gassmann’s equations. Sonic-logging frequencies may or may not be within the range of validity, depending on the rock type and fluid viscosity;
- the rock is isotropic;

- all minerals making up the rock have the same bulk and shear moduli and
- fluid-bearing rock is completely saturated.

4.3. Sandstone models based on laboratory data

The sand models were derived based on laboratory data using the relations presented in the chapter above. Laboratory samples of the sand were dried in an oven at 110°C at room conditions (Bhuiyan & Holt, 2016) that assumes that the ultra-dry artifacts were avoided.

Since laboratory measurements include two dry loads, the models were considered separately for the first and second loads. Furthermore, the modeling of the saturated load was also subdivided into two parts according to two dry loads.

4.3.1. First and second dry load models

The main purpose of our modeling is to derive the models for bulk and shear moduli of the dry rock and then using the main theoretical relation's (Gassmann, Biot, Mavko-Jizba) obtain compressional and shear wave velocities of the saturated rock.

Firstly, we calculated bulk and shear moduli of the rock skeleton using equations:

$$K_{dry} = \rho_{dry} \cdot (Vp_{dry}^2 - \frac{4}{3} Vs_{dry}^2) \quad (1) \text{ and}$$

$$G_{dry} = \rho_{dry} \cdot Vs_{dry}^2 \quad (2),$$

where ρ_{dry} is the density of the rock skeleton, Vp_{dry} is a compressional wave velocity of the rock skeleton and Vs_{dry} is a shear wave velocity of the rock skeleton.

Based on the calculated K_{dry} and G_{dry} values we made the models for bulk and shear moduli of the dry rock as functions of porosity for two dry loads.

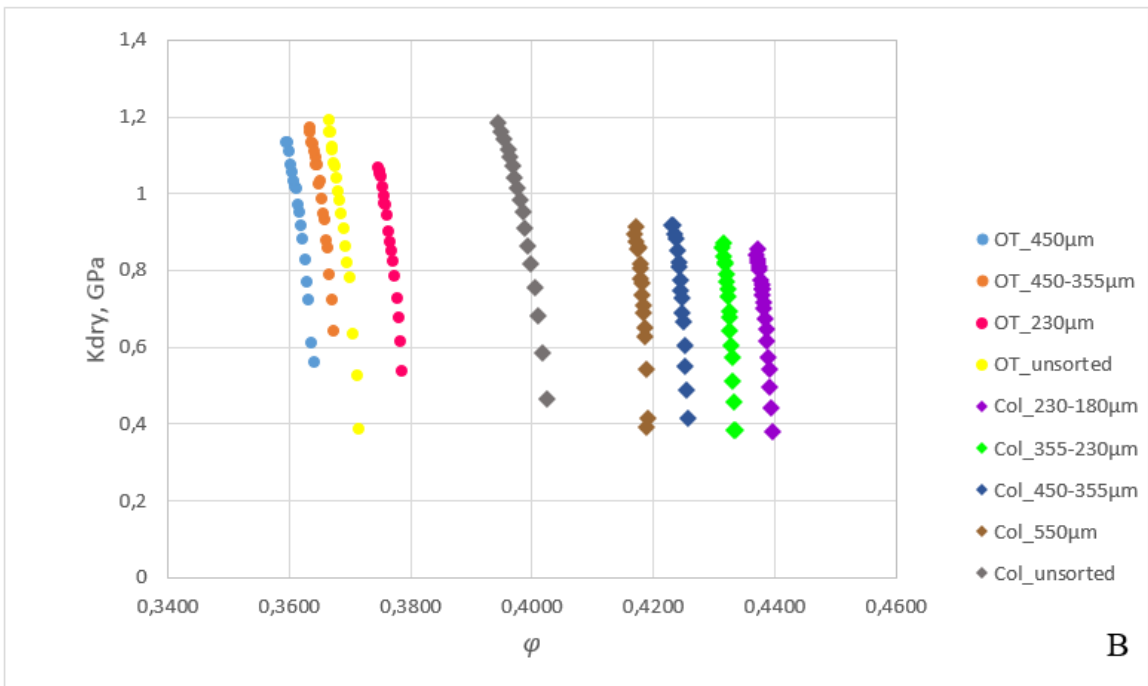
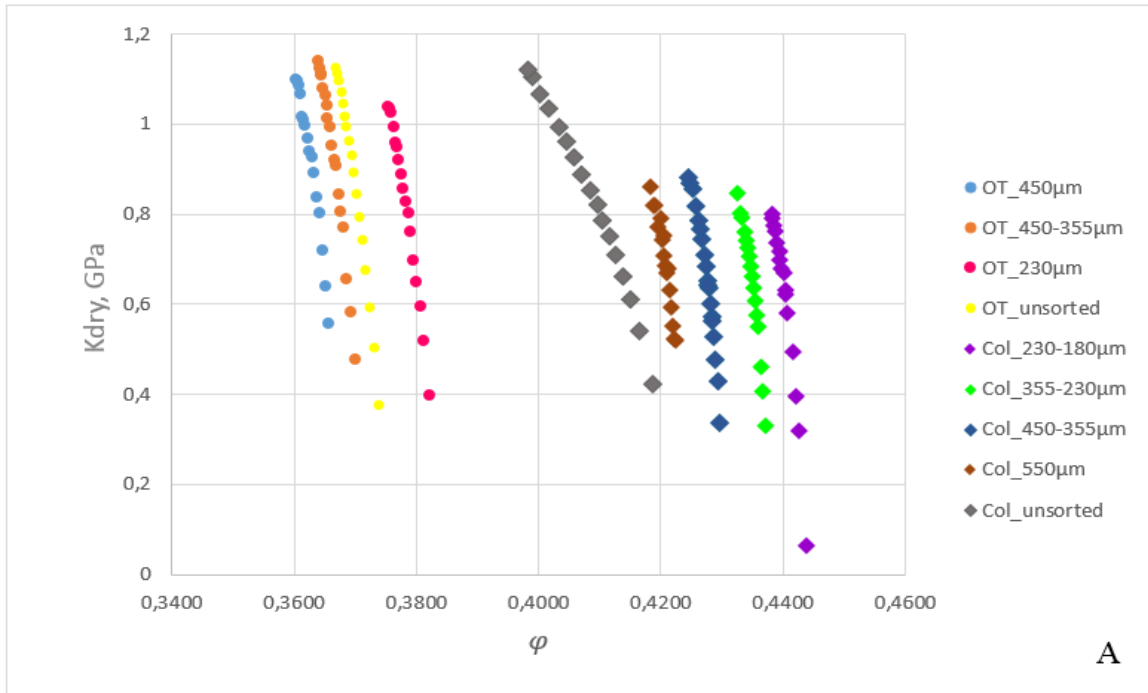


Figure 4.3.1.1. K_{dry} model for all considered types of sand with different grain sizes. A. First dry load. B. Second dry load.

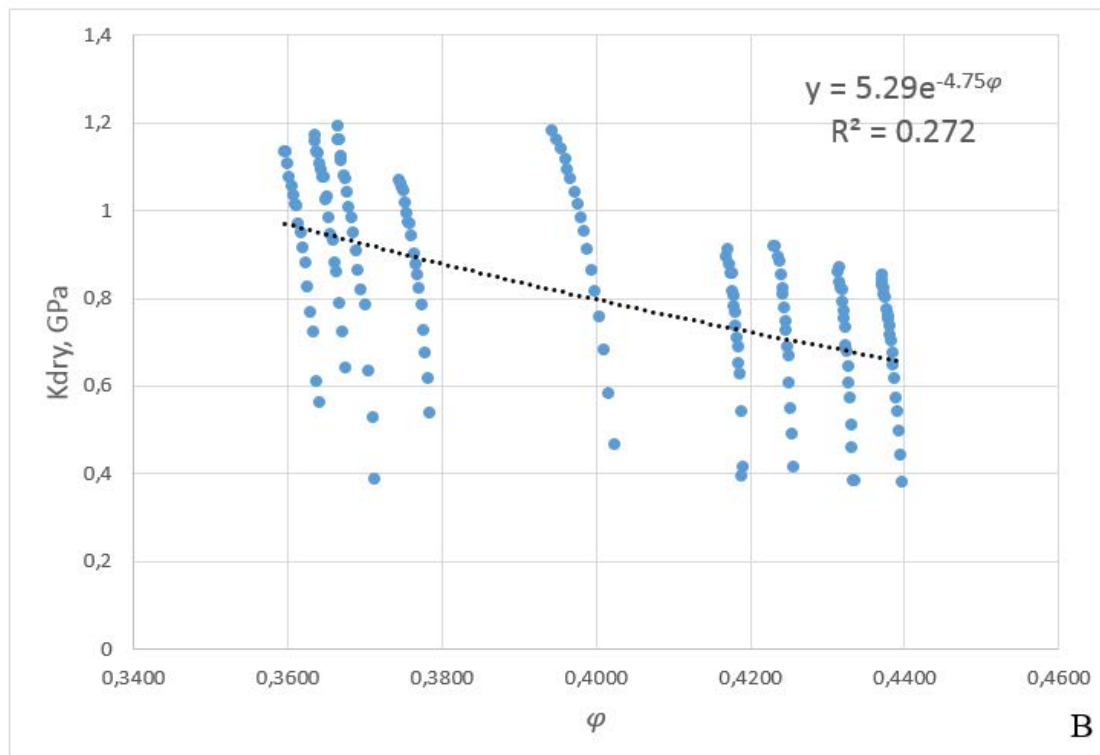
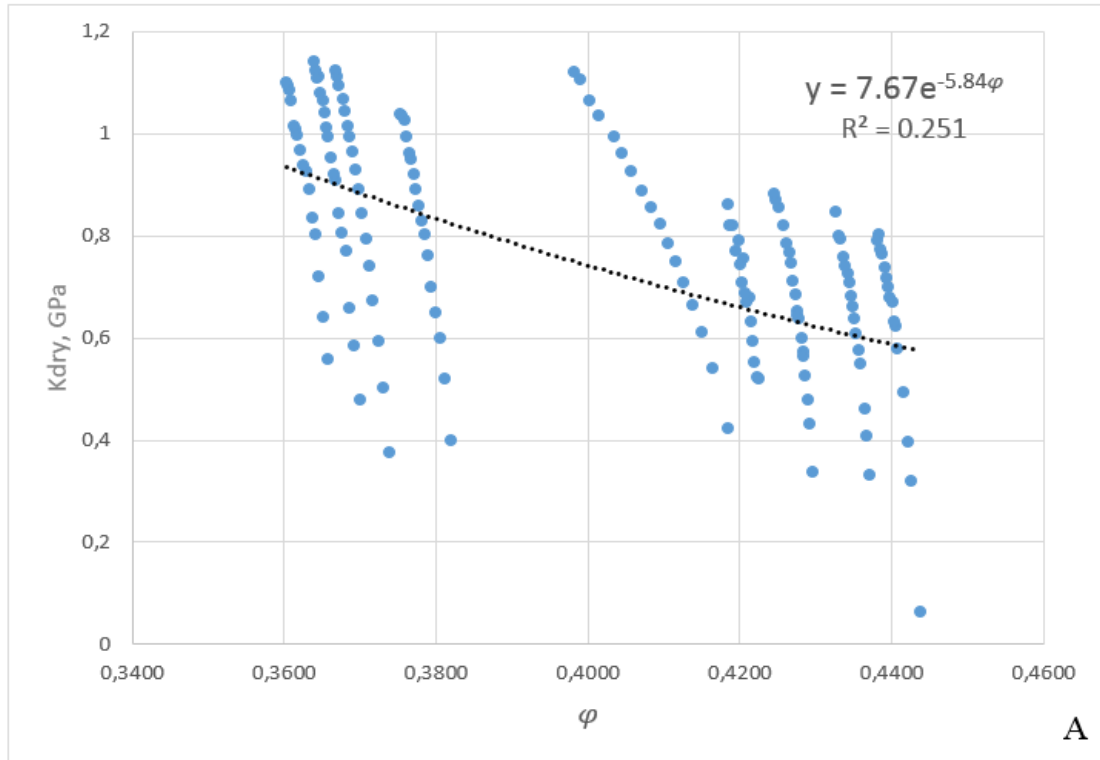


Figure 4.3.1.2. K_{dry} model based on the whole range of values for all considered types of sand with different grain sizes. A. First dry load. B. Second dry load.

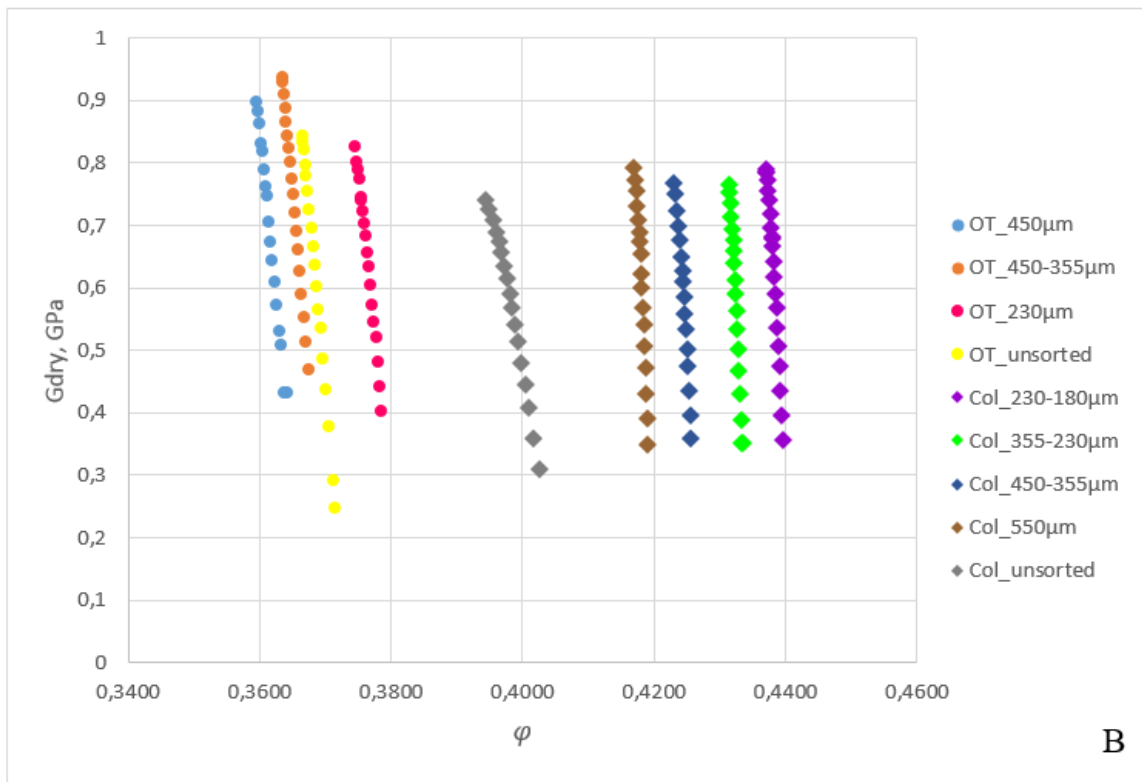
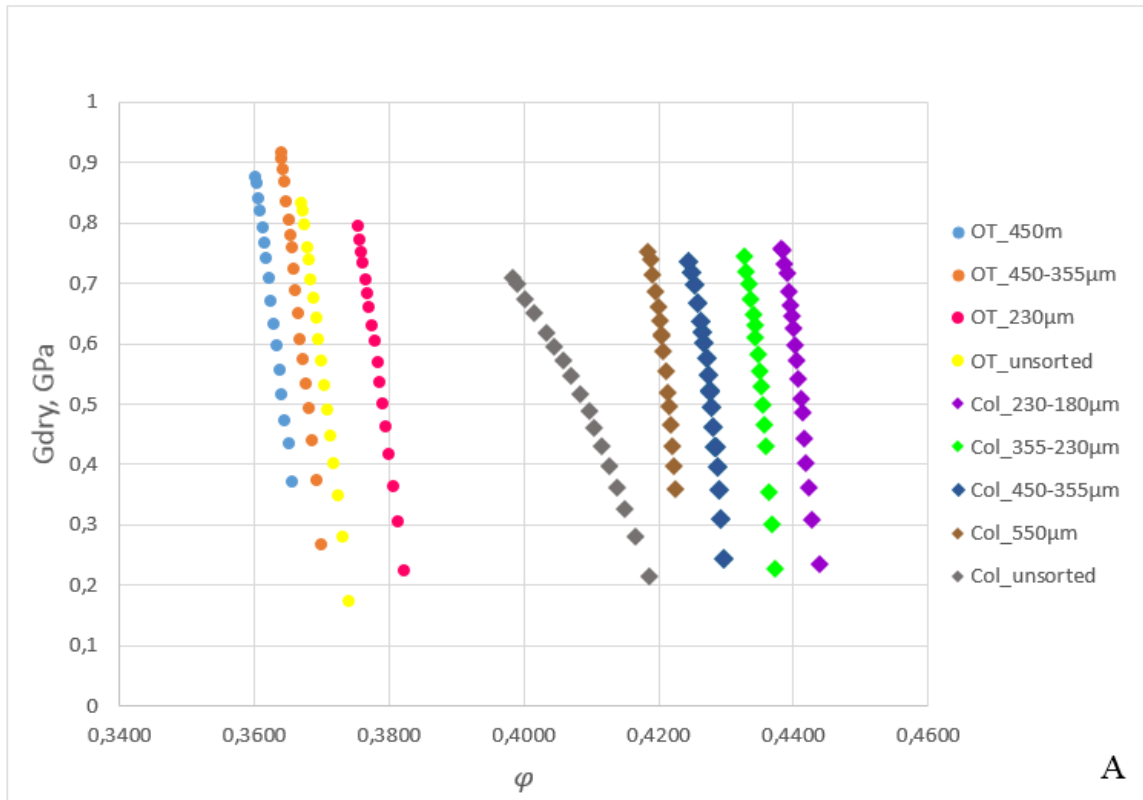


Figure 4.3.1.3. G_{dry} model for all considered types of sand with different grain sizes A. First dry load. B. Second dry load.

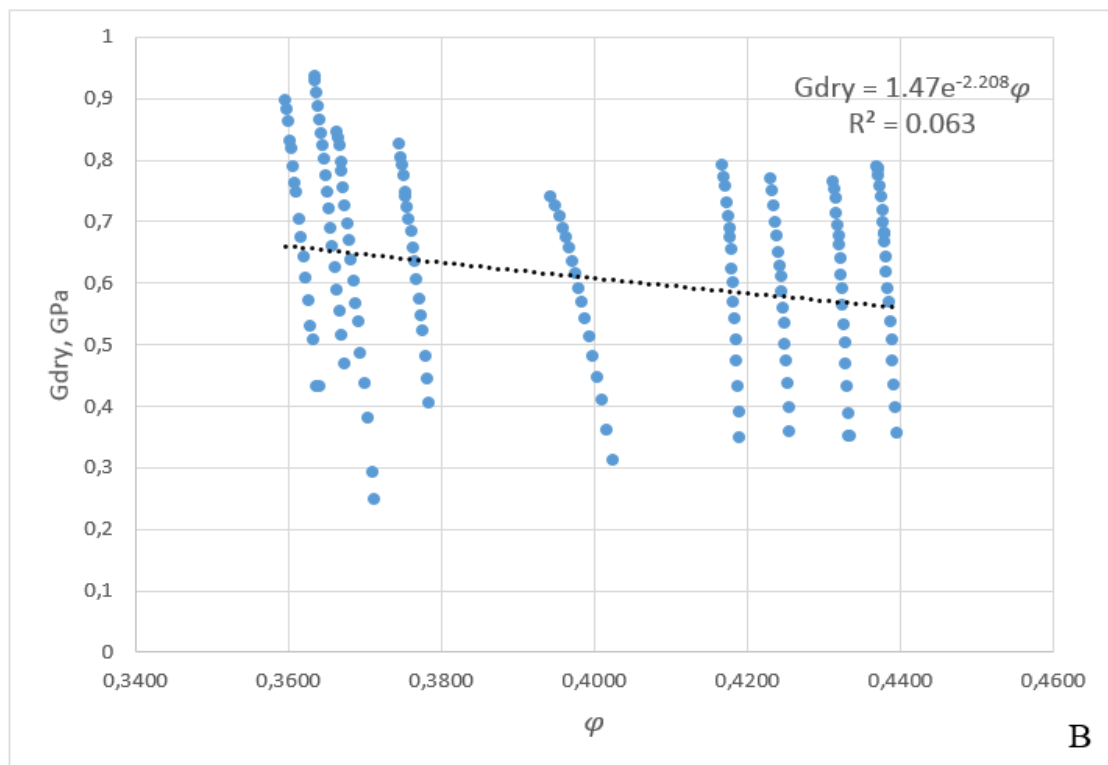
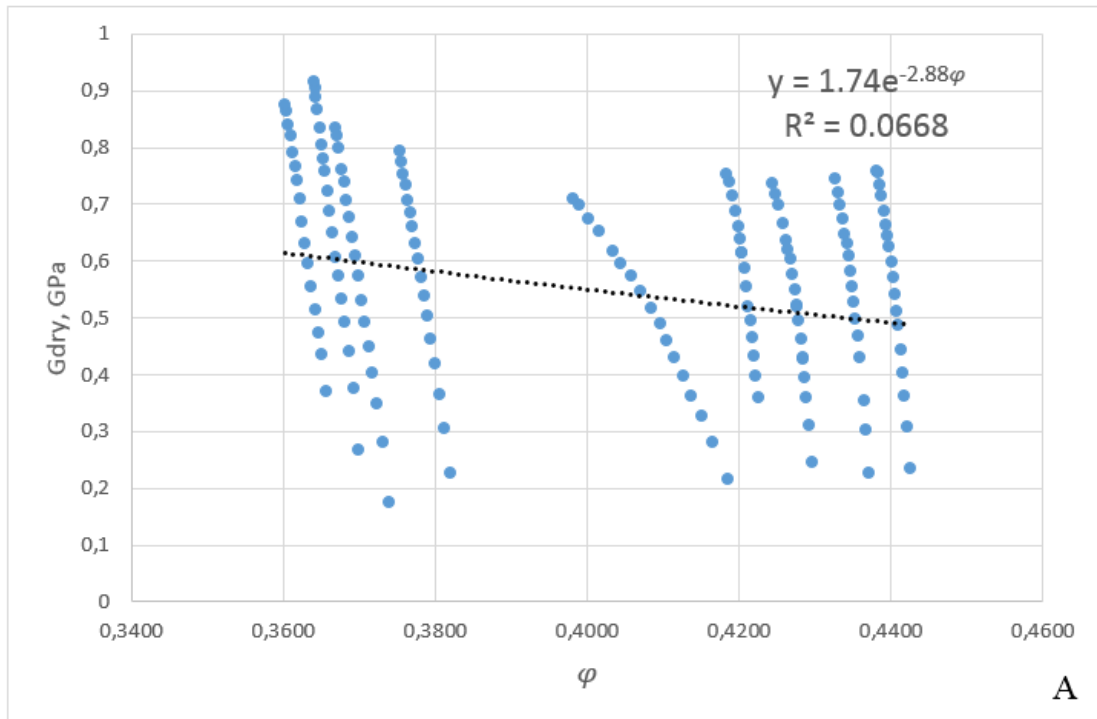


Figure. 4.3.1.4. Gdry model based on the whole range of values for all considered types of sand with different grain sizes. A. First dry load. B. Second dry load.

The Figure 4.3.1.1 (A and B) is identical to the Figure 4.3.1.2 (A and B) and the Figure 4.3.1.3 (A and B) is the same as Figure 4.3.1.4 (A and B). The only difference is in a shown equations for K_{dry} and G_{dry} .

The definition of the models for K_{dry} and G_{dry} was not so clear and simple for the whole range of values. So, instead of using the whole range of values we estimated the average values of K_{dry} and G_{dry} as well as porosity for each type of sand with a certain grain size.

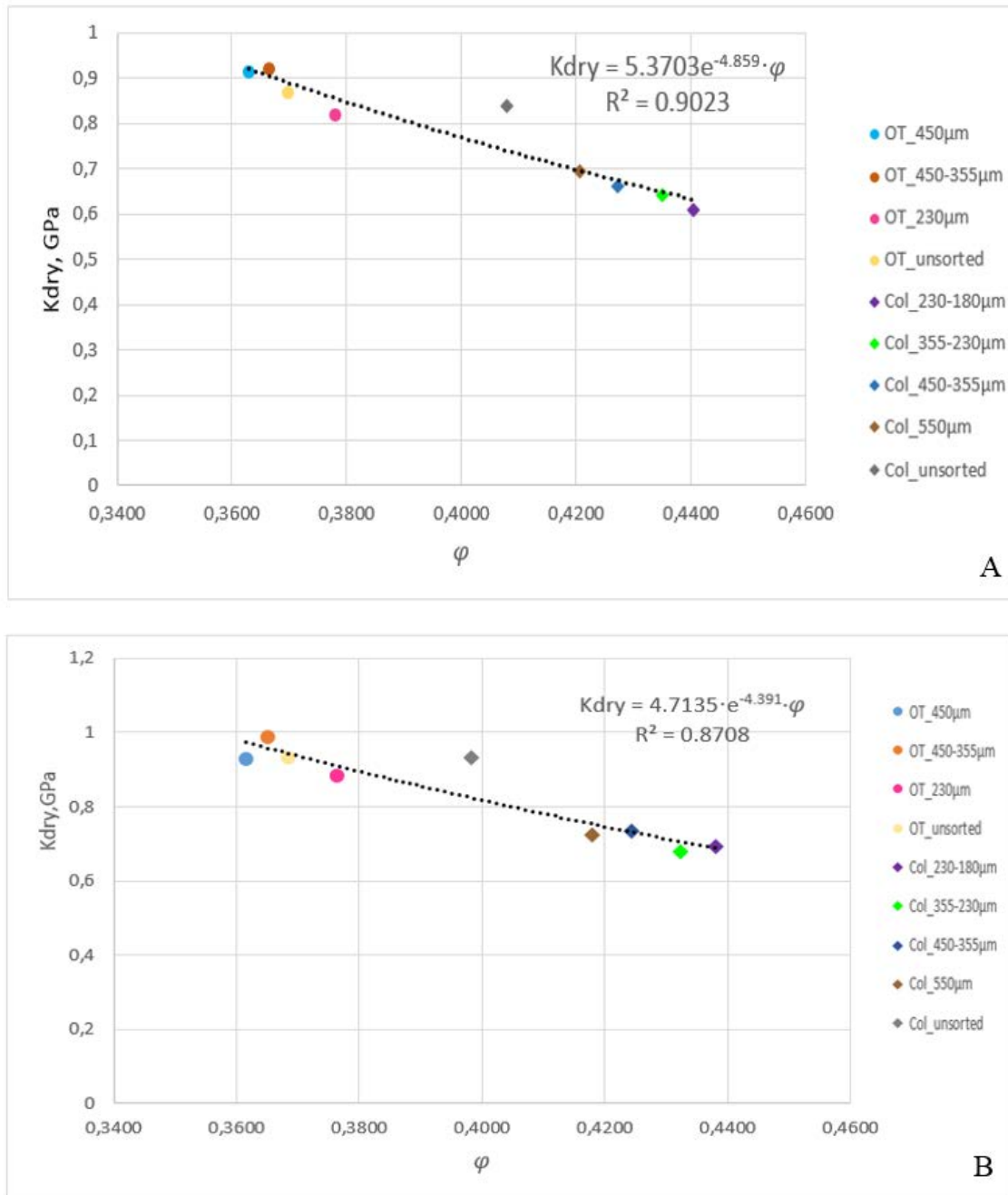


Figure 4.3.1.5. K_{dry} model for all considered types of sand with different grain sizes using average values. A. First dry load. B. Second dry load.

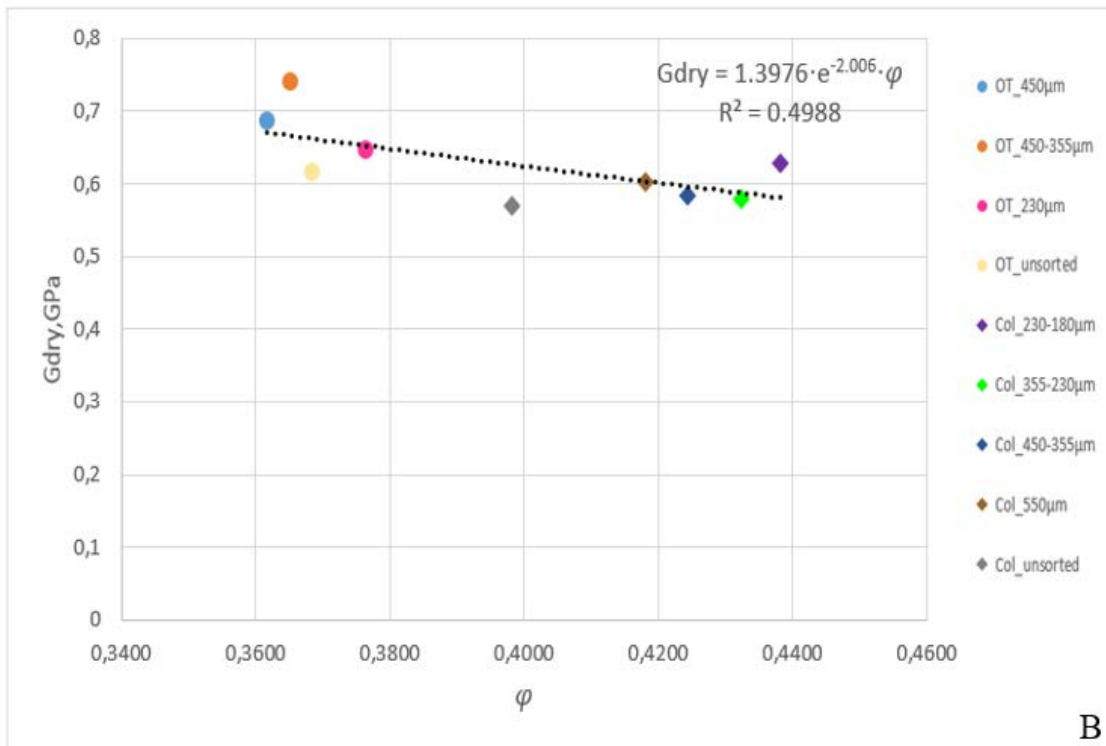
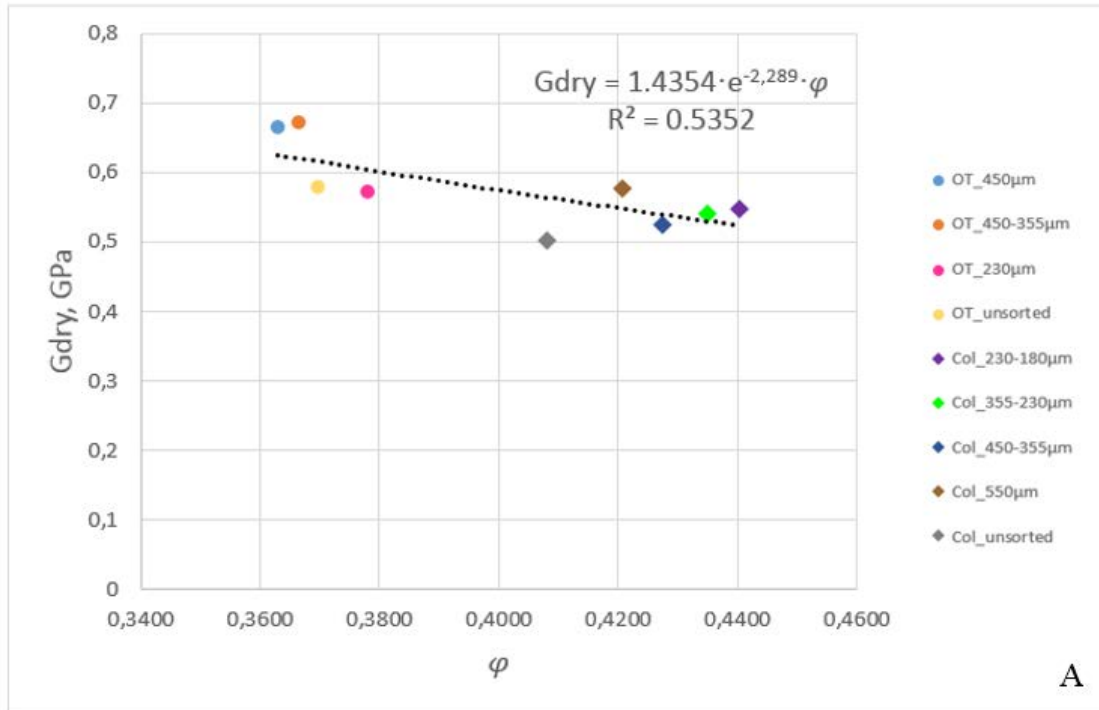


Figure 4.3.1.6. Gdry model for all considered types of sand with different grain sizes using average values. A. First dry load. B. Second dry load.

Kdry and Gdry models derived according to the average values might be more sustainable and accurate. Hence, they were chosen for the calculation of compressional and shear wave velocities of the saturated rock.

The observation of Kdry models showed that in general Kdry tends to increase with increasing of the grain size of sand. However, this tendency is not seemed to be that obvious for Gdry models. It can be seen in both dry loads.

4.3.2. Velocity models based on the first and second dry loads

First of all, we calculated compressional and shear wave velocities using Gassmann's theory and our derived models for Kdry and Gdry.

We got such models for Kdry and Gdry for both dry loads accordingly:

$$K^{1dry} = 5.37 \cdot e^{-4.86 \cdot \varphi} ,$$

$$G^{1dry} = 1.44 \cdot e^{-2.29 \cdot \varphi} ,$$

$$K^{2dry} = 4.71 \cdot e^{-4.39 \cdot \varphi} ,$$

$$G^{2dry} = 1.39 \cdot e^{-2.006 \cdot \varphi} ,$$

Assuming that the bulk modulus of the mineral making up rock is equal to 37GPa and the bulk moduli of the fluid is equal to 2.36 GPa (Mavko et al., 2009, p.459) as well as using our models for Kdry and Gdry, we calculated the bulk modulus of the saturated rock (equation (2) from the Subsection 4.2.1.1). Compressional and shear wave velocities were estimated using formulas (4) and (5) from the subsection 4.2.1.1.

In addition, we calculated the bulk and shear moduli of the saturated rock using Murphy's models for Kdry and Gdry (expressions (1) and (2) from the Subsection 4.2.1.2. for the case when porosity higher that 35%). This allowed us to estimate Vp and Vs velocities based on Gassmann's relations (formulas (4) and (5) from the Subsection 4.2.1.1) as well.

Secondly, we also tested two approximations of Biot's theory. The first Biot-Geertsma approximation was related to the high-frequency limiting velocities (described in the Subsection 4.2.1.3) . We created the programming code based on the formulas (1) and (2) from the subsection 4.2.1.3 in order to calculate high-frequency limiting velocities according to Biot's approximation. The code is shown in Section B4 of Appendix B. The calculations

involve K_{dry} and G_{dry} values as well. In this case we used the models K^1_{dry} , G^1_{dry} for the first load and K^2_{dry} , G^2_{dry} for the second load. We took porosity from the input data and density of the solid material we assumed to be equal to 2.65 g/cm^3 . The bulk moduli of the solid material was taken to be equal to 37 GPa and the bulk moduli of the fluid was set as 2.36 GPa. Density of the brine was calculated using Batzle-Wang's code (Section B3 of Appendix B) and it is constituted 1.02 g/cm^3 taken into account that pressure is 0.11 MPa, salinity is 35000ppm and temperature is 20°C . Tortuosity parameter was considered to be equal to 2 (Winkler, 1985).

Furthermore, we tested the Geertsma-Smit approximation of Biot's theory (Subsection 4.2.1.4). In order to calculate the reference frequency f_c (Subsection 4.2.1.3) we set up the values of permeability by ourselves since we are not aware of them. We have been working with unconsolidated sand, thus, we supposed high permeability values ranging up to 50000mD. The viscosity of the brine η was defined according to the following formula (Mavko et al., 2009, p. 341):

$$\eta = 0.1 + 0.333S + (1.65 + 91.9S^3)\exp\{-[0.42(S^{0.8} - 0.17)^2 + 0.045]T^{0.8}\},$$

where S is salinity that is 35000ppm and T is temperature that is 20°C (room conditions).

We also set up the value of porosity which is equal to about 38% for unconsolidated sand in our case. Frequency was done as an input parameter and it is constituted 500000Hz.

The detailed calculations are presented in the supplementary material in the USB flash-drive which attached to the printed version of the thesis.

The velocity models for the saturated rock obtained based on two dry loads using our models for K_{dry} and G_{dry} as well as Murphy's models for K_{dry} and G_{dry} , Gassmann's relations and approximation of Biot's theory are presented in the Figures 4.3.2.1, 4.3.2.2, 4.3.2.3 and 4.3.2.4 (V_{p1} and V_{p2} , V_{s1} and V_{s2} mean that velocities were calculated based on first and second dry load accordingly).

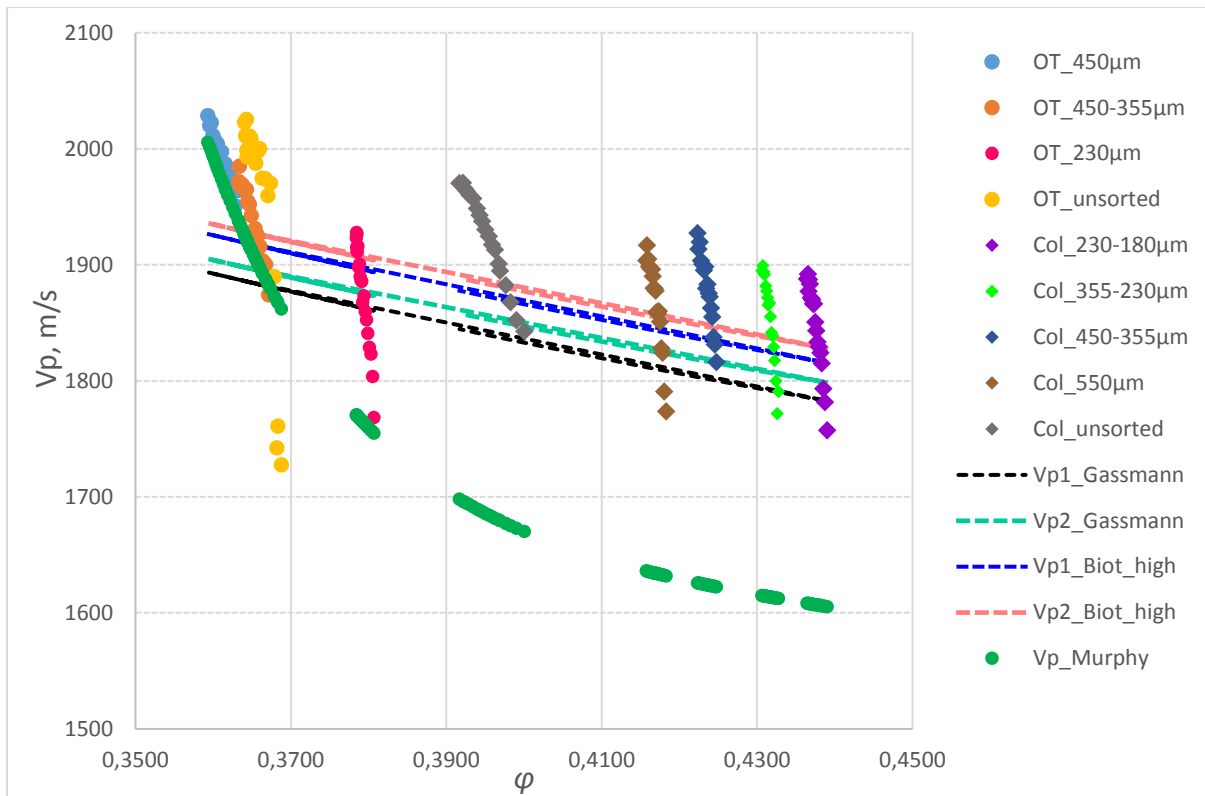


Figure 4.3.2.1. V_p velocity models of the saturated rock based on both dry loads.

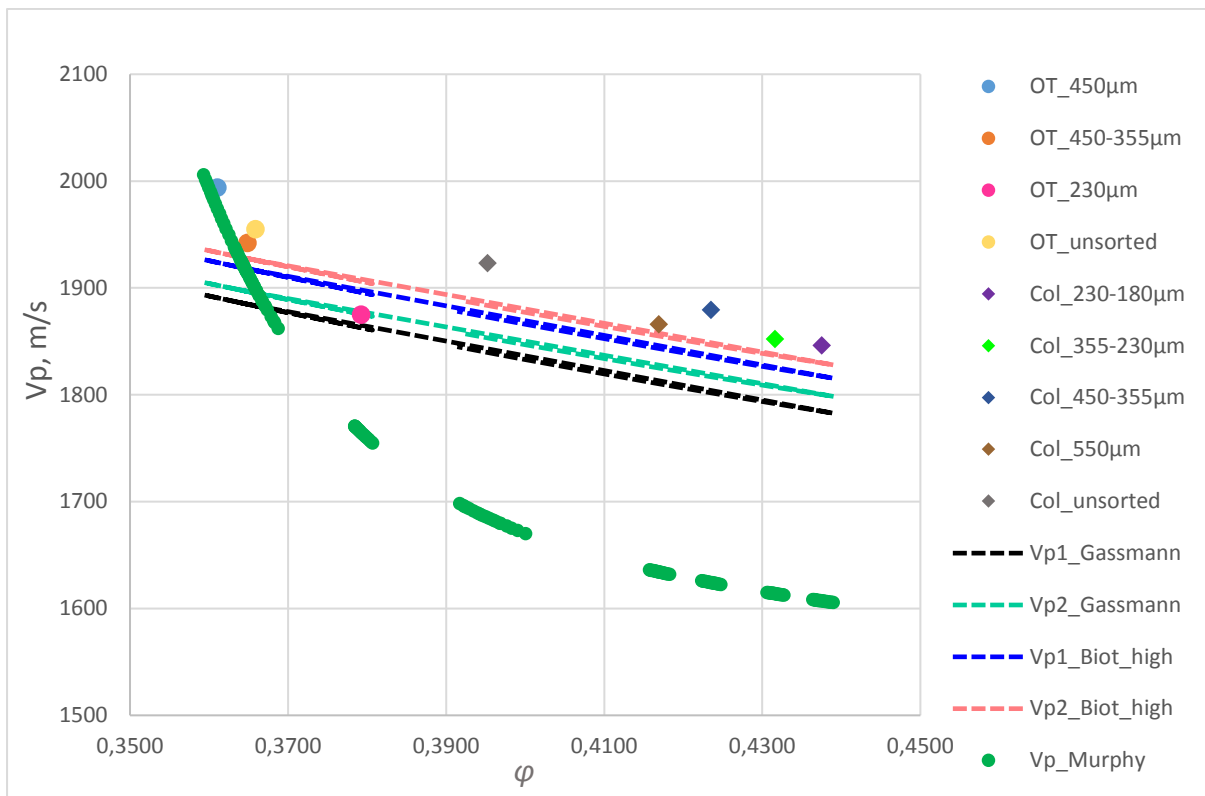


Figure 4.3.2.2. V_p velocity models of the saturated rock based on both dry loads.

The model in the Figure 4.3.2.1 includes the whole range of measured values of V_p , while the model in the Figure 4.3.2.2 involves the average values of measured V_p velocity and porosity for each type of sand.

Similarly we got the models for V_s velocity:

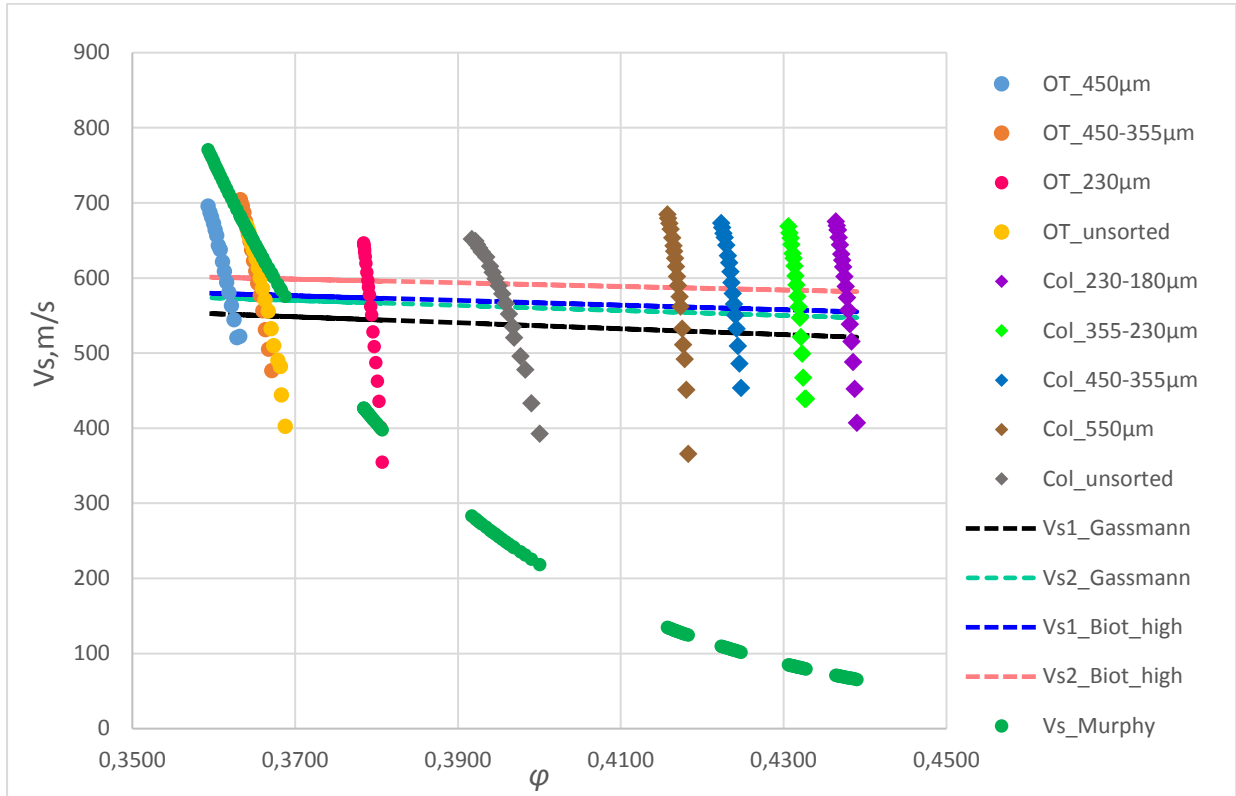


Figure 4.3.2.3. V_s velocity models of the saturated rock based on both dry loads.

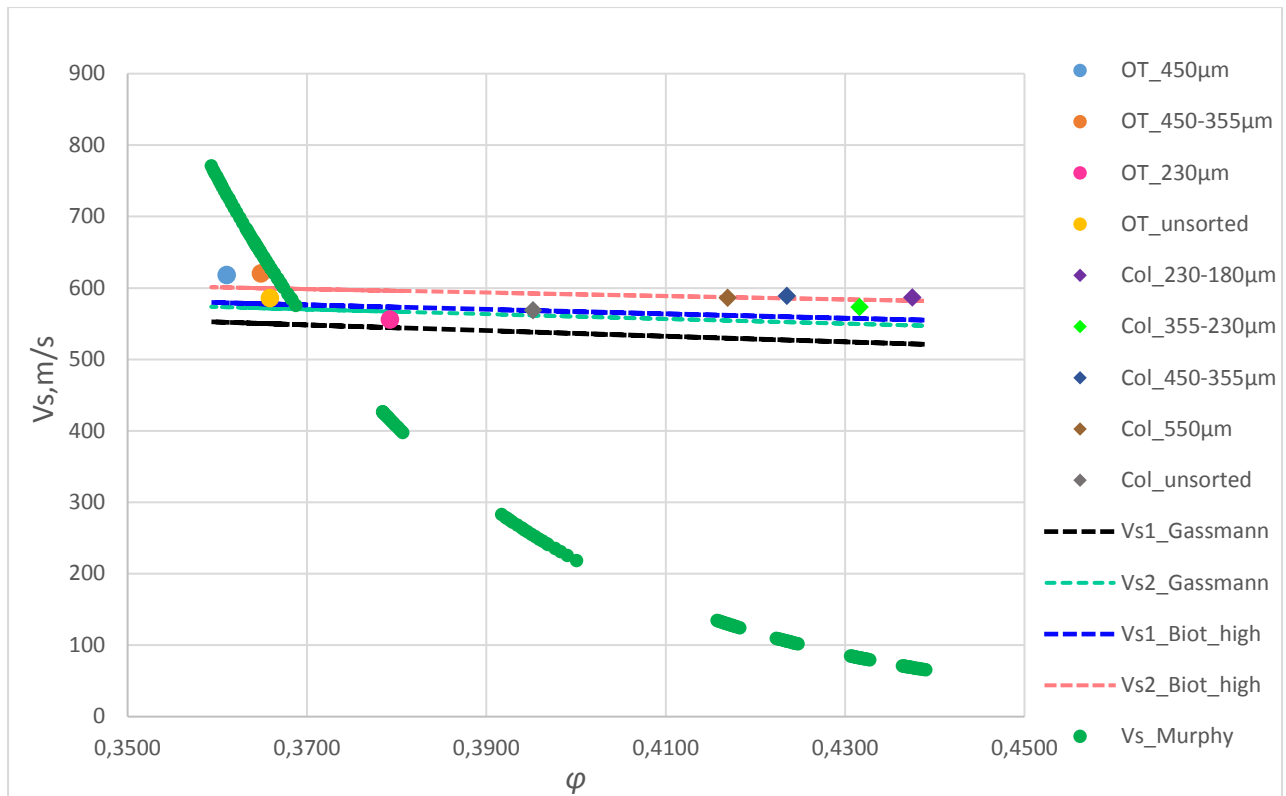


Figure 4.3.2.4. V_s velocity models of the saturated rock based on both dry loads.

The model in the Figure 4.3.2.3 includes the whole range of measured values of V_s , while the model in the Figure 4.3.2.4 involves the average values of measured V_s velocity and porosity for each type of sand.

From the Figures above we noticed that measured velocities are close to the velocities calculated based on Gassmann's relations and Biot-Geertsma high-frequency approximation. In contrast, velocities obtained according to Murphy's models for K_{dry} and G_{dry} show a dramatic difference for both V_p and V_s . One can see that velocities trends based on measured values as well as Gassmann's relations and Biot's approximation have a coincidence with Murphy's trend only up to porosity of about 37%. The porosity of random packing can vary up to 44.7% (Mavko et al., 2009). In the graphs we observed the changing in porosity of sand from approximately 36% to 44%. Hence, the high level of porosity can be explained by the packing of sand. However, according to the graphs we see a slight increasing of V_p velocity with increasing porosity while V_s velocity practically stays constant with rising porosity values that can not be correct due to the fact that in the fluid V_s should approach to zero. We believe that Murphy's trend behaves much more reasonable for V_p and V_s in comparison with the others. We assumed that laboratory data of unconsolidated sand are not completely correct. For this reason, we think that the considered models did not give relevant results.

Testing of the Geertsma-Smit approximation showed that it is not applicable for our case as well. We calculated the reference frequency according to the chosen permeability diapason and made the graph which is presented in the Figure 4.3.2.5.

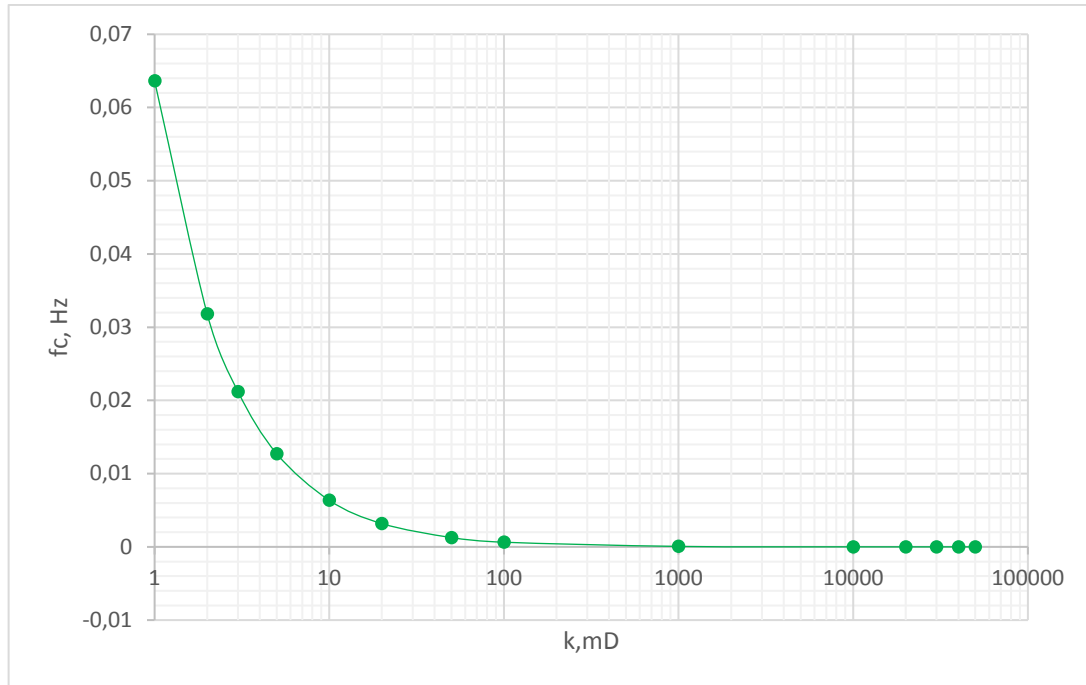


Figure 4.3.2.5. Reference frequency versus permeability.

It can be noticed in the Figure 4.3.2.5 that the reference frequency decreases with increasing permeability. We got the values of the reference frequency which are much lower than the frequency of the measurements. So, one of the requirements of the Biot's approximation $f < f_c$ is not fulfilled. (Subsection 4.2.1.4). Hence, Geertsma-Smit's approximation can not be used for our laboratory data of sand.

We planned to take into consideration the complete Biot's theory as well as Mavko-Jizba squirt relations. However, we think that the laboratory data of sand are biased. Therefore, we decided not to implement the further analysis.

5. Establishment of a well database for Cenozoic sediments in twelve wells of the Johan Sverdrup field

In this Chapter we presented editing as well as main calculations that were done with well logs. Moreover, the Chapter includes the essential part – modeling of shallow unconsolidated sediments and results of the derived models based on well logging data of all wells.

5.1. How were the wells selected

Well logging data of 12 wells considered in the thesis was provided by Petrobank. The location of wells was presented in the Section 1.1.

The wells in general are characterized by a good quality of well logs with a couple of exceptions to be identified later in this thesis. The wells were chosen according to the fact that well logs in most of the wells were recorded practically from the seabed level or close to seabed values. This makes the modeling of the shallow part possible and more correct as well as it allows to avoid significant uncertainties and errors in the final results.

5.2. Basic calculation before logs editing

Before the logs loading we calculated a true vertical depth mud line and a true vertical depth subsea for all considered wells. The formulas for TVDML and TVDSS calculation as wells as values of TVD, water depth and kelly bushing we presented in the Subsection 2.3.1. True vertical depth was determined using minimum curvature algorithm based on inclination, azimuth and depth data.

5.3. Editing of well logs

After loading the well logs it was important to check out the quality of them. The quality of logs in considered wells in general is good. However, there are some flaws that were found in well logs. The correction of logs was implemented in Geolog program.

5.3.1. Editing of gamma-ray logs

In the wells 16/2-20 S, 16/3-4 A and 16/3-8 A there is missing of values in gamma-ray log in some intervals. In order to improve this issue we used a linear interpolation in Geolog program. The wells with intervals where gamma-ray log was edited are presented in the Table 5.3.1.1.

Table 5.3.1.1.

Gamma-ray logs editing.

Well	Edited interval (m)	Missing of values	Type of editing
16/2-20 S	316.4 - 319.4	Hole	Linear interpolation
	605.8 – 609.5	Hole	Linear interpolation
16/3-4 A	758.1 – 761.4	Hole	Linear interpolation
16/3-8 A	210.2– 212.5	Hole	Linear interpolation

5.3.2. Editing of deep resistivity logs

In the wells 16/2-12, 16/2-14 T2, 16/2-20S, 16/2-5, 16/3-4 A, 16/3-7, 16/3-8 A, 16/4-6 S and 16/2-4 there is a missing of values in deep resistivity log in some intervals as well. They were corrected applying linear interpolation in the logarithmic space. The edited intervals are given in the Table 5.3.2.1.

Table 5.3.2.1.

Deep resistivity logs editing.

Well	Edited interval (m)	Flaw	Type of editing
16/2-12	605.0 – 610.8	Missing of values	Linear interpolation in the logarithmic space
	1219.5 -1225	Missing of values	Linear interpolation in the logarithmic space
	1668.6 - 1674.6	Missing of values	Linear interpolation in the logarithmic space
16/2-14 T2	610.1– 616.9	Missing of values	Linear interpolation in the logarithmic space
	1206.4-1208.5	Missing of values	Linear interpolation in the logarithmic space
	1561.3– 1574.3	Missing of values	Linear interpolation in the logarithmic space

Continuation of the Table 5.3.2.1.

Well	Edited interval (m)	Flaw	Type of editing
16/2-20 S	314.6– 317.3	Missing of values	Linear interpolation in the logarithmic space
	604.4– 607.9	Missing of values	Linear interpolation in the logarithmic space
	636.5– 645.5	Missing of values	Linear interpolation in the logarithmic space
16/2-5	509– 516.3	Missing of values	Linear interpolation in the logarithmic space
	1729.3 – 1736.1	Missing of values	Linear interpolation in the logarithmic space
16/3-4 A	503.5– 505.7	Missing of values	Linear interpolation in the logarithmic space
	591.8– 596.2	Missing of values	Linear interpolation in the logarithmic space
	755.3– 763.1	Missing of values	Linear interpolation in the logarithmic space
16/3-7	707.3 – 713.0	Missing of values	Linear interpolation in the logarithmic space
16/3-8 A	208.6– 210.9	Missing of values	Linear interpolation in the logarithmic space
	605.9– 607.0	Missing of values	Linear interpolation in the logarithmic space
16/4-6 S	605.6– 610.7	Missing of values	Linear interpolation in the logarithmic space
	1911.1– 1921.9	Missing of values	Linear interpolation in the logarithmic space
16/2-4	636.4– 645.4	Missing of values	Linear interpolation in the logarithmic space
	1690.1– 1692.1	Missing of values	Linear interpolation in the logarithmic space

5.3.3. Editing of sonic logs

5.3.3.1 Editing of compressional slowness logs

A special technique was applied to edit compressional slowness logs. This technique involves a creation of the synthetic logs. The synthetic logs restore the upper part of the raw DT logs in case when a record of the latter logs starts from the lower point in comparison with other logs. Thus, synthetic logs are a useful tool for the reconstruction of the upper part where values are omitted. Furthermore, synthetic logs allow to get rid of the holes by replacing the intervals with holes in raw logs with filled intervals of the synthetic logs.

The synthetic logs for editing of the raw DT log were made based on the Faust's equations. Faust's modification was considered in 2 forms – standard one and for the shallow part. Faust's equation is described by the following equation:

$$DT \cdot (RDEP_FINAL \cdot TVDML)^{\left(\frac{1}{6}\right)} = a + b \cdot V_CLAY,$$

where DT is a raw compressional slowness log, $RDEP_FINAL$ is the final edited deep resistivity log, $TVDML$ is true vertical depth mud line, a and b are strictly positive empirical constants which are the same for all wells and V_CLAY is the wet clay volume.

For our particular case the Faust's equation has the following formula based on all wells together:

$$DT_FAUST = 1000 \cdot (0.422 + 0.0332 \cdot V_CLAY) \cdot (RDEP_FINAL \cdot TVDML)^{\left(-\frac{1}{6}\right)},$$

where DT_FAUST is the log name for compressional slowness curve calculated based on Faust equation. This equation was used in order to calculate a synthetic DT_FAUST log.

However, the standard Faust equation in always breaks down in the first 100-300 m below the seabed as shown in the article "Faust Revisited – A Shallow Modification of the Faust Empirical Relationship Between Sonic Slowness and Resistivity" accepted for publication in CWLS Insite and included in this thesis before the list with references. The equation for the most shallow part was shown in this article to be:

$$DT_SHALLOW_FAUST = e^{(5.37 - 0.000610 \cdot TVDML)} \cdot RDEP_FINAL^{\left(-\frac{1}{6}\right)},$$

where $DT_SHALLOW_FAUST$ is the log name for compressional slowness curve calculated based on modified Faust equation for shallow part.

Both DT_FAUST and $DT_SHALLOW_FAUST$ calculations were made for all wells in order to compare raw and synthetic logs and to apply editing when it was necessary. The table below shows the intervals of wells where raw DT logs were edited. The correction was applied in the shallow part that missed the curve, intervals with missing values as well as in the bad hole and mud intervals. Bad hole intervals were determined by the large difference between bit size (BS) and caliper (CALI). This has influence also to the density log. If the density correction is big then it has impact to the density as well. If DT is close to mud value (approximately 189 ms/ft) then sonic log reads only mud and not rock.

Table 5.3.3.1.1.

DT logs editing.

Well	Edited interval (m)	Flaw	Type of editing
16/2-4	290.2-598	Absence of the log in the shallow part	DT_SHALLOW_FAUST
	1242.1-1328.8	Bad hole interval	DT_FAUST

Continuation of the Table 5.3.3.1.1.

Well	Edited interval (m)	Flaw	Type of editing
16/2-5	158.2-492.7	Absence of the log in the shallow part	DT_SHALLOW_FAUST
	1726.2 – 1730.7	Missing of values	DT_FAUST
16/2-12	137- 600.8	Absence of the log in the shallow part	DT_SHALLOW_FAUST
	1212.3 – 1234.6	Missing of values	DT_FAUST
16/2-20S	188.0-189.4	Mud interval	DT_FAUST
	276.8-277.8	Missing of values	DT_FAUST
	305.1-307.1	Missing of values	DT_FAUST
	595.2-597.4	Missing of values	DT_FAUST
	623.9-625.1	Missing of values	DT_FAUST
	654.1-655.1	Missing of values	DT_FAUST
	707.0-721.6	Mud interval, hole	DT_FAUST
16/2-14T2	135-581.4	Absence of the log in the shallow part	DT_SHALLOW_FAUST
16/3-4A	142.2-763.7	Absence of the log in the shallow part	DT_SHALLOW_FAUST
16/3-7	142.0-327.2	Absence of the log in the shallow part	DT_SHALLOW_FAUST
	692.5-718.7	Missing of values	DT_FAUST
16/3-8A	595.4-607	Missing of values	DT_FAUST
16/4-5	134.6-902.2	Absence of the log in the shallow part	DT_SHALLOW_FAUST
	1763.5-1770.1	Missing of values	DT_FAUST
16/4-6S	226.7-228.9	Missing of values	DT_FAUST
	242.0-245.7	Missing of values	DT_FAUST
	588.6-602.3	Missing of values	DT_FAUST
	1905.0-1909.0	Missing of values	DT_FAUST
16/5-4	696.5-710.2	Missing of values	DT_FAUST

The final DT log is a combination of the raw DT, DT_FAUST and DT_SHALLOW_FAUST logs. DT_SHALLOW_FAUST logs were used to restore the curve where the raw DT logs were missed in the shallow part. DT_FAUST logs were applied to fill the intervals with missing values as well as mud and bad holes intervals. In some wells the raw DT logs have no issues and, thus, they were not corrected, so the final log in this case is the same as the raw log.

5.3.3.2 Editing of shear slowness logs

We also edited raw DTS logs. In order to fill the intervals with missing values we created a synthetic DTS curve and merged it with a raw one. For every edited interval we derived a separate model. Using Archie formula for the water saturated case we get (Archie, 1942):

$$\text{Log}_{10}(RDEP_FINAL) = \text{Log}_{10}(aR_w) - m\text{Log}_{10}(\varphi),$$

where $RDEP_FINAL$ is the final edited deep resistivity log, a, m, R_w are constants and φ is porosity.

DTS is a function of porosity and porosity itself is related to resistivity according to the Archie formula. Thus, we determined models for DTS correction as functions of logarithm resistivity for each interval to be corrected. The intervals with missing values and equations for their correction are presented in the table below.

Table 5.3.3.2.

DTS logs editing.

Well	Edited interval (m)	Flaw	Type of editing
			DTS models for filling the holes
16/2-12	1215.3-1231.5	Missing of values	$DTS = 347.67 - 372.54\text{Log}_{10}(RDEP_FINAL)$
16/2-20S	499.8-515.6	Missing of values	$DTS = 482.70 - 15.06\text{Log}_{10}(RDEP_FINAL)$
	592.3-602.1	Missing of values	$DTS = 370.75 - 215.60\text{Log}_{10}(RDEP_FINAL)$
	621.2-628.5	Missing of values	$DTS = 526.63 - 721.02\text{Log}_{10}(RDEP_FINAL)$
	652.1-656.8	Missing of values	$DTS = 56.31 + 1554.51\text{Log}_{10}(RDEP_FINAL)$
	696.9-730.2	Missing of values	$DTS = 285.77 - 531.99\text{Log}_{10}(RDEP_FINAL)$
	959.3-980.7	Missing of values	$DTS = 388.94 - 760.13\text{Log}_{10}(RDEP_FINAL)$

Continuation of the Table 5.3.3.2.

Well	Edited interval (m)	Flaw	Type of editing
			DTS models for filling the holes
16/2-4	1670-1691	Missing of values	$DTS = 405.26 - 339.17 \text{Log}_{10}(RDEP_FINAL)$
16/2-5	1720.1-1743.8	Missing of values	$DTS = 386.55 - 106.60 \text{Log}_{10}(RDEP_FINAL)$
16/3-6	688.4-704.2	Missing of values	$DTS = 353.59 + 433.13 \text{Log}_{10}(RDEP_FINAL)$
16/3-7	694.2-718.3	Missing of values	$DTS = 371.56 + 28.79 \text{Log}_{10}(RDEP_FINAL)$
	1032.5-1060.8	Missing of values	$DTS = 292.09 + 542.68 \text{Log}_{10}(RDEP_FINAL)$
16/3-8A	593.1-610.9	Missing of values	$DTS = 436.62 + 6.93 \text{Log}_{10}(RDEP_FINAL)$
	1383.5-1421.8	Missing of values	$DTS = 347.01 + 30.93 \text{Log}_{10}(RDEP_FINAL)$
	1457.4-1534.3	Missing of values	$DTS = 216.38 - 667.55 \text{Log}_{10}(RDEP_FINAL)$
16/4-5	1228.9-1231.5	Missing of values	$DTS = 362.08 - 404.16 \text{Log}_{10}(RDEP_FINAL)$
	1418.1-1503.1	Missing of values	$DTS = 349.18 - 230.26 \text{Log}_{10}(RDEP_FINAL)$
	1540.6-1779.3	Missing of values	$DTS = 363.39 + 459.72 \text{Log}_{10}(RDEP_FINAL)$
16/5-4	478.8-485.9	Missing of values	$DTS = 802.45 - 1448.23 \text{Log}_{10}(RDEP_FINAL)$
	693.2-704.3	Missing of values	$DTS = 395.09 - 52.19 \text{Log}_{10}(RDEP_FINAL)$
	1340-1405	Missing of values	$DTS = 419.27 + 315.11 \text{Log}_{10}(RDEP_FINAL)$
	1422.6-1486	Missing of values	$DTS = 419.27 + 315.11 \text{Log}_{10}(RDEP_FINAL)$

5.3.4. Editing of density logs

The density logs correction included creation of the synthetic logs which allowed to restore a shallow part of the logs if it was missed in wells. Moreover, the synthetic density logs were applied to remove cavings and fill the intervals with missing values. The possible presence of cavings intervals in some wells was defined by the visible decreasing of raw density values. For the editing of density curves we used the Gardner's formula (Gardner, Gardner, & Gregory, 1974):

$$RHOB \cdot DT_FINAL^{\left(\frac{1}{4}\right)} = A + B \cdot V_CLAY,$$

where $RHOB$ is the raw density log, DT_FINAL is the final edited compressional slowness log, A and B are empirical constants.

For our particular case the Gardner's equation was reformulated as follows:

$$RHOB_SYNT = 1000 \cdot (0.0706 + 0.00223 \cdot V_CLAY) \cdot DT_FINAL^{(-\frac{1}{4})},$$

where $RHOB_SYNT$ is the synthetic density log.

We used this equation for all wells to calculate the synthetic density logs. The wells with intervals where density logs were edited are given in the Table 5.3.4.1.

Table 5.3.4.1.

Density logs editing.

Well	Edited interval (m)	Flaw	Type of editing
16/2-12	210.9-612.6	Absence of the log in the shallow part	RHOB_SYNT
	1196-1671.4	Missing of values	RHOB_SYNT
16/2-14T2	203.6-622	Absence of the log in the shallow part	RHOB_SYNT
	1163.6-1249	Caving	RHOB_SYNT
	1550.0-1567.0	Missing of values	RHOB_SYNT
16/2-20S	140.7-725.6	Absence of the log in the shallow part	RHOB_SYNT
	904.4-952.6	Caving	RHOB_SYNT
	965.5-971.3	Caving	RHOB_SYNT
16/2-4	290.2-645.5	Absence of the log in the shallow part	RHOB_SYNT
	942.7-1058.2	Caving	RHOB_SYNT
	1241.3-1324.7	Caving	RHOB_SYNT
	1681.7-1707.8	Missing of values	RHOB_SYNT
16/2-5	282.4-756.2	Caving, absence of the log in the shallow part	RHOB_SYNT
	969.1-999.3	Caving	RHOB_SYNT
	1124.5-1187.5	Caving	RHOB_SYNT
	1682.8-1756	Caving	RHOB_SYNT
16/3-4A	142.2-766.7	Absence of the log in the shallow part	RHOB_SYNT
16/3-6	156.9-712.1	Absence of the log in the shallow part	RHOB_SYNT

Continuation of the Table 5.3.4.1.

Well	Edited interval (m)	Flaw	Type of editing
16/3-7	141.8-722.5	Absence of the log in the shallow part	RHOB_SYNT
16/3-8A	141.2-610.7	Absence of the log in the shallow part	RHOB_SYNT
16/4-5	135.3-610.7	Absence of the log in the shallow part	RHOB_SYNT
	955.6-963.9	Caving	RHOB_SYNT
	1769.5-1779.5	Missing of values	RHOB_SYNT
16/4-6S	125.8-622.71	Absence of the log in the shallow part	RHOB_SYNT
	1006.2-1080.1	Caving	RHOB_SYNT
	1126.5-1196.3	Caving	RHOB_SYNT
	1338.4-1360.2	Caving	RHOB_SYNT
	1871.6-1914.5	Missing of values	RHOB_SYNT
16/5-4	133.3-768.1	Absence of the log in the shallow part	RHOB_SYNT
	1141.3-1246	Caving	RHOB_SYNT

The final density log is a combination of the raw and synthetic logs. The raw density log was used in a good intervals with no issues while the synthetic one was applied in edited intervals.

All logs editing includes log flag curves which serve as visual tools for indicating correction that was done. A log flag curve which is equal to 1 shows the intervals with no correction, whereas a log flag curve that is equal to 0 means the interval with correction. The following log flag curves were made in the thesis: GR_FLAG, RDEP_FLAG, DT_FLAG, DTS_FLAG and RHOB_FLAG.

5.4. Main calculation done on well logs

V_CLAY log was calculated from the GR log based on the following equation (Malcolm, 1996):

$$V_CLAY = \frac{GR_FINAL - GR_MIN}{GR_MAX - GR_MIN},$$

where V_CLAY is the volume of the wet clay, GR_FINAL is the final edited gamma-ray log, GR_MIN is the minimum of the gamma-ray log and GR_MAX is the maximum of the gamma-ray log. GR_MAX log was picked only in shale intervals, while GR_MIN log only in sand intervals.

Differential pressure was calculated from the density log using the following equation:

$$PRESS_DIFF = PRESS_OB - PRESS_HYDRO,$$

where $PRESS_DIFF$ is differential (effective) pressure, $PRESS_OB$ is overburden pressure and $PRESS_HYDRO$ is hydrostatic pressure.

The overburden pressure at a depth z is given by (Karimi, Adelzadeh, & Mohammadypour, 2014):

$$PRESS_OB = P_0 + g \int_0^z \rho(z) d(z),$$

where ρ_z is the density of the overlying rock at depth z , g is acceleration due to gravity and P_0 is the datum pressure (pressure at the surface). Since the values of the density close to seabed were missed in some wells, from the cross-plot in the Figure 5.5.1 we assumed one reasonable value of density which is equal to 2.1 g/cm^3 .

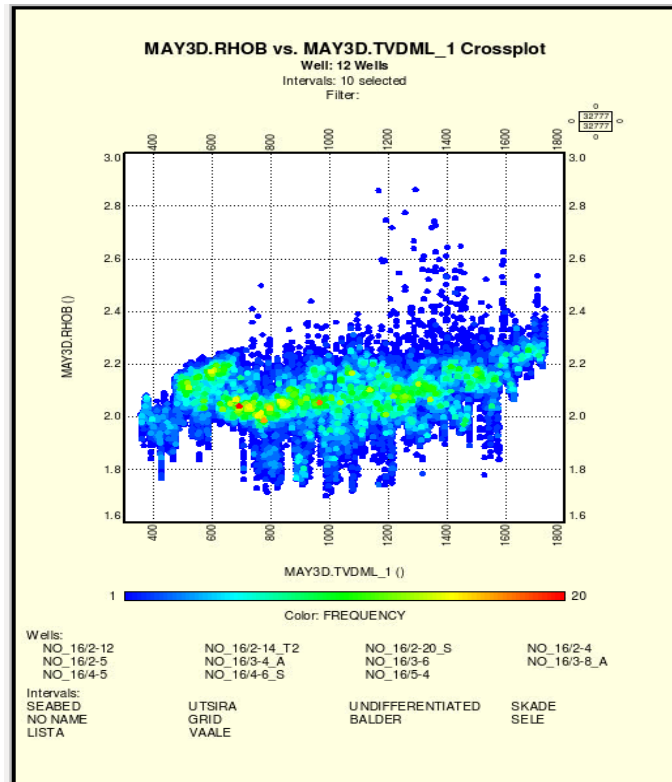


Figure 5.4.1. Density versus TVDML.

The hydrostatic pressure in its turn was calculated based on the following equation (Malcolm, 1996):

$$PRESS_{HYDRO} = PRESS_{OB} + g \cdot 0.01 \cdot \rho_{fl} \cdot TVDML,$$

where 0.01 is a conversion unit, ρ_{fl} is density of the fluid (equal to 1.03g/cm³).

At seabed the values of hydrostatic and overburden pressures are equal or practically equal.

Porosity was calculated using the following formula (Malcolm, 1996):

$$PHIT = (\rho_{ma} - RHOB_{FINAL}) / (\rho_{ma} - \rho_{fl}),$$

where ρ_{ma} is the density of the rock matrix (equal to 2.65g/cm³), $RHOB_{FINAL}$ is the final edited density log. The lowest and highest limits for the porosity curve are 0.01 and 0.5 respectively.

Calculation of velocities on well logs were done according to the formulas (Malcolm, 1996):

$$VP = 304800 / DT_{FINAL},$$

where VP is the compressional wave velocity log, DT_{FINAL} is the final edited compressional slowness log and

$$VS = 304800/DTS_FINAL,$$

where VS is the shear wave velocity log, DTS_FINAL is the final edited shear slowness log.

The results of logs editing as well as main calculations done on well logs we showed in CPI plots for three main formations: Utsira, Skade and Grid for every well.

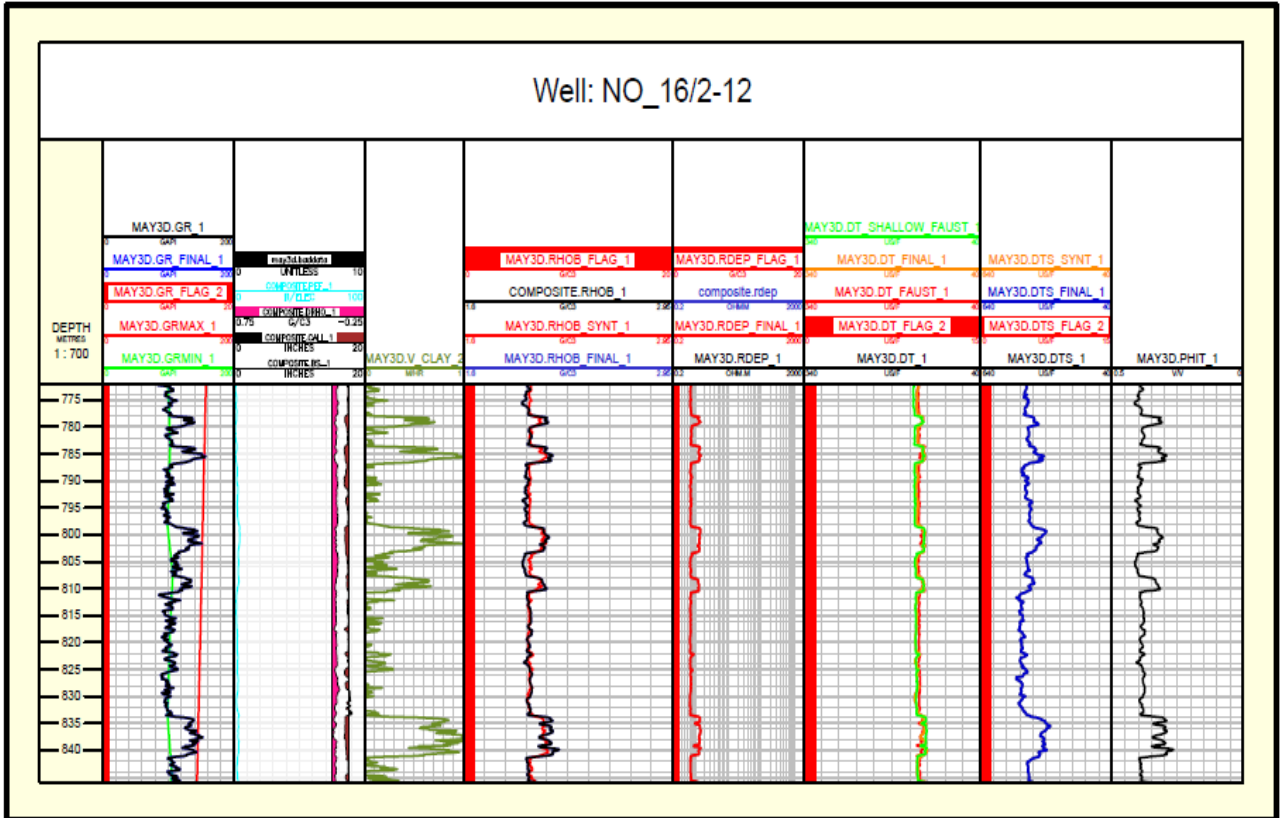


Figure 5.4.2. CPI showing well logs editing and main calculations for the Utsira formation in the well 16/2-12.

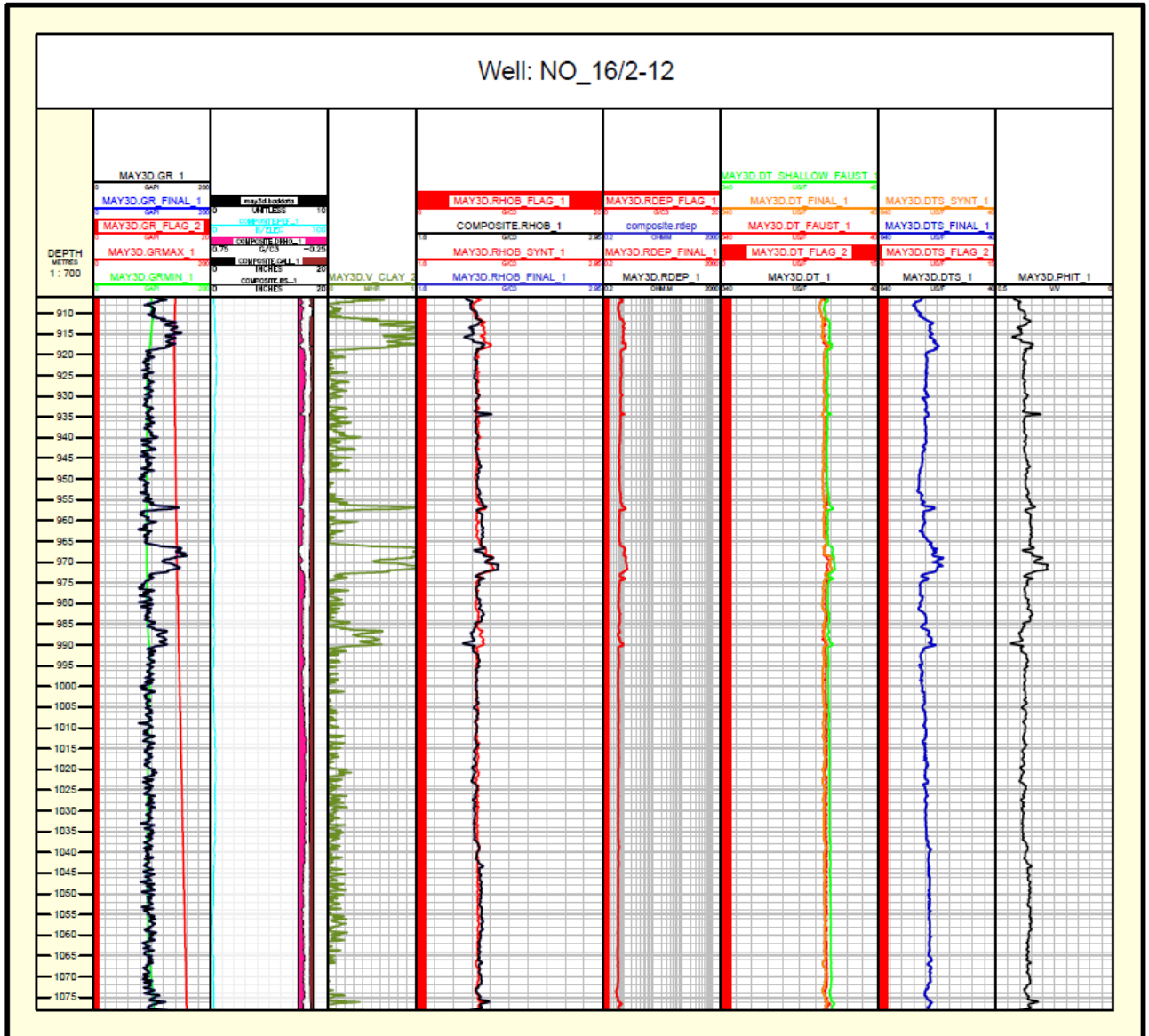


Figure 5.4.3. CPI showing well logs editing and main calculations for the Skade formation in the well 16/2-12.

In this particular well the Grid formation does not exist. Hence, there is no CPI for this formation in this particular well.

The CPI plots for the remaining wells are presented in Appendix C. We would like to make a small remark about these CPI plots. Some tracks include several curves, due to exact scale for all logs in one track, the curves are overlapped. Because of this small issue of the program in some wells one can not see both edited (final) and raw logs in one track at once. However, the Flag logs indicate where the logs were edited.

6. Sonic modeling from well logs

This Chapter presents the sonic models that we obtained based on well logging data. We considered two sonic models and we made our conclusion which model is better for the shallow formations.

6.1. Motivation for two sonic models

There are two natural boundary conditions in sand/shale:

1. Finite values of sonic velocities at seabed where a lower bound of compressional wave velocity may be estimated by the Coppen's and Batzle-Wang's models.
2. For large TVDML velocities are approximately constant or slightly increase. The power model satisfy both conditions while a second order polynomial model satisfy only the one (first condition).

Based on the investigation of laboratory data of shale we also concluded that a power model seems to be the best model for sonic velocities. In the well logs sonic modeling part we considered two models.

First of all we tried out a power model on well logs. The power model on well logs has the same equation as we had for our laboratory studies. For compressional wave velocity we get:

$$VP = VP_b + A \cdot \sigma^B,$$

where VP is compressional wave velocity, VP_b is compressional wave velocity of the brine at seabed, σ is effective pressure, A and B are coefficients of the equation. Similarly we have equation for shear wave velocity:

$$VS = VS_b + A' \cdot \sigma^{B'},$$

where VS is shear wave velocity, VS_b is shear wave velocity of the brine at seabed, σ is effective pressure, A' and B' are coefficients of the equation.

The second approach of the considered models involves resistivity in addition to differential pressure. The model represents a generalization of both the power and the Faust models. The Faust model for compressional wave velocity has the following general form:

$$VP = A'' \cdot RDEP_FINAL^{1/6} \cdot TVDML^{1/6},$$

where A'' is coefficient of the equation, $RDEP_FINAL$ is the final edited deep resistivity log, $TVDML$ is true vertical depth mud line. The true vertical depth mud line versus differential

pressure has in general a linear trend for all twelve wells in the range 0 m TVDML – 1200 m TVDML that can be seen in the figure below.

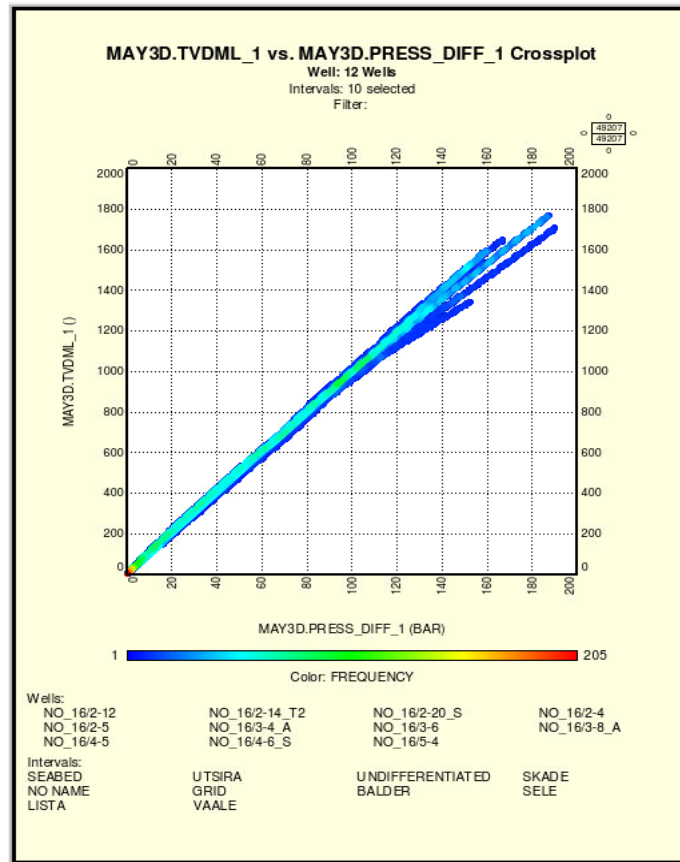


Figure 6.1.1. TVDML versus differential pressure.

It allowed us to make an assumption that true vertical depth mud line can be roughly equal to differential pressure at least down to about 1200 m TVDML. Thus, in the second model in stead of TVDML we used differential pressure parameter. The second model then has the following form for compressional wave velocity:

$$VP = VP_b + A'' \cdot RDEP_FINAL^m \cdot \sigma^n,$$

where VP_b is compressional wave velocity of the brine at seabed, A'' is coefficient of the equation, m, n are exponents of the equation, $RDEP_FINAL$ is the final edited deep resistivity curve, σ is differential pressure. Similarly we get the formula for shear wave velocity:

$$Vs = Vs_b + A''' \cdot RDEP_FINAL^{m'} \cdot \sigma^{n'},$$

where Vs_b is shear wave velocity of the brine at seabed, A''' is coefficient of the equation and m', n' are exponents of the equation.

Notice that in order to get finite limits for Vp and Vs close to the seabed we need to have n and $n' \geq 0$. Further, the previous equations may be inverted to give:

$$\sigma = \left(\frac{VP - VP_b}{A''}\right)^p \cdot \left(\frac{VS - VS_b}{A'''}\right)^q$$

$$RDEP_FINAL = \left(\frac{VP - VP_b}{A''}\right)^{p'} \cdot \left(\frac{VS - VS_b}{A'''}\right)^{q'}$$

where

$$p = \frac{m'}{nm' - n'm}$$

$$q = \frac{-m}{nm' - n'm}$$

$$p' = \frac{-n'}{nm' - n'm} \text{ and}$$

$$q' = \frac{n}{nm' - n'm}$$

Thus, for $m'/m \neq n'/n$ there is a one to one correspondence between points in the (VP, VS) space and the (RDEP_FINAL, σ) space. In particular, in water-filled sand the Archie equation gives the porosity as a function of VP and VS:

$$\varphi = \left(\frac{RDEP_FINAL}{aR_w}\right)^{1/m}$$

where a , m and R_w are constants.

6.2. The first models for compressional and shear wave velocities - optimization is based on all wells simultaneously

In this section we considered the first and second models for Vp and Vs based on the optimization for all wells simultaneously.

6.2.1. The first model for compressional wave velocity

In well logging part the values of compressional wave velocity of the brine at seabed for sand and shale we obtained from the cross-plots showing Vp versus differential pressure for the twelve wells. This is the value of velocity at zero differential pressure.

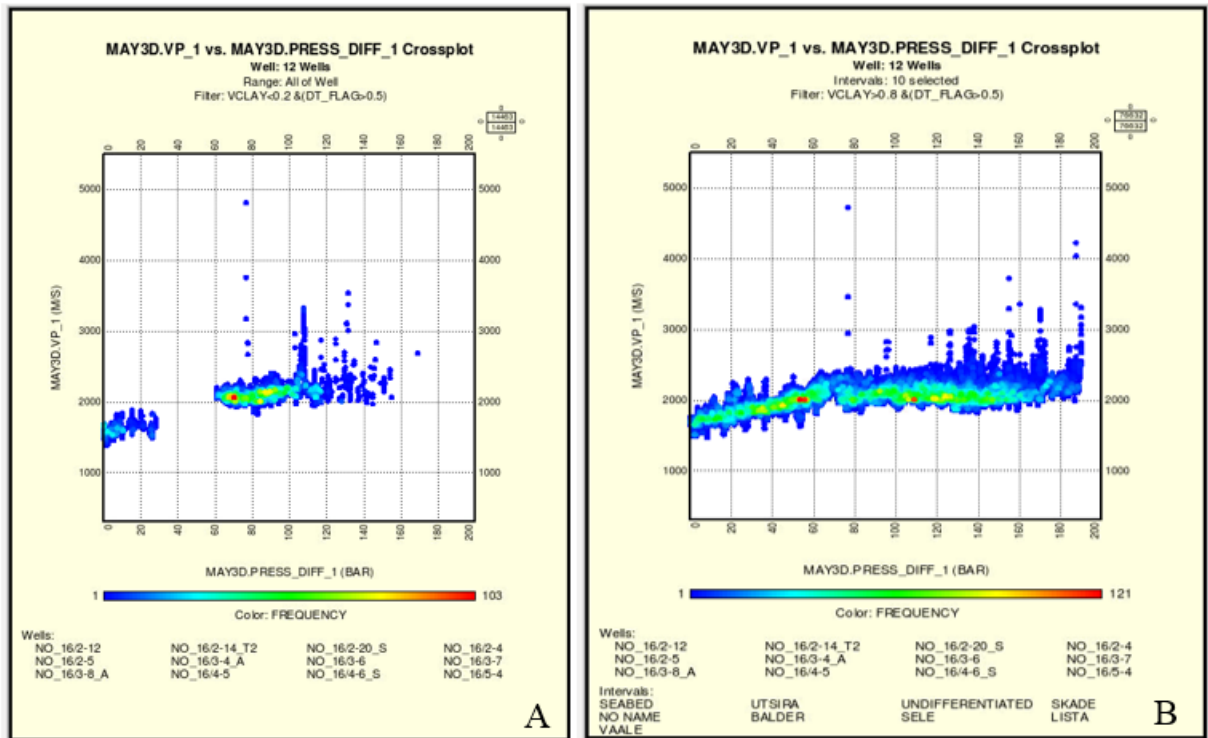


Figure 6.2.1.1. Cross-plot “Vp versus σ ”. A. For sand B. For shale.

For the sand the compressional wave velocity at the seabed is equal to about 1470m/s, whereas for shale the value is a bit higher and it constitutes around 1610 m/s. The remaining coefficients for the first model were obtained by taking logarithm of the differential pressure values and logarithm of the difference between raw values of compressional wave velocity and the values of the compressional wave velocity at seabed which are presented in the cross-plots in the Figure 6.2.1.2.

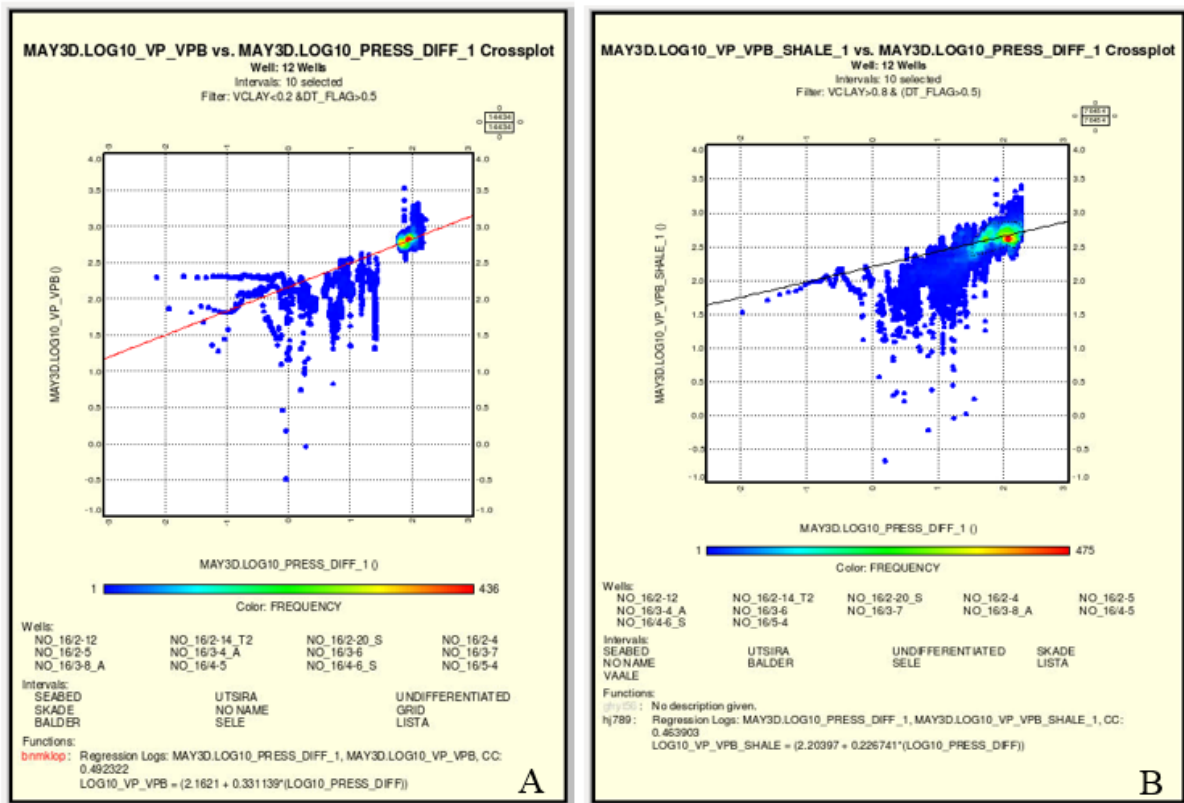


Figure 6.2.1.2. Compressional wave velocity model. A. For sand B. For shale

Having changed the logarithm form of the equations, we got the following power compressional wave velocity models for sand and shale:

$$VP_{sand} = 1470 + 145 \cdot \sigma^{0.331},$$

$$VP_{shale} = 1610 + 159 \cdot \sigma^{0.227}.$$

6.2.2. The first model for shear wave velocity

We found the shear wave velocities of the brine at seabed for sand and shale in the same way as for compressional wave models. We also used cross-plots showing shear wave velocity against differential pressure for all wells.

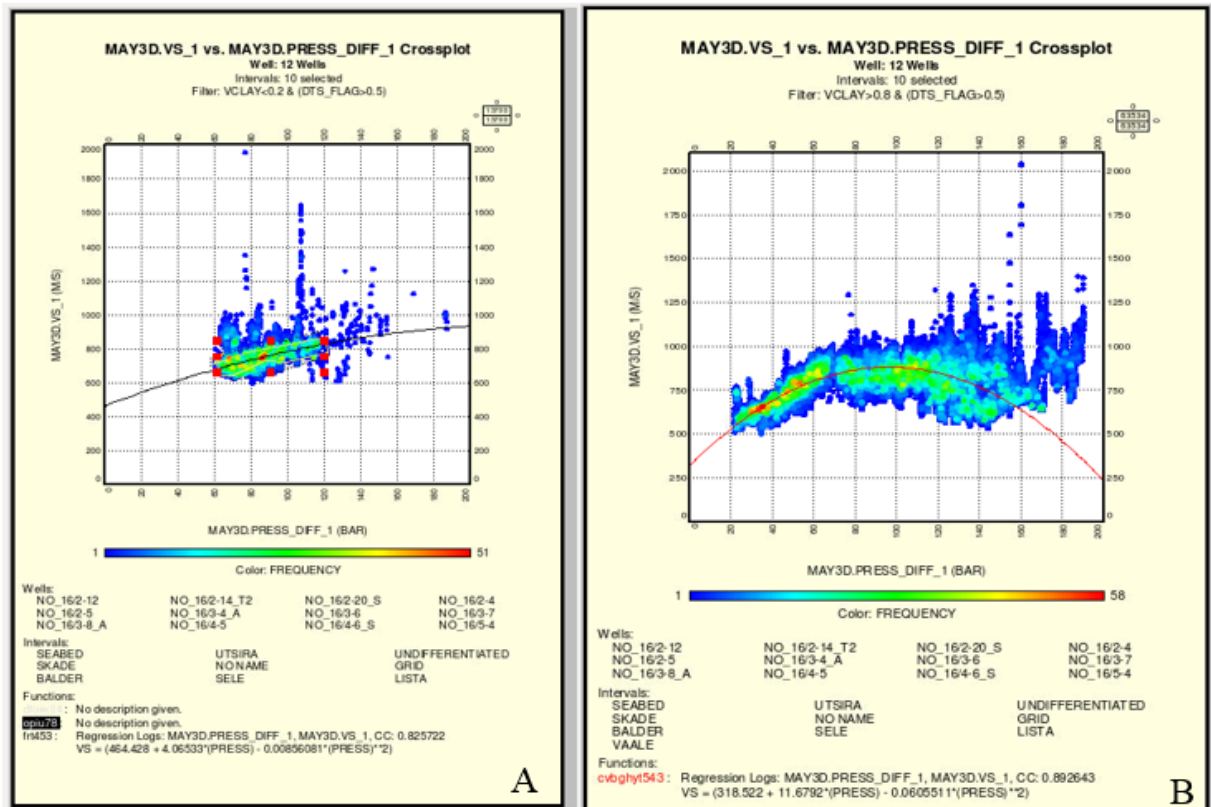


Figure 6.2.2.1. Cross-plot “Vs versus σ ” for sand. A. For sand B. For shale.

In this case it was not so clear to define the shear wave velocity of the brine at zero differential pressure. We used a second order polynomial models in order to define shear wave velocity of the brine at seabed. We assumed the value for sand which is equal to about 460m/s and for shale it is around 330m/s.

The remaining coefficients for the first model for shear wave velocity we got by taking logarithm of the differential pressure values and logarithm of the difference between raw values of shear wave velocity and the values of the shear wave velocity at seabed, and showing it in the cross-plots in the Figure 6.2.2.2.

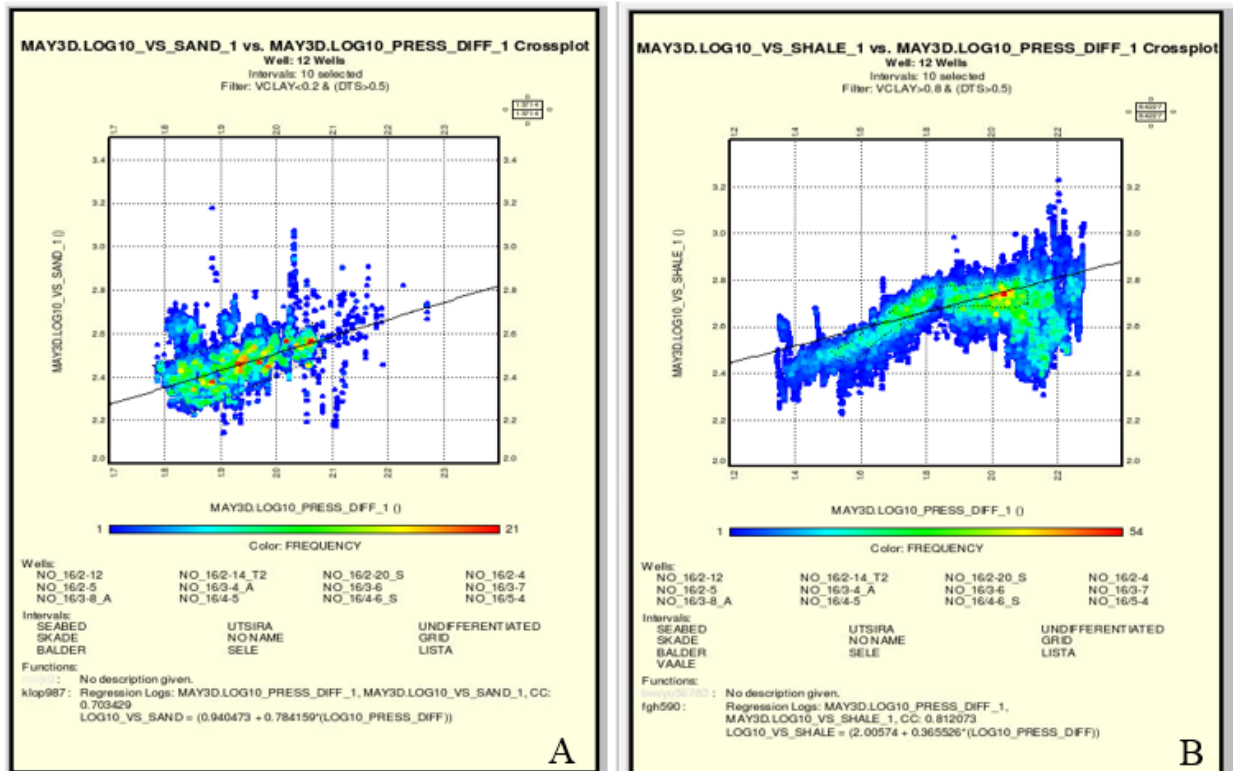


Figure 6.2.2.2. Shear wave velocity model. A. For sand B. For shale.

Having changed the logarithm form of the equations, we got the following power shear wave velocity models for sand and shale:

$$VS_{sand} = 460 + 8.72 \cdot \sigma^{0.784},$$

$$VS_{shale} = 330 + 101 \cdot \sigma^{0.366}.$$

6.3. Consistency of the seabed velocities

We decided to check if the estimated values of velocities at seabed were chosen correctly. The Poisson's ratio is directly related to the V_p/V_s ratio as follows (Mavko et al., 2009):

$$\nu = \frac{(VP/VS)^2 - 2}{2[(VP/VS)^2 - 1]}$$

The results are given in the Table 6.3.1.

Table 6.3.1. Poisson's ratio values at seabed.

Lithology	VP _b (m/s)	VS _b (m/s)	PR _b
Sand	1470	460	0.45
Shale	1610	330	0.48

For both sand and shale the values at seabed satisfy the following consistency requirements at seabed (Mavko et al., 2009):

1. $VP_b > VS_b$.
2. $0 < PR_b < 0.5$
3. PR_b should be close to the fluid limit 0.5.

Therefore, the chosen values of compressional and shear wave velocities for sand and shale at seabed seem to be reasonable.

6.4. The second models for compressional and shear wave velocities – optimization is based on all wells

6.4.1. The second model for compressional wave velocity

Using the multiple regression in Geolog program we got the coefficients of the equation for compressional wave velocity in logarithmic form. They are listed in the Tables 6.4.1.1 and 6.4.1.2.

Table 6.4.1.1.

Resulting coefficients of the multiple regression for sand from output of Geolog generated report.

LOG	COEFFICIENT
CONSTANT	1.87879
LOG10_PRESS_DIFF	0.49324
LOG10_RDEP_FINAL	0.27703

Table 6.4.1.2.

Resulting coefficients of the multiple regression for shale from output of Geolog generated report.

LOG	COEFFICIENT
CONSTANT	1.37648
LOG10_PRESS_DIFF	0.64307
LOG10_RDEP_FINAL	0.50672

The final equations of the second compressional wave velocity model for sand and shale are as follows:

$$VP_{sand} = 1470 + 75.9 \cdot RDEP_FINAL^{0.277} \cdot \sigma^{0.493},$$

$$VP_{shale} = 1610 + 23.9 \cdot RDEP_FINAL^{0.507} \cdot \sigma^{0.643}.$$

6.4.2. The second model for shear wave velocity

Using the multiple regression in Geolog we calculated the coefficients of the equation for shear wave velocity in logarithmic form. They are shown in the Tables 6.4.2.1 and 6.4.2.2.

Table 6.4.2.1.

Resulting coefficients of the multiple regression for sand from output of Geolog generated report.

LOG	COEFFICIENT
CONSTANT	1.49902
LOG10_PRESS_DIFF	0.52913
LOG10_RDEP_FINAL	0.39090

Table 6.4.2.2.

Resulting coefficients of the multiple regression for shale from output of Geolog generated report .

LOG	COEFFICIENT
CONSTANT	1.86449
LOG10_PRESS_DIFF	0.40887
LOG10_RDEP_FINAL	0.35859

The final equations of the second shear wave velocity model for sand and shale are as follows:

$$Vs_{sand} = 460 + 31.6 \cdot RDEP_FINAL^{0.391} \cdot \sigma^{0.529},$$

$$Vs_{shale} = 330 + 73.1 \cdot RDEP_FINAL^{0.359} \cdot \sigma^{0.409}.$$

6.5. The first models for compressional and shear wave velocities – optimization is based on every well

The models that we described earlier are based on optimization for all wells simultaneously. Since the formations intervals vary from well to well, we also derived the velocity models based on optimization in every well. We assumed that it would allow to improve the models.

6.5.1. The first model for compressional wave velocity

Making the cross-plots of compressional wave velocities versus differential pressure the got the coefficients of the models for every well. They are presented in Table 6.5.1.1.

Table 6.5.1.1.

The coefficients of the first model for compressional wave velocity for 12 wells, where VP_b is equal to 1470m/s in sand and VP_b is equal to 1610 m/s in shale.

Well	Sand		Shale	
	A_{sand}	B_{sand}	A_{shale}	B_{shale}
16/2-12	18.44	0.79	8.91	0.80
16/2-14T2	17.27	0.81	108.79	0.32
16/2-20S	17.93	0.77	208.68	0.16

Continuation of the Table 6.5.1.1.

Well	Sand		Shale	
	A _{sand}	B _{sand}	A _{shale}	B _{shale}
16/2-4	14.59	0.86	7.61	0.90
16/2-5	21.99	0.78	41.23	0.47
16/3-4A	18.86	0.79	150.09	0.23
16/3-6	280.83	0.19	135.45	0.23
16/3-7	324.59	0.14	138.80	0.23
16/3-8A	121.87	0.34	133.72	0.23
16/4-5	6.11	1.05	170.06	0.23
16/4-6S	151.54	0.32	27.09	0.59
16/5-4	116.94	0.39	49.45	0.47

6.5.2. The first model for compressional wave velocity

We got the coefficients of the first model for shear wave velocity similarly as for compressional wave velocity. The results are presented in the Table 6.5.2.1.

Table 6.5.2.1.

The coefficients of the first model for shear wave velocity for 12 wells, where VS_b is equal to 460 m/s in sand and VS_b is equal to 330 m/s in shale.

Well	Sand		Shale	
	A' _{sand}	B' _{sand}	A' _{shale}	B' _{shale}
16/2-12	21.12	0.62	30.97	0.58
16/2-14T2	49.82	0.41	24.33	0.66
16/2-20S	39.77	0.46	36.01	0.59
16/2-4	1.66	1.14	56.95	0.45
16/2-5	22.47	0.53	54.37	0.40
16/3-4A	40.28	0.56	243.35	0.18
16/3-6	83.90	0.29	71.73	0.43
16/3-7	5.39	0.92	54.92	0.49
16/3-8A	97.00	0.24	84.11	0.39
16/4-5	1.12	1.26	239.86	0.14

Continuation of the Table 6.5.2.1.

Well	Sand		Shale	
	A'_{sand}	B'_{sand}	A'_{shale}	B'_{shale}
16/4-6S	6.59	0.82	168.73	0.24
16/5-4	39.46	0.45	230.36	0.17

6.6. The second models for compressional and shear wave velocities – optimization is based on every well

Using multiple regression in Geolog we got the coefficients of the second models for compressional and shear wave velocities in logarithmic form for every well separately. Having inverted the logarithmic form we presented the coefficients of the second models for V_p and V_s for every well in the Subsections 6.6.1 and 6.6.2.

6.6.1. The second model for compressional wave velocity

The resulting coefficients of the second model for V_p are listed in the Table 6.6.1.1.

Table 6.6.1.1.

The coefficients of the second model for compressional wave velocity for 12 wells, where VP_b is equal to 1470m/s in sand and VP_b is equal to 1610 m/s in shale.

Well	Sand			Shale		
	A''_{sand}	m_{sand}	n_{sand}	A''_{shale}	m_{shale}	n_{shale}
16/2-12	138.93	0.12	0.36	30.73	0.54	0.62
16/2-14T2	62.18	0.42	0.56	27.14	0.73	0.64
16/2-20S	24.75	0.35	0.75	34.34	0.52	0.57
16/2-4	95.10	0.13	0.44	41.03	0.60	0.51
16/2-5	23.01	0.68	0.81	33.04	0.58	0.58
16/3-4A	288.07	0.19	0.17	8.39	0.82	0.85
16/3-6	50.74	0.15	0.59	15.59	0.57	0.76
16/3-7	20.06	0.36	0.80	21.78	0.46	0.65
16/3-8A	131.23	-0.21	0.31	19.42	0.67	0.69

Continuation of the Table 6.6.1.1.

Well	Sand			Shale		
	A''_{sand}	m_{sand}	n_{sand}	A''_{shale}	m_{shale}	n_{shale}
16/4-5	65.51	0.02	0.51	3.79	0.71	1.05
16/4-6S	133.63	0.06	0.34	10.47	0.78	0.78
16/5-4	38.92	0.93	0.66	21.54	0.55	0.65

6.6.2. The second model for shear wave velocity

For shear wave velocity we got the resulting coefficients that are shown in the Table 6.6.2.1.

Table 6.6.2.1.

The coefficients of the second model for shear wave velocity for 12 wells, where VS_b is equal to 460 m/s in sand and VS_b is equal to 330 m/s in shale.

Well	Sand			Shale		
	A'''_{sand}	m'_{sand}	n'_{sand}	A'''_{shale}	m'_{shale}	n'_{shale}
16/2-12	10.98	-0.06	0.73	88.59	0.74	0.37
16/2-14T2	21.91	0.46	0.62	47.14	0.79	0.51
16/2-20S	4.00	0.55	1.02	18.66	0.78	0.74
16/2-4	15.59	0.32	0.66	36.25	0.72	0.51
16/2-5	0.74	0.80	1.39	50.52	0.58	0.47
16/3-4A	215.95	0.01	0.17	208.57	0.16	0.21
16/3-6	317.26	1.29	0.06	52.91	0.46	0.49
16/3-7	44.91	0.51	0.46	40.09	0.61	0.54
16/3-8A	122.35	0.85	0.25	55.75	0.40	0.49
16/4-5	12.28	0.08	0.74	72.84	-0.48	0.42
16/4-6S	33.83	0.42	0.48	63.16	0.66	0.40
16/5-4	9.36	0.68	0.80	83.38	0.12	0.38

6.7. Comparison of the first and second sonic models based on optimization for all wells simultaneously and well by well

Compressional and shear slowness that we calculated using our derived sonic models we presented in CPI plots. As we mentioned in the earlier, first of all, we estimated DT and DTS based on the first and second models for compressional and shear wave velocities optimized taking all twelve wells simultaneously and then we did the same calculations in wells separately. Taking the well 16/2-12 like an example we got the following results for the Utsira and Skade formations (since the Grid formation does not exist in this well, it was not included in this particular case). We should mention that CPIs for the remaining wells are similar to those shown in this section and they are presented in Appendix D and E. In Appendix D we presented the CPI plots showing DT and DTS calculated based on the first and second sonic models optimized for all wells together for the Utsira, Skade and Grid formations. In Appendix E there are CPIs showing DT and DTS calculated based on the first and second sonic models optimized for 10 wells separately for the Utsira, Skade and Grid formations. Further, we would exclude the wells 16/3-4 A and 16/4-5 from the final models and, thus, we did not include them in the final CPIs.

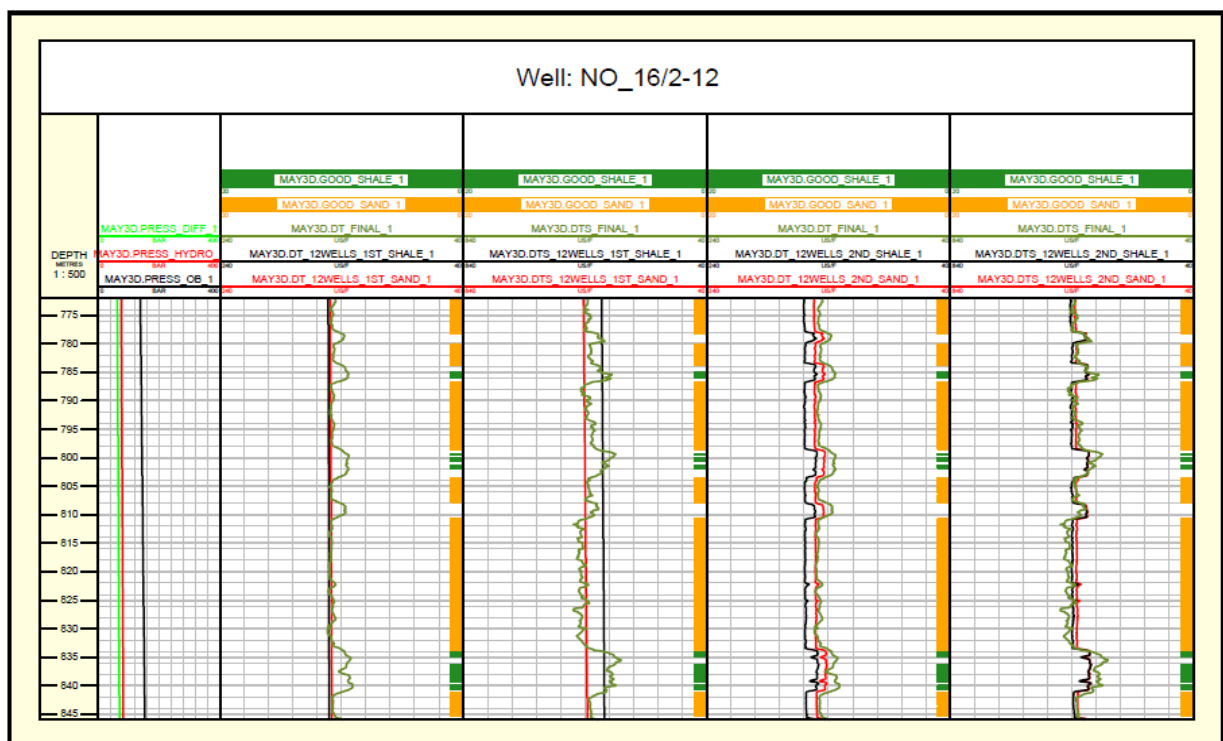


Figure 6.7.1. DT and DTS calculated based on the first and second sonic models for the Utsira formation in the well 16/2-12. The optimization was done based on all wells together.

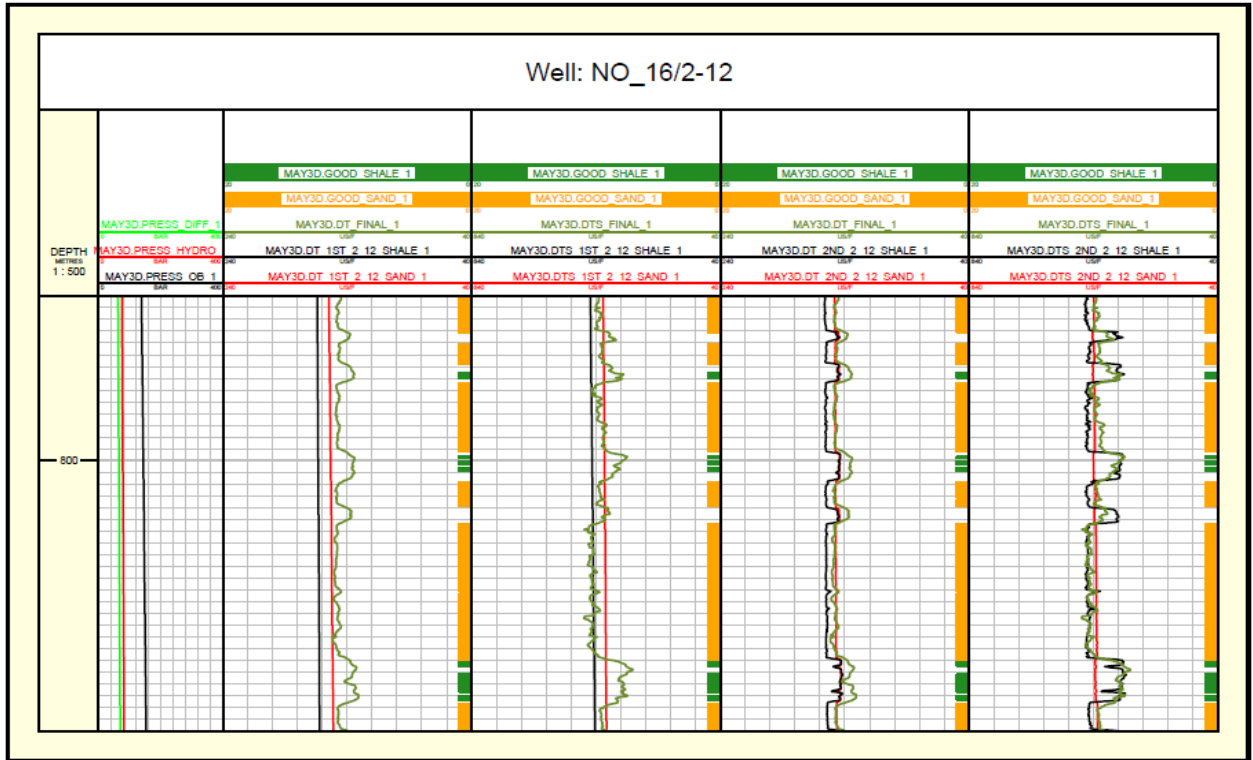


Figure 6.7.2. DT and DTS calculated based on the first and second sonic models for the Utsira formation in the well 16/2-12. The optimization was done based only on this well.

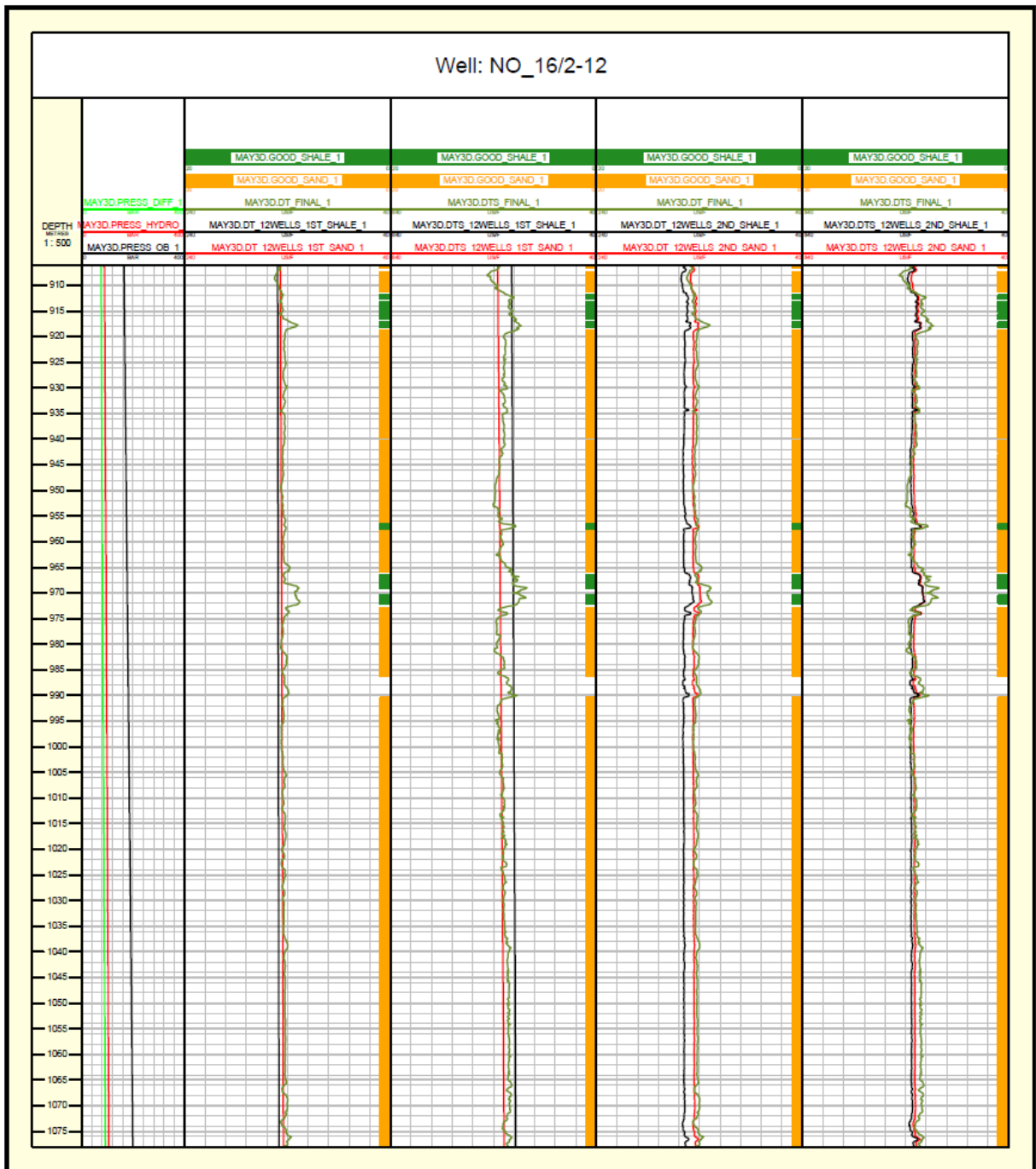


Figure 6.7.3. DT and DTS calculated based on the first and second sonic models for the Skade formation in the well 16/2-12. The optimization was done based on all wells together.

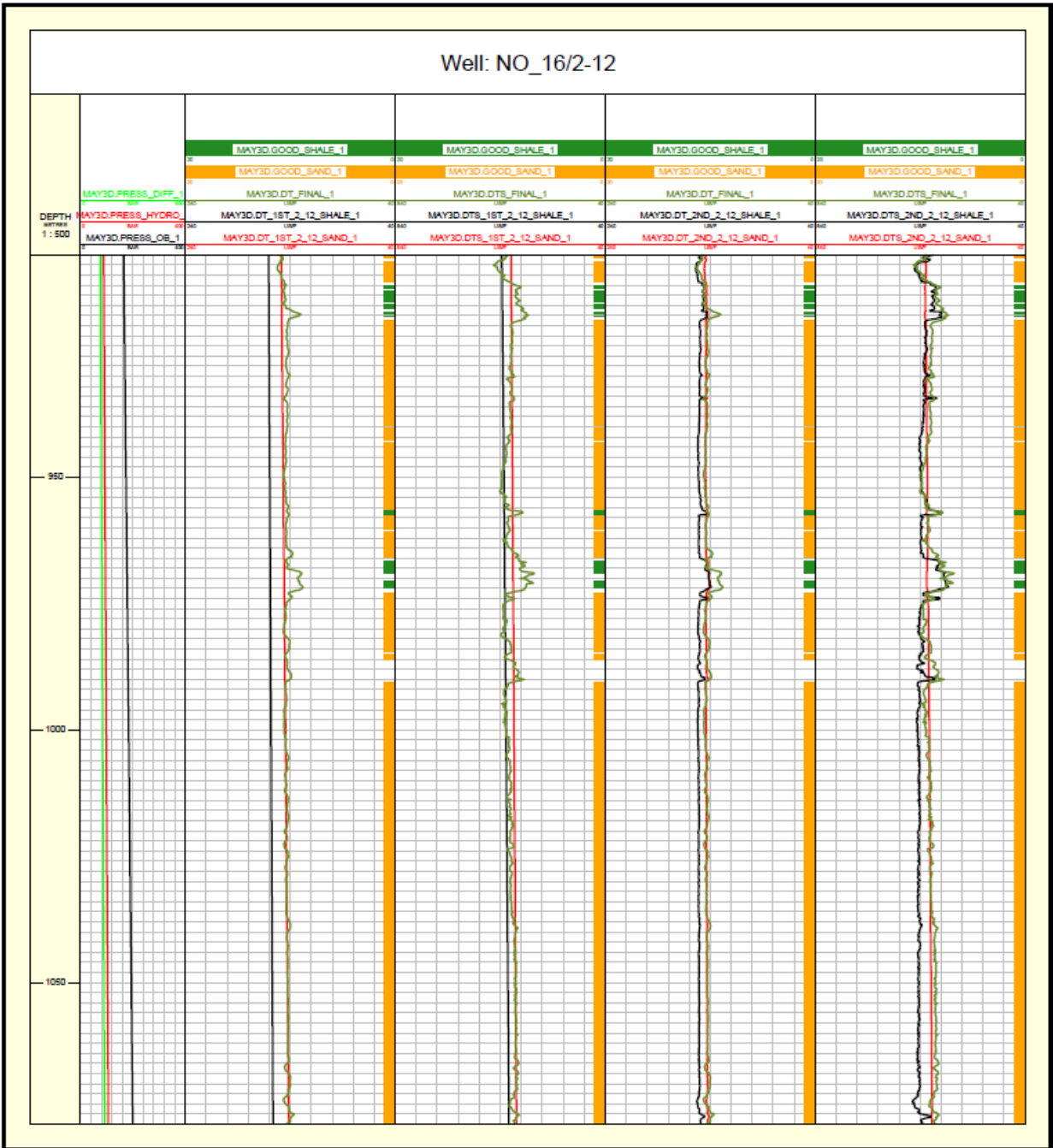


Figure 6.7.4. DT and DTS calculated based on the first and second sonic models for the Skade formation in the well 16/2-12. The optimization was done based only on this well.

In these CPI plots the second and third tracks display DT and DTS calculated based on the first sonic model while the third and fourth tracks show DT and DTS obtained according to the second sonic model. Estimated DT and DTS curves are compared with raw DT and DTS in sand and shale intervals. The raw curves are highlighted with green color. For DT curve we used the limits from 240 to 40 and for DTS one the limits are 840 to 40. The high limit for DTS log is explained by the low values of velocities at seabed. The first thing that can be noticed in

the Figures above that DT and DTS assessed based on the second models follow the shape of the raw DT and DTS curves which allows to compare behavior of the curves in both shale and sand intervals. In contrast, according to the first model we got a straight shape of DT and DTS curves which makes comparison of raw and calculated DT and DTS logs more uncertain. Therefore, we assumed that the second model for compressional and shear wave velocities is better than the first and we concluded that resistivity is a crucial parameter and it should be included to the model.

Another moment that we observed is that the optimization of the models by calculating DT and DTS well by well gives more precise results.

Resuming all of the above, we can make a conclusion that our sand and shale modeling showed that the derived second models for compressional and shear wave velocities are better than the first ones because the former ones involve resistivity which is an important parameter. The models work good for shallow sand and shale formations we are interested in in the thesis. Finally, the models should be applied in every well independently because the depth of formations can vary from well to well and calculation of DT and DTS in each well will show more correct result.

6.8. QC and removal of outliers

During the modeling we found out that wells 16/3-4 A and 16/4-5 could be considered as outliers and they should be excluded from the final result of the modeling. We realized that the quality of DT and DTS has impact to the final modeling result. In order to explain why we eventually omitted two wells, we showed the values of depth from which raw DT and DTS curves start in every well in the Table 6.8.1.

Table 6.8.1.

Starting depth of raw DT and DTS curves in all wells.

Well	DT (m)	DTS (m)
16/4-6S	125	612
16/3-8A	141	381
16/5-4	133	410
16/2-20 S	141	375
16/3-6	158	380
16/3-7	323	407
16/2-5	491	503
16/2-14 T2	580	620
16/2-4	598	625
16/2-12	605	605
16/3-4A	763	773
16/4-5	903	925

The reviewing of logs quality indicated that 16/3-4A and 16/4-5 wells have raw DT and DTS logs what miss the biggest shallow part in comparison with other wells. Moreover, the quality of raw DTS logs in these two particular wells is not good either due to missing of values in many intervals.

Our models are based on the raw DT and DTS logs and, thus, they define the quality of the models as well. Since DT and DTS curves include bad data in the wells 16/3-4A and 16/4-5, we eliminated these wells from the final evaluation of the models.

Considering the rest ten wells, we calculated the error of our models for Vp and Vs using the formula:

$$Error = \frac{Raw - Model}{Raw} \cdot 100\%,$$

where Raw are raw values of Vp and Vs, Model are the values of Vp and Vs obtained from the models. Notice that only those parts with a good flag for the raw curves were included. Presenting the error of Vp and Vs in histograms we got the following results for sand and shale.

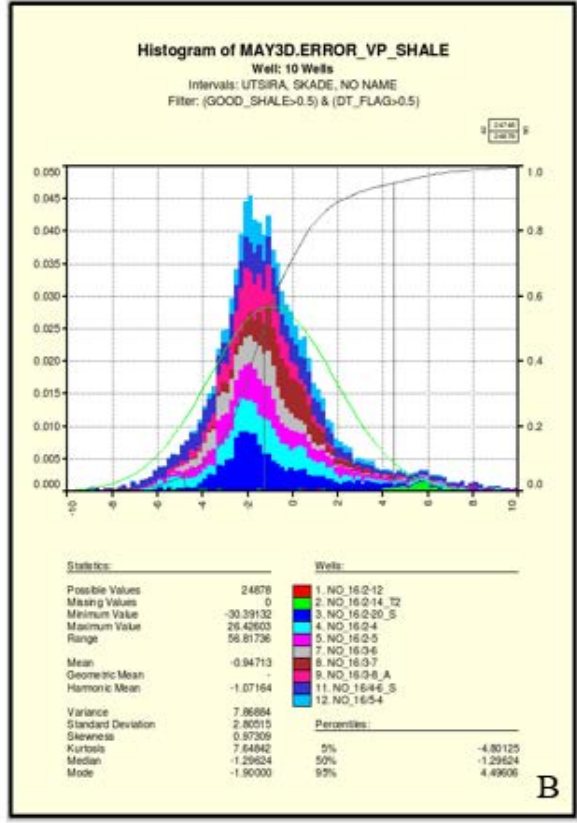
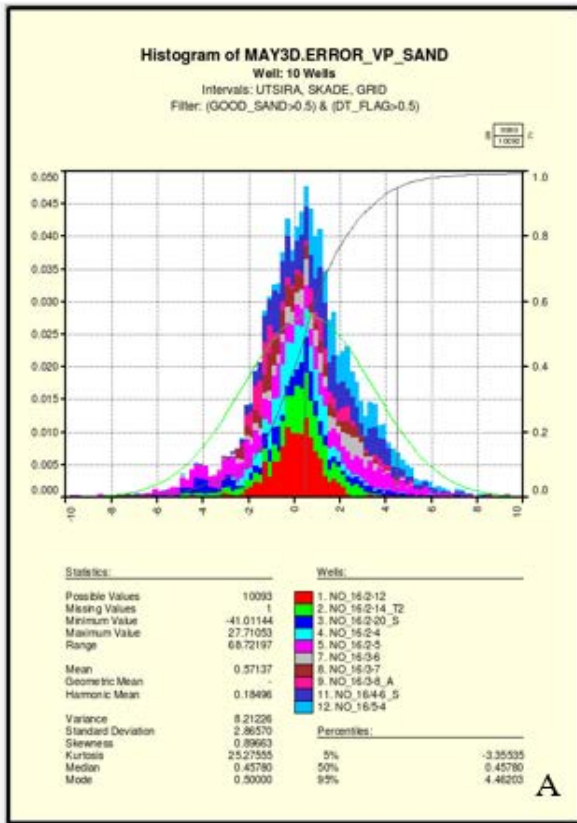


Figure 6.8.1. Error of Vp. A. For sand. B. For shale.

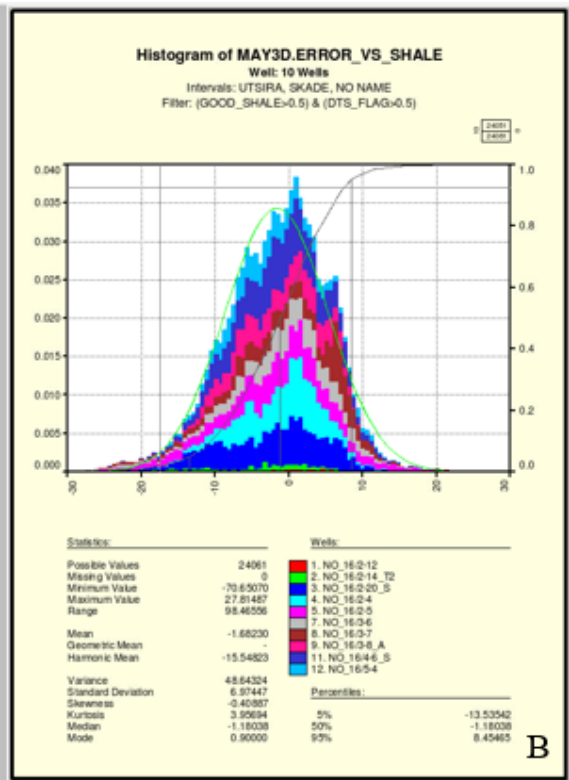
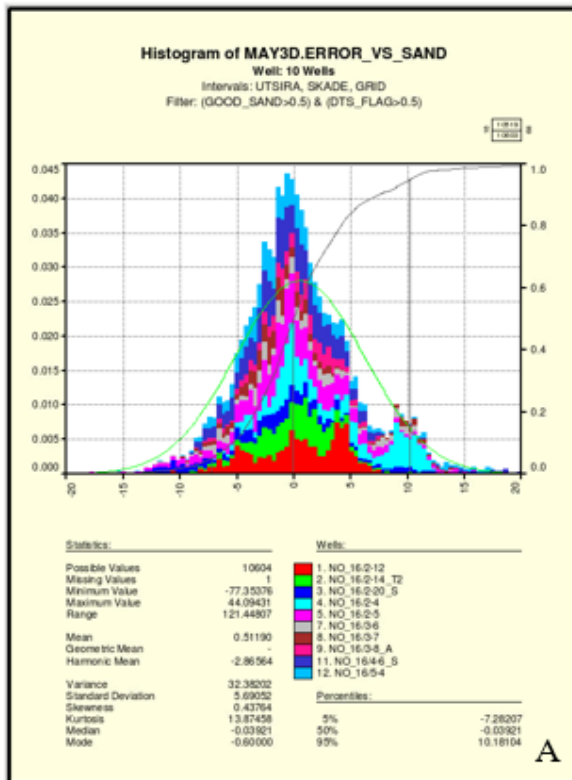


Figure 6.8.2. Error of Vs. A. For sand. B. For shale.

The Figure 6.8.1 shows that the error of V_p for sand for three formations (Utsira, Skade and Grid) varies from about -5 to 5 % and for shale for three formations (Utsira, Skade and No name) it is approximately in the same range from -5 to 5%. The negative percentage of the error means that modeled values of V_p or V_s are higher than raw ones.

In the Figure 6.8.2 it can be seen that the error of V_s for sand for three formations (Utsira, Skade and Grid) is in the diapason from around -10 to 10 % and for shale for three formations (Utsira, Skade and No name) it changes from roughly -20 to 15%.

The insignificant values of the error up to 20% proved that our chosen second models for V_p and V_s are reliable.

6.9. Are the standard Greenberg and Castagna relations optimal for any depth?

One of the most critical points in this thesis is that we tried to clarify if the standard empirical Greenberg and Castagna model is proper for any depth. In order to find the answer to this question we constructed the cross-plots showing the raw data trend (based on raw log values of V_p and V_s) as well as models trend (based on values of V_p and V_s obtained using our sonic models) in relation with the standard Greenberg and Castagna model. We did this for three formations for both sand and shale including all ten wells. We got the following results presented in the cross-plots below. The standard Greenberg and Castagna empirical model in the Figures in this Section for sand as well as shale is shown with purple color. Black, green and red lines in the graphs in this section present the real data trends for the Utsira, Skade and Grid formations for sand. It is similar for shale, the only one difference that instead of Grid we used the No name formation.

In order to make the Greenberg and Castagna model for sand and shale we took approximate minimum and maximum values of compressional wave velocity from the plots which are 1800 and 2800m/s, using standard regression coefficients for sand and shale, we determined respective values of shear wave velocity for both sand and shale according to the Greenberg and Castagna relations (Section 1.2).

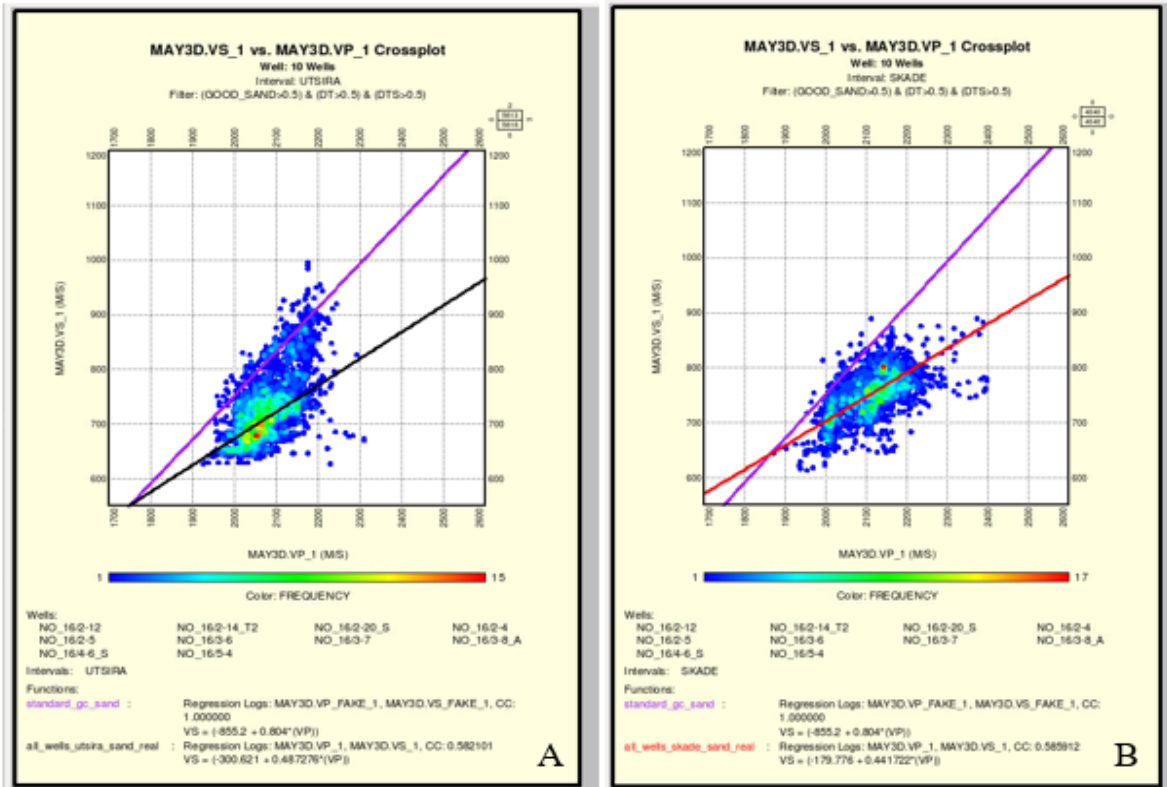


Figure 6.9.1. Raw Vs versus Raw Vp compared with the standard Greenberg and Castagna model for sand. A. Utsira formation. B. Skade formation.

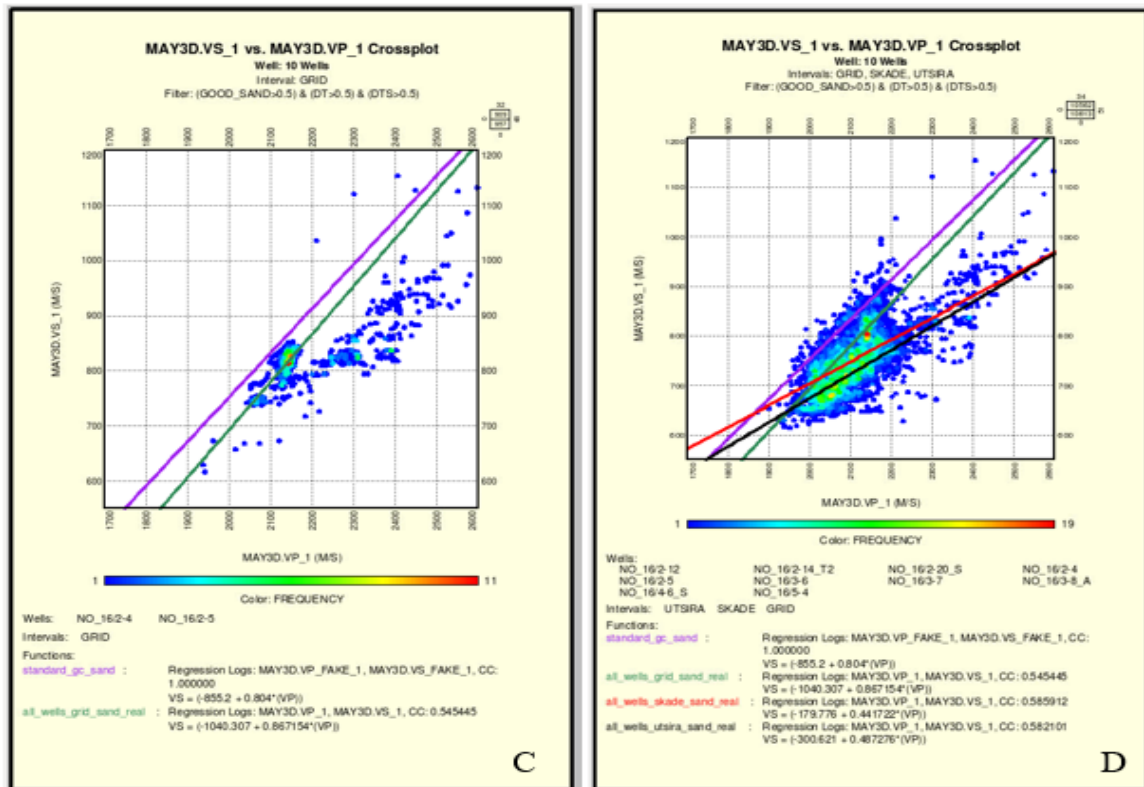


Figure 6.9.2. Raw Vs versus raw Vp compared with the standard Greenberg and Castagna model for sand. C. Grid formation. D. Utsira, Skade and Grid formations together.

As we can see from the Figure 6.9.1. (A and B) the trends based on the raw logs of Vp and Vs deviate from Greenberg and Castagna line for sand in the Utsira and Skade formations. In contrast, in the Grid formation the raw data trend is visibly closer to the standard Greenberg and Castagna model as well as they have similar direction. It can be noticed in the Figure 6.9.2 (C).

The plots for shale are shown in the Figures 6.9.3 and 6.9.4. Notice that for shale case we used the No name formation which is in the range between Skade and Grid formations, since the latter one is not representative for shale.

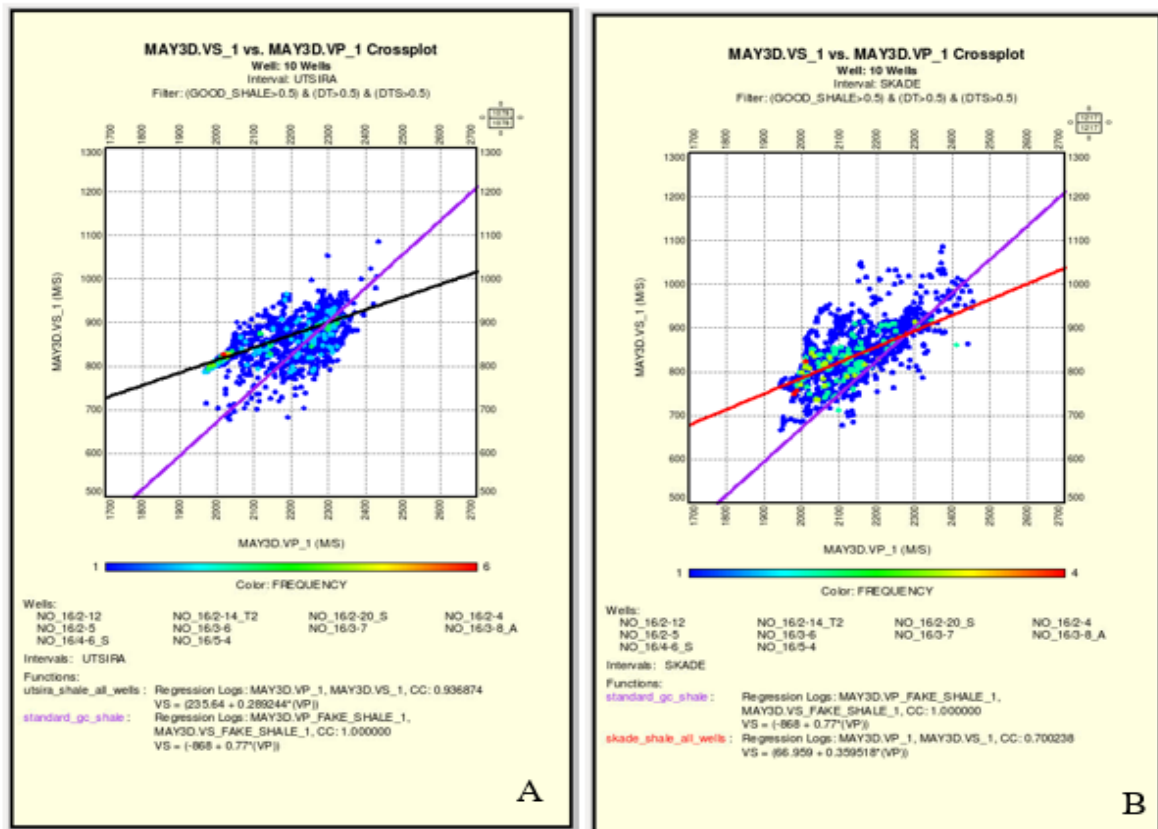


Figure 6.9.3. Raw Vs versus raw Vp compared with the standard Greenberg and Castagna model for shale. A. Utsira formation. B. Skade formation.

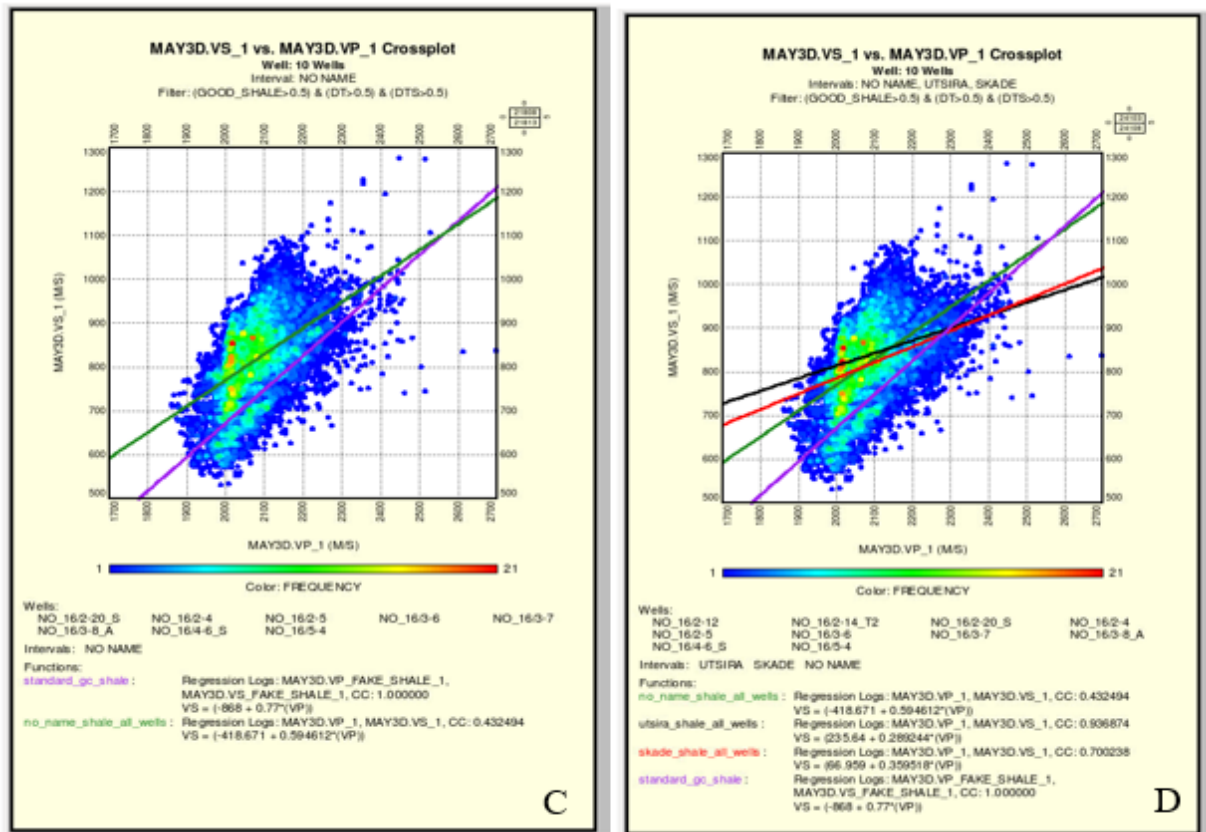


Figure 6.9.4. Raw Vs versus raw Vp compared with the standard Greenberg and Castagna model for shale. C. No name formation. D. Utsira, Skade and No name formations together.

For shale we have a similar pattern as for sand. From the Figure 6.9.3 (A and B) one can see that raw data trends in the Utsira and Skade formations have different behavior in comparison with Greenberg and Castagna model for shale. In the No name formation the raw data trend is closer to the Greenberg and Castagna one as well as they have similar orientation which can be noticed in the Figure 6.9.4 (C).

The raw data trends for sand and shale are rotated relative to the standard Greenberg and Castagna model in the Utsira and Skade formations. The angle of rotation between standard Greenberg and Castagna and the raw data trend for sand in the Utsira formation constitutes approximately 13°, whereas in shale it is equal to about 21°.

The comparison between standard Greenberg and Castagna model and our models for sand and shale showed the following results.

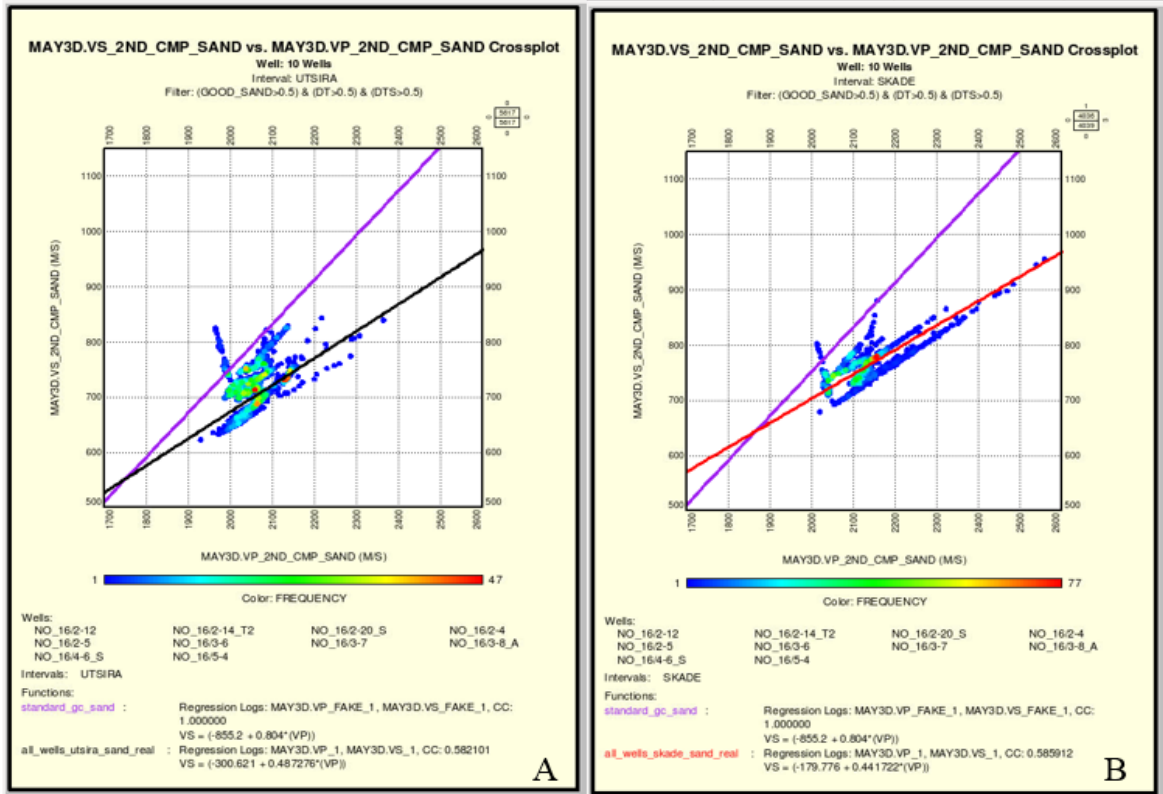


Figure 6.9.5. Modeled Vs versus modeled Vp compared with the standard Greenberg and Castagna model for sand and with the raw data trend. A. Utsira formation. B. Skade formation.

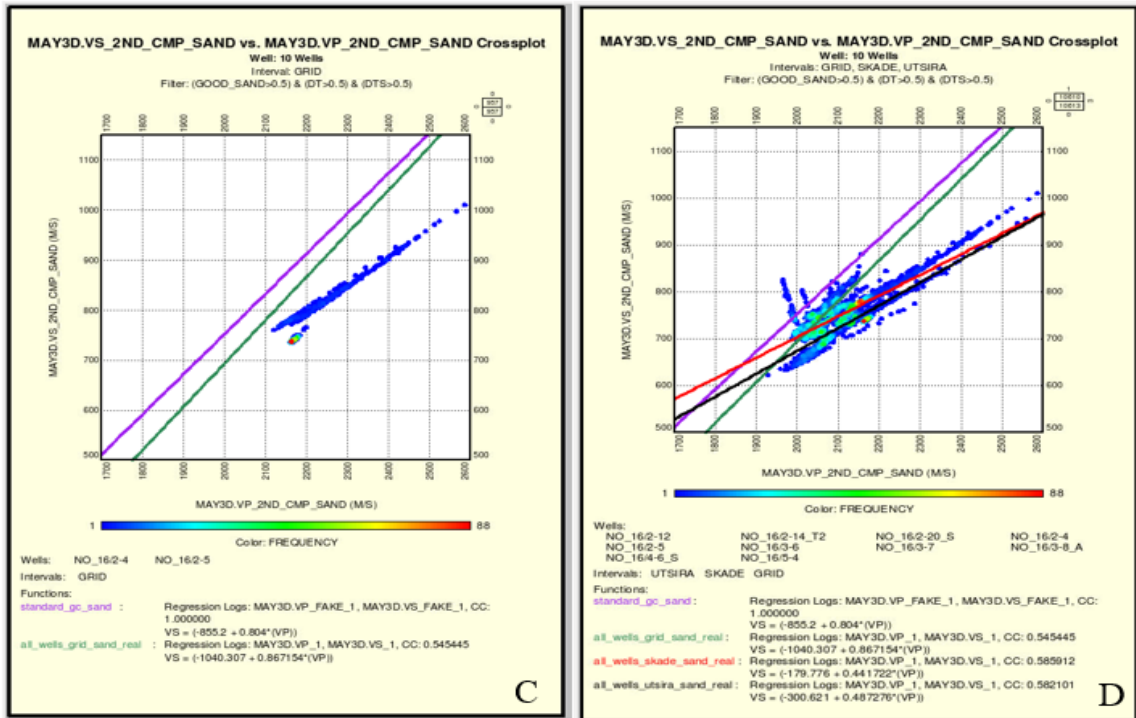


Figure 6.9.6. Modeled Vs versus modeled Vp compared with the standard Greenberg and Castagna model for sand and with the raw data trend C. Grid formation. D. Utsira, Grid and Skade formations together.

One can notice that in the Utsira and Skade formations the models trend for sand have a quite good coincidence with the raw data trends, while Greenberg and Castagna model deviates from them. In the Grid formation the model trend differs from the raw data and their directions are divergent (Figure 6.9.6 C). From the Figure 6.9.6 D we also can see that our model trends behave good only in the Utsira and Skade formations.

The plots for shale are presented in the Figures 6.9.7, 6.9.8 ,6.9.9 and 6.9.10. For better comparison in the shale case for every considered formation except models trend we also included the raw data points.

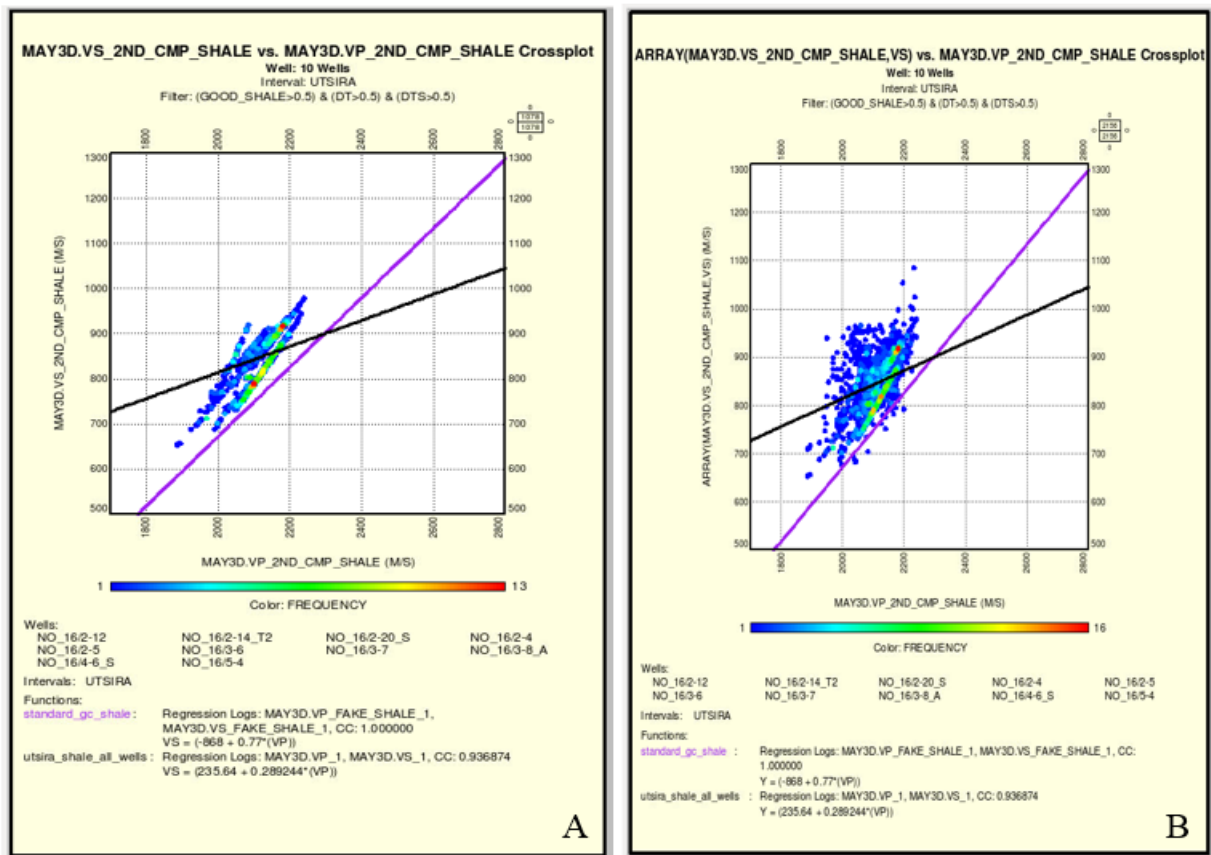


Figure 6.9.7. Modeled Vs versus modeled Vp compared with the standard Greenberg and Castagna model for shale and with the raw data trend in the Utsira formation. A. Without raw data points. B. Including raw data points.

Similar plots we have for two other formations.

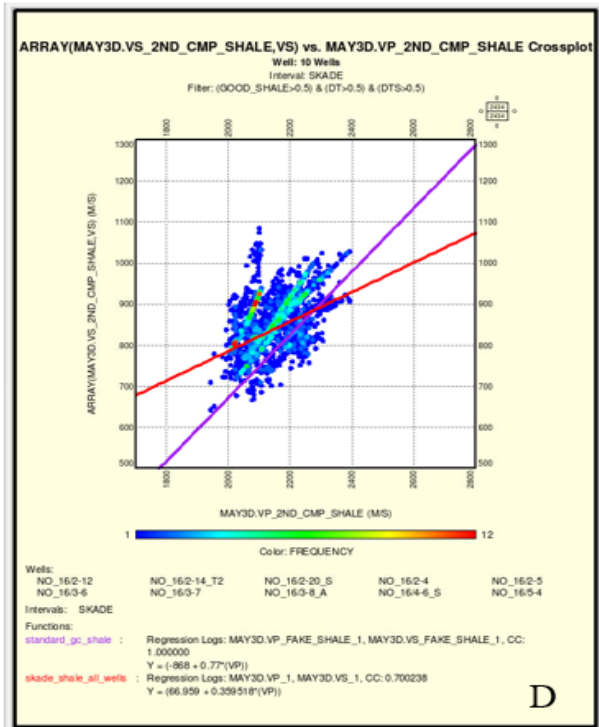
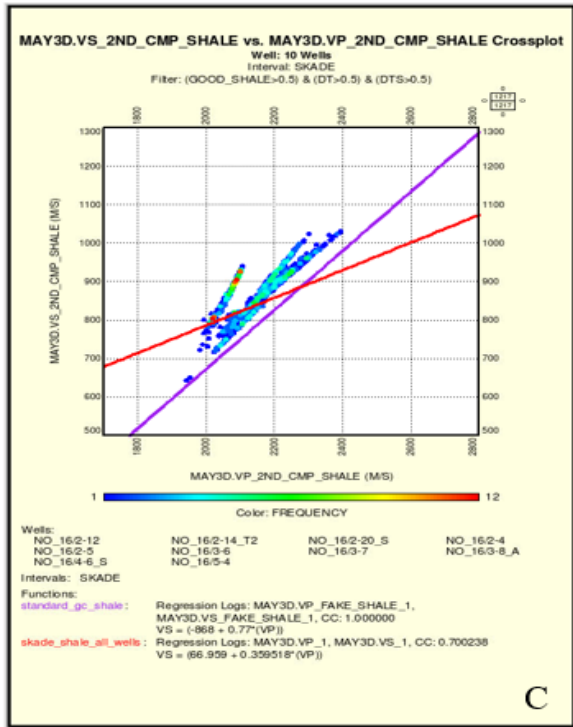


Figure 6.9.8. Modeled Vs versus modeled Vp compared with standard Greenberg and Castagna model for shale and with the raw data trend in the Skade formation. C. Without raw data points. D. Including raw data points.

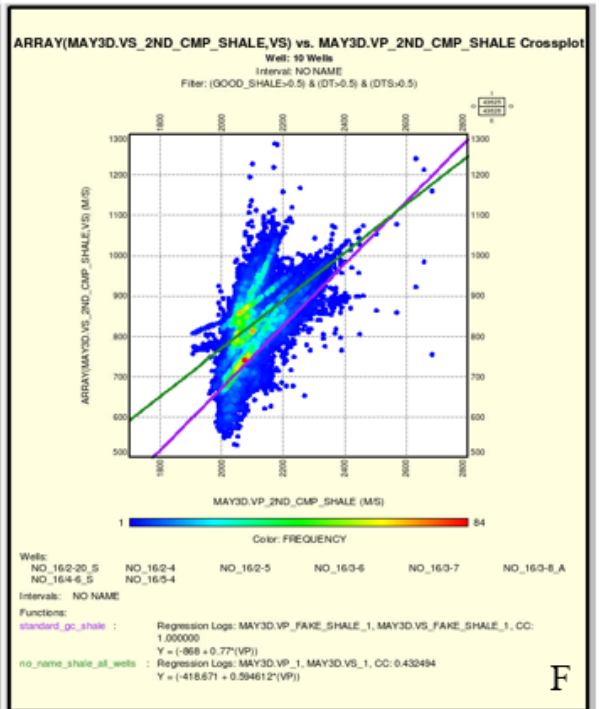
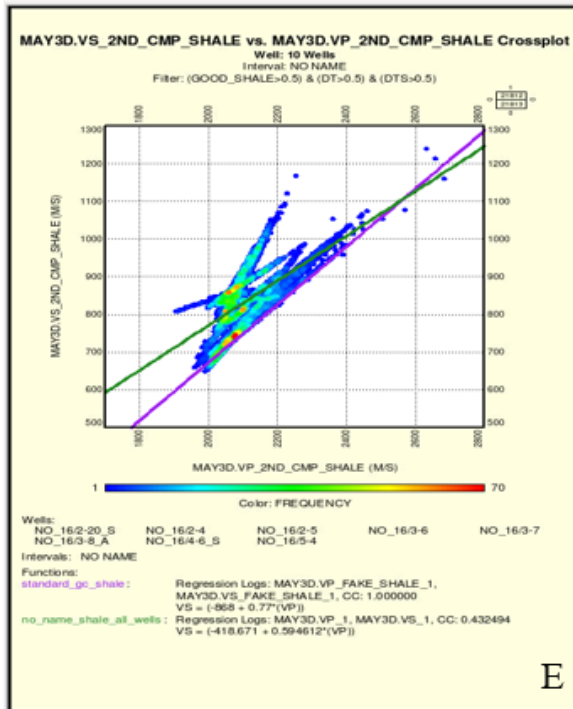


Figure 6.9.9. Modeled Vs versus modeled Vp compared with standard Greenberg and Castagna model for shale and with the raw data trend in the No name formation. E. Without raw data points. F. Including raw data points.

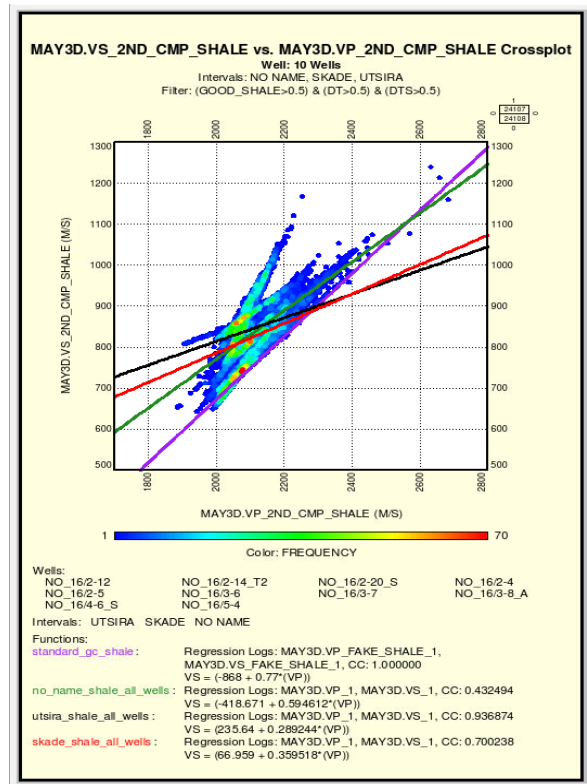


Figure 6.9.10. Modeled Vs versus modeled Vp compared with the standard Greenberg and Castagna model for shale and with the raw data trend in the Utsira, Skade and No name formations.

From the Figures 6.9.7 and 6.9.8 we figured out that in the Utsira and Skade formations most of the points of the model trends are close to the raw data ones except the lowest most part where the models trend points are close to the Greenberg and Castagna line. The orientation of the models trend varies from the Greenberg and Castagna model in the Utsira and Skade formations. In the No name formation the models trend is closer to the raw data trend as well as to the Greenberg and Castagna line. Moreover, they have the same direction.

These cross-plots for both sand and shale allowed us to assume that our sonic models behave good in the shallow part, in particular, in the Utsira and Skade formations in comparison with the standard Greenberg and Castagna empirical model. However, the pattern of the trends in deeper formations, such as the Grid or No name, showed that our models start to break at certain depth where the standard Greenberg and Castagna empirical model seems to be more appropriate. We assessed that particular depth that is equal to around 1100m in our case and we believe that our derived sonic models are applicable up to this point. This observation coincides with the depth range according to the porosity trend (Subsection 2.3.2) and Murphy's porosity boundary (35%) between unconsolidated and consolidated part.

7. Discussion of results and conclusions

Laboratory data analysis of shale and sand implemented in the thesis gave the understanding about controlling variable, such as, effective (differential) pressure that is essential for the modeling of compressional and shear wave velocities. We assumed that both lithologies are isotropic linear elastic materials, thus, V_p and V_s velocities are relevant. Laboratory data studying by itself can be considered as an independent investigation but on the same time it served as a motivation for the further well logging modeling. The modeling of laboratory data of shale allowed us to determine the useful power model for the optimal modeling of compressional and shear wave velocities in relation with variable differential pressure. For the laboratory shale data we obtained the following models for V_p and V_s :

For the smectite/kaolinite/brine systems we got sonic velocities:

$$V_p = (-10 \cdot V_{\text{smec}} + 1470) + (-46.5 \cdot V_{\text{smec}} + 77.3) \cdot \sigma^{(-0.0828 \cdot V_{\text{smec}} + 0.8016)} \text{ and}$$

$$V_s = (-69.4 \cdot V_{\text{smec}} + 395) + (-19.7 \cdot V_{\text{smec}} + 34.9) \cdot \sigma^{(0.012 \cdot V_{\text{smec}} + 0.8057)},$$

For the kaolinite/silt/brine system the sonic velocities in the power model are

$$V_p = (-72.6 \cdot V_{\text{silt}} + 1495) + (-47.8 \cdot V_{\text{silt}} + 66.9) \cdot \sigma^{(0.195 \cdot V_{\text{silt}} + 0.687)} \text{ and}$$

$$V_s = (12.1 \cdot V_{\text{silt}} + 325) + (-53.7 \cdot V_{\text{silt}} + 75.5) \cdot \sigma^{(0.549 \cdot V_{\text{silt}} + 0.465)}.$$

The observation of laboratory data of unconsolidated sand was more ambiguous than we expected. We realized that it is not easy to establish a direct link between high-frequency laboratory studies of sand with well logging data. Based on the laboratory data of sand we obtained the following dry models, under the assumption that the data are correct:

$$K^1_{dry} = 5.37 \cdot e^{-4.86 \cdot \varphi},$$

$$G^1_{dry} = 1.44 \cdot e^{-2.29 \cdot \varphi}.$$

$$K^2_{dry} = 4.71 \cdot e^{-4.39 \cdot \varphi},$$

$$G^2_{dry} = 1.39 \cdot e^{-2.006 \cdot \varphi},$$

where φ is porosity.

On well logs we used the concept of the power model determined based on the modeling of laboratory data of shale. We tested the power models for V_p and V_s on well logging data as the first option of the sonic modeling. However, the first sonic power models did not show good final results.

Motivated by Faust we derived the second models for Vp and Vs prediction. In these models we introduced resistivity as an important parameter that should be included to the models. Furthermore, we found out that the second sonic models should be applied in every well independently. Since the depth of formations can vary from well to well, the calculation of Vp and Vs well by well optimizes the final results. This let us to choose the second sonic models as the final models for Vp and Vs estimation. The additional process of QC of the final models showed two wells (16/3-4 A and 16/4-5) with bad raw DT and DTS data. Thus, we excluded them and did not present in the final CPIs and cross-plots. Moreover, during the QC analysis of DT data we found out that close to seabed the Faust's relation has a singularity. According to all wells we modified the functional form of the Faust equation to be on the form:

$$DT_FINAL \cdot RDEP_FINAL^{\frac{1}{6}} = A \cdot \exp(-B \cdot TVDML),$$

where DT_FINAL is the final edited compressional slowness log, $RDEP_FINAL$ is the final edited deep resistivity log, A and B positive constants.

The first 100-300 meters TVDML below seabed clearly need this modified version. Further details can be found in the article presented in the thesis.

In fact, the final sonic models may be considered as generalization as well as extension of Faust's relation including DTS in addition to DT.

The comparison of our sonic models with the standard Greenberg and Castagna empirical model showed that our models are applicable in the shallow formations up to roughly 1100 meters TVDML. This is approximately the depth obtained using the porosity trend simultaneously with the Murphy's porosity boundary between unconsolidated and consolidated sand which constitutes around 35%. It is consistent with the claim that our sonic models are correct for unconsolidated siliciclastic sediments which was the main goal of the thesis.

We would like also to present here the workflow of the well logging sonic modeling in more details:

1. It is necessary to identify the wells with shallow DT and DTS logs as well as to check the presence of resistivity log in every well.
2. It is needed to calculate differential pressure in all considered wells.
3. It is necessary to determine velocities at seabed using cross-plots of Vp and Vs velocities versus TVDML and a second order model. All wells are needed.
4. It is needed to do the multiple regression in every well separately and get the coefficients of the equations for Vp and Vs in the logarithmic form:

$$\text{Log (VP-VPb)} = \alpha_p + \beta_p \text{Log (RDEP_FINAL)} + \gamma_p \text{Log (PRESS_DIFF)}$$

$$\text{Log (VS-VSb)} = \alpha_s + \beta_s \text{Log (RDEP_FINAL)} + \gamma_s \text{Log (PRESS_DIFF)},$$

where α_p , β_p , γ_p , α_s , β_s and γ_s are coefficients of the models and PRESS_DIFF is differential pressure. From the logarithmic form we may obtain the power law form.

5. It is necessary to calculate the error of the models, to do QC analysis and make cross-plots of the final results.
6. It is needed to define the range of the models applicability comparing with porosity trend for considered wells and Murphy's porosity boundary.

8. Suggestion for the future work

We hope that our derived sonic models for V_p and V_s prediction will find a use in the other wells in the Johan Sverdrup field. We suggest to use a bigger range of wells for the modeling testing if it is possible. Moreover, the models can be tried out in the fields with different geological environments. Most likely the work-flow presented in the previous Chapter may only be applied in siliciclastic sediments.

Last but not least, as we mentioned in conclusion, in addition to the differential pressure, resistivity is also a crucial parameter for sonic modeling. Hence, we think that it should be determined within laboratory studies as well.

The following article “Faust Revisited – A Shallow Modification of the Faust Empirical Relationship Between Sonic Slowness and Resistivity” is accepted for publication by the Canadian Well Logging Society (CWLS) InSite.

Faust Revisited – A Shallow Modification of the Faust Empirical Relationship Between Sonic Slowness and Resistivity

Adelya Bilalova, University of Stavanger

Inge H. A. Pettersen, Statoil

Introduction

Velocity-depth trends are useful for predicting abnormal pressures during drilling (Dutta 1986, Storvoll et al. 2005) and they are often used to make synthetic logs for QCing sonic logs (Smith 2011). While many different relationships have been published (Hacikoyhu et al. 2006, Hubert 2008), the Faust equation (Faust 1951, Faust 1953) remains unique both in terms of its simplicity and in terms of its power of prediction in water-filled sediments (Ojala 2009).

Based on three recent wells with good resistivity and compressional slowness logs completely up to seabed in the Johan Sverdrup field (<https://www.statoil.com/en/what-we-do/johan-sverdrup.html>) in the Norwegian sector of the North Sea, it has become clear to us that the standard Faust relationship between resistivity and sonic needs a modification in the upper part of the overburden.

In the first section below, we will give a theoretical argument for why the standard functional form of the Faust equation will break down close to the seabed. In the second section, we show empirically how to determine a natural modification of the standard Faust equation close to the seabed. Finally, we make a summary where the range of applicability is suggested.

Breakdown of standard Faust close to the seabed

One quality control on the compressional slowness log DT is to calculate a synthetic log DT_FAUST based on the Faust equation

$$DT \cdot (RT \cdot TVDML)^{1/6} = a, \quad (1.1)$$

where RT is the true resistivity, TVDML is the true vertical depth with seabed as datum and with positive direction downwards in the gravitational field, and a is a strictly positive empirical constant.

If we separate out the explicit depth factor of the standard Faust equation, this relation may be reformulated as

$$\ln(DT \cdot RT^{1/6}) = \ln(a) - \ln(TVDML) / 6$$

When TVDML approaches the seabed, the right hand is diverging. However, in water-filled sediments both DT and RT will remain positive and bounded. The left hand will therefore stay finite and we have thus a contradiction.

Testing the standard Faust equation close to seabed for three wells in the Johan Sverdrup field

Based on three recent wells in the same basin with good logs completely up to seabed, we plotted $\ln(DT \cdot RT^{1/6})$ versus TVDML varying from 0 m TVDML to 500 m TVDML. The crossplot in Figure 1 show that $\ln(DT \cdot RT^{1/6})$ has a linear dependency on TVDML on this range – as opposed to the divergent behaviour predicted by the standard Faust equation in the previous section. Thus, we have a shallow modification of Faust in an exponential form

$$DT \cdot RT^{1/6} = A \cdot \exp(-B \cdot TVDML), \quad (1.2)$$

where A and B are positive constants. Finally, the well CPIs in Figure 2 show the green shallow Faust slowness DT_FAUST_SH that is consistent with the raw DT log down to ca. 700 m – 800 m TVDML. The red standard Faust slowness DT_FAUST is consistent with the raw DT log from ca. 100 m TVDML - 300 m TVDML and downwards except for zones containing hydrocarbons.

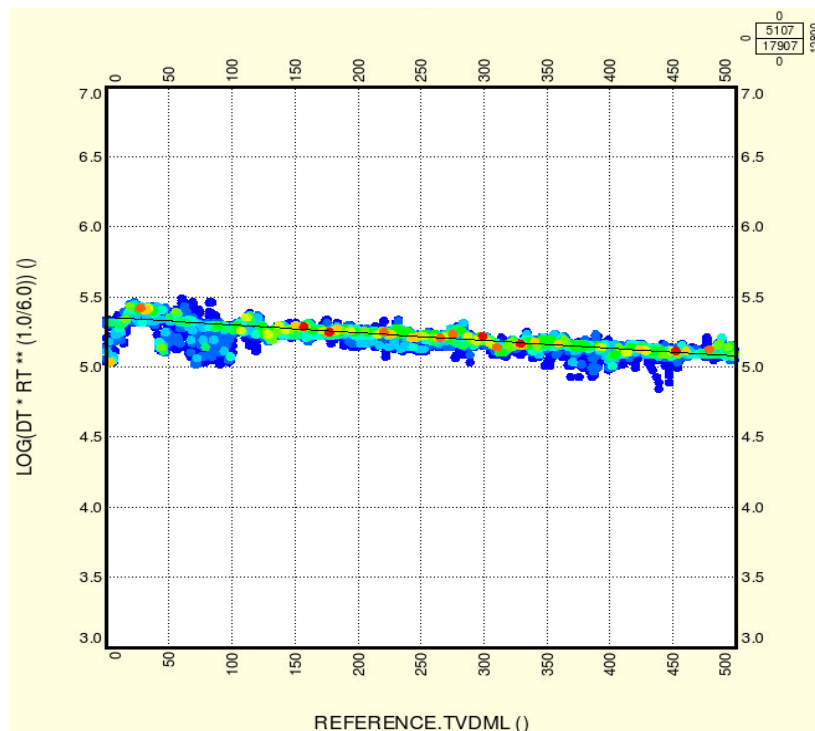


Figure 1. Best fit of $\ln(DT \cdot RT^{1/6})$ versus TVDML close to seabed for three wells in the Johan Sverdrup field.

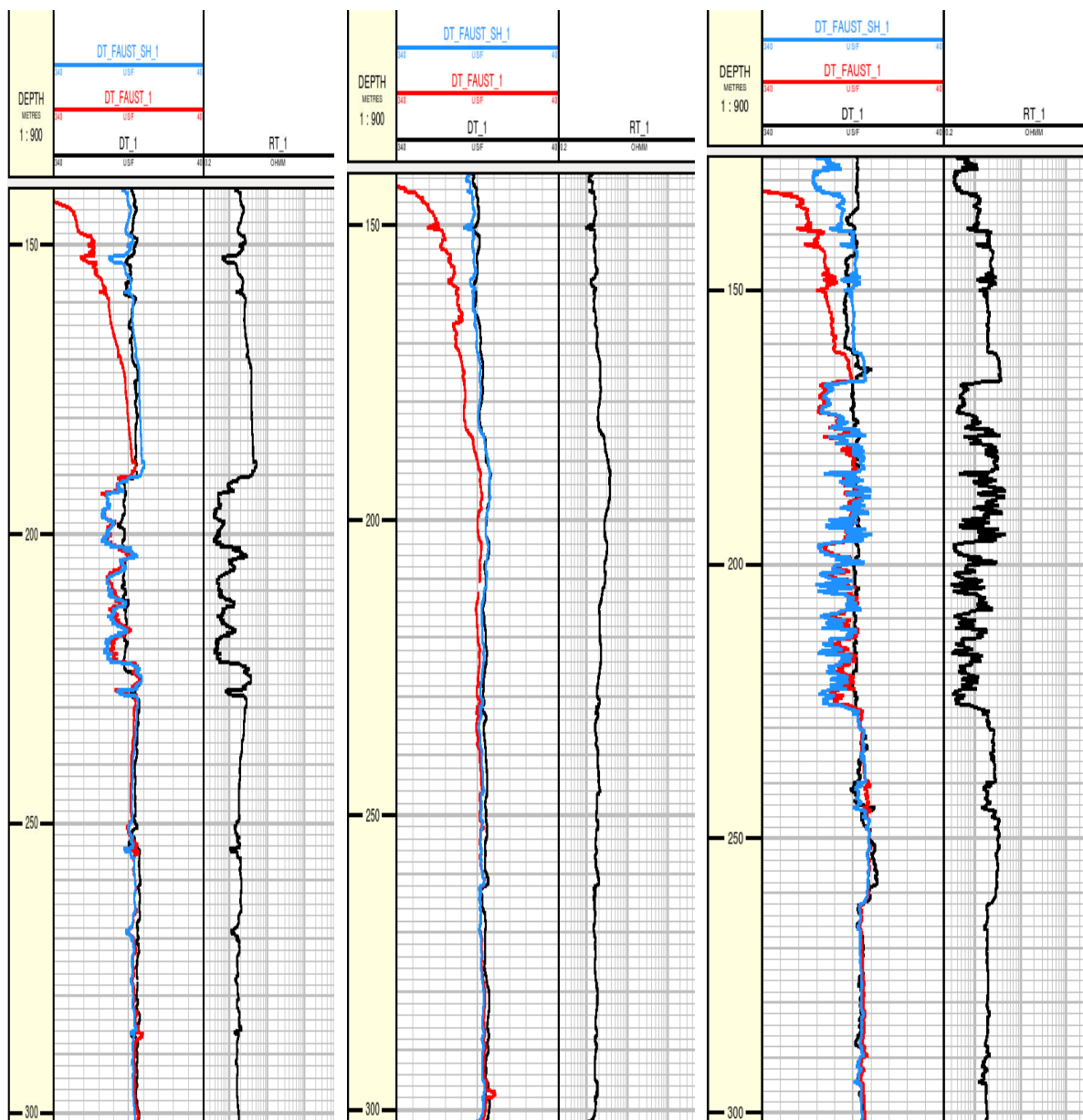


Figure 2. Comparing measured slowness DT (black curve), standard Faust DT_FAUST (red curve), and shallow Faust DT_FAUST_SH (blue curve) in track 2 for three wells in Johan Sverdrup. Deep resistivity is shown in track 3.

Conclusion

The standard Faust relation between sonic slowness, deep resistivity, and depth is shown to break down the first 100 m – 300 m below seabed in three Johan Sverdrup wells. A simple modification of Faust gives an exponential relationship that is trustworthy the first 700 m – 800 m below the seabed for these wells. Even though the modification was derived for a particular field, we conjecture that the same functional form should also apply in other offshore wells in water-filled sediments sufficient close to seabed.

Acknowledgements

The authors want to thank the partners of Johan Sverdrup for the opportunity to use the well logs of three wells in this work.

References

- Dutta, N.C., 1986. Shale Compaction, Burial Diagenesis, and Geopressures: A Dynamic Model, Solution, and Some Results in Thermal Modeling in Sedimentary Basins. In ed. J. Burrus, *Thermal Modeling in Sedimentary Basins*, Paris, Editions Technip, 149-172.
- Faust, L. Y., 1951. Seismic velocity as a function of depth and geologic time. *Geophysics*, 16, 192 – 206.
- Faust, L. Y., 1953. A velocity function including lithologic variations. *Geophysics*, 18, 271-288.
- Hacikoylu, P., Dvorkin, J., and Mavko, G., 2006. Resistivity-velocity transform revisited. *The Leading Edge*, August, 1006 – 1009.
- Hubert, L. , 2008. Velocity to resistivity transform for the Norwegian Sea. 7th EAGE conference and exhibition, Rome, Italy, 9 – 12 June 2008.
- Ojala, I. O., 2009. Using rock physics for constructing synthetic sonic logs. In eds. M. Diederichs and G. Grasselli, *ROCKENG09: Proceedings of the 3rd CANUS Rock Mechanics Symposium*, Toronto, May 2009.
- Smith, T. M., 2011. Practical seismic petrophysics: The effective use of log data for seismic analysis. *The Leading Edge*, October 2011, 30 (10), 1128 – 1141.
- Storvoll, V., Bjørlykke, K., and Mondol N. H., 2005. Velocity-depth trends in Mesozoic and Cenozoic sediments from the Norwegian shelf. *AAPG Bulletin*, 89, 359 – 381.

References

- Aljarrah, F. (2009). Methods of Fitting Compressional and Shear Wave Velocities Versus Saturation Curves and the Interpretation of Laboratory Velocity Measurements in Partially Saturated Rocks. (Master's Thesis), University of Houston.
- Archie, G. E. (1942). The electrical resistivity log as an aid in determining some reservoir characteristics. *Transactions of the AIME*, 146(01), 54-62.
- Athy, L. F. (1930). Density, porosity, and compaction of sedimentary rocks. *AAPG Bulletin*, 14(1), 1-24.
- Avseth, P., Flesche, H., & Van Wijngaarden, A.-J. (2003). AVO classification of lithology and pore fluids constrained by rock physics depth trends. *The Leading Edge*, 22(10), 1004-1011.
- Batzle, M., & Wang, Z. (1992). Seismic properties of pore fluids. *Geophysics*, 57(11), 1396-1408.
- Bhuiyan, M., & Holt, R. (2016). Variation of shear and compressional wave modulus upon saturation for pure pre-compacted sands. *Geophysical Journal International*, 206(1), 487-500.
- Biot, M. A. (1956). Theory of propagation of elastic waves in a fluid-saturated porous solid. I. Low-frequency range. *The Journal of the acoustical Society of america*, 28(2), 168-178.
- Bjørlykke, K. (2010). *Petroleum Geoscience: From Sedimentary Environments to Rock Physics.*: Springer Science, pp. 121-122.
- Coppens, A. B. (1981). Simple equations for the speed of sound in Neptunian waters. *The Journal of the Acoustical Society of America*, 69(3), 862-863.
- Domenico, S. (1977). Elastic properties of unconsolidated porous sand reservoirs. *Geophysics*, 42(7), 1339-1368.
- Faleide, J. I., Bjørlykke, K., & Gabrielsen, R. H. (2015). Geology of the Norwegian continental shelf *Petroleum Geoscience* (pp. 603-637): Springer.
- Gabrielsen, R., Færseth, R., Steel, R., Idil, S., & Kløvjan, O. (1990). Architectural styles of basin fill in the northern Viking Graben. *Tectonic Evolution of the North Sea Rifts*. Clarendon Press, Oxford, 158-179.
- Gardner, G., Gardner, L., & Gregory, A. (1974). Formation velocity and density—The diagnostic basics for stratigraphic traps. *Geophysics*, 39(6), 770-780.
- Gassmann, F. (1951). Über die Elastizität poröser Medien. *Veierteljahrsschrift der Naturforschenden Gesellschaft in Zurich*, 96, 91-23.
- Gautier, D. L. (2005). *Kimmeridgian shales total petroleum system of the North Sea graben province*.
- Geertsma, J., & Smit, D. (1961). Some aspects of elastic wave propagation in fluid-saturated porous solids. *Geophysics*, 26(2), 169-181.
- Greenberg, M., & Castagna, J. (1992). SHEAR-WAVE VELOCITY ESTIMATION IN POROUS ROCKS: THEORETICAL FORMULATION, PRELIMINARY VERIFICATION AND APPLICATIONS1. *Geophysical prospecting*, 40(2), 195-209.
- Gregersen, U., Michelsen, O., & Sørensen, J. C. (1997). Stratigraphy and facies distribution of the Utsira Formation and the Pliocene sequences in the northern North Sea. *Marine and Petroleum geology*, 14(7-8), 893-914.
- Huffman, A. R., & Castagna, J. P. (2001). The petrophysical basis for shallow-water flow prediction using multicomponent seismic data. *The Leading Edge*, 20(9), 1030-1052.

- Joerstad, A. (2012). Johan Sverdrup - Offshore Norway: The story behind the Giant Sverdrup Discovery
Paper presented at the International Conference and Exhibition, Singapore. Search and Discovery
Article #20177 retrieved from:
http://www.searchanddiscovery.com/pdfz/documents/2012/20177jorstad/ndx_jorstad.pdf.html (visited
on 05/30/2017)
- Justwan, H., Dahl, B., & Isaksen, G. (2006). Geochemical characterisation and genetic origin of oils and
condensates in the South Viking Graben, Norway. *Marine and Petroleum geology*, 23(2), 213-239.
- Karimi, M., Adelzadeh, M., & Mohammadypour, M. (2014). Formula of definite point overburden pressure of
reservoir layers. *Egyptian Journal of Petroleum*, 23(2), 175-182.
- Malcolm, R. (1996). *The Geological Interpretation of Well Logs*: Gulf publishing company. Houston-London,
Paris, Zurich, Tokyo.
- Mavko, G., & Jizba, D. (1991). Estimating grain-scale fluid effects on velocity dispersion in rocks. *Geophysics*,
56(12), 1940-1949.
- Mavko, G., Mukerji, T., & Dvorkin, J. (2009). *The rock physics handbook: Tools for seismic analysis of porous
media*: Cambridge university press.
- Murphy, W. F., Schwartz, L. M., & Hornby, B. (1991). *Interpretation physics of Vp and Vs in sedimentary rocks*.
Paper presented at the SPWLA 32nd Annual Logging Symposium.
- Murphy, W., Reischer, A., & Hsu, K. (1993). Modulus decomposition of compressional and shear velocities in
sand bodies. *Geophysics*, 58(2), 227-239.
- Mondol, N. H., Bjørlykke, K., Jahren, J., & Høeg, K. (2007). Experimental mechanical compaction of
clay mineral aggregates—Changes in physical properties of mudstones during burial. *Marine and
Petroleum geology*, 24(5), 289-311.
- NPD. Retrieved from:
<http://factpages.npd.no/FactPages/Default.aspx?nav1=wellbore&nav2=PageView|Exploration|All&nav3=6952&culture=en> (visited on 05/25/2017)
- NPD. Retrieved from:
<http://www.npd.no/en/System/Search/?quicksearchquery=utsira+formation&activetab=0&cat=all&lng=en&con=all> (visited on 05/28/2017)
- NPD. Retrieved from:
<http://www.npd.no/en/Publications/Reports/Compiled-CO2-atlas/4-The-Norwegian-North-Sea/41-Geology-of-the-North-Sea/The-Hordaland-Group---Claystones/> (visited on 05/28/2017)
- NPD. Retrieved from:
<http://www.npd.no/en/publications/reports/compiled-co2-atlas/4-the-norwegian-north-sea/41-geology-of-the-north-sea/the-hordaland-group---skade-formation/> (visited on 05/28/2017)
- NPD. Retrieved from:
<http://www.npd.no/en/publications/reports/compiled-co2-atlas/4-the-norwegian-north-sea/41-geology-of-the-north-sea/the-nordland-group---utsira-formation/> (visited on 05/28/2017)
- Olsen, H., Briedis, N. A., & Renshaw, D. (2017). Sedimentological analysis and reservoir characterization of a
multi-darcy, billion barrel oil field—The Upper Jurassic shallow marine sandstones of the Johan
Sverdrup field, North Sea, Norway. *Marine and Petroleum geology*, 84, 102-134.

- Riber, L., Dypvik, H., & Senile, R. (2015). Altered basement rocks on the Utsira High and its surroundings, Norwegian North Sea. *NORWEGIAN JOURNAL OF GEOLOGY*, 95(1), 57-89.
- Sayers, C. M. (1999). Stress-dependent seismic anisotropy of shales. *Geophysics*, 64(1), 93-98.
- Stoll, R. D. (1974). Acoustic waves in saturated sediments *Physics of sound in marine sediments* (pp. 19-39): Springer.
- Wesenlund, F., & Karlsen, D. (2016). *The Petroleum Geochemistry of the Johan Sverdrup Field, Southern Utsira High, Norwegian North Sea*. (Master's Thesis), University of Oslo.
- Winkler, K. W. (1985). Dispersion analysis of velocity and attenuation in Berea sandstone. *Journal of Geophysical Research: Solid Earth*, 90(B8), 6793-6800.
- Ziegler, P. (1992). North Sea rift system. *Tectonophysics*, 208(1-3), 55-75.
- Zimmer, M. A. (2004). *Seismic velocities in unconsolidated sands: Measurements of pressure, sorting, and compaction effects*.
- Wikipedia. Retrieved from:
<https://en.wikipedia.org/wiki/Salinity> (visited on 06/17/2017)

Appendix A. Fitting clay models from data

In Appendix A we presented the second order polynomial and power models for compressional and shear wave velocities in smectite/kaolinite/brine and kaolinite/silt/brine systems. We showed the models for fitting compressional and shear wave velocities for different clay composition that were not included in the Chapter 3. The second order polynomial models for V_p have the following equation:

$$V_p = A \cdot \sigma^2 + B \cdot \sigma + C,$$

where V_p is compressional wave velocity σ is effective pressure and A, B, C are coefficients of the equation.

We assumed that for shear wave velocity the polynomial models are similar and the have the following form:

$$V_s = A' \cdot \sigma^2 + B' \cdot \sigma + C',$$

where V_s is shear wave velocity and A', B', C' are coefficients of the equation.

The power models for V_p are described by the following equations:

$$V_p = V_{p_b} + A'' \cdot \sigma^{B''},$$

where V_{p_b} is compressional wave velocity of the brine at seabed and A'', B'' are coefficients of the equation.

For V_s the equation is as follows:

$$V_s = V_{s_b} + A''' \cdot \sigma^{B'''},$$

where V_{s_b} is shear wave velocity of the brine at seabed and A''', B''' are coefficients of the equation.

These equations we used in both clay systems. In the Chapter 3 we mentioned that the second order polynomial models were constructed in order to define the values of V_p and V_s velocities at seabed, while the power models we consider as the most reliable for our data. We described it in the Chapter 3.

The models below contain error bars. The error for V_p and V_s measurements constitutes 2 and 4% respectively.

A1. Vp fitting

A1.1. Polynomial models for Vp fitting in a smectite/kaolinite/brine system

The models in this section show fitting compressional wave velocity for different relative volume fractions of clay in a second order polynomial model. Here are the models that were not considered in the Subsection 3.3.1.

Table A1.1.1.

Results of fitting of laboratory data of Vp to the second order polynomial model in a smectite/kaolinite/brine system.

Relative smectite volume	Relative kaolinite volume	A	B	C	R ²
0.2	0.8	-0.248	27.9	1420	0.981
0.4	0.6	-0.204	23.7	1380	0.988
0.6	0.4	-0.214	23.9	1530	0.992
0.8	0.2	-0.188	20.0	1450	0.990
1	0	-0.169	17.6	1510	0.991

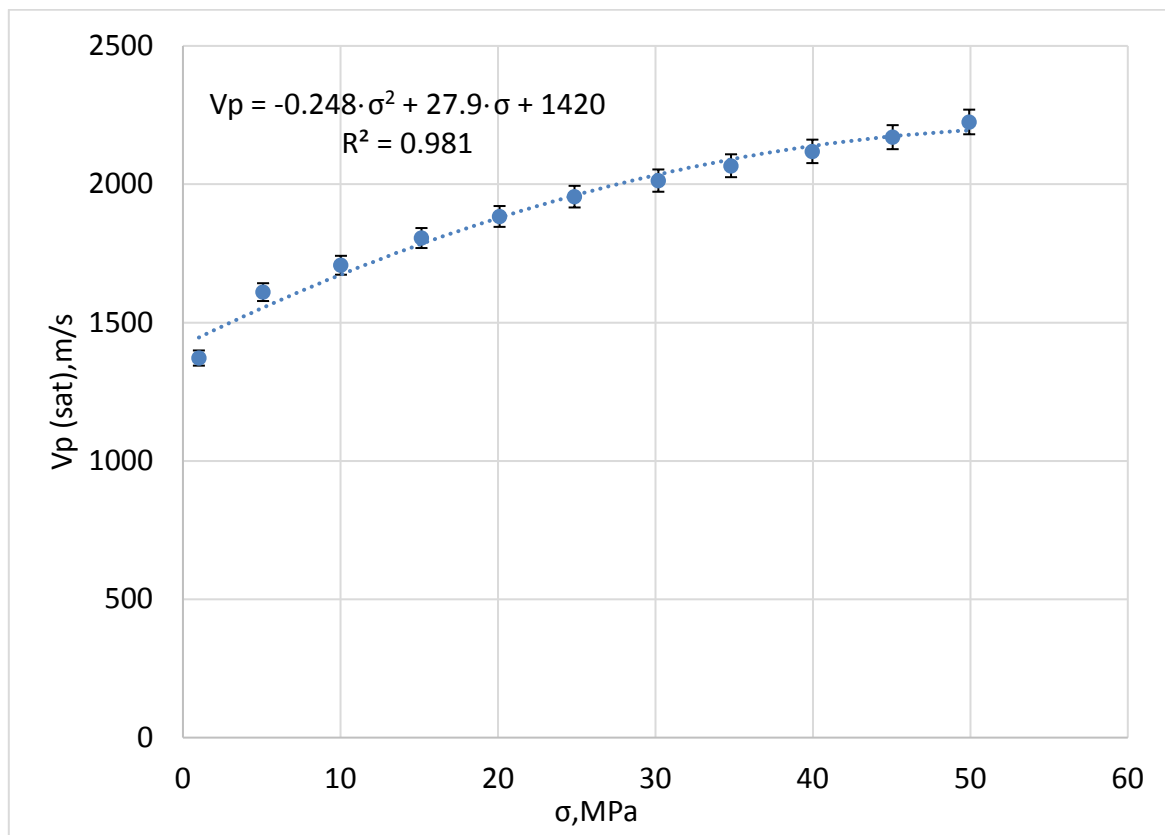


Figure A1.1.1. Second order polynomial model for Vp fitting when relative volume fraction of kaolinite is 0.8 and relative volume fraction of smectite is 0.2.

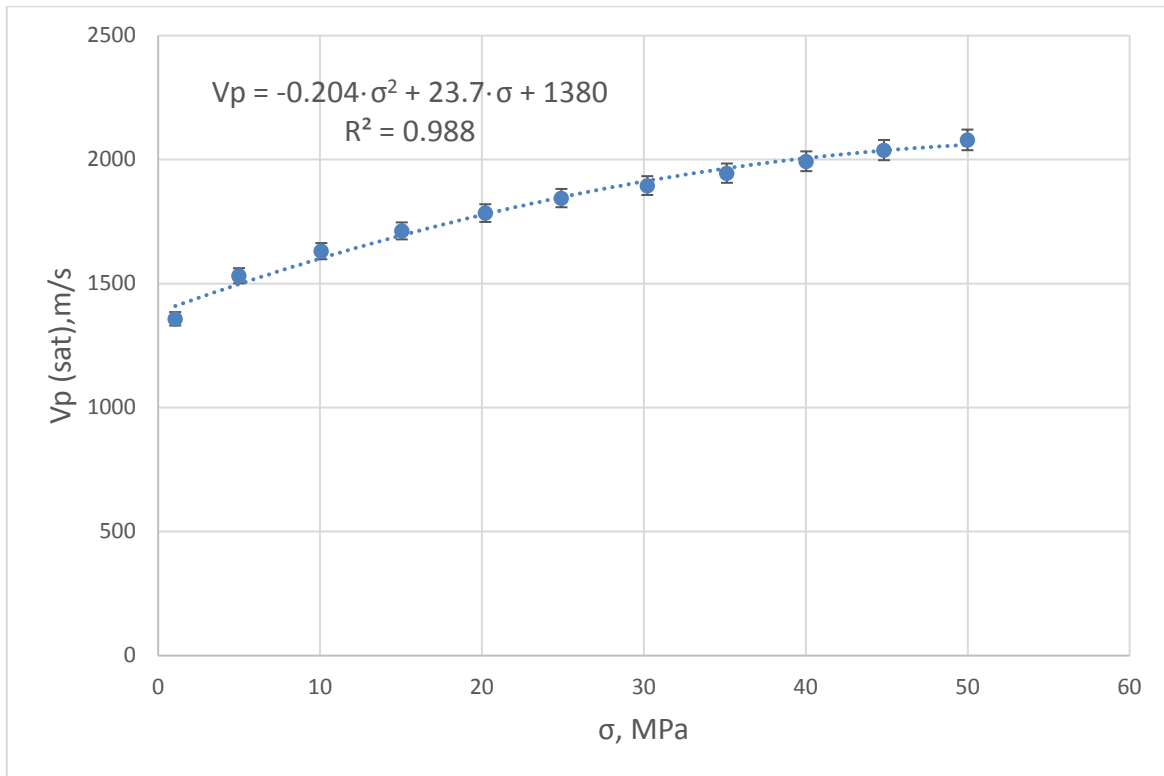


Figure A1.1.2. Second order polynomial model for V_p fitting when relative volume fraction of kaolinite is 0.6 and relative volume fraction of smectite is 0.4.

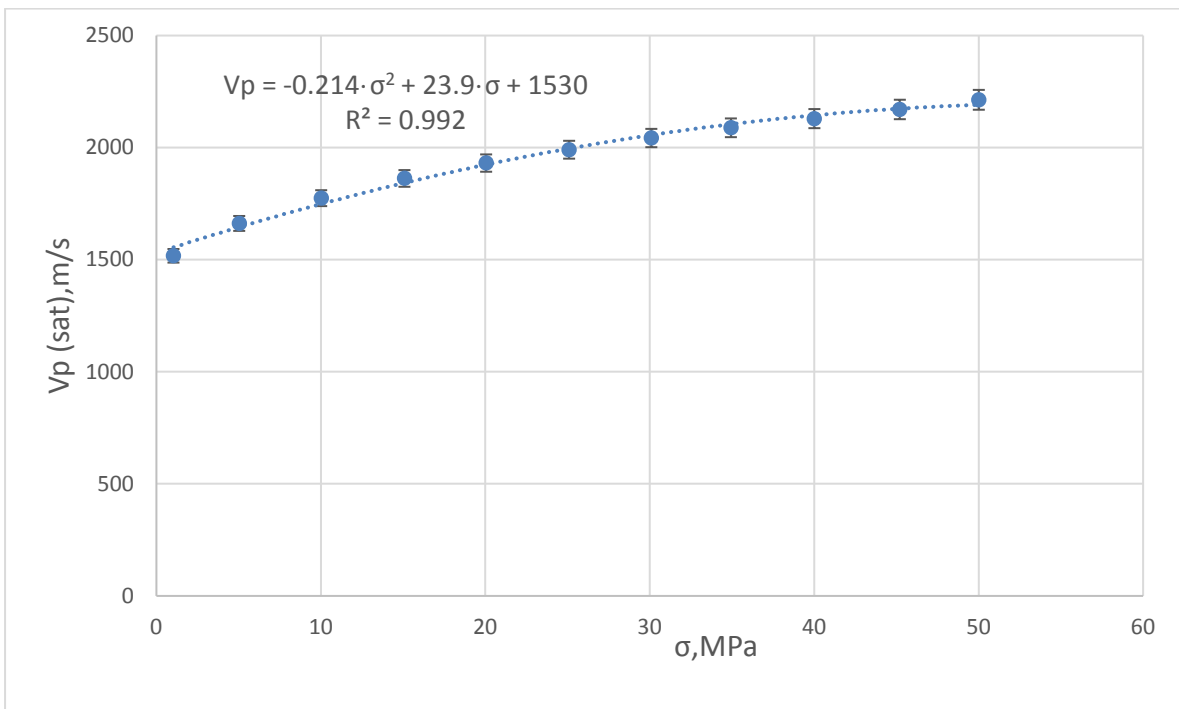


Figure A1.1.3. Second order polynomial model for V_p fitting when relative volume fraction of kaolinite is 0.4 and relative volume fraction of smectite is 0.6.

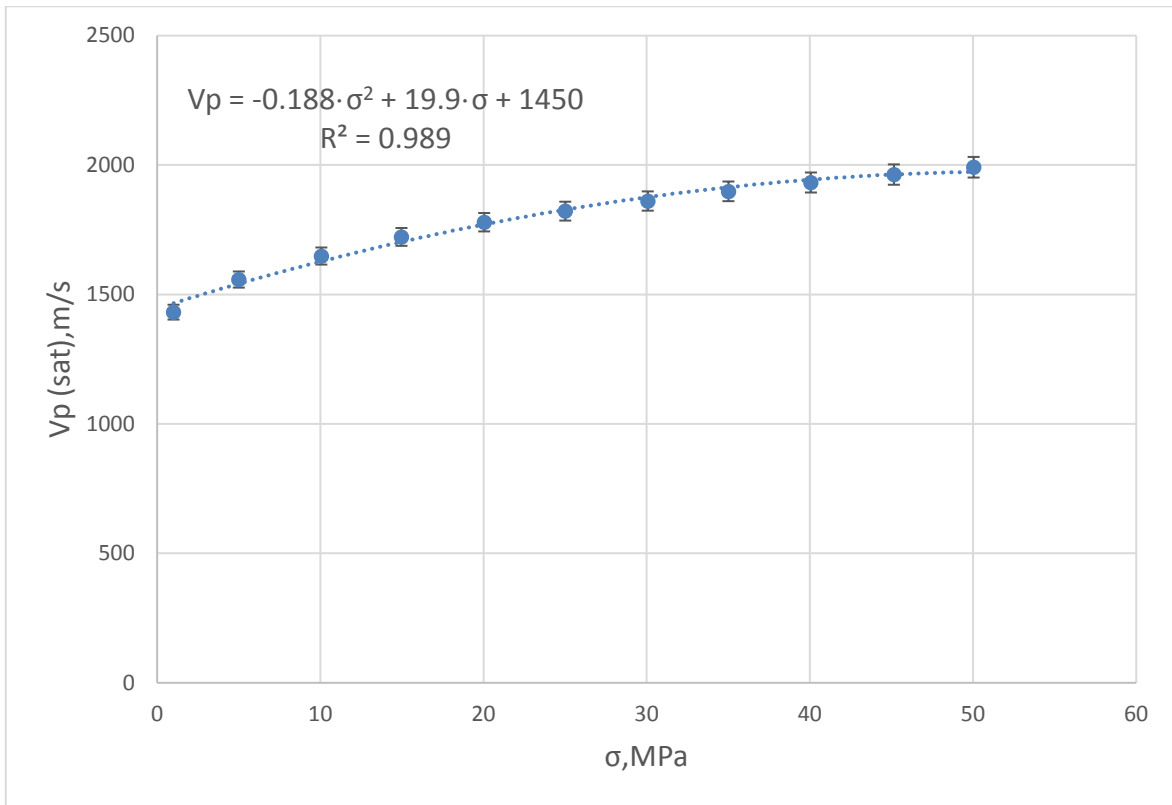


Figure A1.1.4. Second order polynomial model for V_p fitting when relative volume fraction of kaolinite is 0.2 and relative volume fraction of smectite is 0.8.

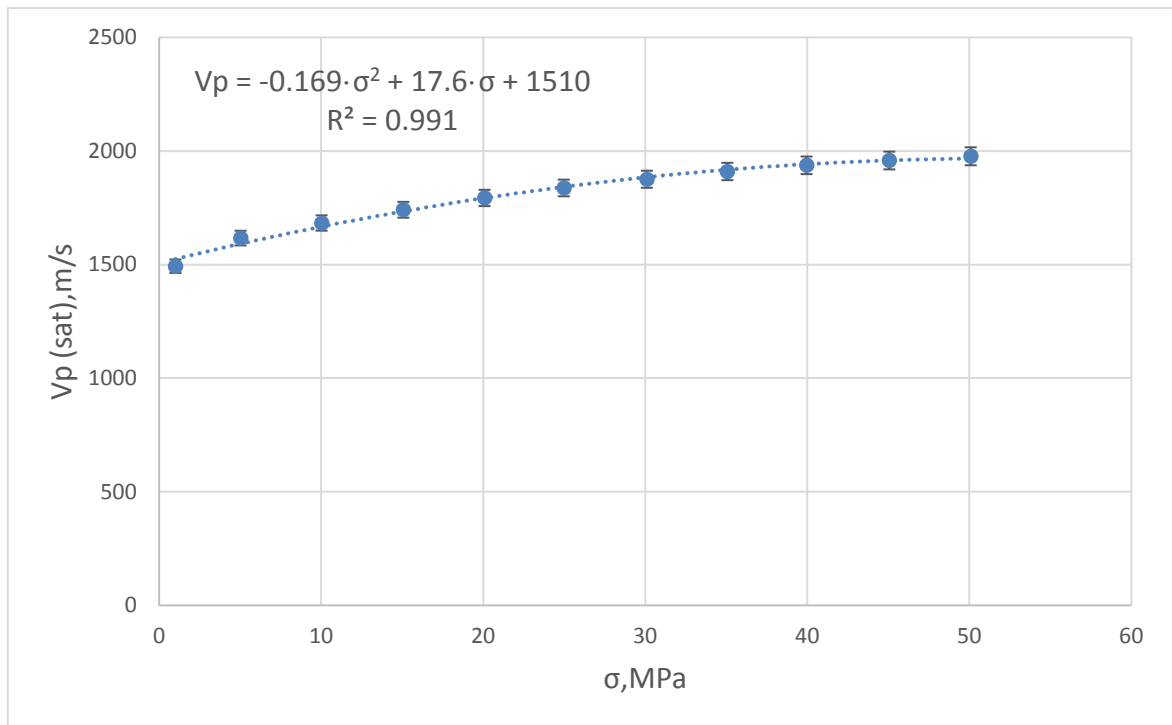


Figure A1.1.5. Second order polynomial model for V_p fitting when relative volume fraction of kaolinite is 0 and relative volume fraction of smectite is 1.

A1.2. Power models for Vp fitting in a smectite/kaolinite/brine system

In A1.2 section we presented the power models for Vp fitting in a smectite/kaolinite/brine system for different clay composition that were not presented in the Subsection 3.3.2.

Table A1.2.1.

Results of fitting of laboratory data of Vp to the power model in a smectite/kaolinite/brine system.

Volume smectite	Volume kaolinite	A	B	Vp _b
0	1	28.2	0.846	1470
0.4	0.6	15.9	0.957	1470
0.6	0.4	46.8	0.698	1530
0.8	0.2	41.5	0.673	1450
1	0	31.1	0.756	1470

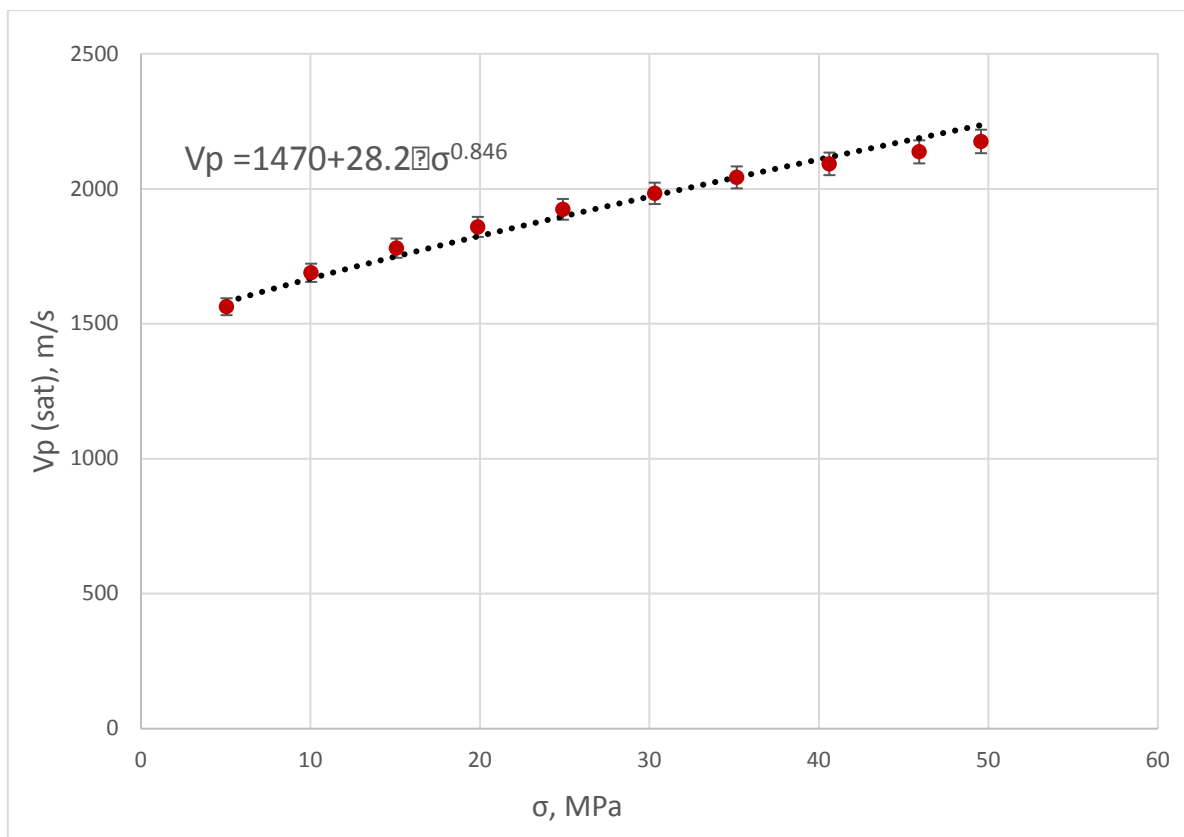


Figure A1.2.1. Power model for Vp fitting when relative volume fraction of kaolinite is 1 and relative volume fraction of smectite is 0.

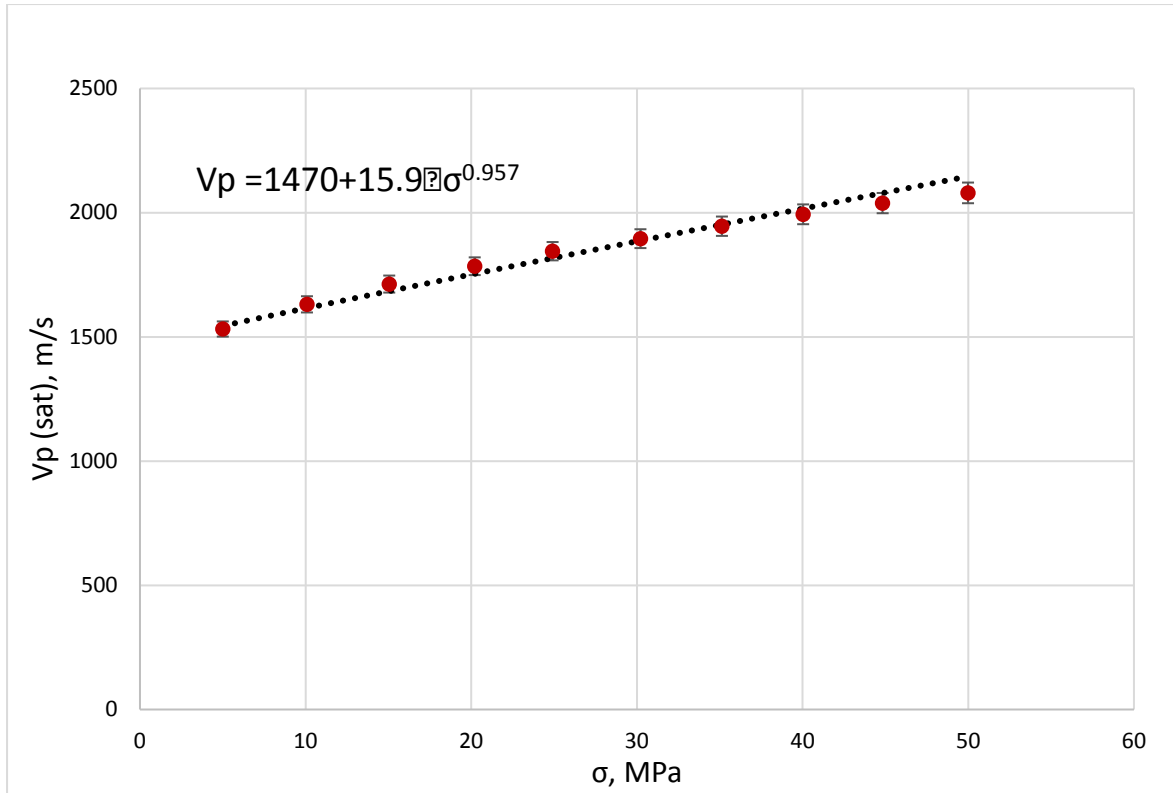


Figure A1.2.2. Power model for V_p fitting when relative volume fraction of kaolinite is 0.6 and relative volume fraction of smectite is 0.4.

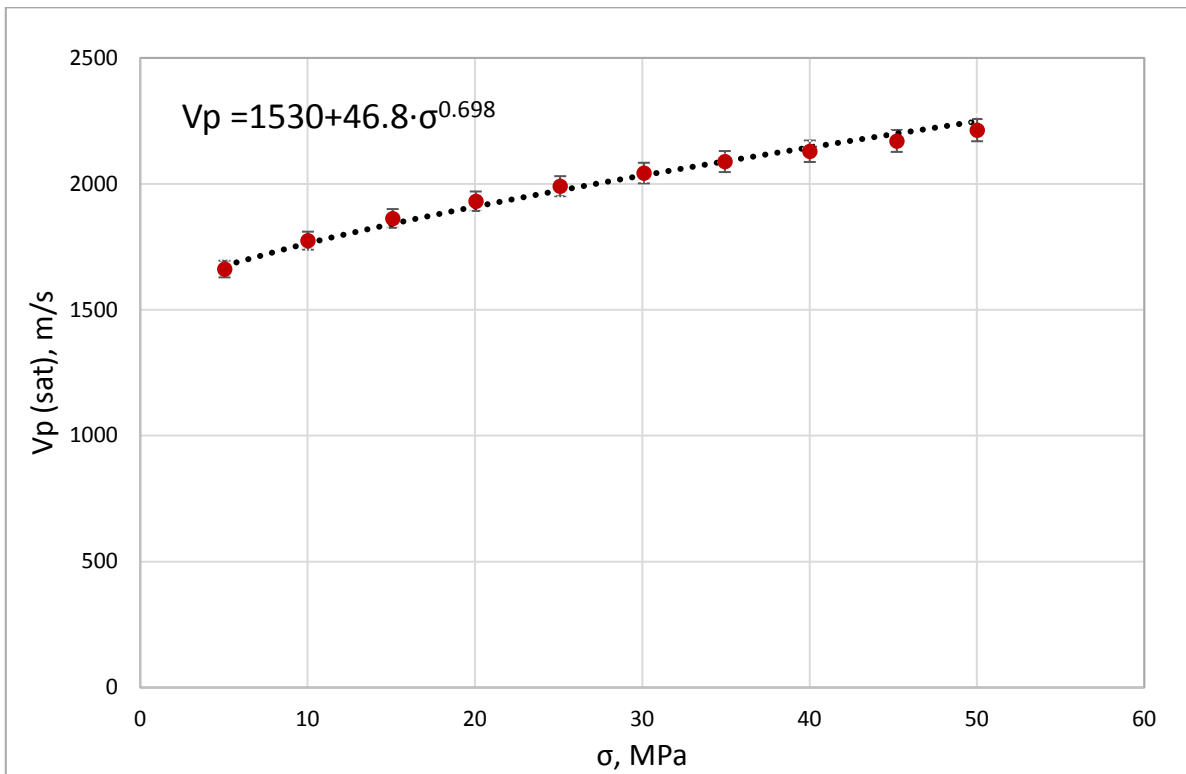


Figure A1.2.3. Power model for V_p fitting when relative volume fraction of kaolinite is 0.4 and relative volume fraction of smectite is 0.6.

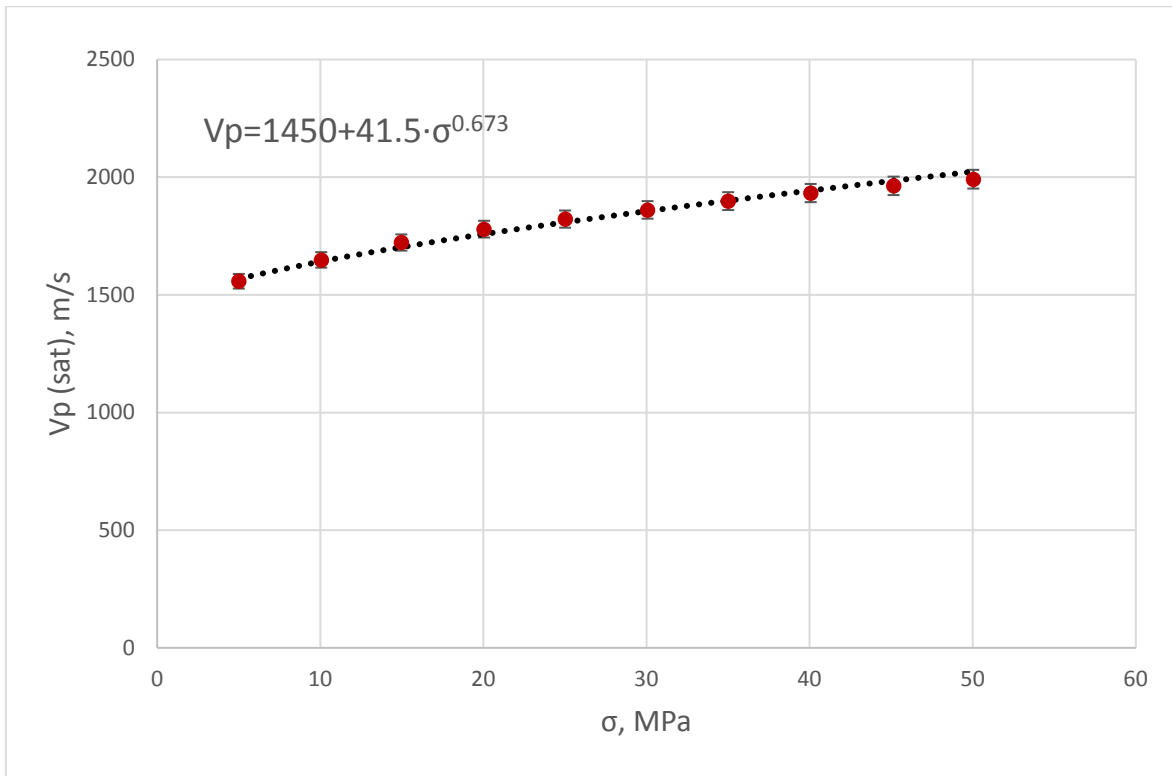


Figure A1.2.4. Power model for V_p fitting when relative volume fraction of kaolinite is 0.2 and relative volume fraction of smectite is 0.8.

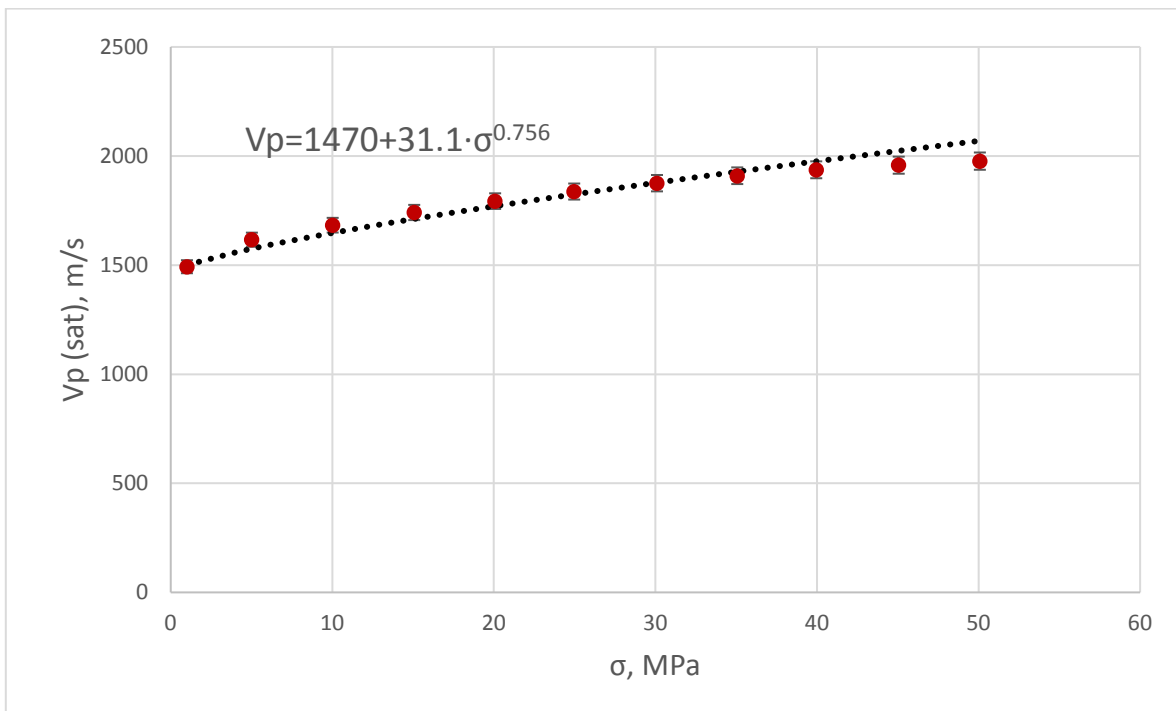


Figure A1.2.5. Power model for V_p fitting when relative volume fraction of kaolinite is 0 and relative volume fraction of smectite is 1.

A1.3. Second order polynomial models for Vp fitting in a kaolinite/silt/brine system

In this section we showed the second order polynomial models for Vp fitting in a kaolinite/silt/brine system for the particular clay composition. These are the models that were not included in the Subsection 3.4.1.

The values of the second order polynomial models for different clay composition in a kaolinite/silt/brine system are presented in the Table A1.3.1.

Table A1.3.1.

Results of fitting of laboratory data of Vp to the second order polynomial in a kaolinite/silt/brine system.

Relative silt volume	Relative kaolinite volume	A	B	C	R ²
0.75	0.25	-0.389	41.3	1500	0.984
0.5	0.5	-0.495	48.2	1320	0.969
0.25	0.75	-0.478	45.7	1320	0.978

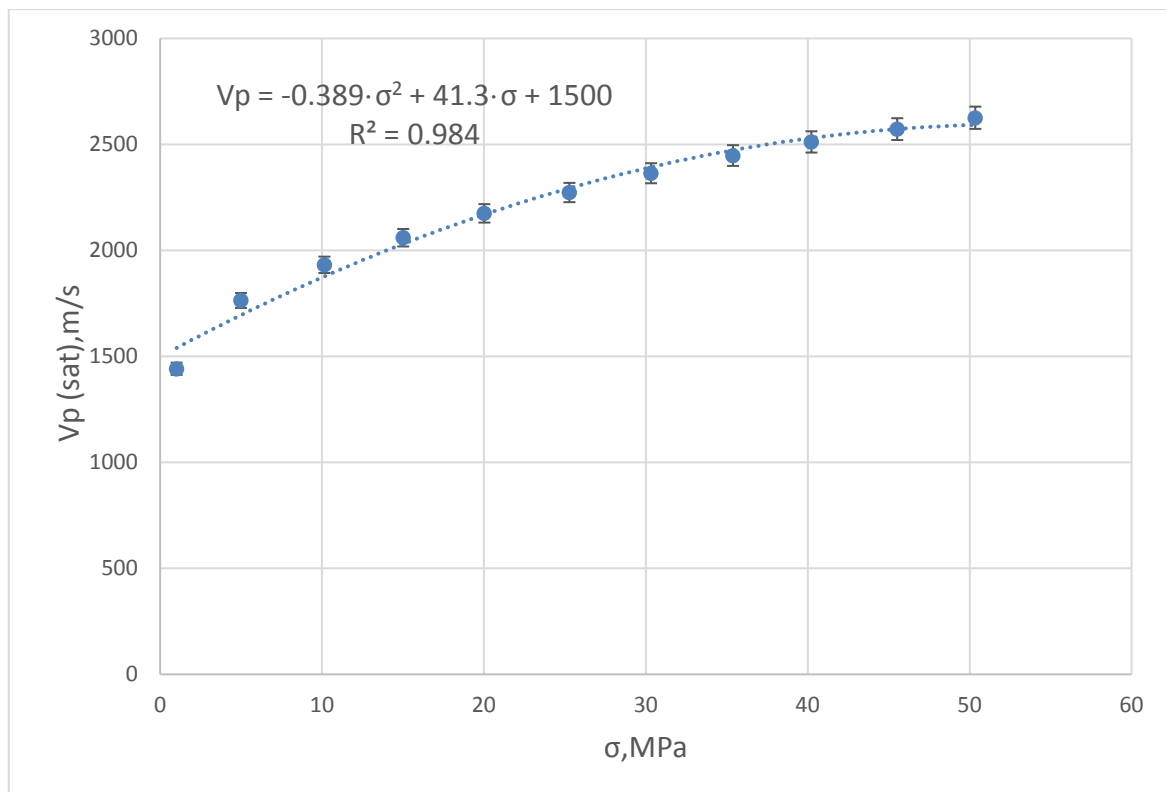


Figure A1.3.1. Second order polynomial model for Vp fitting when relative volume fraction of kaolinite is 0.25 and relative volume fraction of silt is 0.75.

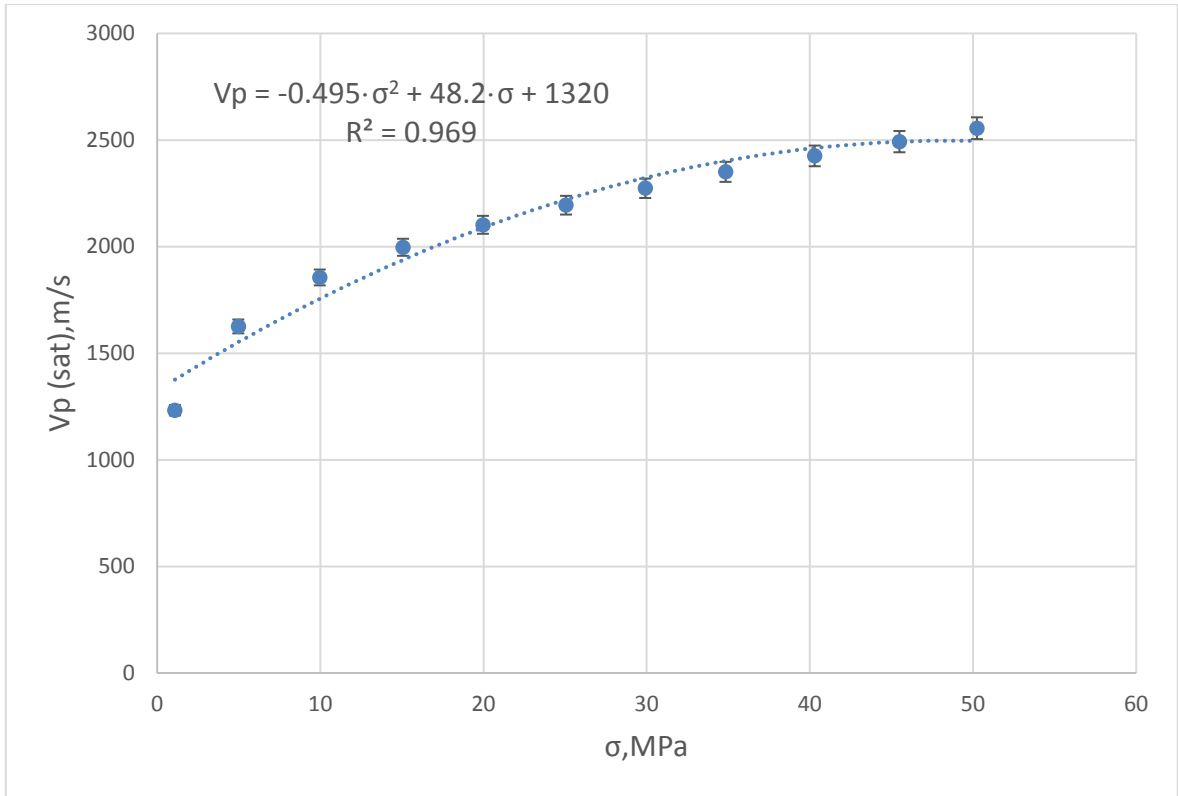


Figure A1.3.2. Second order polynomial model for V_p fitting when relative volume fraction of kaolinite is 0.5 and relative volume fraction of silt is 0.5.

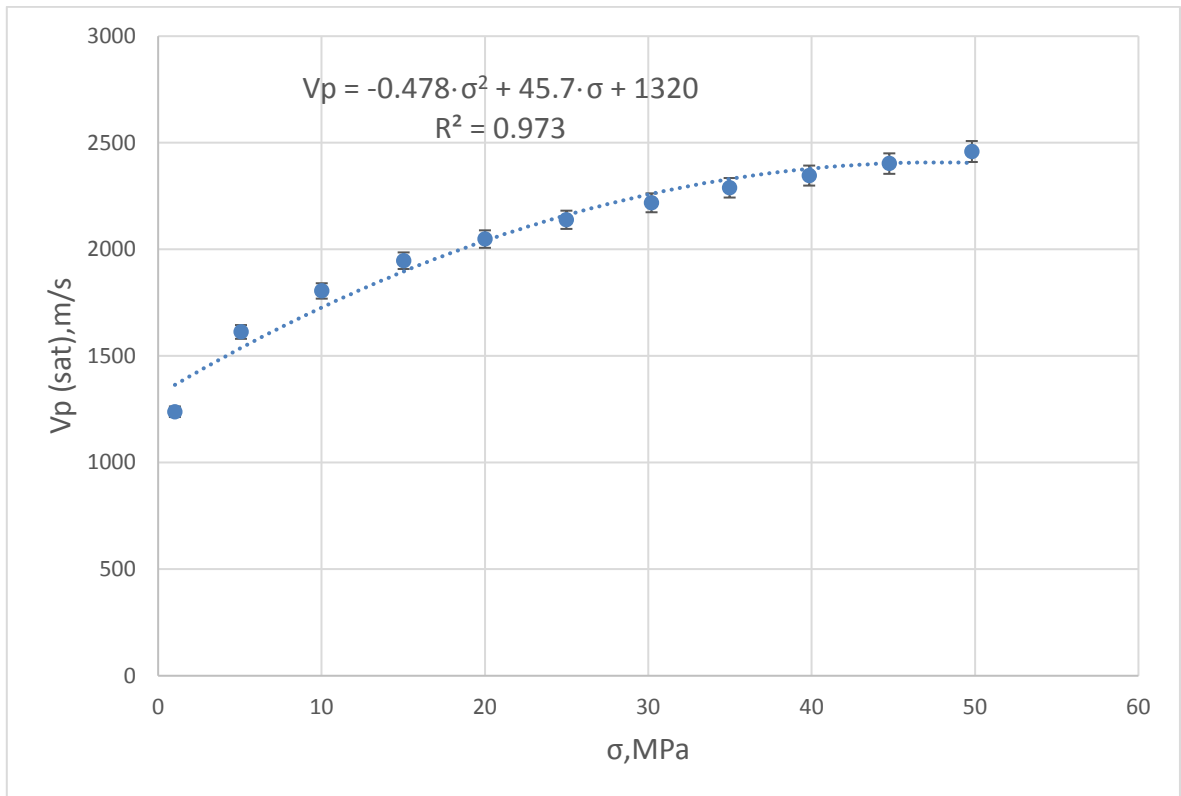


Figure A1.3.3. Second order polynomial model for V_p fitting when relative volume fraction of kaolinite is 0.75 and relative volume fraction of silt is 0.25.

A1.4. Power models for Vp fitting in a kaolinite/silt/brine system

In the section A1.4. there are the power models for Vp fitting in a kaolinite/silt/brine system that were not listed in the Subsection 3.4.2.

The resulting values of the power models for Vp fitting for a kaolinite/silt/brine system are presented in the Table 1.4.1.

Table A.1.4.1.

Result of fitting of laboratory data of Vp to the power model in a kaolinite/silt/brine system.

Relative silt volume	Relative kaolinite volume	A	B	V _{p_b}
1	0	15.2	1.020	1420
0.5	0.5	54.8	0.785	1470
0.25	0.75	47.2	0.805	1470

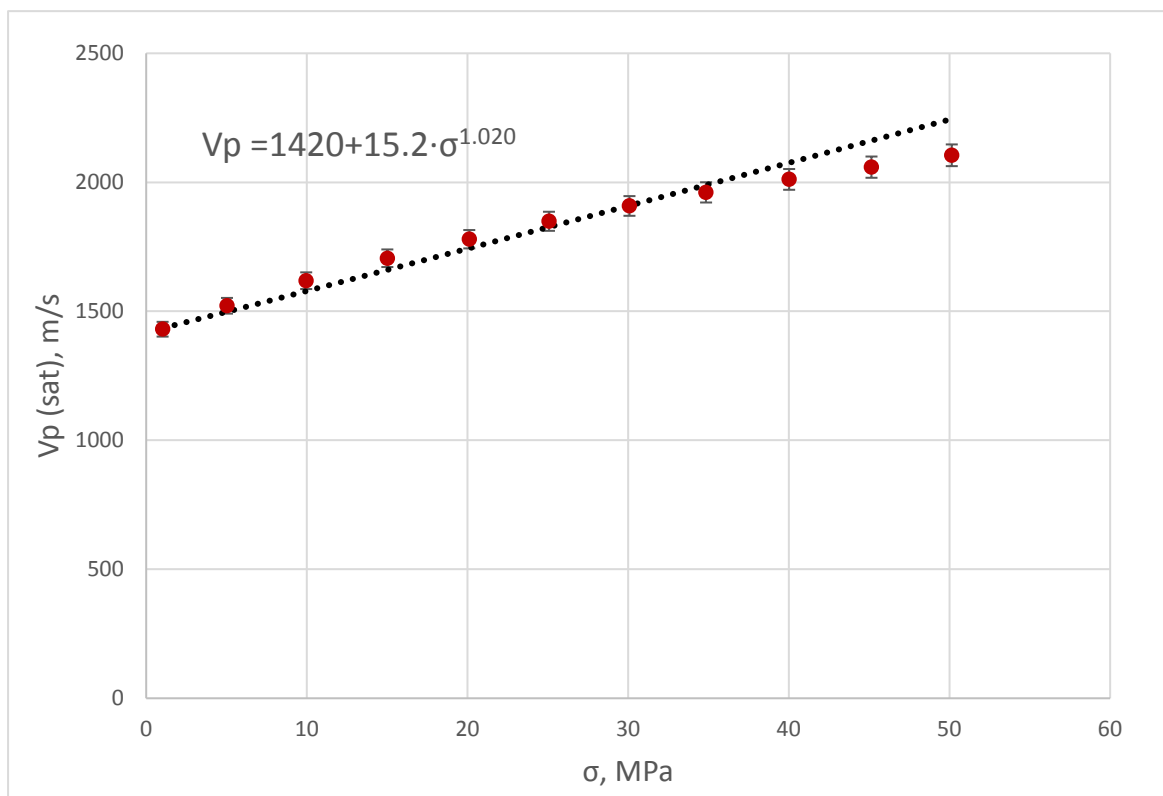


Figure A1.4.1. Power model for Vp fitting when relative volume fraction of kaolinite is 0 and relative volume fraction of silt is 1.0.

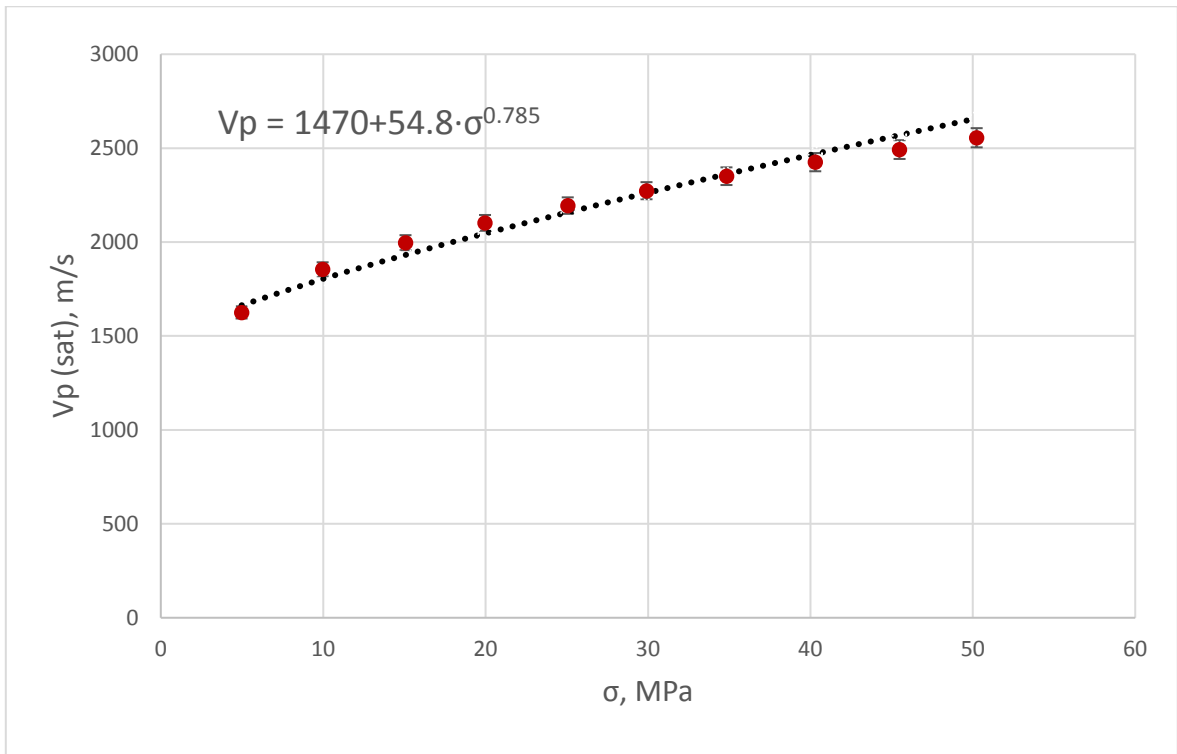


Figure A1.4.2. Power model for V_p fitting when relative volume fraction of kaolinite is 0.5 and relative volume fraction of silt is 0.5.

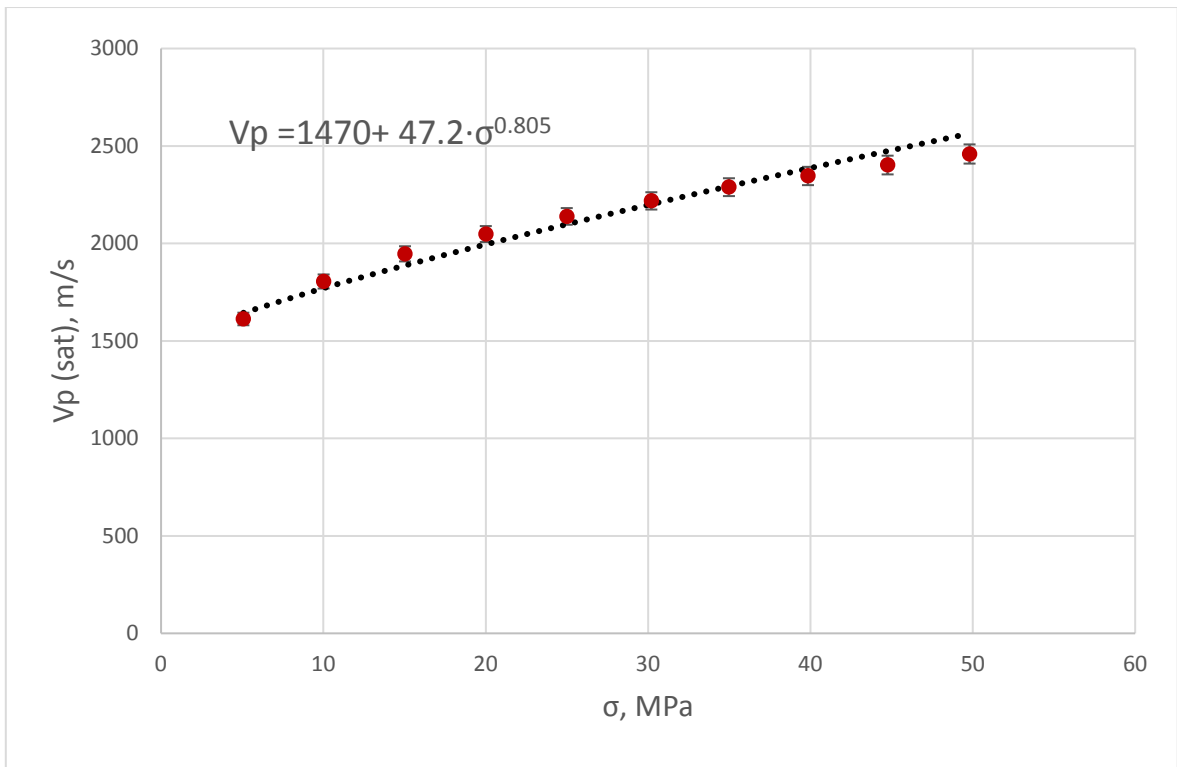


Figure A1.4.3. Power model for V_p fitting when relative volume fraction of kaolinite is 0.75 and relative volume fraction of silt is 0.25.

A2. Vs fitting

A2.1. Polynomial models for Vs fitting in a smectite/kaolinite/brine system

In this section we presented the second order polynomial models for shear wave velocity fitting in a smectite/kaolinite/brine system. Here are the models that were not shown in the Subsection 3.5.1. The resulting values of fitting laboratory data of Vs to the second order polynomial model in a smectite/kaolinite/brine system are given in the Table 2.1.1.

Table 2.1.1.

Results of fitting of laboratory data of Vs to the second order polynomial model in a smectite/kaolinite/brine system.

Relative smectite volume	Relative kaolinite volume	A	B	C	R ²
0.2	0.8	-0.152	17.6	395	0.996
0.4	0.6	-0.127	15.2	374	0.997
0.6	0.4	-0.119	15.04	384	0.999
0.8	0.2	-0.103	13.3	324	0.994
1	0	-0.0675	8.81	313	0.996

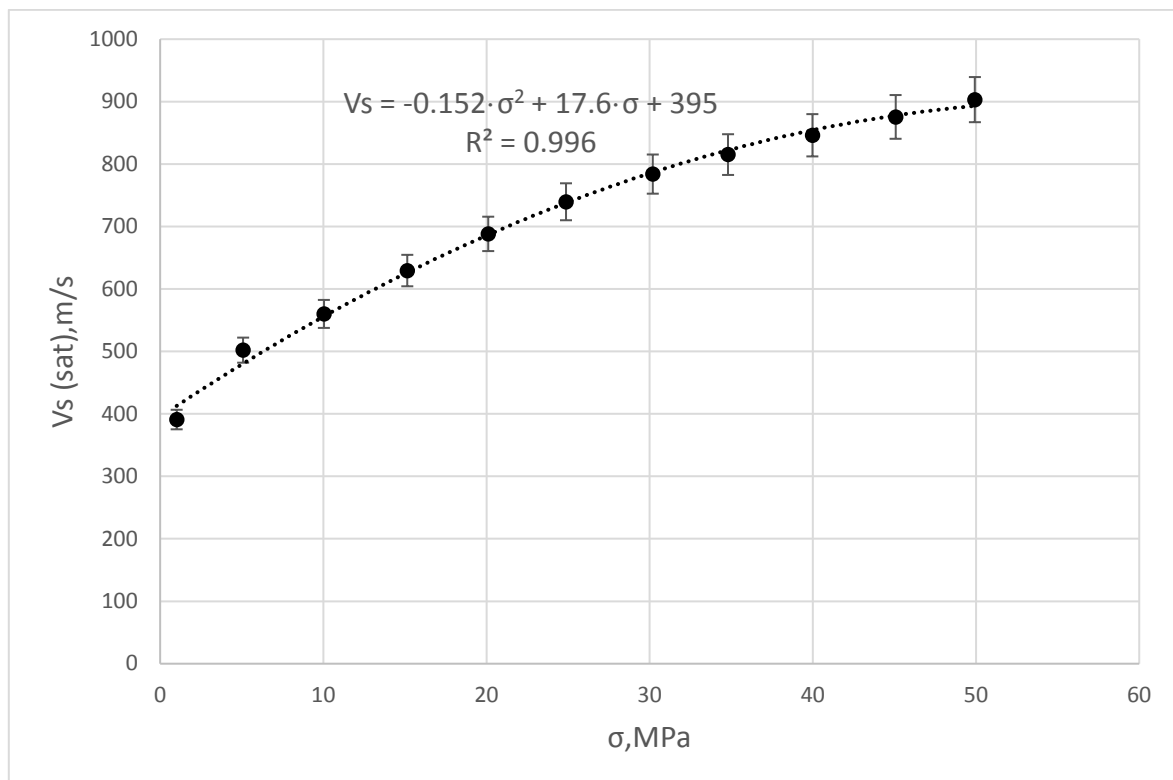


Figure A2.1.1. Second order polynomial model for Vs fitting when relative volume fraction of kaolinite is 0.8 and relative volume fraction of smectite is 0.2.

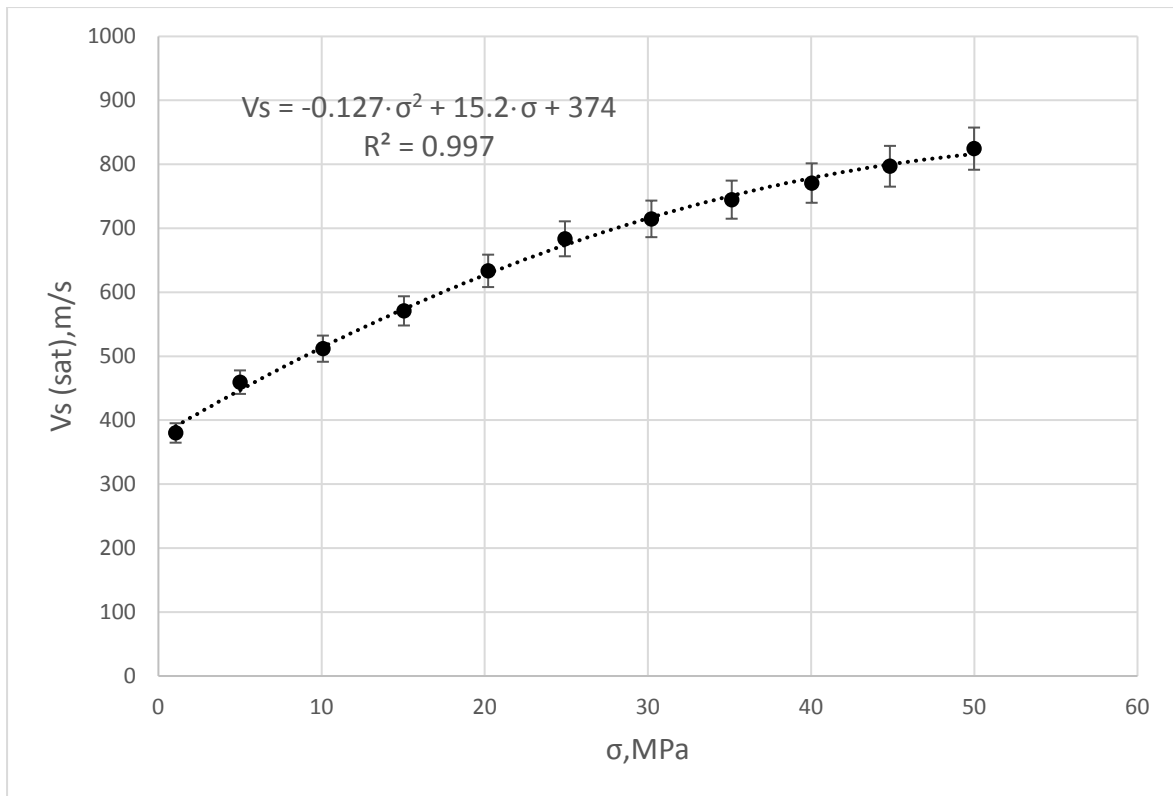


Figure A2.1.2. Second order polynomial model for V_s fitting when relative volume fraction of kaolinite is 0.6 and relative volume fraction of smectite is 0.4.

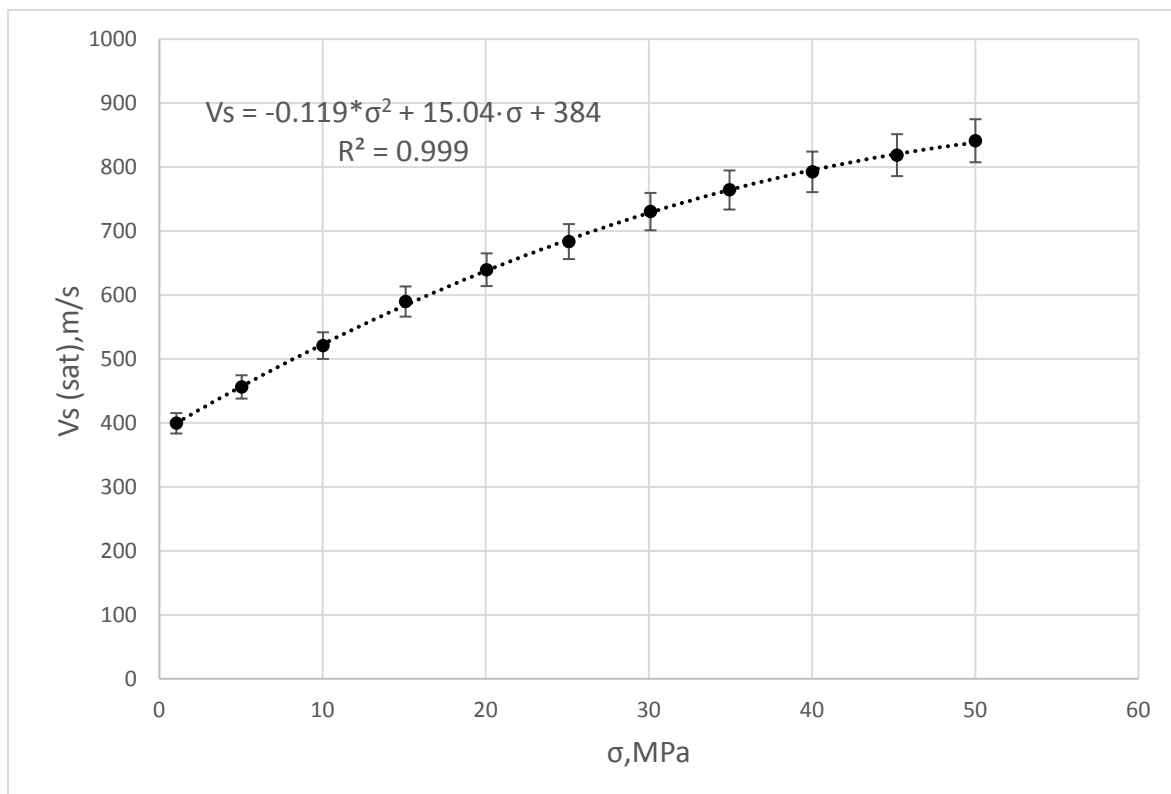


Figure A2.1.3. Second order polynomial model for V_s fitting when relative volume fraction of kaolinite is 0.4 and relative volume fraction of smectite is 0.6.

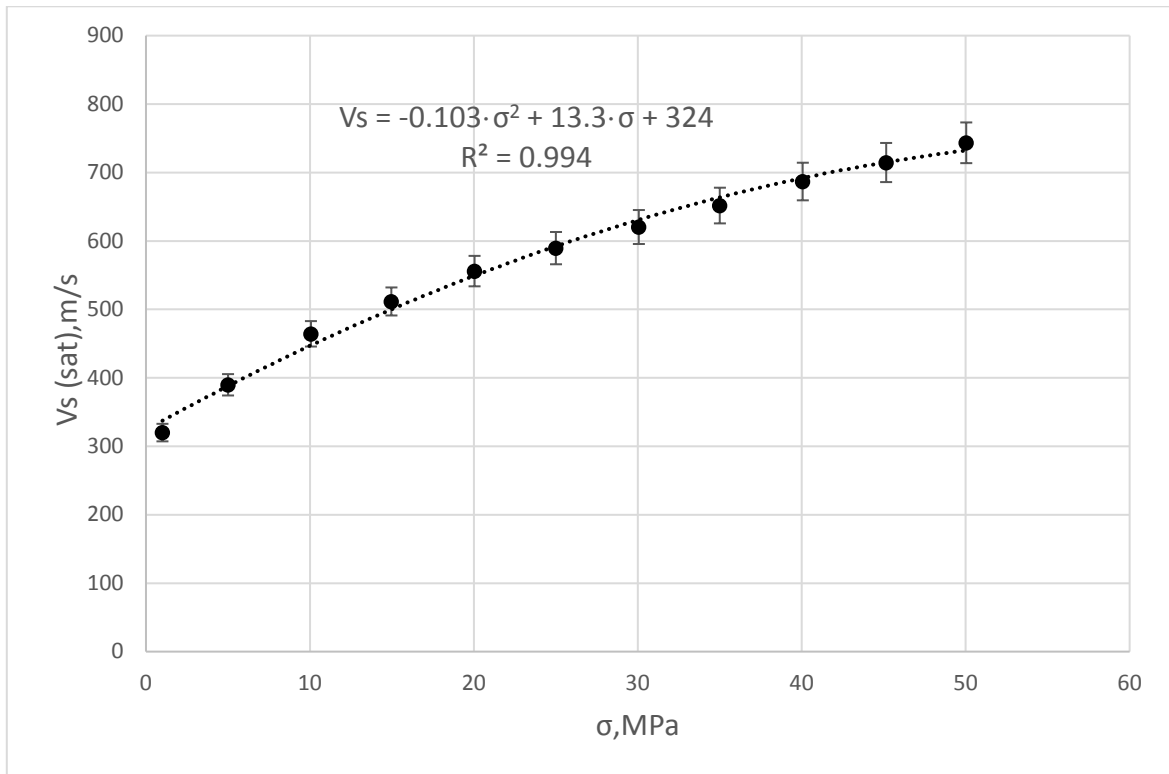


Figure A2.1.4. Second order polynomial model for V_s fitting when relative volume fraction of kaolinite is 0.2 and relative volume fraction of smectite is 0.8.

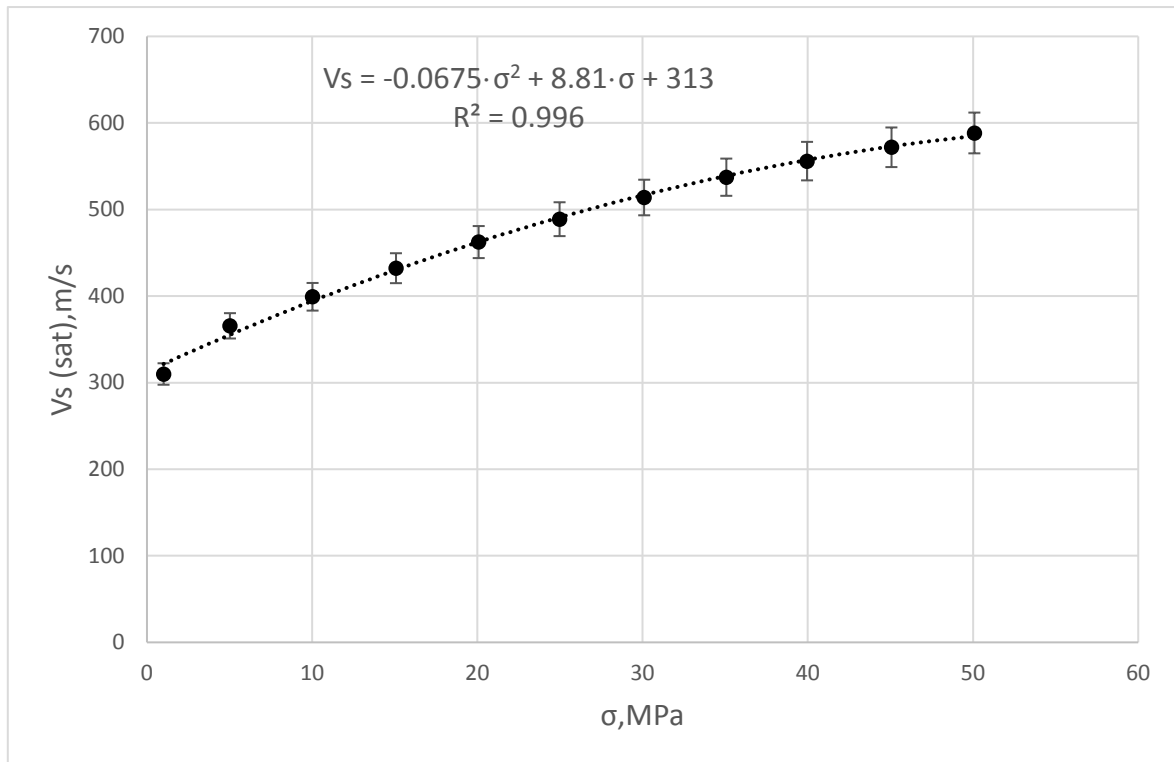


Figure A2.1.5. Second order polynomial model for V_s fitting when relative volume fraction of kaolinite is 0 and relative volume fraction of smectite is 1.

A2.2. Power models for Vs fitting in a smectite/kaolinite/brine system

In this section we presented the power models for Vs fitting in a smectite/kaolinite/brine system that were not included in the Subsection 3.5.2. Results of fitting laboratory data of Vs to the power models in a smectite/kaolinite/brine system for certain clay composition are shown in the Table 2.2.1.

Table 2.2.1.

Results of fitting laboratory data of Vs to the power model in a smectite/kaolinite/brine system.

Relative smectite volume	Relative kaolinite volume	A	B	V _{Sb}
0.2	0.8	34.6	0.699	395
0.4	0.6	8.99	1.068	374
0.6	0.4	16.5	0.885	384
0.8	0.2	21.7	0.769	324
1	0	16.4	0.731	313

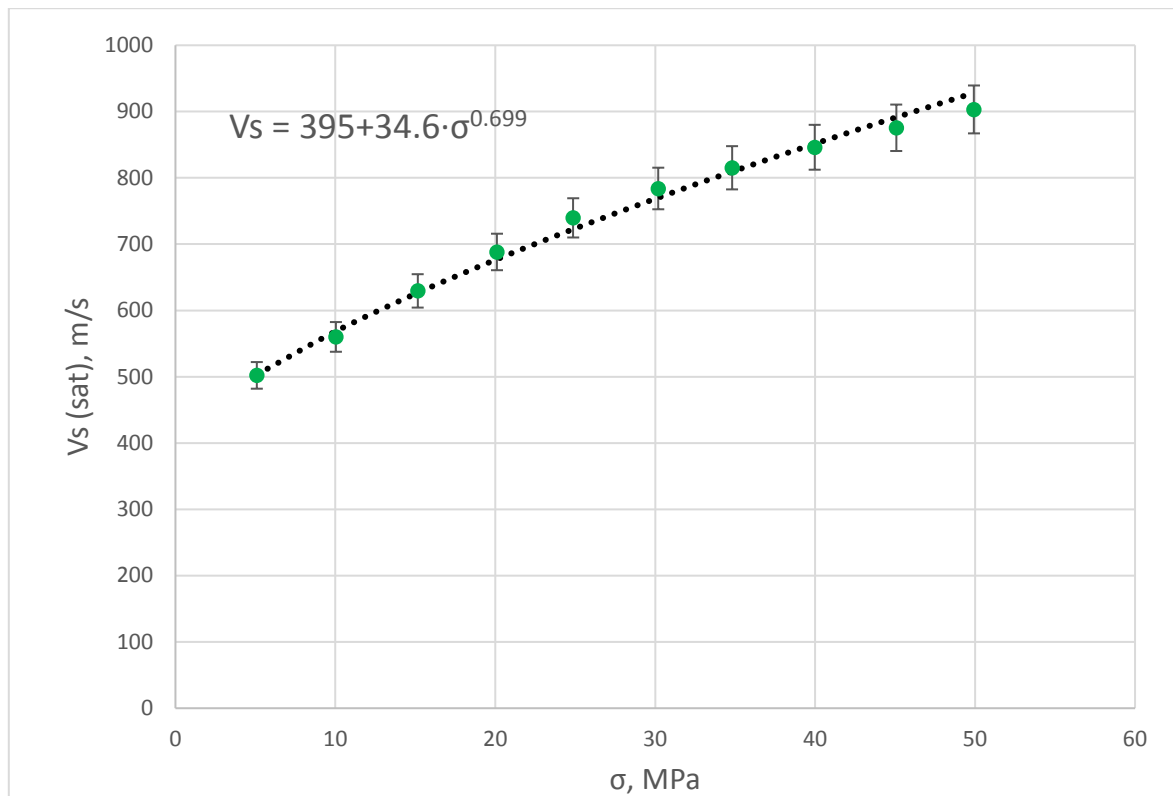


Figure A2.2.1. Power model for Vs fitting when relative volume fraction of kaolinite is 0.8 and relative volume fraction of smectite is 0.2.

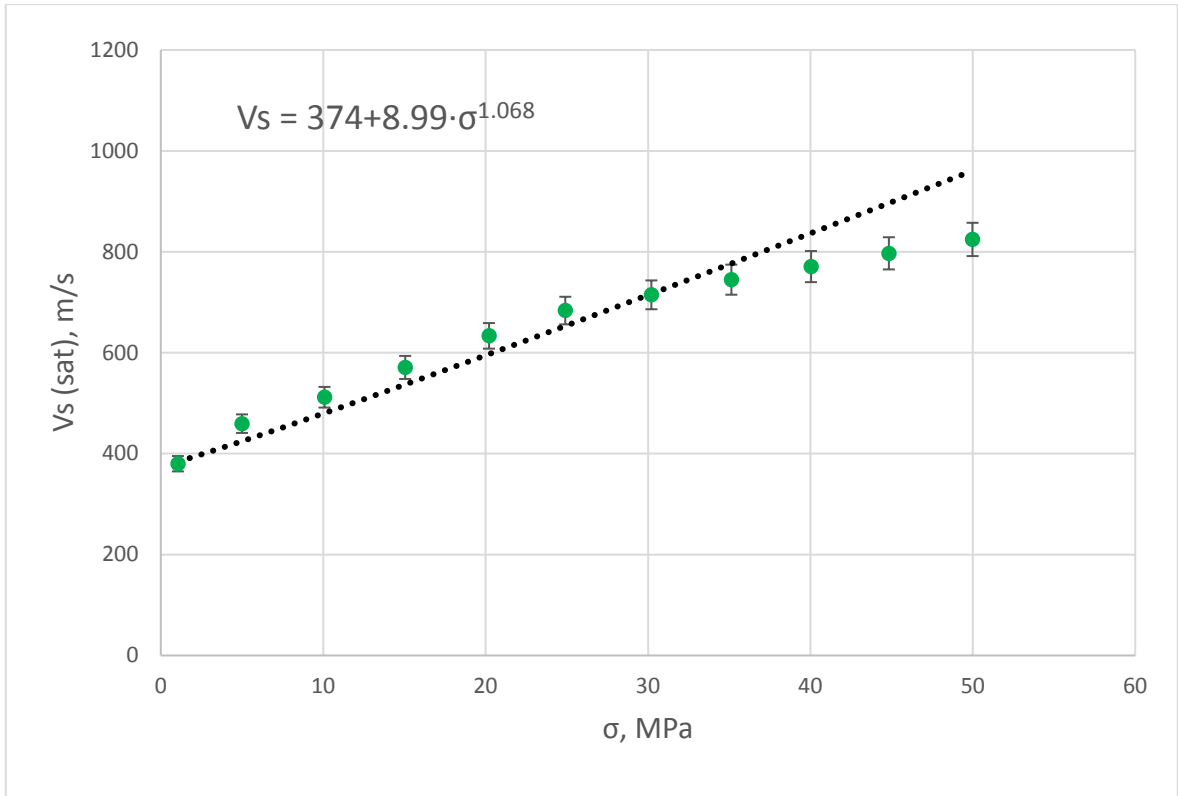


Figure A2.2.2. Power model for V_s fitting when relative volume fraction of kaolinite is 0.6 and relative volume fraction of smectite is 0.4.

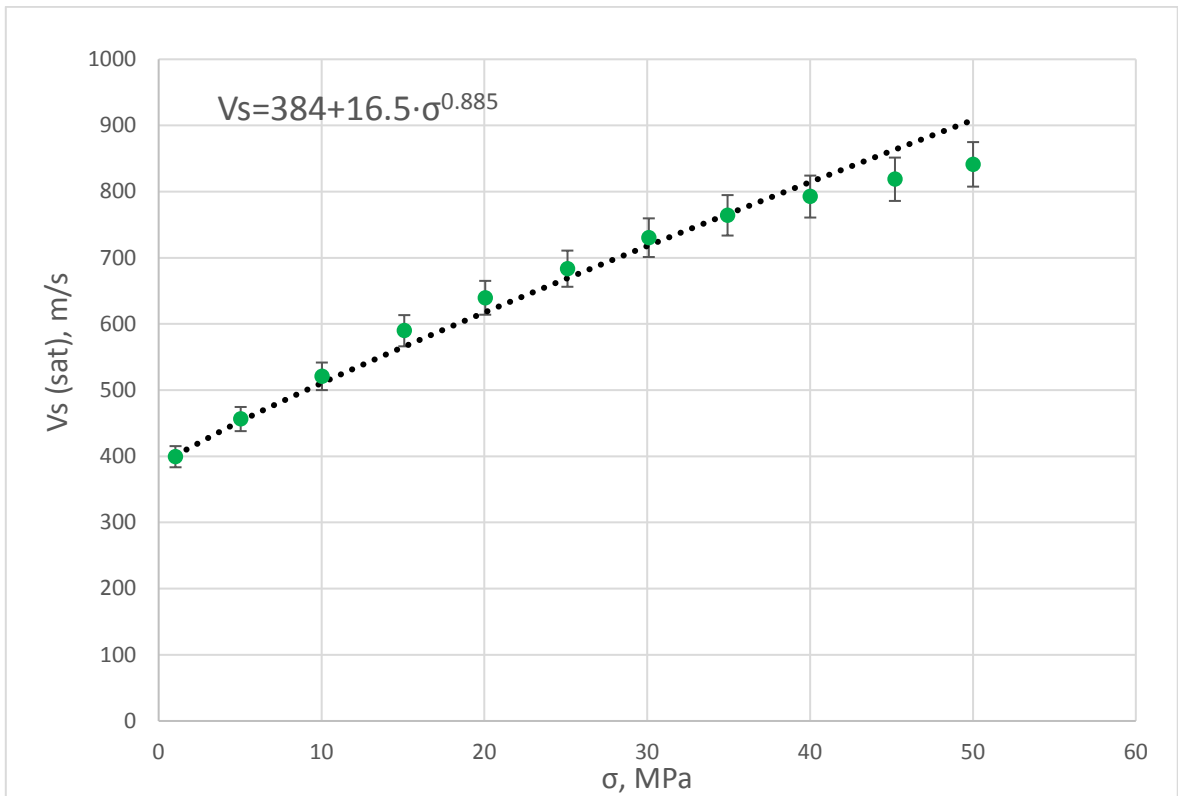


Figure A2.2.3. Power model for V_s fitting when relative volume fraction of kaolinite is 0.4 and relative volume fraction of smectite is 0.6.

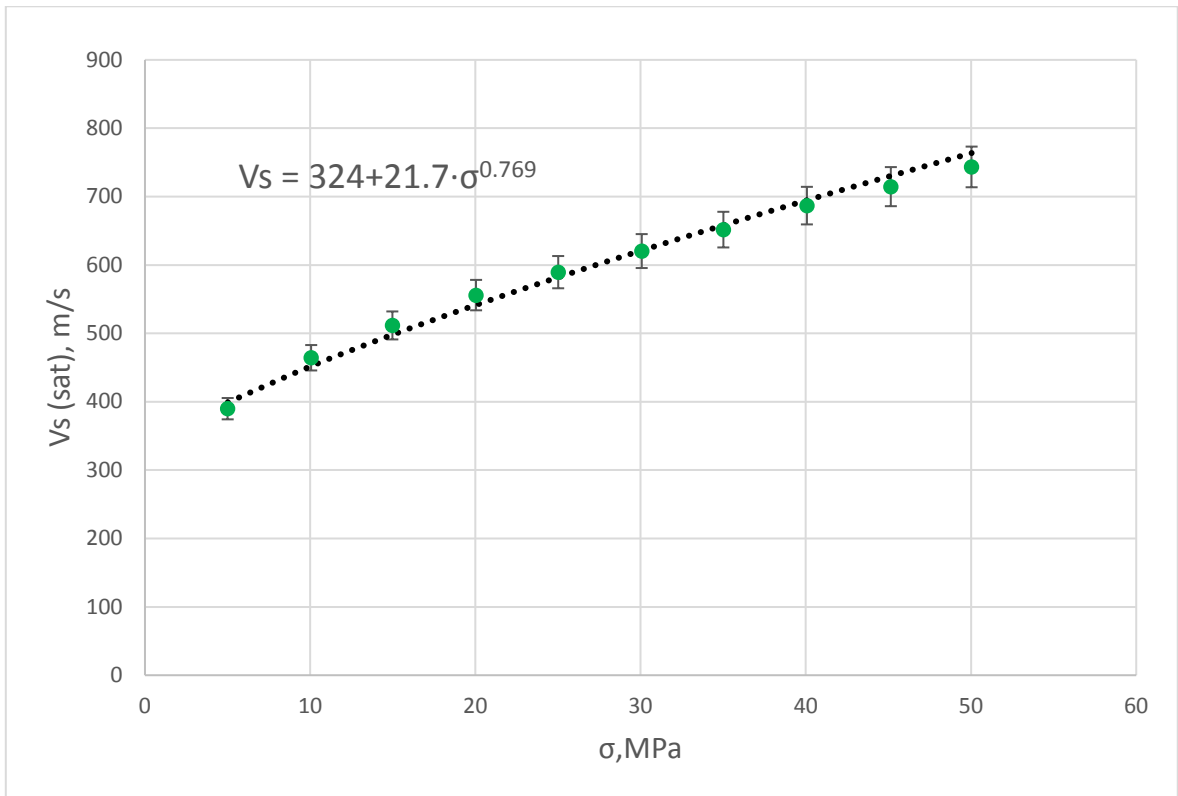


Figure A2.2.4. Power model for V_s fitting when relative volume fraction of kaolinite is 0.2 and relative volume fraction of smectite is 0.8.

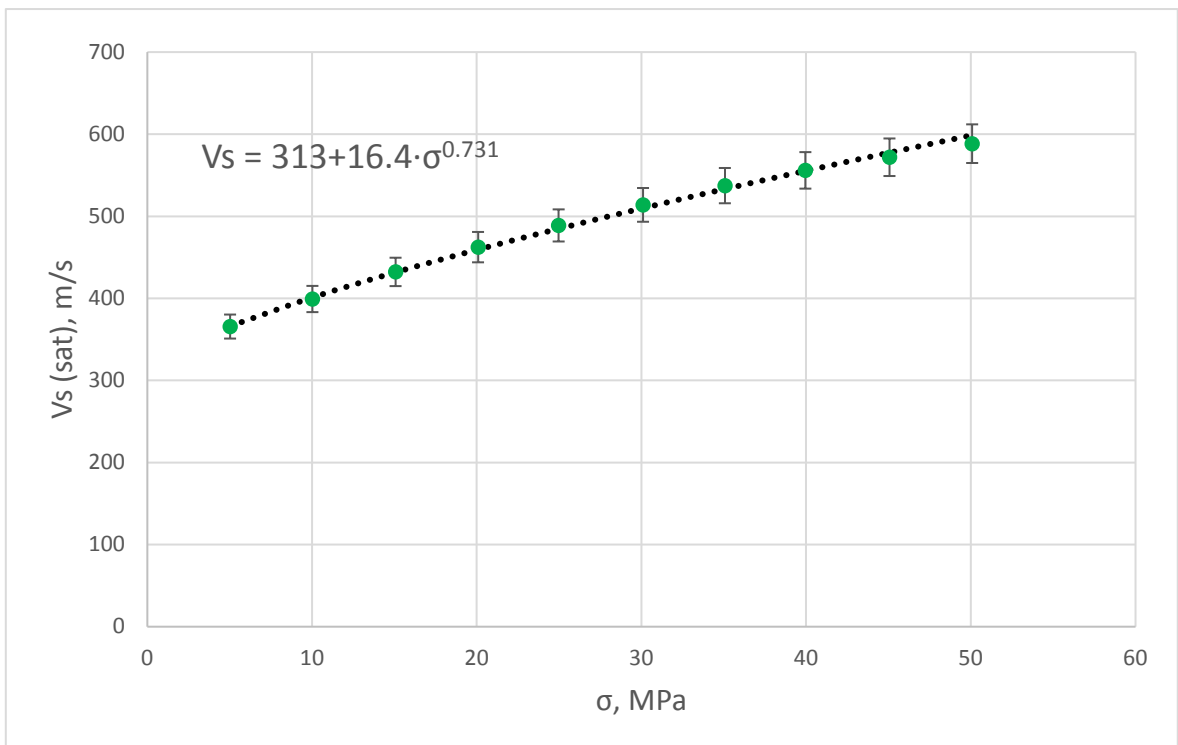


Figure A2.2.5. Power model for V_s fitting when relative volume fraction of kaolinite is 0 and relative volume fraction of smectite is 1.

A2.3. Polynomial models for Vs fitting in a kaolinite/silt/brine system

In the section 2.3. we showed the second order polynomial models for Vs fitting in a kaolinite/silt/brine system for certain clay composition that were not included in the Subsection 3.6.1. Resulting values of fitting laboratory data of Vs to the second order polynomial model in a kaolinite/silt/brine system are listed in the Table 2.3.1.

Table 2.3.1.

Results of fitting of laboratory data of Vs to second order polynomial model in a kaolinite/silt/brine system.

Relative silt volume	Relative kaolinite volume	A	B	C	R ²
0.75	0.25	-0.251	27.7	379	0.993
0.5	0.5	-0.281	29.3	334	0.987
0.25	0.75	-0.229	25.4	311	0.993

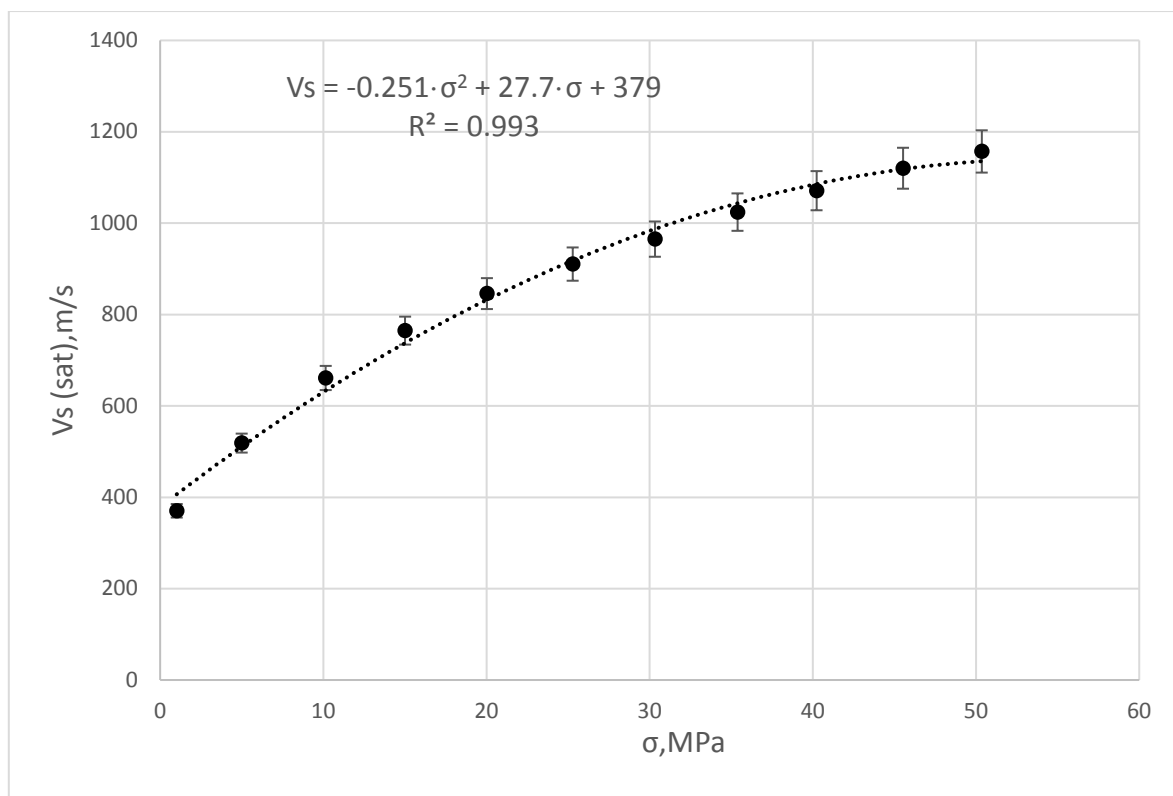


Figure A2.3.1. Second order polynomial model for Vs fitting when relative volume fraction of kaolinite is 0.25 and relative volume fraction of silt is 0.75.

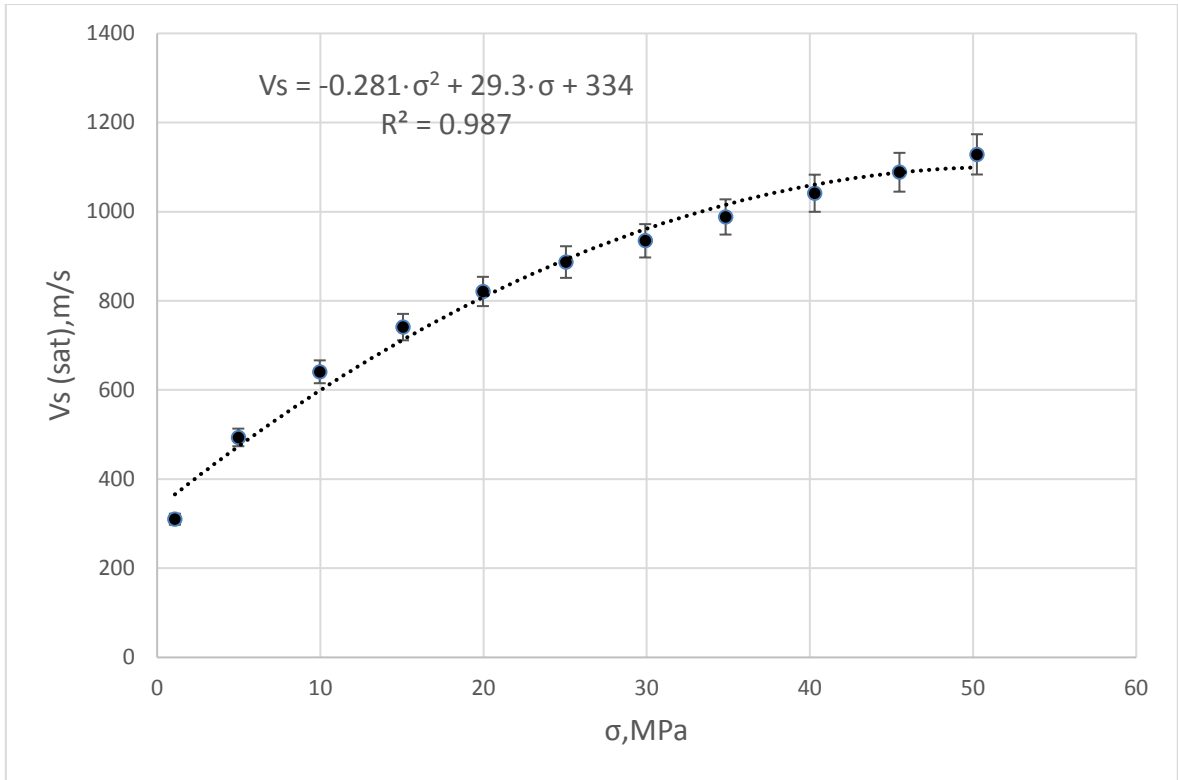


Figure A2.3.2. Second order polynomial model for V_s fitting when relative volume fraction of kaolinite is 0.5 and relative volume fraction of silt is 0.5

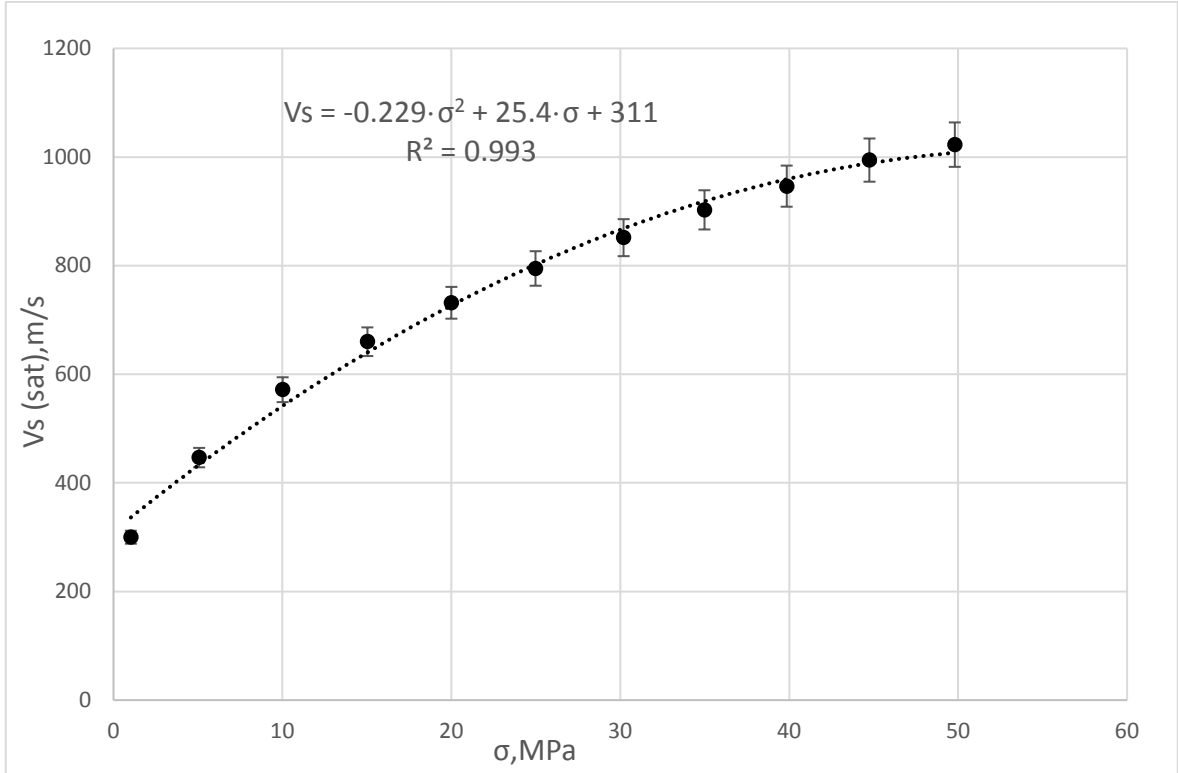


Figure A2.3.3. Second order polynomial model for V_s fitting when relative volume fraction of kaolinite is 0.75 and relative volume fraction of silt is 0.25.

A2.4. Power models for Vs fitting in a kaolinite/silt/brine system

In this section there are the power models for Vs fitting in a kaolinite/silt/brine system for particular clay composition that were not presented in the Subsection 3.6.2. The resulting values of fitting of laboratory data of Vs to the power model in a kaolinite/silt/brine system are given in the Table 2.4.1.

Table 2.4.1.

Results of fitting of laboratory data of Vs to the power model in a kaolinite/silt/brine system.

Relative silt volume	Relative kaolinite volume	A	B	V _{Sb}
1	0	7.32	1.15	305.7
0.5	0.5	61.8	0.667	334
0.25	0.75	48.3	0.7055	311

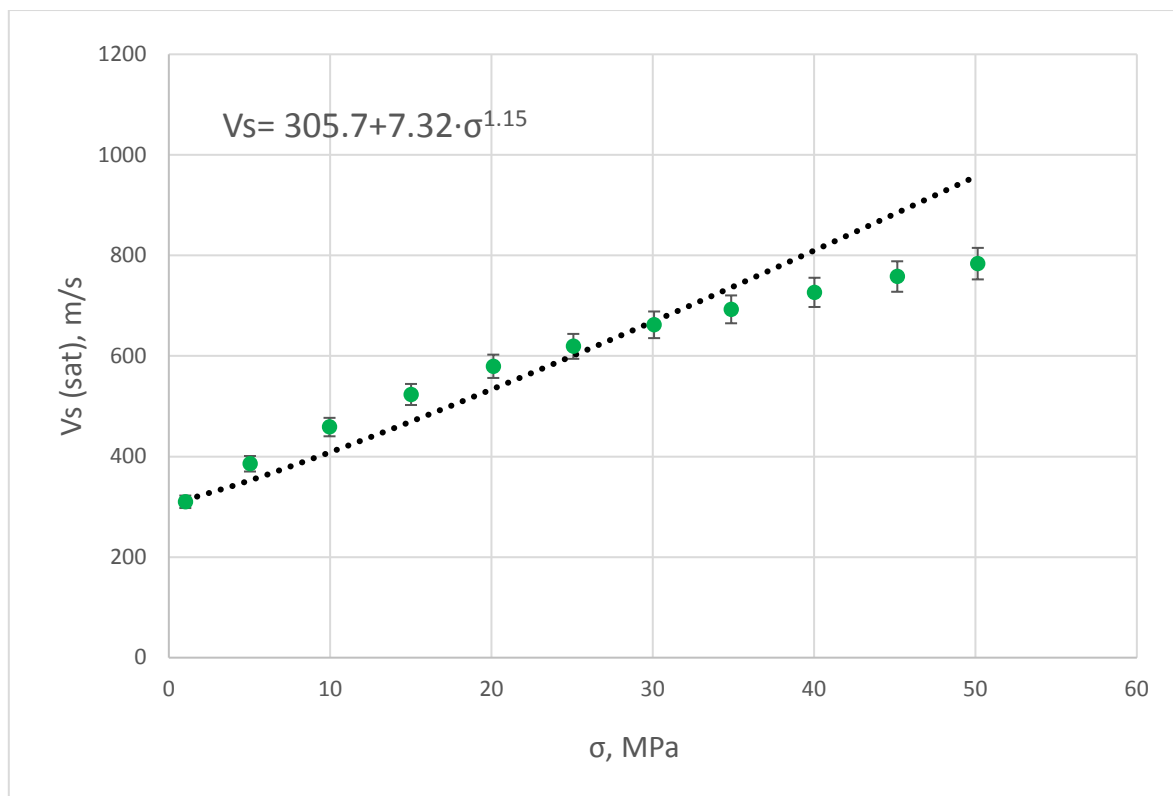


Figure A2.4.1. Power model for Vs fitting when relative volume fraction of kaolinite is 0 and relative fraction of silt is 1.0.

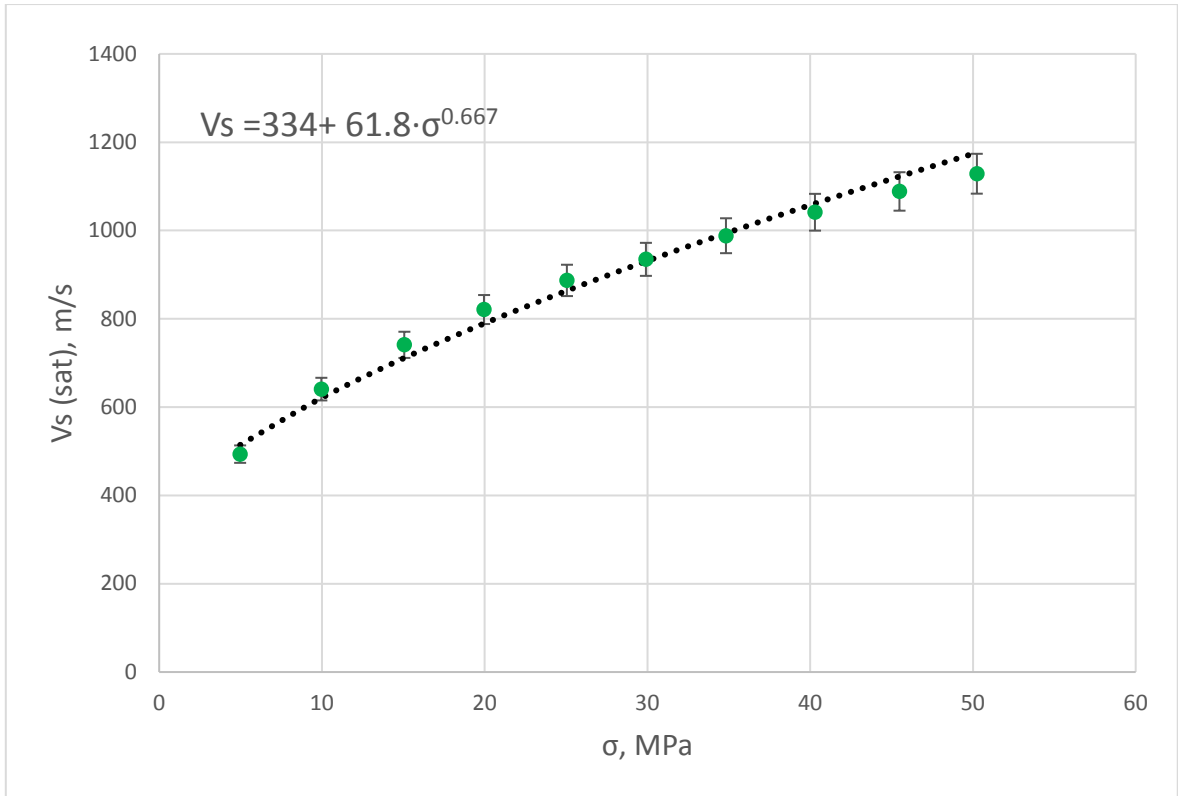


Figure A2.4.2. Power model for V_s fitting when relative volume fraction of kaolinite is 0.5 and relative volume fraction of silt is 0.5.

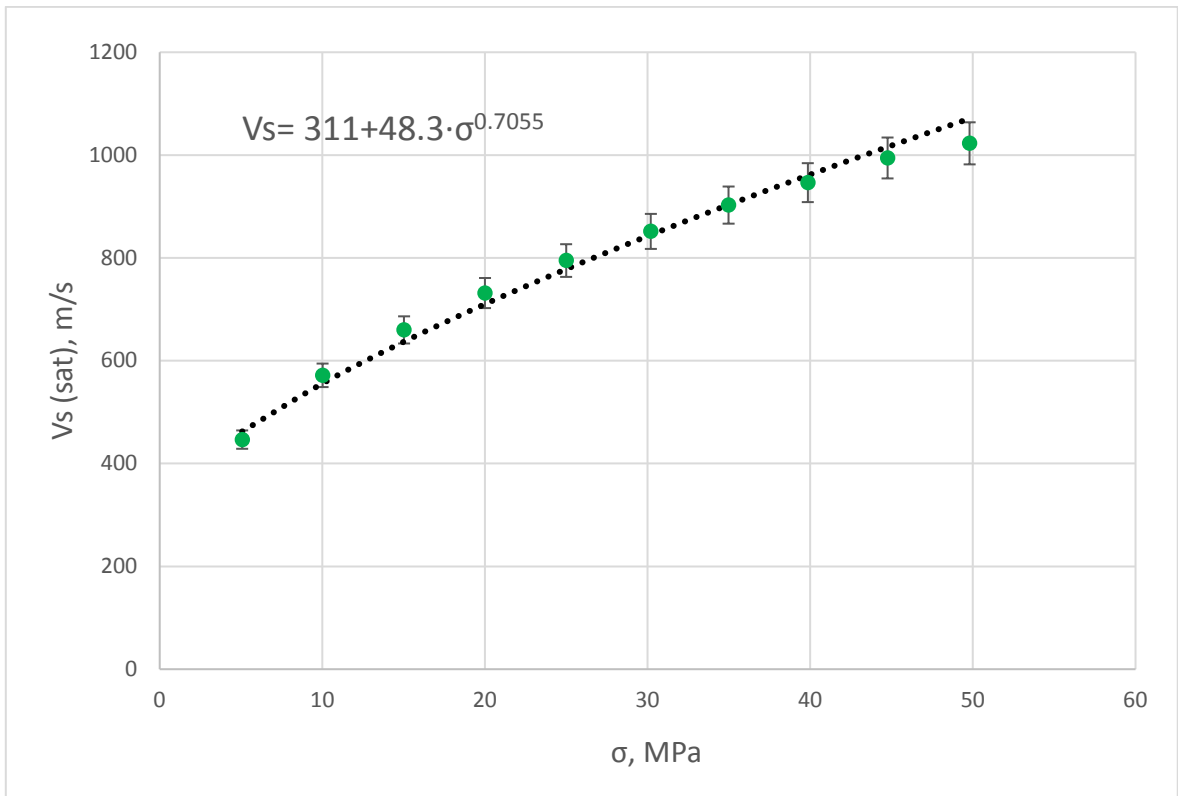


Figure A2.4.3. Power model for V_s fitting when relative volume fraction of kaolinite is 0.75 and relative volume fraction of silt is 0.25.

A3. Summary of second order polynomial models

Since we considered second order polynomial only to obtain the values of the velocities at seabed, we decided not to include the final form of these models in the Section 3.7. We presented them here.

For the smectite/kaolinite/brine systems the sonic velocities in a second order polynomial system are given by the equations

$$V_p = (0.0903 \cdot V_{\text{smec}} - 0.259) \cdot \sigma^2 + (-10.94 \cdot V_{\text{smec}} + 29.02) \cdot \sigma + (114 \cdot V_{\text{smec}} + 1390)$$

$$V_s = (0.0967 \cdot V_{\text{smec}} - 0.172) \cdot \sigma^2 + (-9.046 \cdot V_{\text{smec}} + 19.3) \cdot \sigma + (-69.4 \cdot V_{\text{smec}} + 395),$$

For the kaolinite/silt/brine system the sonic velocities in the second order polynomial model are

$$V_p = (0.443 \cdot V_{\text{silt}} - 0.654) \cdot \sigma^2 + (-32.7 \cdot V_{\text{silt}} + 59.4) \cdot \sigma + (190.9 \cdot V_{\text{silt}} + 1271)$$

$$V_s = (0.129 \cdot V_{\text{silt}} - 0.3038) \cdot \sigma^2 + (-12.05 \cdot V_{\text{silt}} + 32.1) \cdot \sigma + (12.1 \cdot V_{\text{silt}} + 325).$$

Appendix B. Programming codes applied in the thesis

B.1. Coppens's code for the brine velocity calculation

```
' Output:
' SBV_Coppens = acoustic velocity of brine water at sea bed(m/s)
' Input:
' D= depth (m)
' S = salinity (fractions of one)
' T = temperature (degC)
' Notes:
' 1. Horner form of polynomials to reduce loss of accuracy
' Reference:
' Coppens 1981
' Simple equations for the speed of sound in Neptunian waters, 3nd
ed, page 862
Public Function SBV_Coppens (Temp As Double, Depth As Double, PSU As Double) As Double
    Dim c_T0S_a, c_T0S_b, c_T0S As Double
    Dim a0, a1, a2
    c_T0S_a = 1449.05 + Temp * (4.57 + Temp * (-0.0521 + 0.00023 * Temp))
    c_T0S_b = (1.333 + Temp * (-0.0126 + 0.00009 * Temp)) * (PSU - 35)
    c_T0S = c_T0S_a + c_T0S_b
    a0 = (0.0000016 + 0.00000002 * (PSU - 35)) * (PSU - 35) * Temp * Depth
    a1 = (0.01623 + 0.0000253 * Temp) * Depth
    a2 = (0.000000213 - 0.00000001 * Temp) * Depth ^ 2
    SBV_Coppens = c_T0S + a0 + a1 + a2
End Function
```

B.2. Batzle-Wang's code for the brine velocity calculation

```
' Output:
' V_b = acoustic velocity of brine water (m/s)
' Input:
' P = pressure (MPa)
' S = salinity (fractions of one)
' T = temperature (degC)
' Notes:
' 1. 1 MPa = 10 bar
' 2. Horner form of polynomials to reduce loss of accuracy
' Reference:
' Batzle and Wang 1992
' Rock Physics Handbook, 2nd ed, page 340
Public Function V_b(P As Double, S As Double, T As Double) As
Double
    Dim om00, om10, om20, om30, om40 As Double
    Dim om01, om11, om21, om31, om41 As Double
```

```

Dim om02, om12, om22, om32, om42 As Double
Dim om03, om13, om23, om33, om43 As Double
Dim a, b, c, d, e, V_w As Double
Dim sr, aa, bb, cc As Double
' Find first the acoustic velocity of pure water
om00 = 1402.85
om10 = 4.871
om20 = -0.04783
om30 = 0.0001487
om40 = -0.0000002197
om01 = 1.524
om11 = -0.0111
om21 = 0.0002747
om31 = -0.0000006503
om41 = 0.000000007987
om02 = 0.003437
om12 = 0.0001739
om22 = -0.000002135
om32 = -0.0000001455
om42 = 0.000000000523
om03 = -0.00001197
om13 = -0.000001628
om23 = 0.00000001237
om33 = 0.0000000001327
om43 = -4.614E-13
a = om00 + P * (om01 + P * (om02 + P * om03))
b = T * (om10 + P * (om11 + P * (om12 + P * om13)))
c = T * T * (om20 + P * (om21 + P * (om22 + P * om23)))
d = T * T * T * (om30 + P * (om31 + P * (om32 + P * om33)))
e = T * T * T * T * (om40 + P * (om41 + P * (om42 + P * om43)))
V_w = a + b + c + d + e
' Then the velocity of brine
sr = Sqr(S)
aa = 1170 + T * (-9.6 + T * (0.055 - 0.000085 * T))
bb = P * (2.6 - 0.0029 * T - 0.0476 * P)
cc = sr * sr * sr * ((780 + P * (-10 + 0.16 * P)) - 1820 * sr)
V_b = V_w + S * (aa + bb) + cc
End Function

```

B3. Batzle-Wang's code for the brine density calculation

```

' Output:
' rho_b = density of brine (g/cc)
' Input:
' P = pressure (MPa)
' S = salinity (fractions of one)
' T = temperature (degC)
' Notes:
' 1. 1 MPa = 10 bar
' 2. Horner form of polynomials to reduce loss of accuracy

```



```
' Reference:
' Batzle and Wang 1992
' Rock Physics Handbook, 2nd ed, page 340
Public Function rho_b(P As Double, S As Double, T As Double) As Double
  Dim a, b, c, d, e, f, rho_w As Double
  ' Calculate the density of pure water
  a = T * (-80 + T * (-3.3 + 0.00175 * T))
  b = P * (489 - 0.333 * P)
  c = T * P * (-2 - 0.002 * P + T * (0.016 - 0.000013 * T))
  rho_w = 1# + 0.000001 * (a + b + c)
  ' Calculate the density of brine
  d = 0.668 + 0.44 * S
  e = P * (300 - 2400 * S)
  f = T * (80 + 3 * T - 3300 * S + P * (47 * S - 13))
  rho_b = rho_w + S * (d + 0.000001 * (e + f))
End Function
```

B4. Biot-Geertsma code for velocities prediction

```
' Output:
' High-frequency limit of shear velocity according to Biot-Geertsma for 1st loading
' Input:
' phi = total porosity
' rho_m = density of solid material
' rho_f = density of fluid
' alpha = tortuosity parameter
' Assumption:
' 1st load sandstone model
Public Function VS_hf_BiotGeertsma_1st(phi As Double, rho_m As Double, rho_f As Double, alpha As
Double) As Double
  Dim G_d As Double
  ' Sand model for first load
  G_d = 1.44 * Exp(-2.29 * phi)
  ' Biot-Geertsma calculations
  VS_hf_BiotGeertsma_1st = 1000# * Sqr(G_d / ((1 - phi) * rho_m + (1 - 1 / alpha) * phi * rho_f))
End Function
```

```

' Output:
' High-frequency limit of shear velocity according to Biot-Geertsma for 2nd loading
' Input:
' phi = total porosity
' rho_m = density of solid material
' rho_f = density of fluid
' alpha = tortuosity parameter
' Assumption:
' 2nd load sandstone model
Public Function VS_hf_BiotGeertsma_2nd(phi As Double, rho_m As Double, rho_f As Double, alpha As
Double) As Double
    Dim G_d As Double
    ' Sand model for second load
    G_d = 1.4 * Exp(-2.01 * phi)
    ' Biot-Geertsma calculations
    VS_hf_BiotGeertsma_2nd = 1000# * Sqr(G_d / ((1 - phi) * rho_m + (1 - 1 / alpha) * phi * rho_f))
End Function

```

```

' Output:
' High-frequency limit of compressional velocity according to Biot-Geertsma for 1st loading
' Input:
' phi = total porosity
' rho_m = density of solid material
' rho_f = density of fluid
' K_m = bulk modulus of solid material
' K_f = bulk modulus of fluid
' alpha = tortuosity parameter
' Assumption:
' 1st load sandstone model
Public Function VP_hf_BiotGeertsma_1st(phi As Double, rho_m As Double, rho_f As Double, K_m As
Double, K_f As Double, alpha As Double) As Double
    Dim rho11, rho22, rho12 As Double
    Dim A, B, D, P, Q, R As Double
    Dim G_d, K_d As Double
    ' Sand model for first load
    G_d = 1.44 * Exp(-2.29 * phi)

```

```

K_d = 5.37 * Exp(-4.86 * phi)
' Biot-Geertsma calculations
rho12 = (1# - alpha) * phi * rho_f
rho22 = phi * rho_f - rho12
rho11 = (1# - phi) * rho_m - rho12
B = rho11 * rho22 - rho12 * rho12
D = 1# - phi - K_d / K_m + phi * K_m / K_f
Q = (1# - phi - K_d / K_m) * phi * K_m / D
R = phi * phi * K_m / D
P = ((1 - phi) * (1 - phi - K_d / K_m) * K_m + phi * (K_m / K_f) * K_d) / D + 4# * G_d / 3#
A = P * rho22 + R * rho11 - 2# * Q * rho12
VP_hf_BiotGeertsma_1st = 1000# * Sqr((A + Sqr(A * A - 4 * B * (P * R - Q * Q))) / (2 * B))
End Function

' Output:
' High-frequency limit of compressional velocity according to Biot-Geertsma for 2nd loading
' Input:
' phi = total porosity
' rho_m = density of solid material
' rho_f = density of fluid
' K_m = bulk modulus of solid material
' K_f = bulk modulus of fluid
' alpha = tortuosity parameter
' Assumption:
' 2nd load sandstone model
Public Function VP_hf_BiotGeertsma_2nd(phi As Double, rho_m As Double, rho_f As Double, K_m As
Double, K_f As Double, alpha As Double) As Double
Dim rho11, rho22, rho12 As Double
Dim A, B, D, P, Q, R As Double
Dim G_d, K_d As Double
' Sand model for second load
G_d = 1.4 * Exp(-2.01 * phi)
K_d = 4.71 * Exp(-4.39 * phi)
' Biot-Geertsma calculations
rho12 = (1# - alpha) * phi * rho_f
rho22 = phi * rho_f - rho12
rho11 = (1# - phi) * rho_m - rho12
B = rho11 * rho22 - rho12 * rho12
D = 1# - phi - K_d / K_m + phi * K_m / K_f
Q = (1# - phi - K_d / K_m) * phi * K_m / D

```

```

R = phi * phi * K_m / D
P = ((1 - phi) * (1 - phi - K_d / K_m) * K_m + phi * (K_m / K_f) * K_d) / D + 4# * G_d / 3#
A = P * rho22 + R * rho11 - 2# * Q * rho12
VP_hf_BiotGeertsma_2nd = 1000# * Sqr((A + Sqr(A * A - 4 * B * (P * R - Q * Q))) / (2 * B))
End Function

```

Appendix C. CPI plots displaying editing and main calculations that were done on well logs

Here we presented the CPI plots showing editing and main calculations that were done on well logs for the three formations (Utsira, Skade and Grid) for the wells that were not included in the Section 5.5.

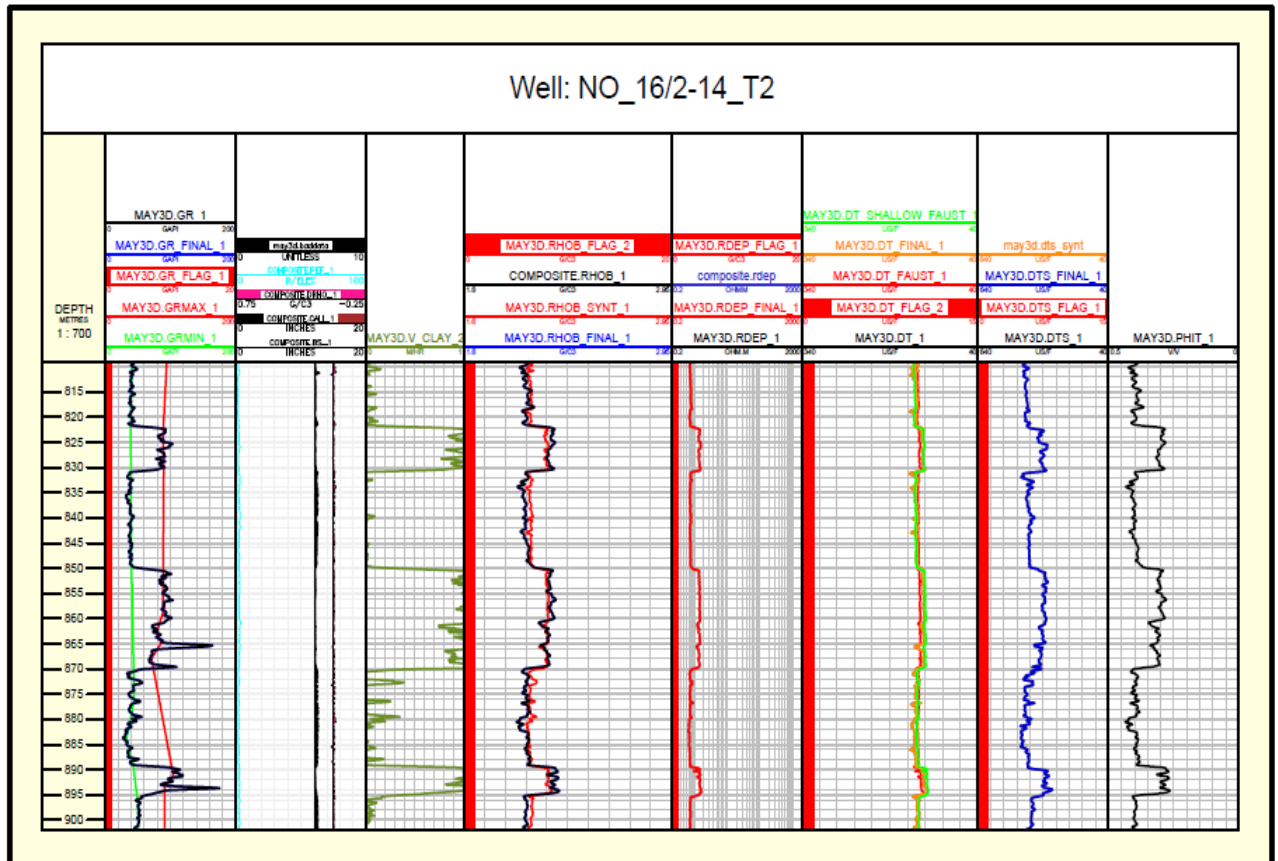


Figure C1. CPI plot showing editing and calculations for the Utsira formation in the well 16/2-14 T2.

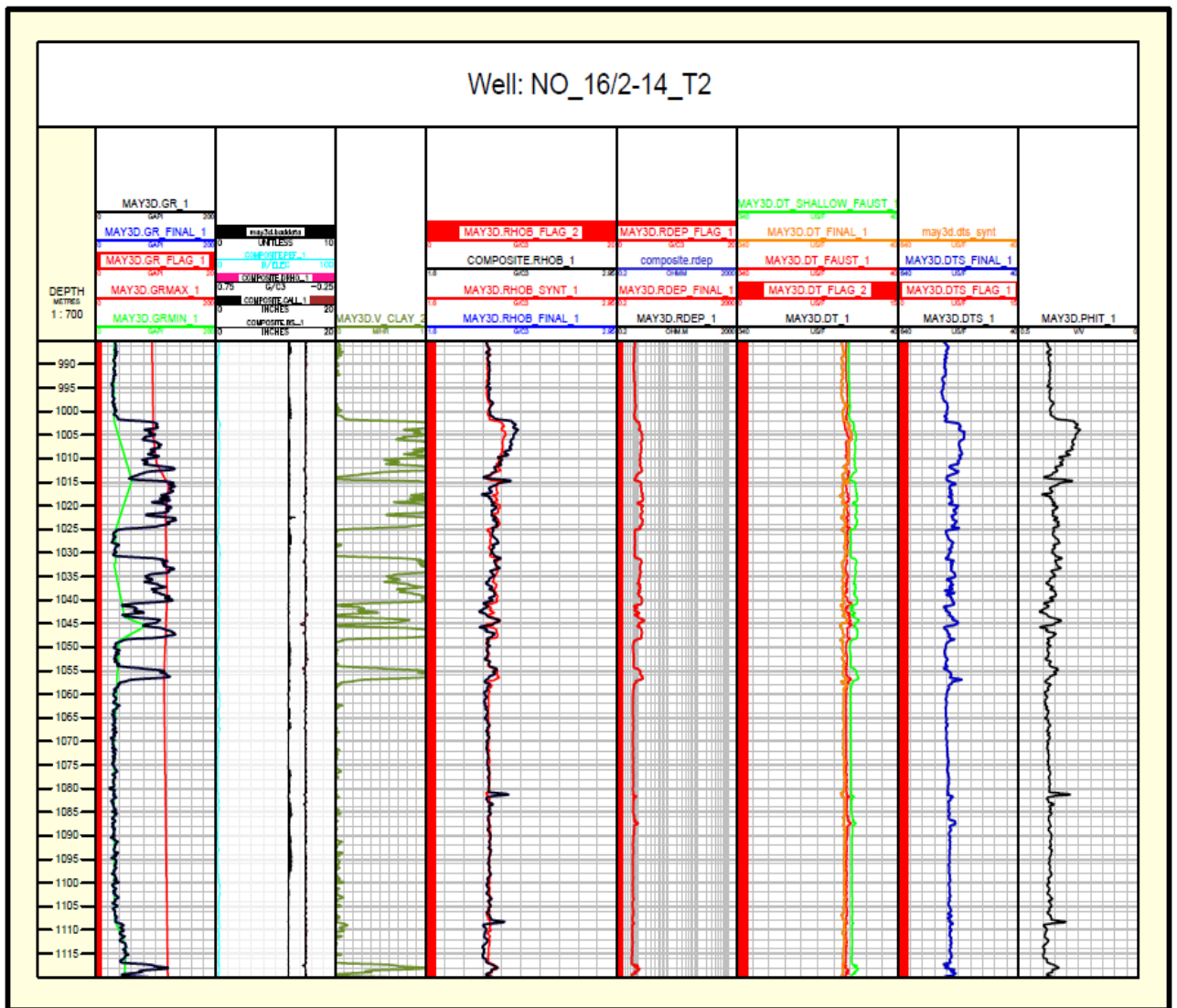


Figure C2. CPI plot showing editing and calculations for the Skade formation in the well 16/2-14 T2.

The Grid formation does not exist in this well, so there is no CPI plot for this formation in this certain well.

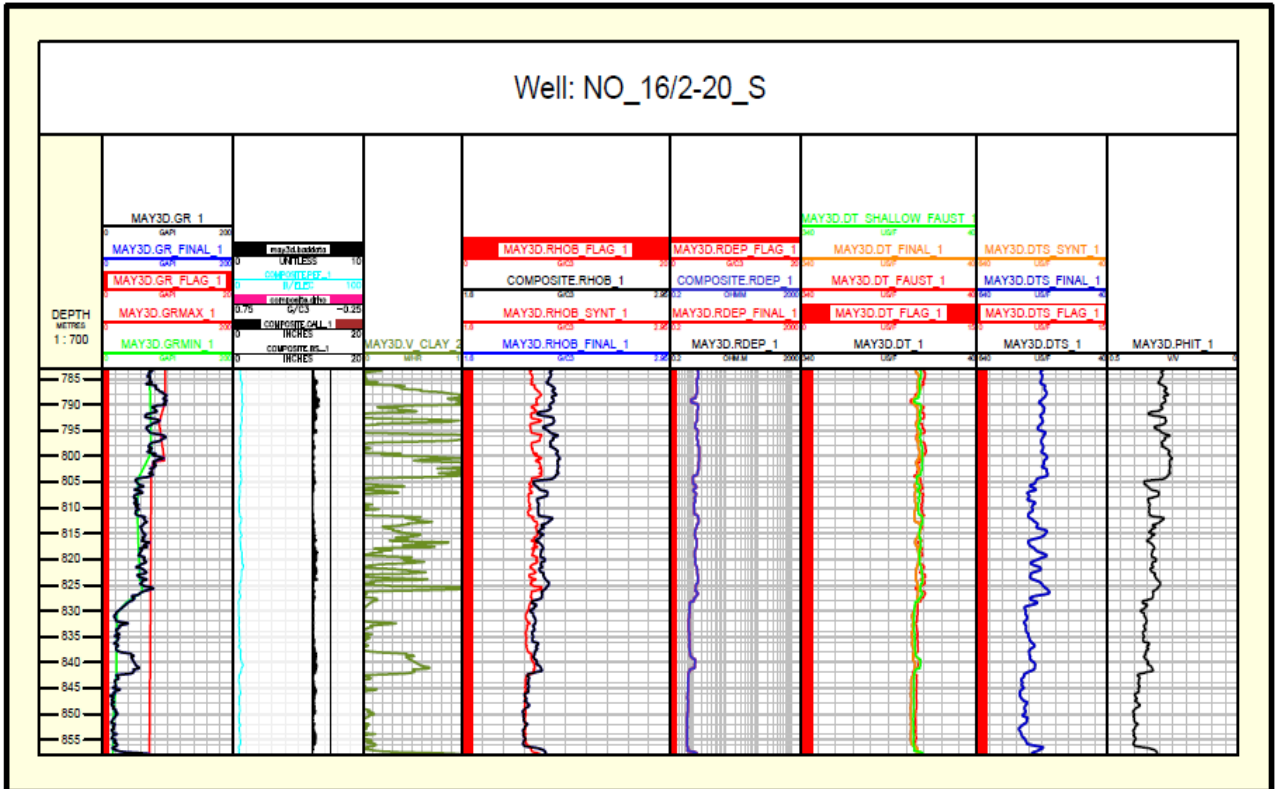


Figure C3. CPI plot showing editing and calculations for the Utsira formation in the well 16/2-20 S.

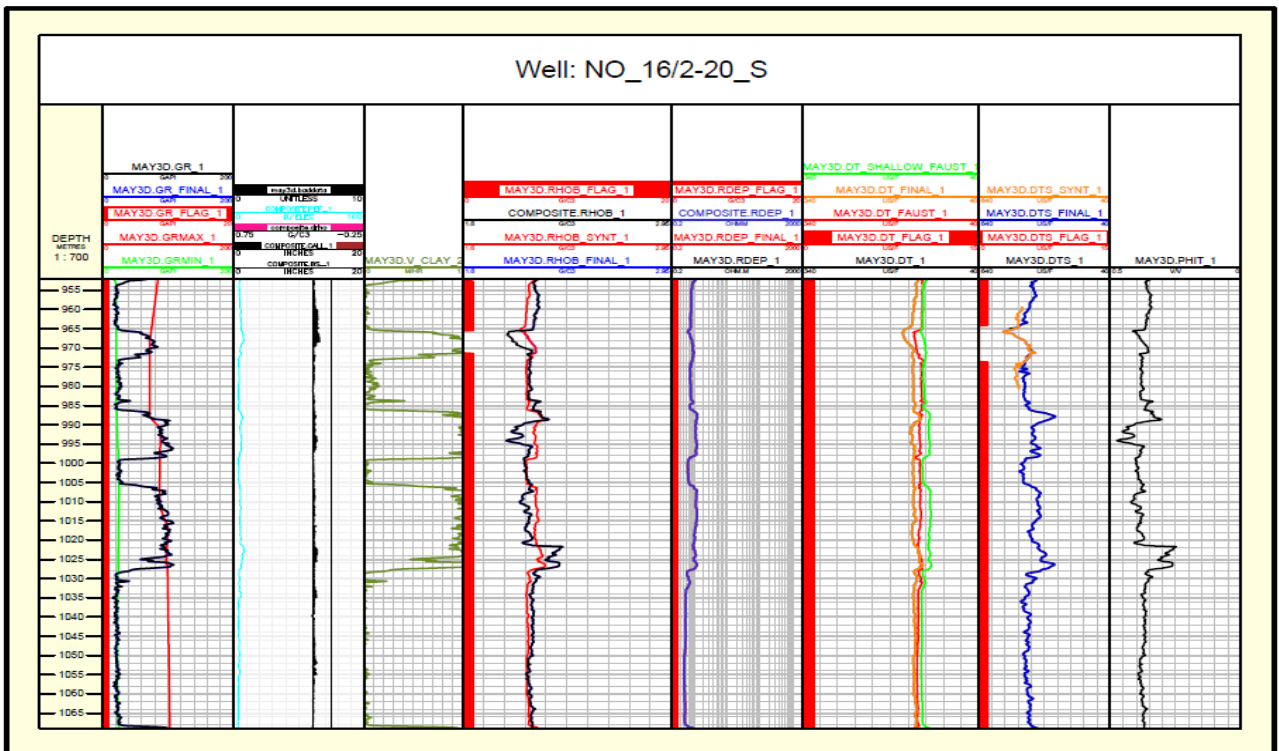


Figure C4. CPI plot showing editing and calculations for the Skade formation in the well 16/2-20 S.

The Grid formation does not exist in well 16/2-20 S and so there is no CPI plot for this formation in this certain well.

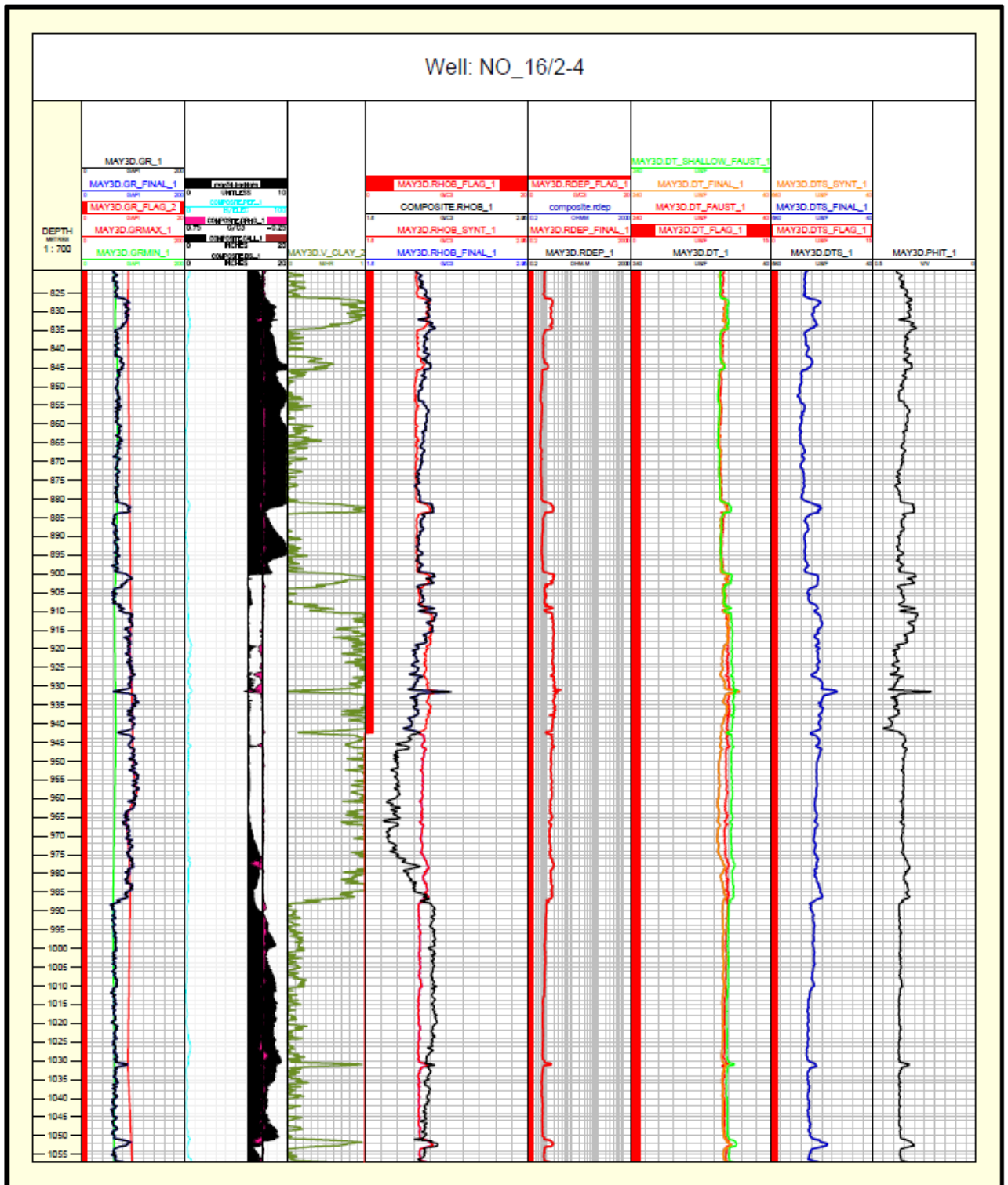


Figure C5. CPI plot showing editing and calculations for the Utsira formation in the well 16/2-4.

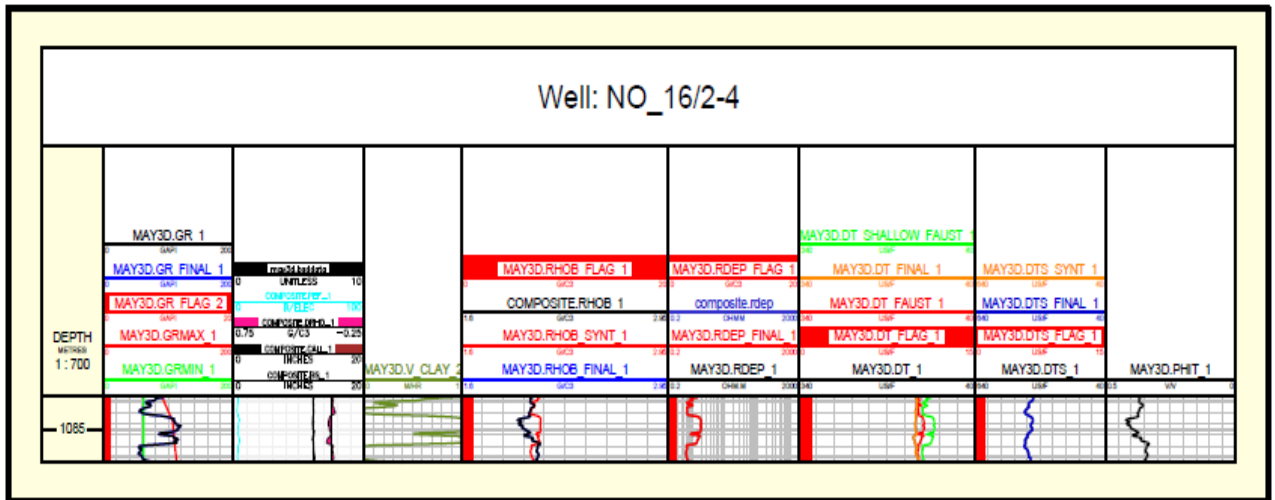


Figure C6. CPI plot showing editing and calculations for the Skade formation in the well 16/2-4.

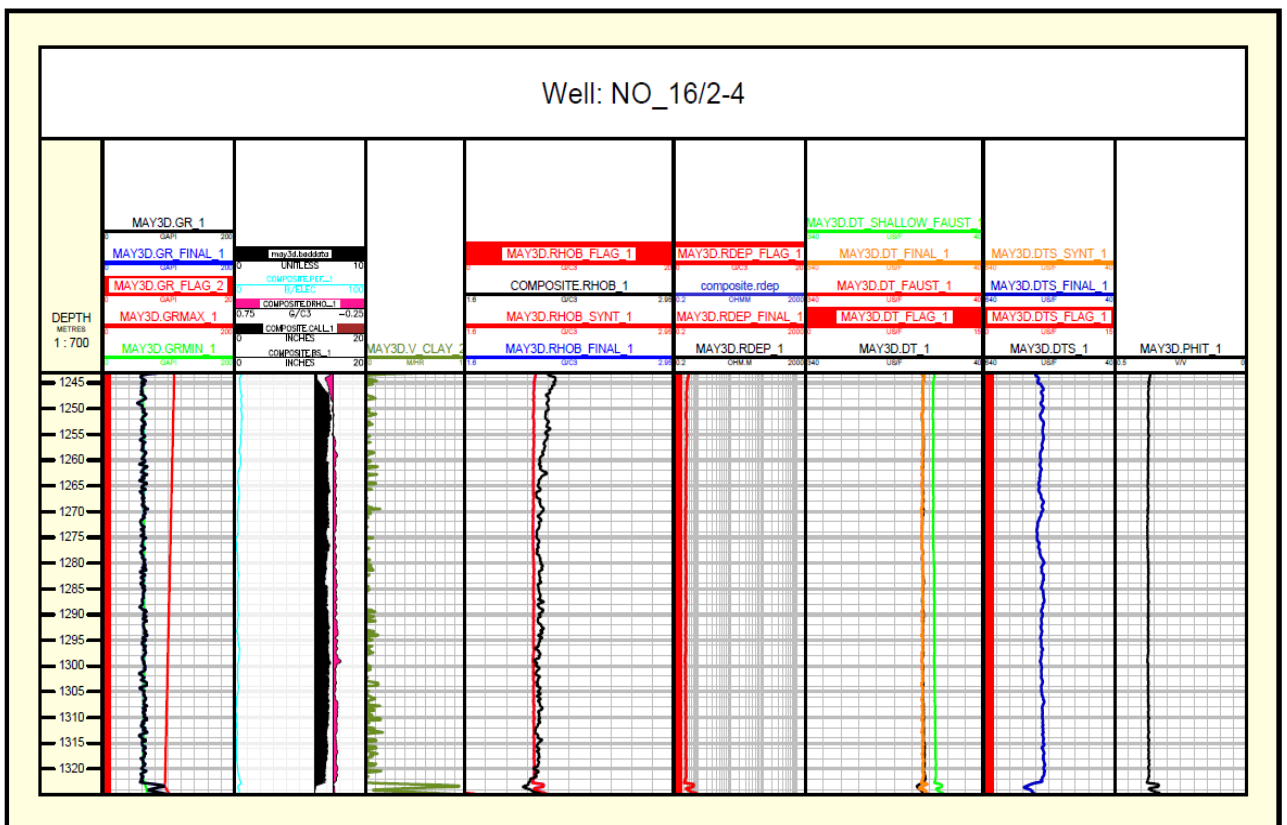


Figure C7. CPI plot showing editing and calculations for the Grid formation in the well 16/2-4.

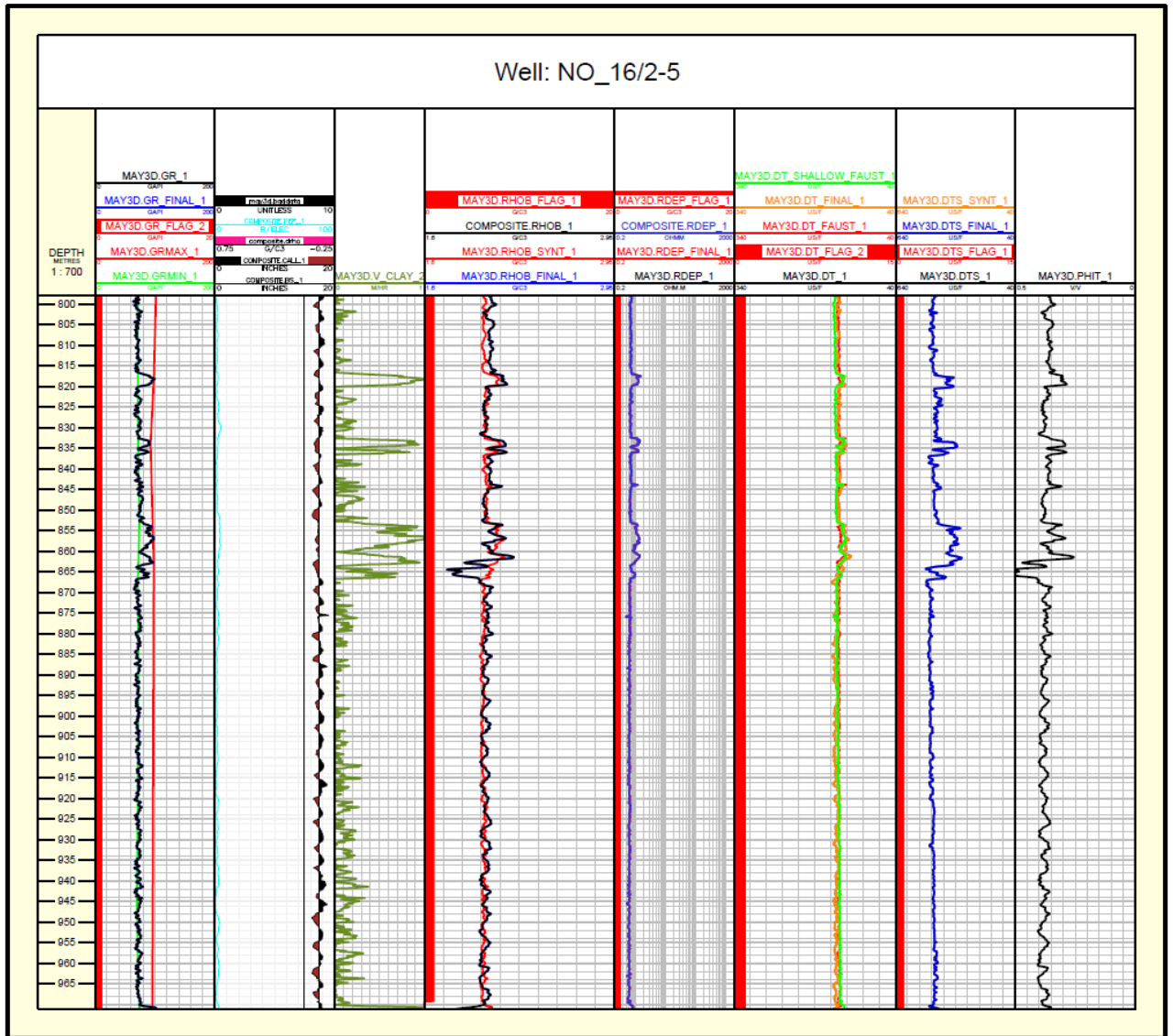


Figure C8. CPI plot showing editing and calculations for the Utsira formation in the well 16/2-5.

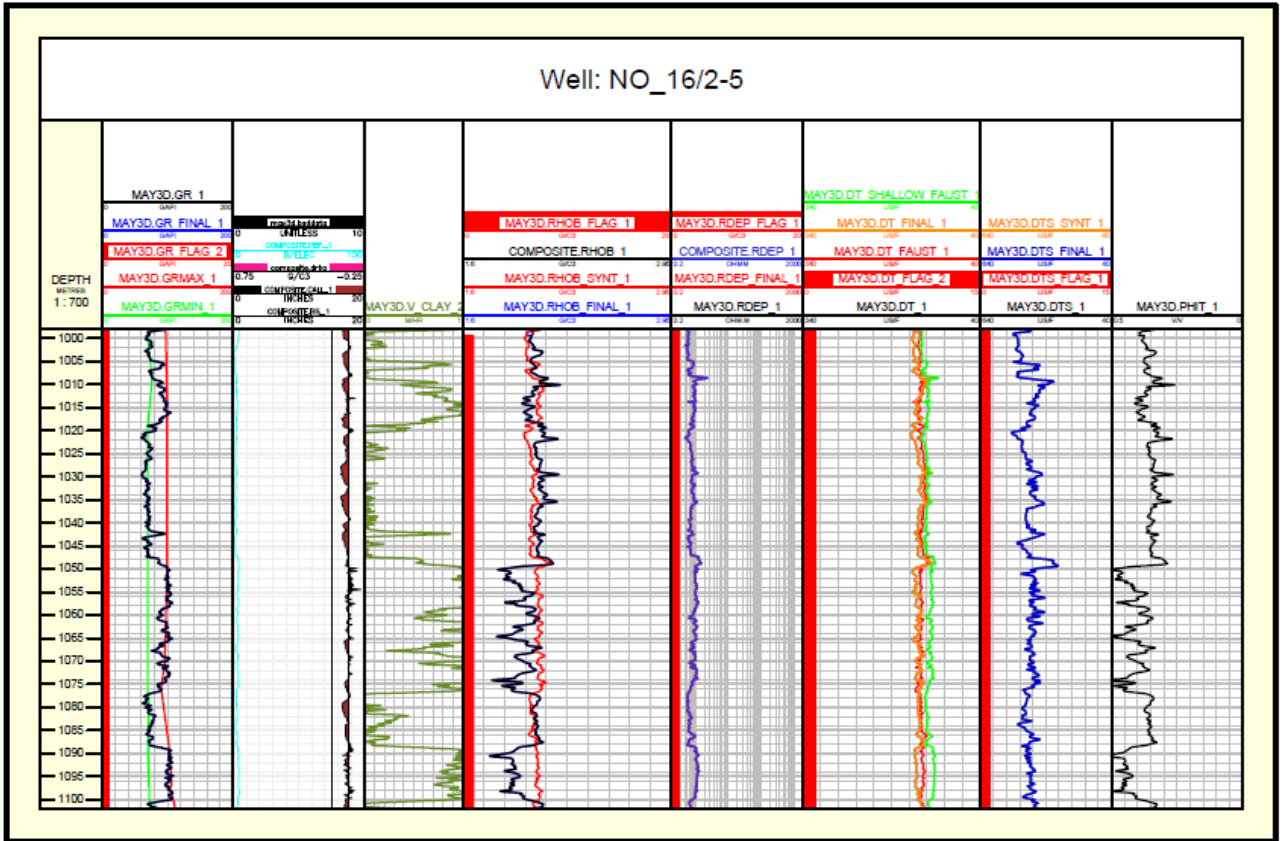


Figure C9. CPI plot showing editing and calculations for the Skade formation in the well 16/2-5.

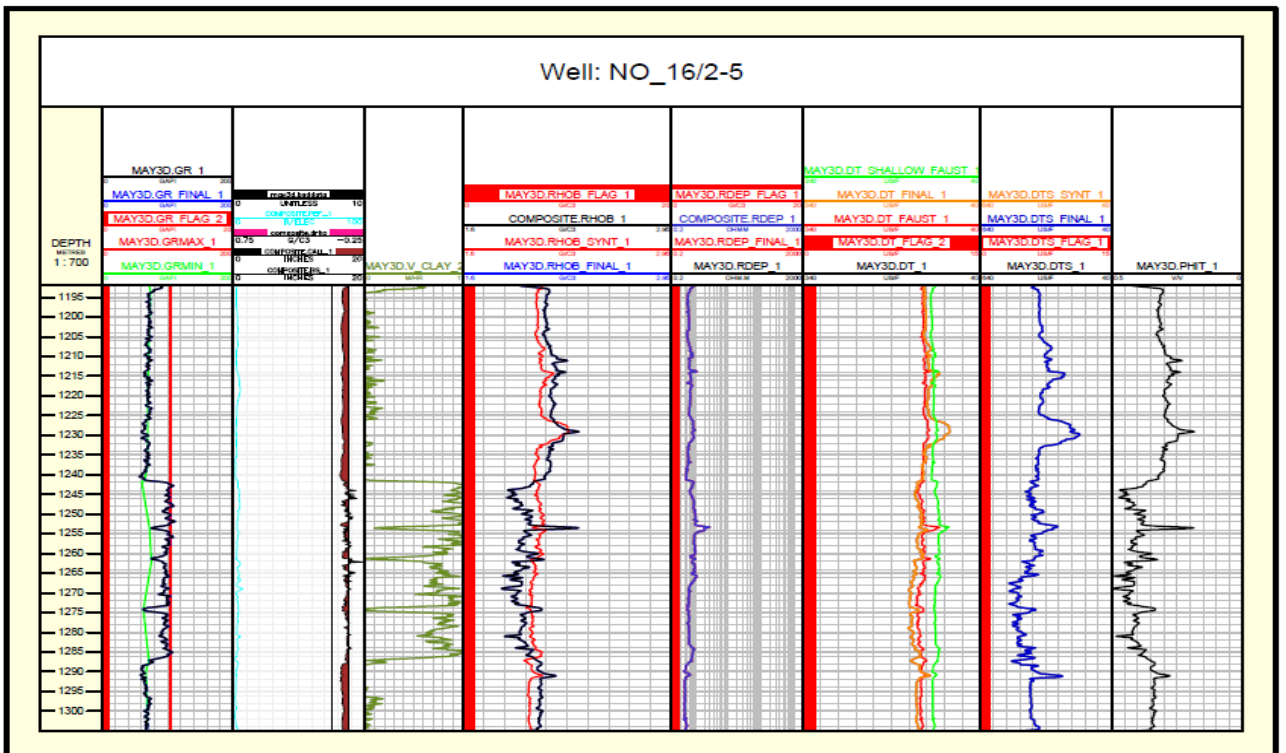


Figure C10. CPI plot showing editing and calculations for the Grid formation in the well 16/2-5.

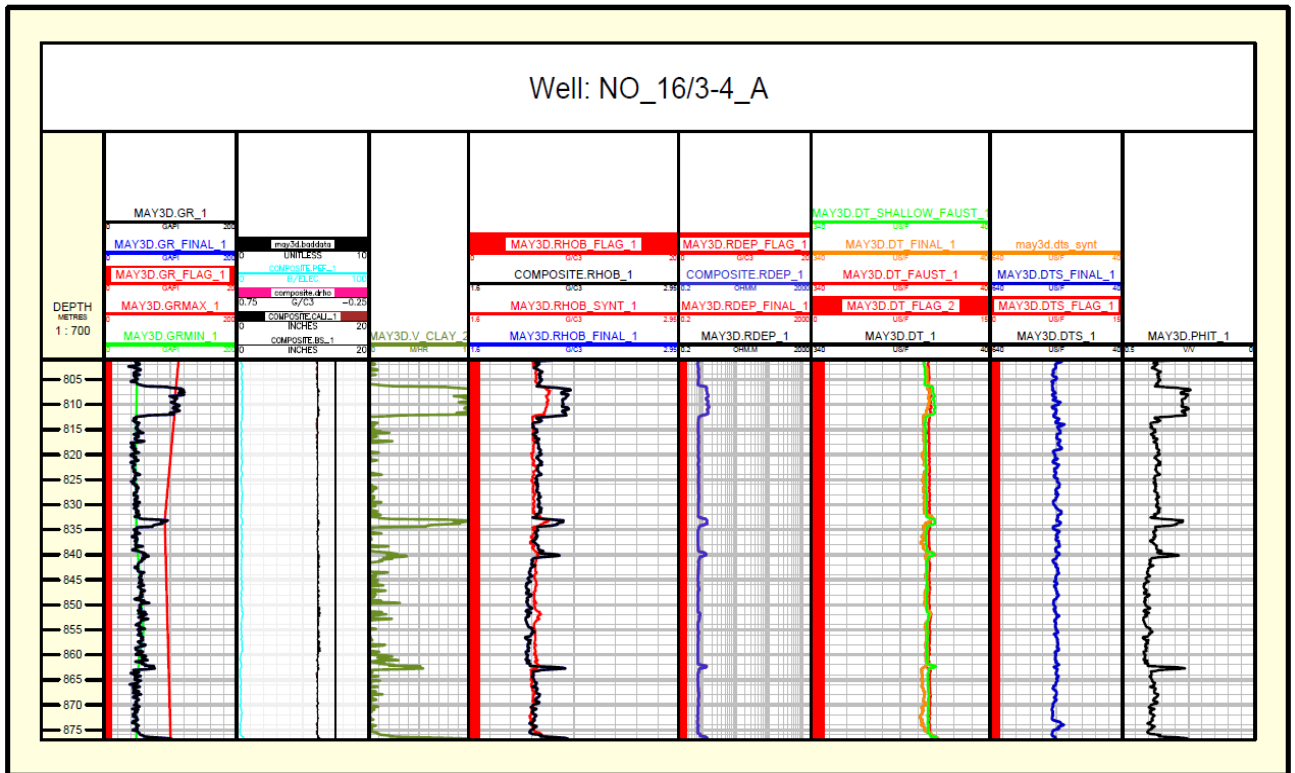


Figure C11. CPI plot showing editing and calculations for the Utsira formation in the well 16/3-4.

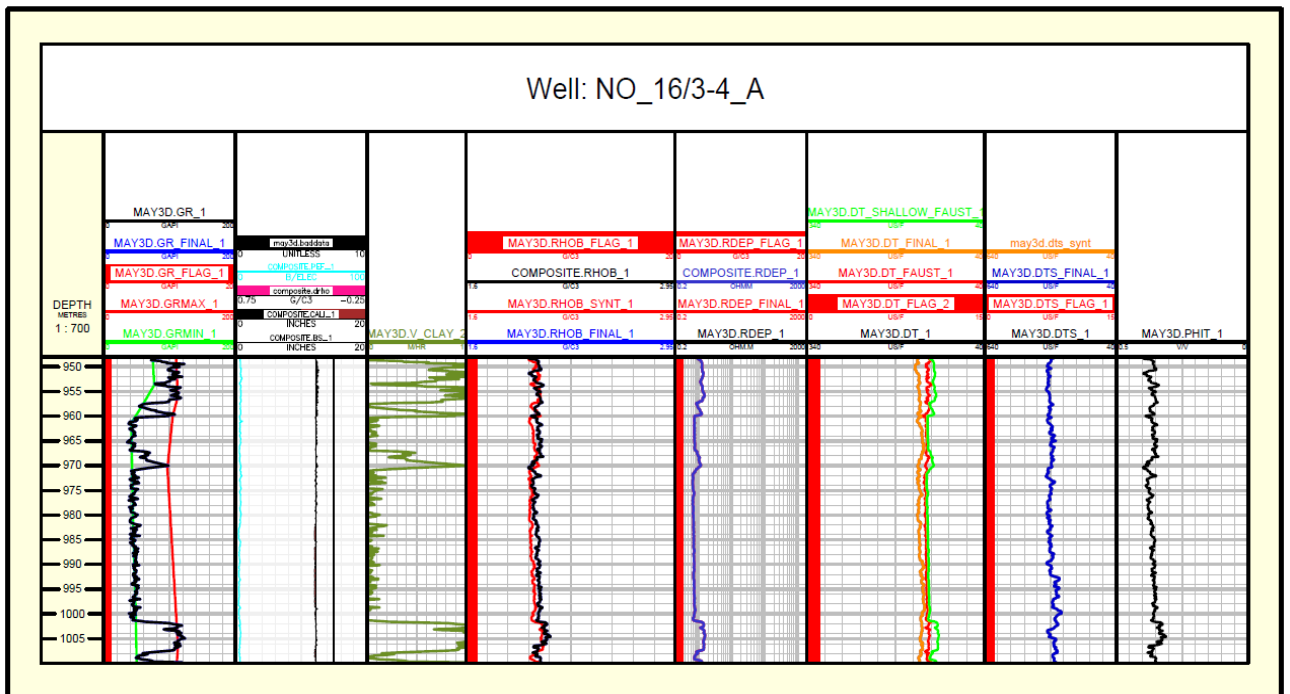


Figure C12. CPI plot showing editing and calculations for the Skade formation in the well 16/3-4.

The Grid formation does not exist in the well 16/3-4 and, thus, there is no CPI for it.

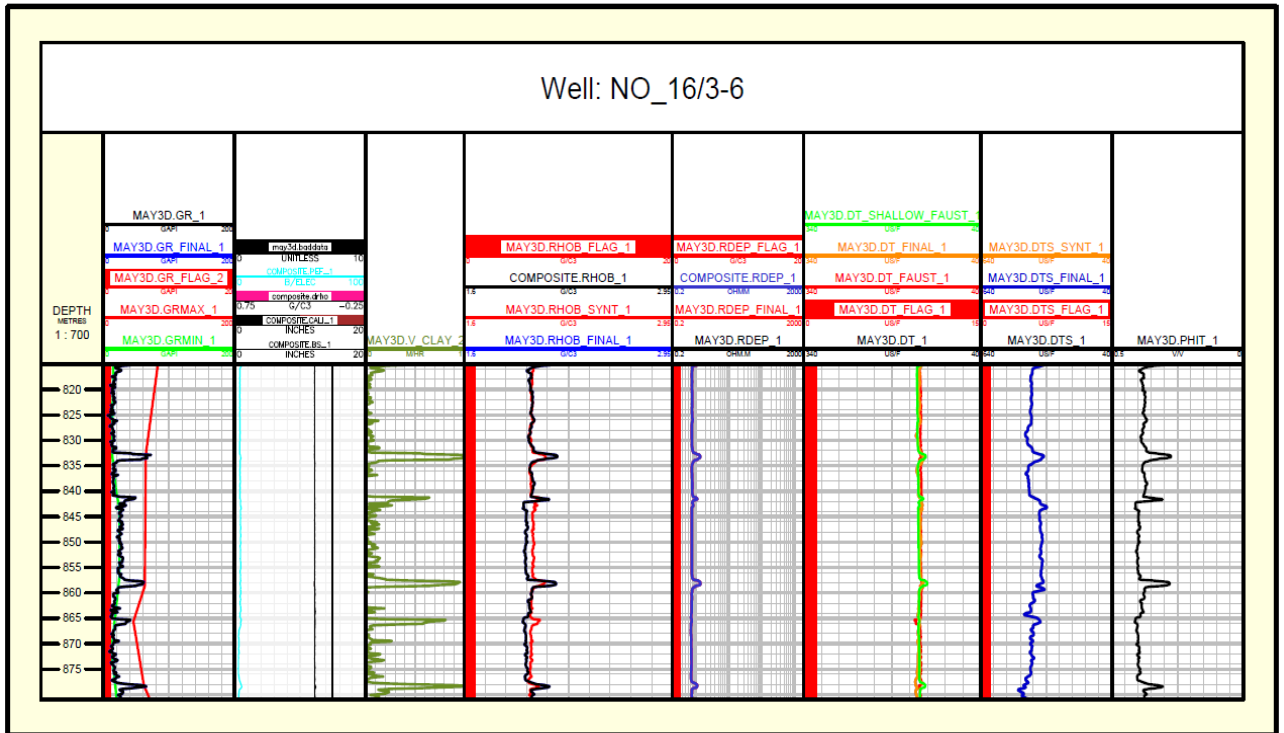


Figure C13. CPI plot showing editing and calculations for the Utsira formation in the well 16/3-6.

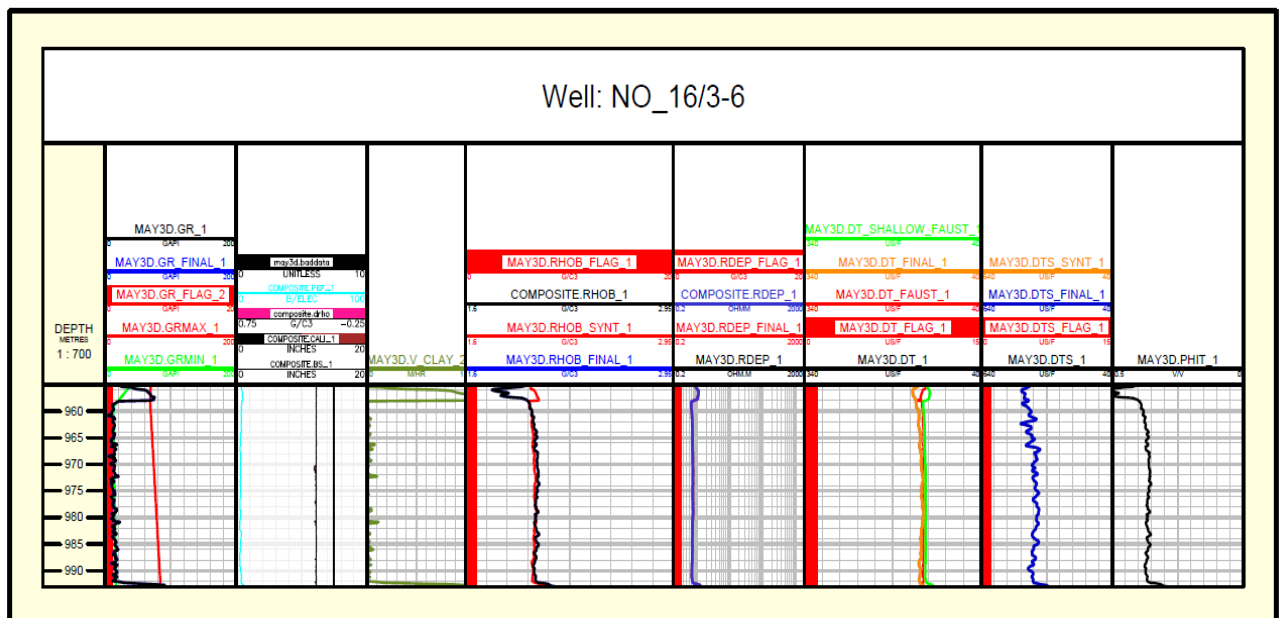


Figure C14. CPI plot showing editing and calculations for the Skade formation in the well 16/3-6.

The Grid formation does not exist in the well 16/3-6 and there is no CPI plot showing it.

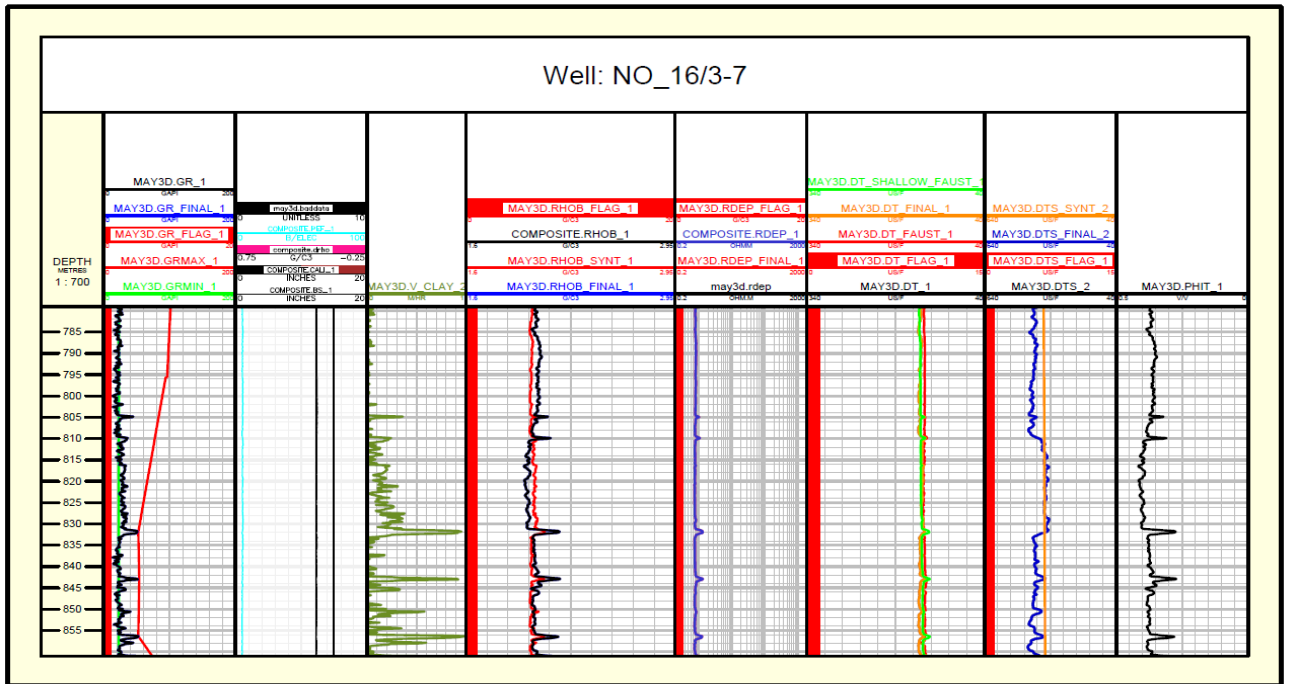


Figure C15. CPI plot showing editing and calculations for the Utsira formation in the well 16/3-7.

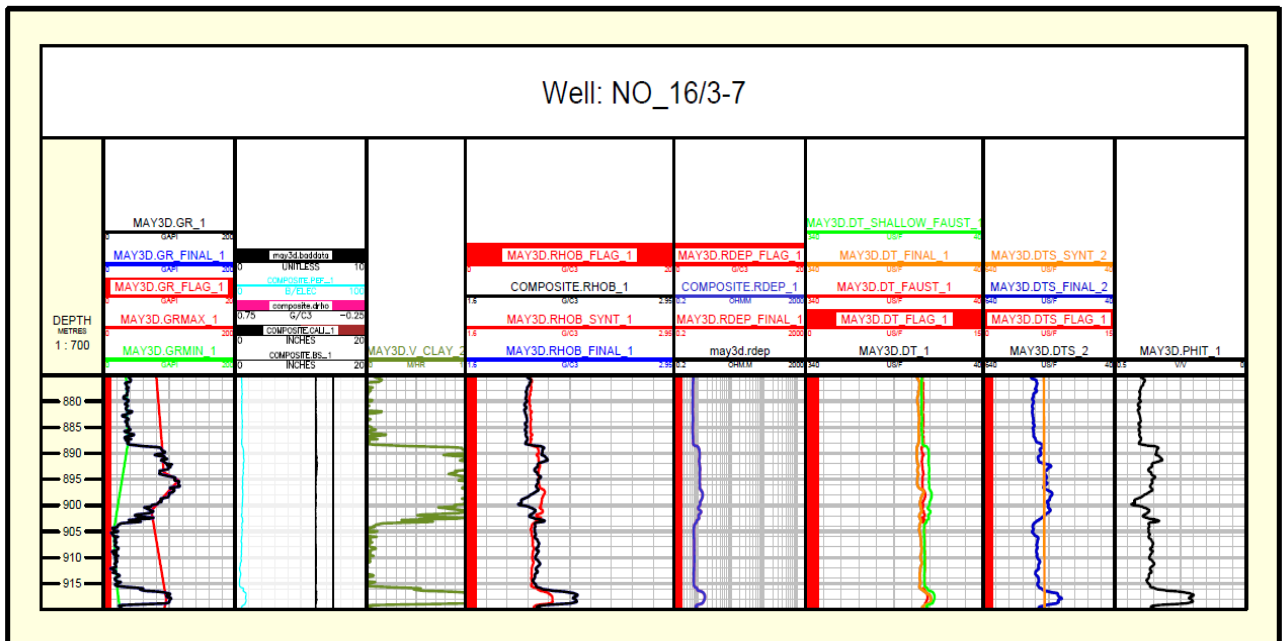


Figure C16. CPI plot showing editing and calculations for the Skade formation in the well 16/3-7.

The Grid formation does not exist in this well as well, thus, there is no CPI plot for it.

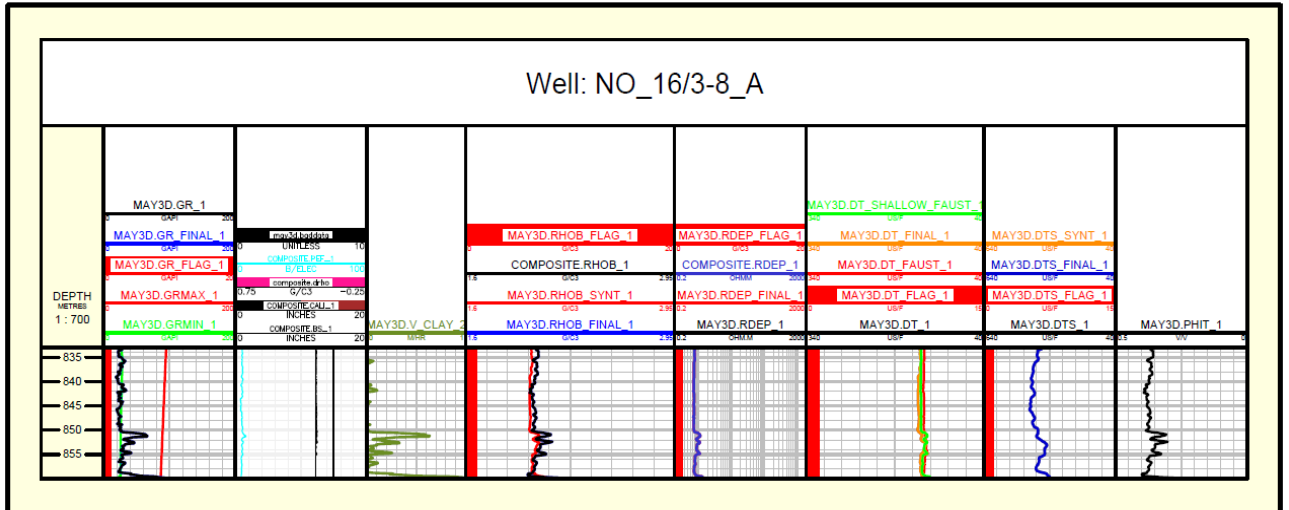


Figure C17. CPI plot showing editing and calculations for the Utsira formation in the well 16/3-8 A.

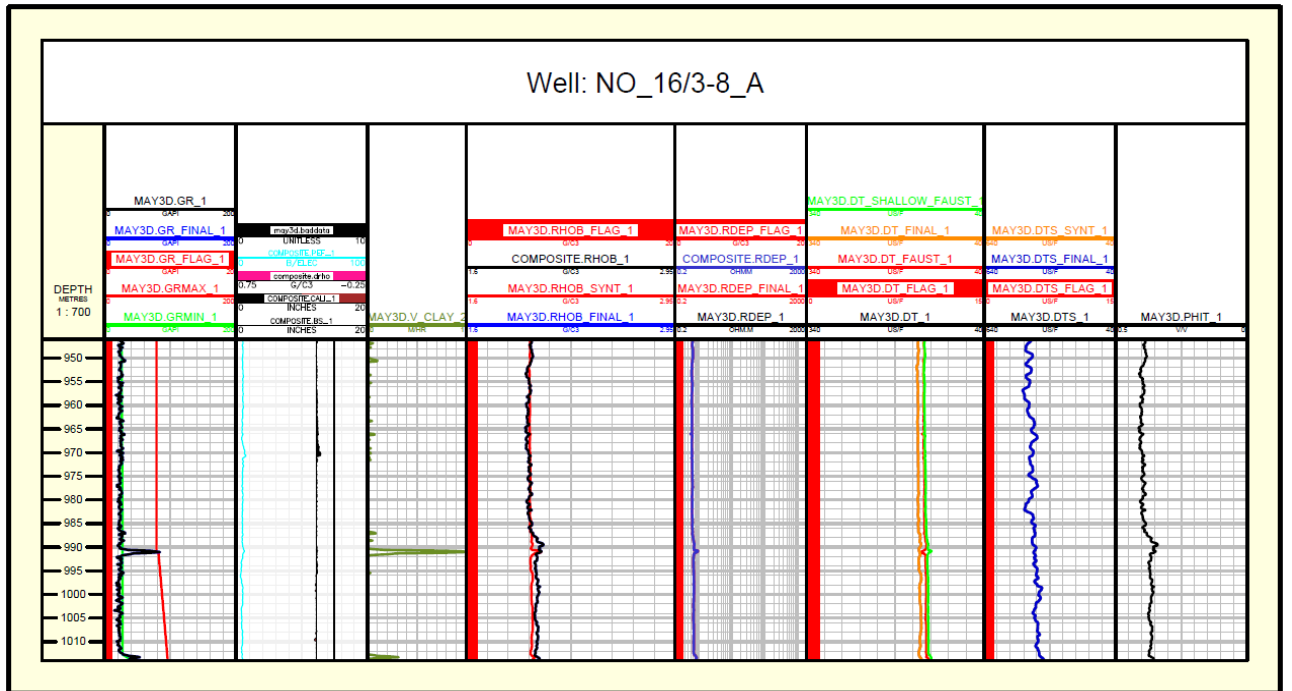


Figure C18. CPI plot showing editing and calculations for the Skade formation in the well 16/3-8 A.

The Grid formation does not exist in this well and there is no CPI plot showing it.

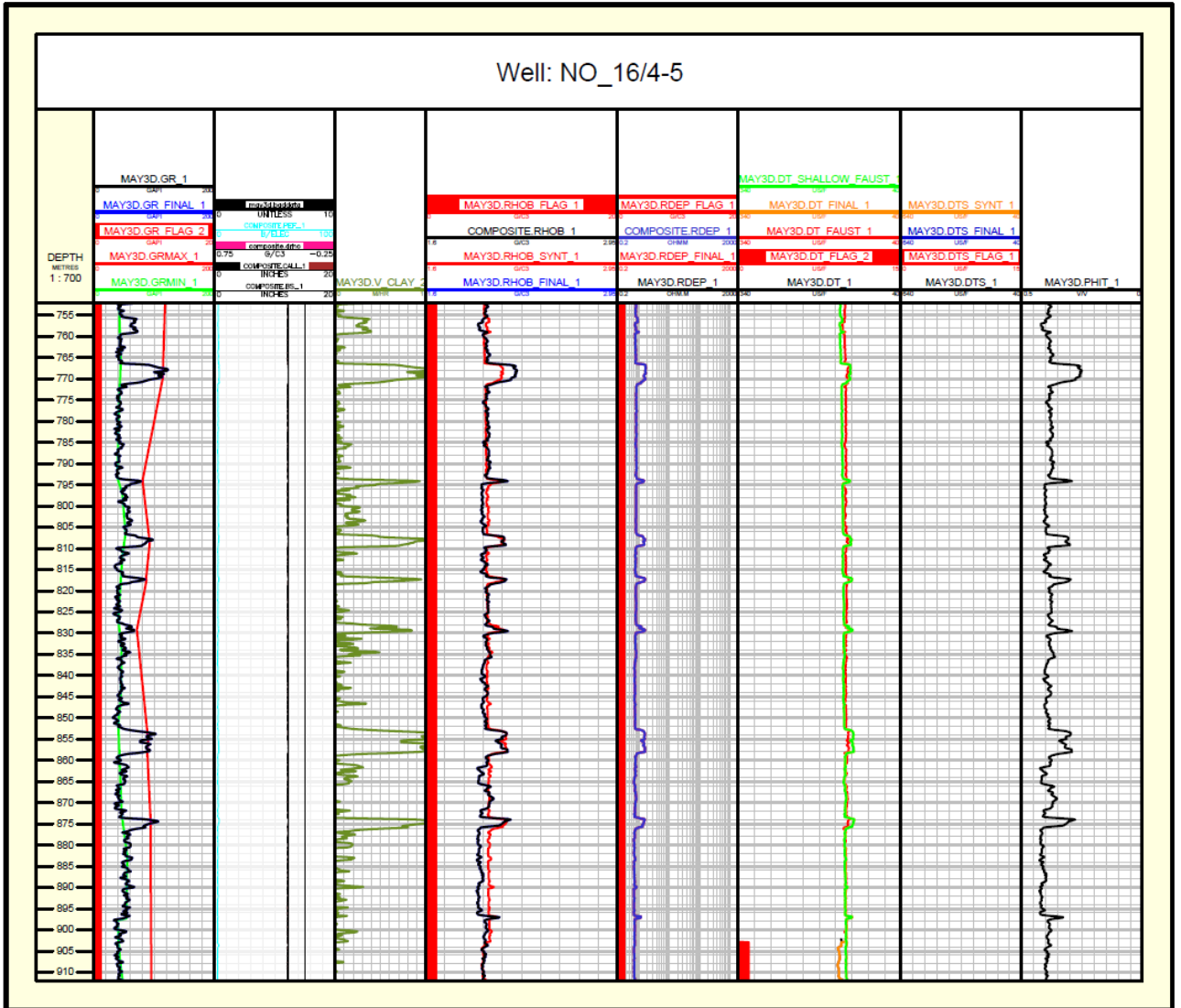


Figure C19. CPI plot showing editing and calculations for the Utsira formation in the well 16/4-5.

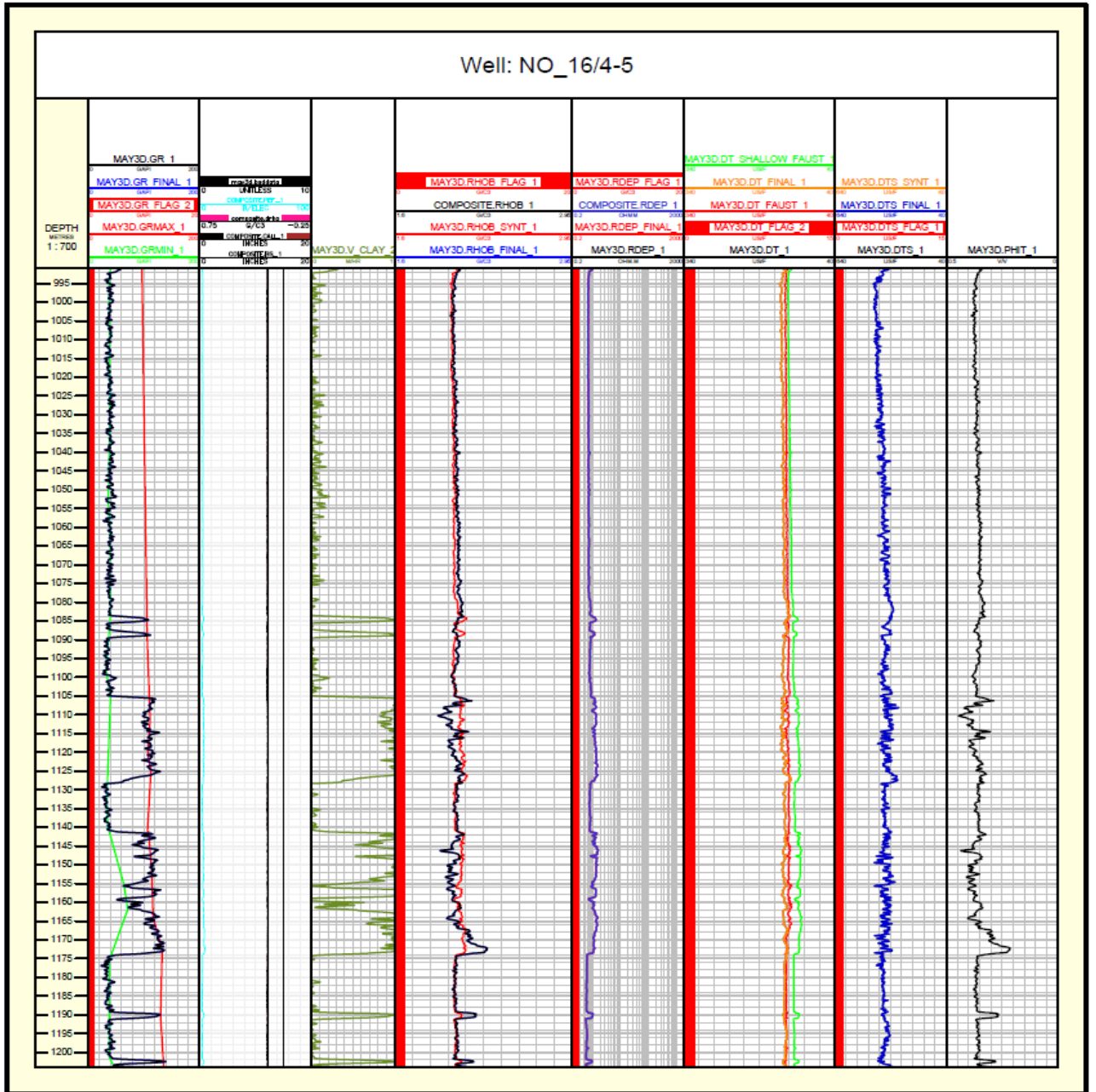


Figure C20. CPI plot showing editing and calculations for the Skade formation in the well 16/4-5.

The Grid formation does not present in this particular well and there is no CPI plot for it.

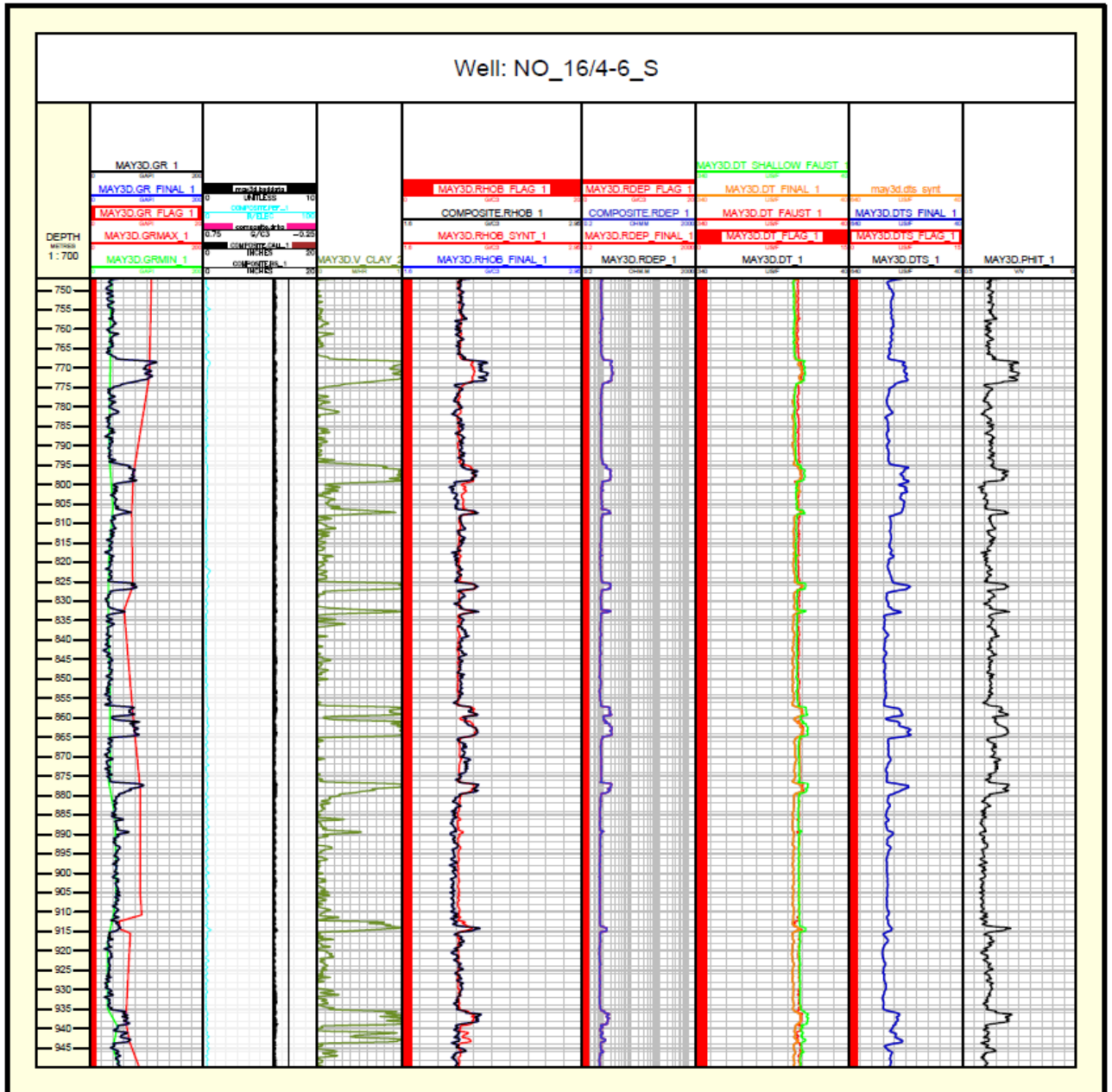


Figure C21. CPI plot showing editing and calculations for the Utsira formation in the well 16/4-6 S.

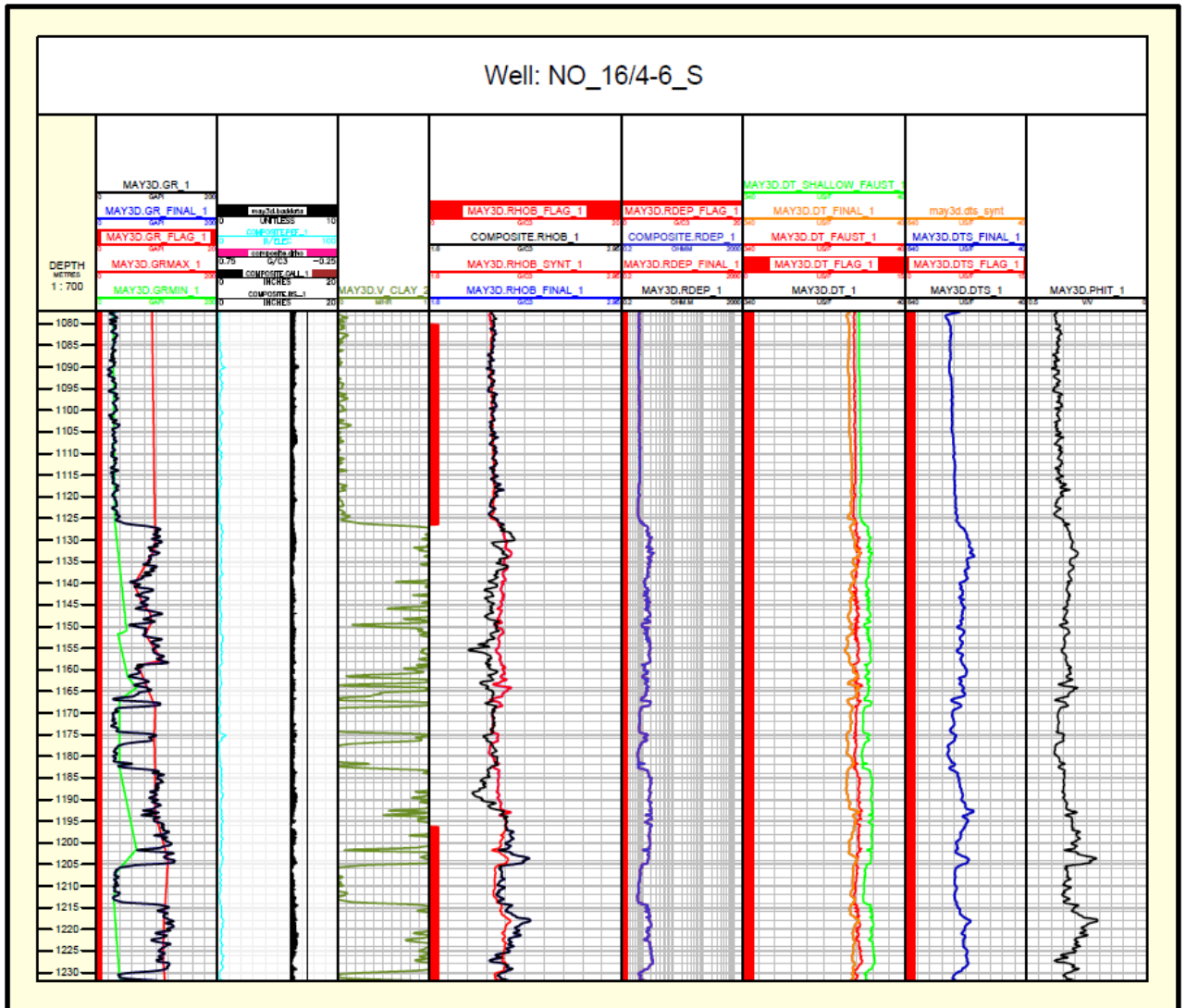


Figure C22. CPI plot showing editing and calculations for the Skade formation in the well 16/4-6 S.

The Grid formation does not exist in the wells 16/4-6 S and 16/5-4 and there is no CPI plots showing Grid formation in these particular wells as well.

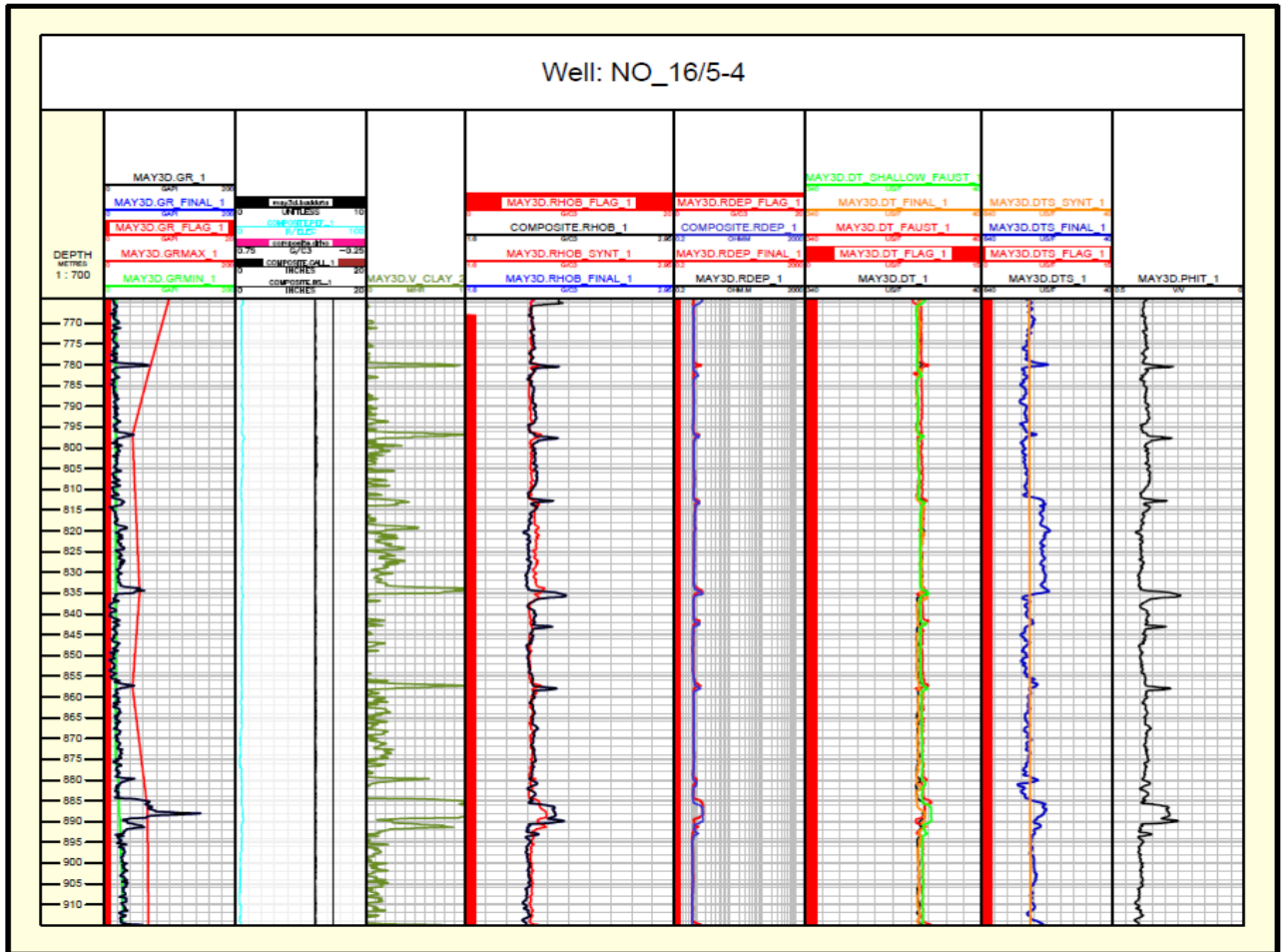


Figure C23. CPI plot showing editing and calculations for the Utsira formation in the well 16/5-4.

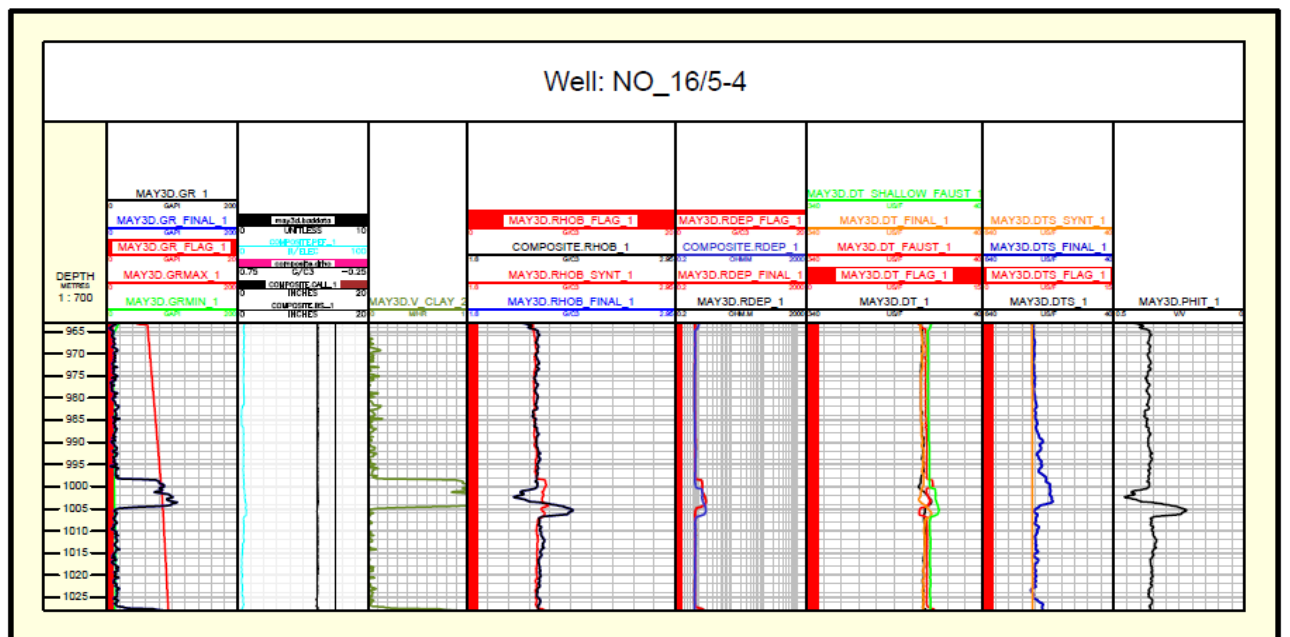


Figure C24. CPI plot showing editing and calculations for the Skade formation in the well 16/5-4.

Appendix D. CPI plots showing DT and DTS calculated based on the first and second sonic models for the Utsira, Skade and Grid formations – optimization is based on all wells

There are CPI plots showing DT and DTS calculated using the first and second sonic models optimized for all 12 wells simultaneously for the Utsira, Skade and Grid formations. In the Section 6.9 we presented CPI plots for the one particular well 16/2-12. The remaining CPIs are shown below. We should mention that Grid formation exists only in wells 16/2-4 and 16/2-5. Hence, only for these certain wells we presented CPIs for all three sand formations.

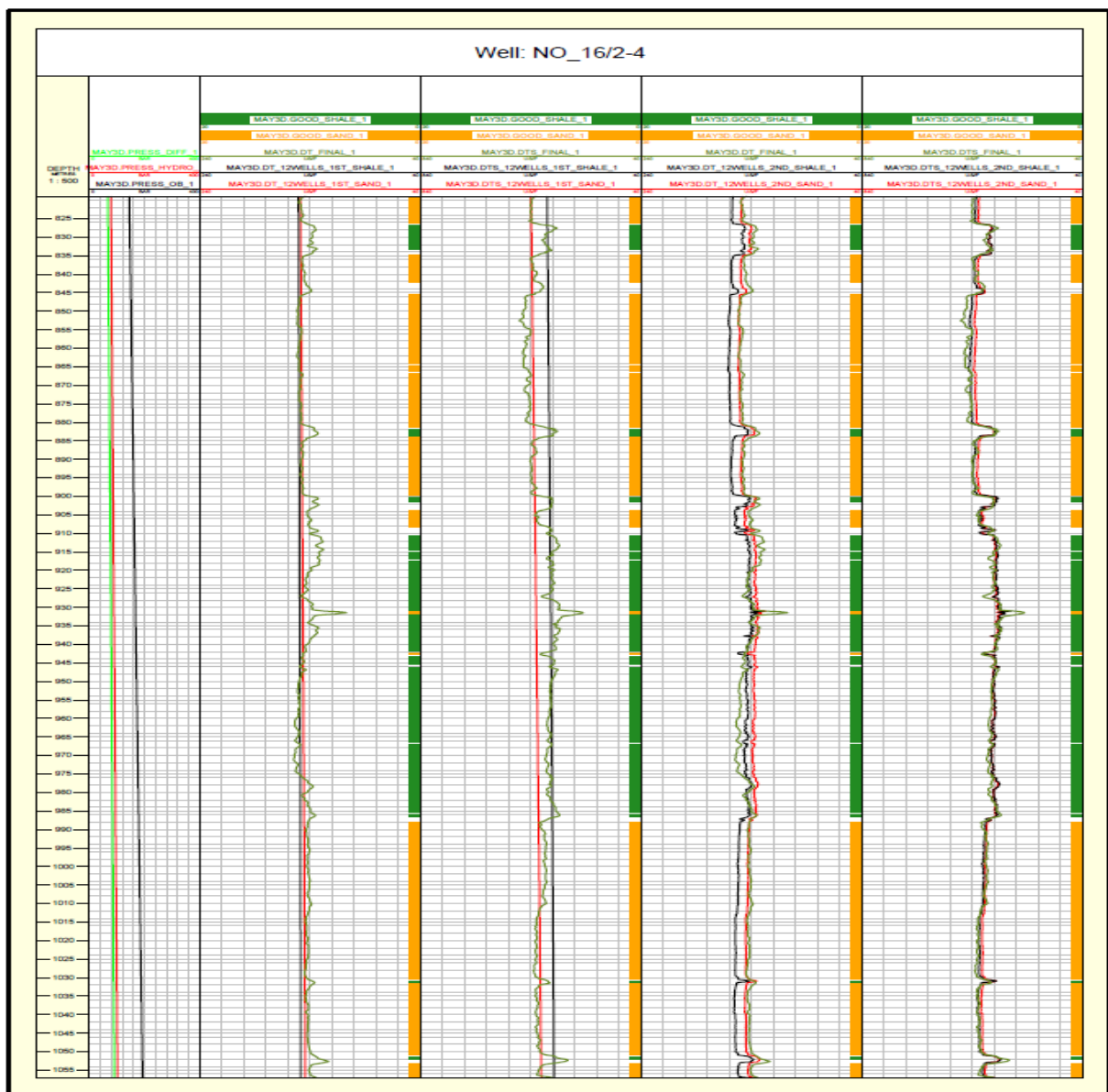


Figure D1. DT and DTS calculated based on the first and second sonic for the Utsira formation in the well 16/2-4. The optimization was based on all wells together.

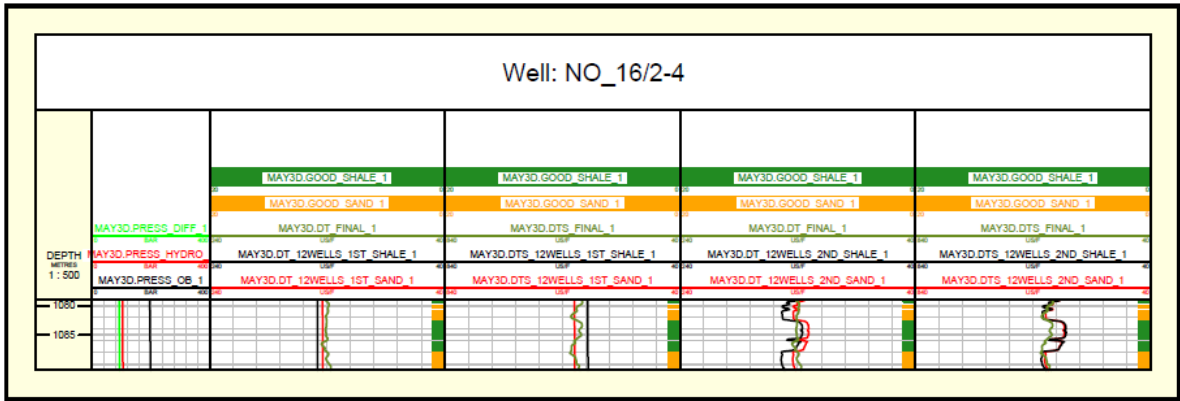


Figure D2. DT and DTS calculated based on the first and second sonic for the Skade formation in the well 16/2-4. The optimization was based on all wells together.

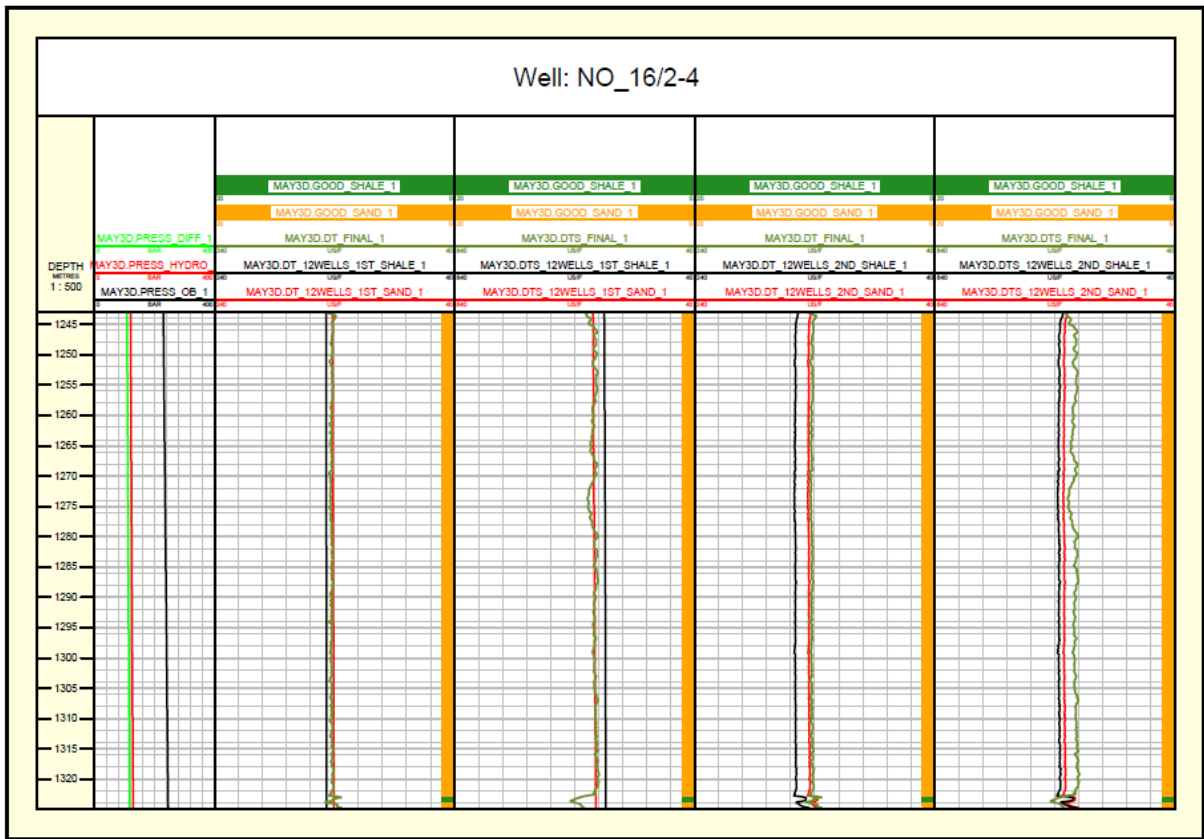


Figure D3. DT and DTS calculated based on the first and second sonic for the Grid formation in the well 16/2-4. The optimization was based on wells together.

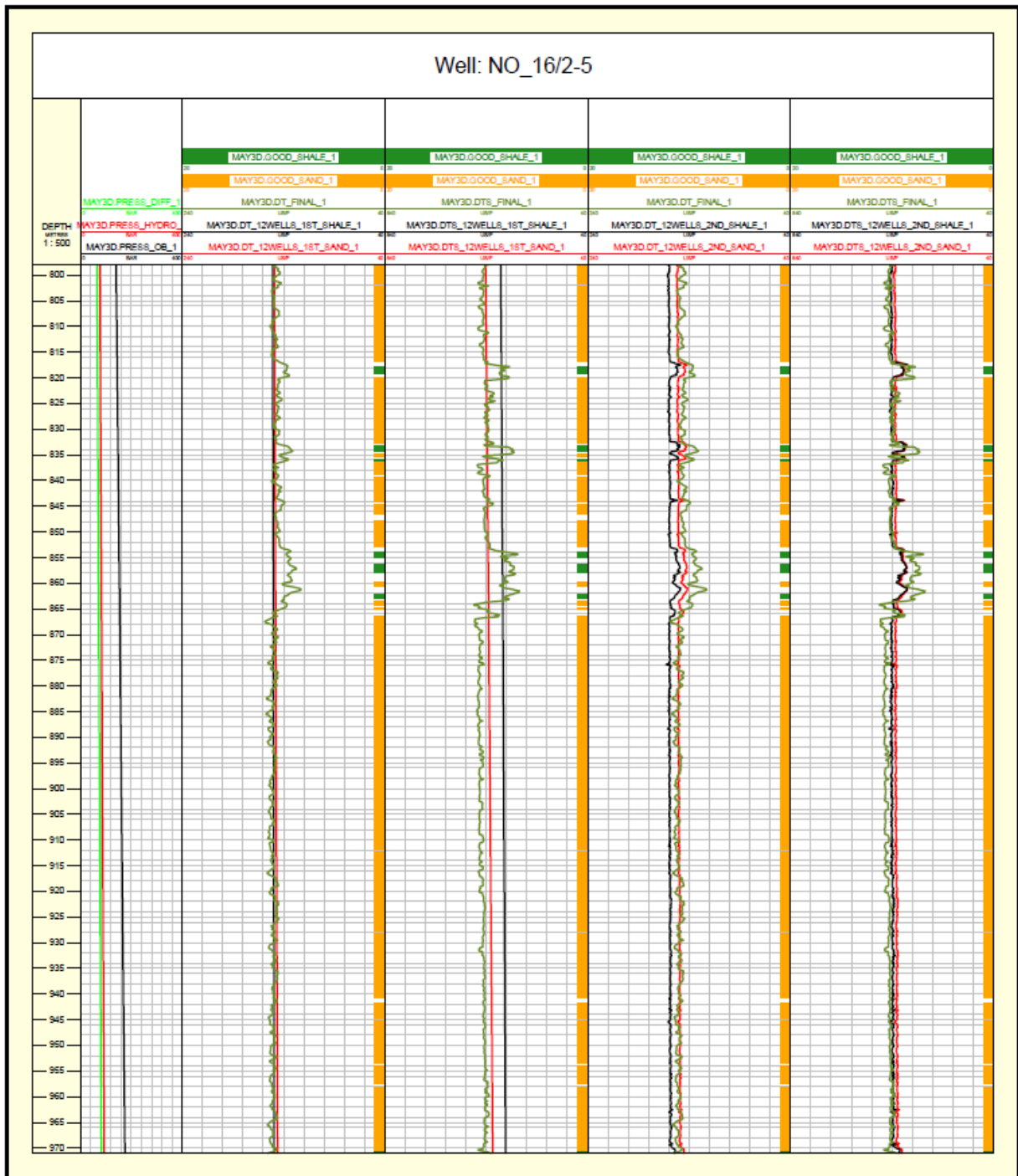


Figure D4. DT and DTS calculated based on the first and second sonic for the Utsira formation in the well 16/2-5. The optimization was based on all wells together.

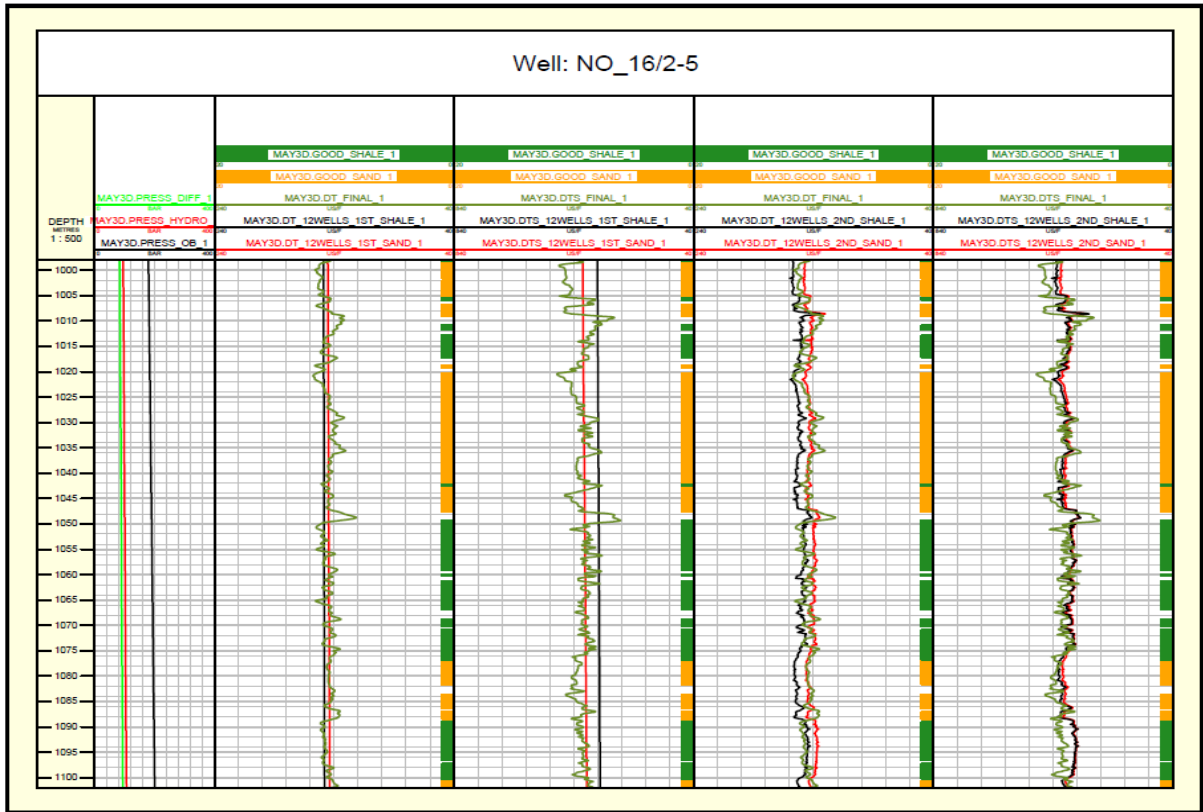


Figure D5. DT and DTS calculated based on the first and second sonic for the Skade formation in the well 16/2-5. The optimization was based on all wells together.

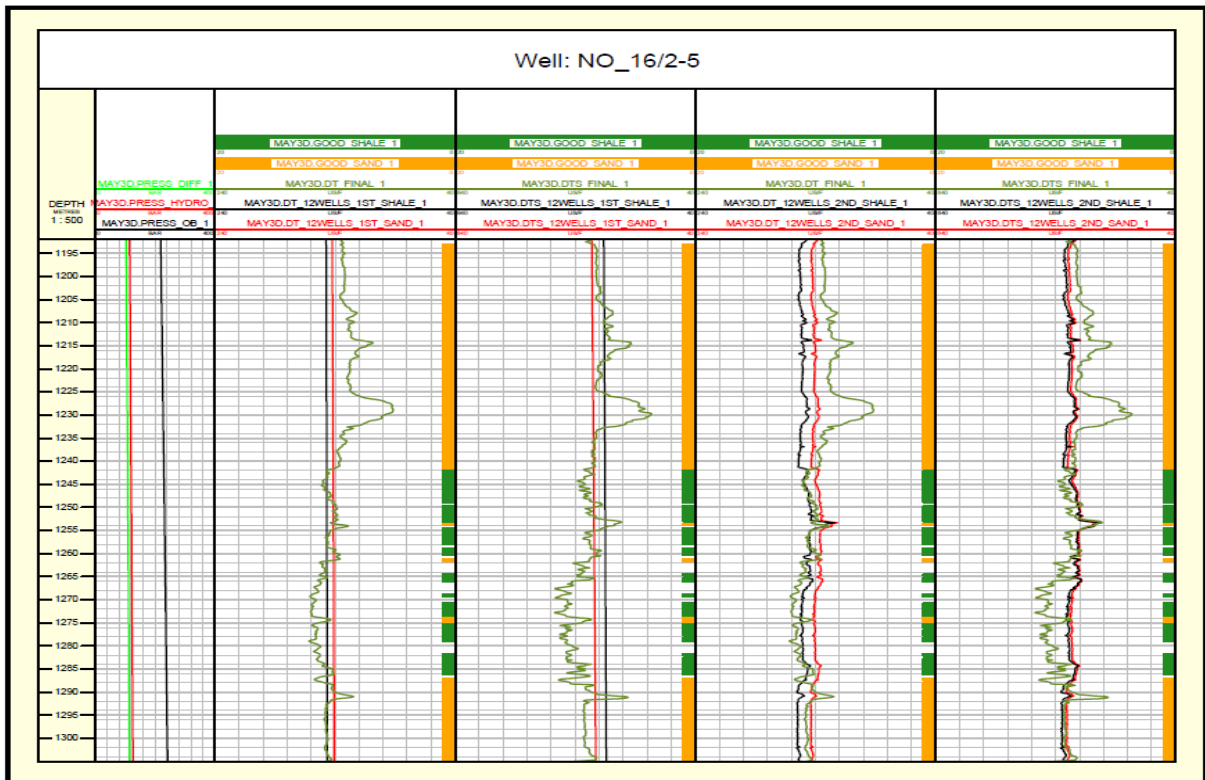


Figure D6. DT and DTS calculated based on the first and second sonic for the Grid formation in the well 16/2-5. The optimization was based on all wells together.

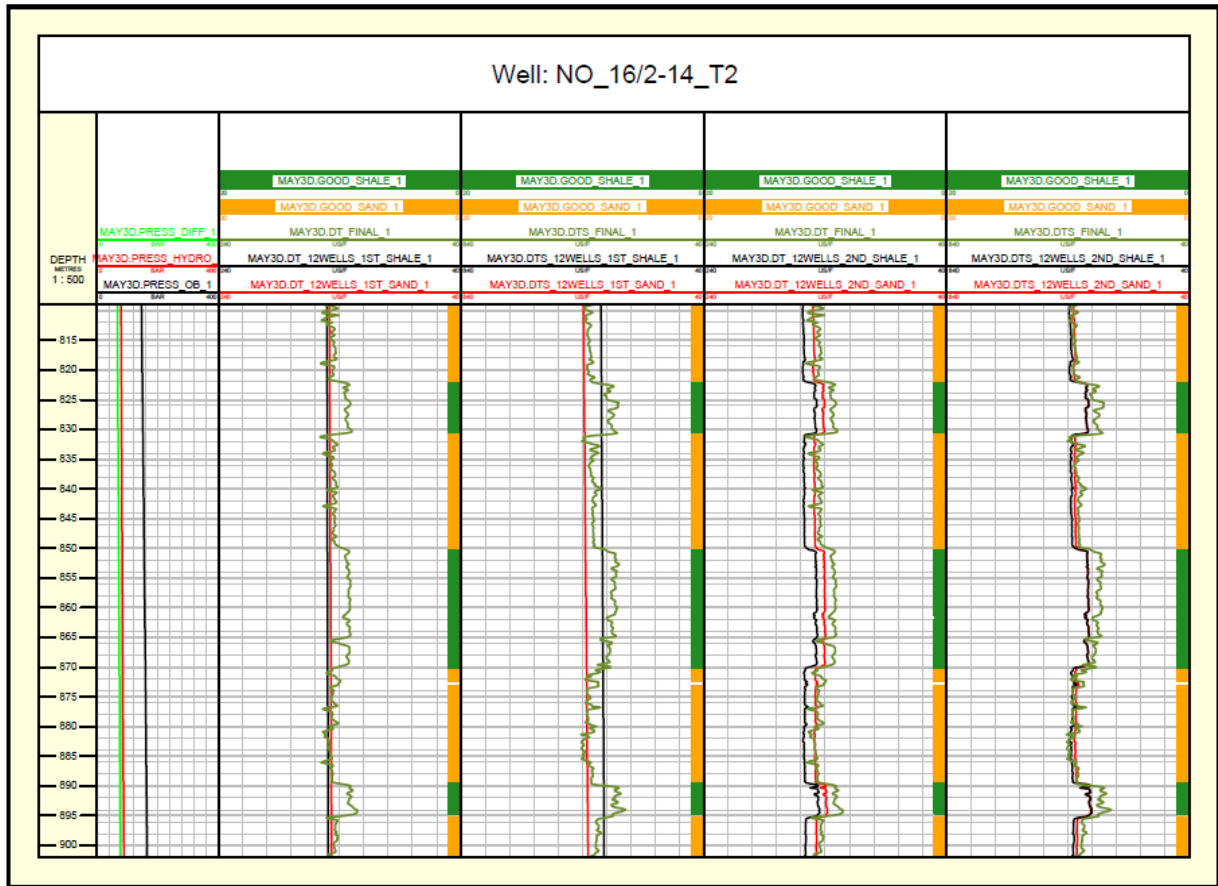


Figure D7. DT and DTS calculated based on the first and second sonic models for the Utsira formation in the well 16/2-14 T2. The optimization was based on wells together.

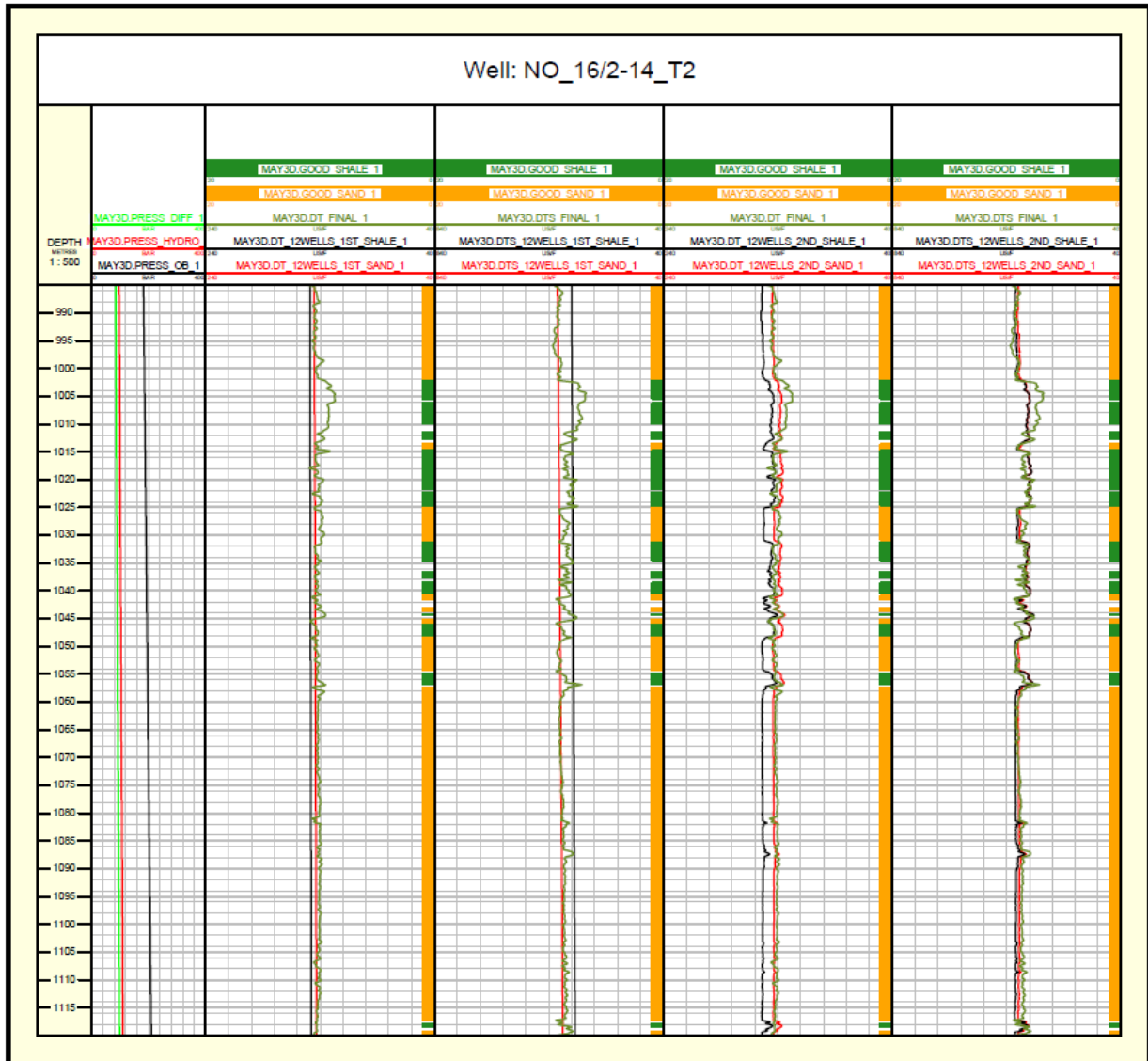


Figure D8. DT and DTS calculated based on the first and second sonic models for the Skade formation in the well 16/2-14 T2. The optimization was based on all wells together.

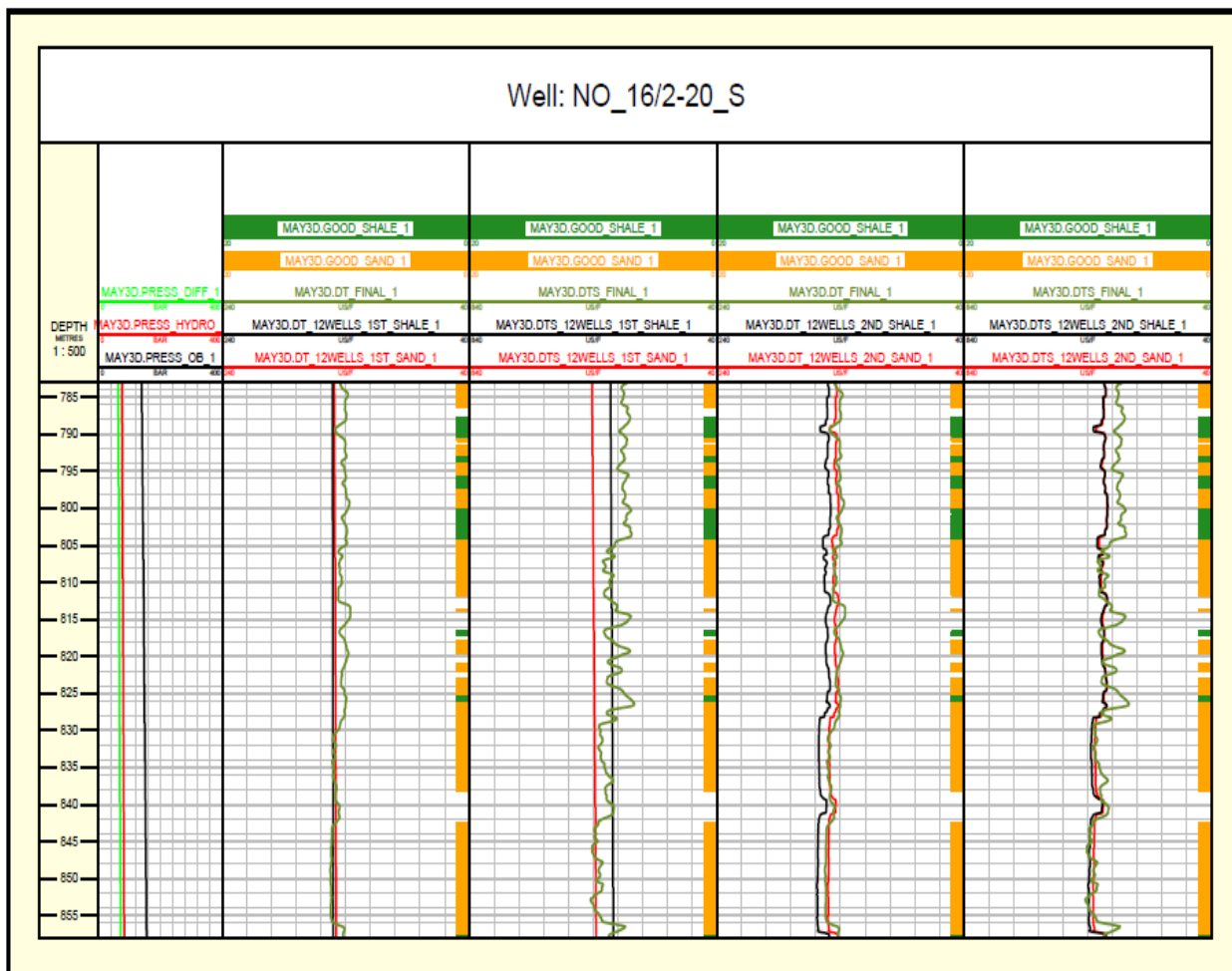


Figure D9. DT and DTS calculated based on the first and second sonic models for the Utsira formation in the well 16/2-20 S. The optimization was based on all wells together.

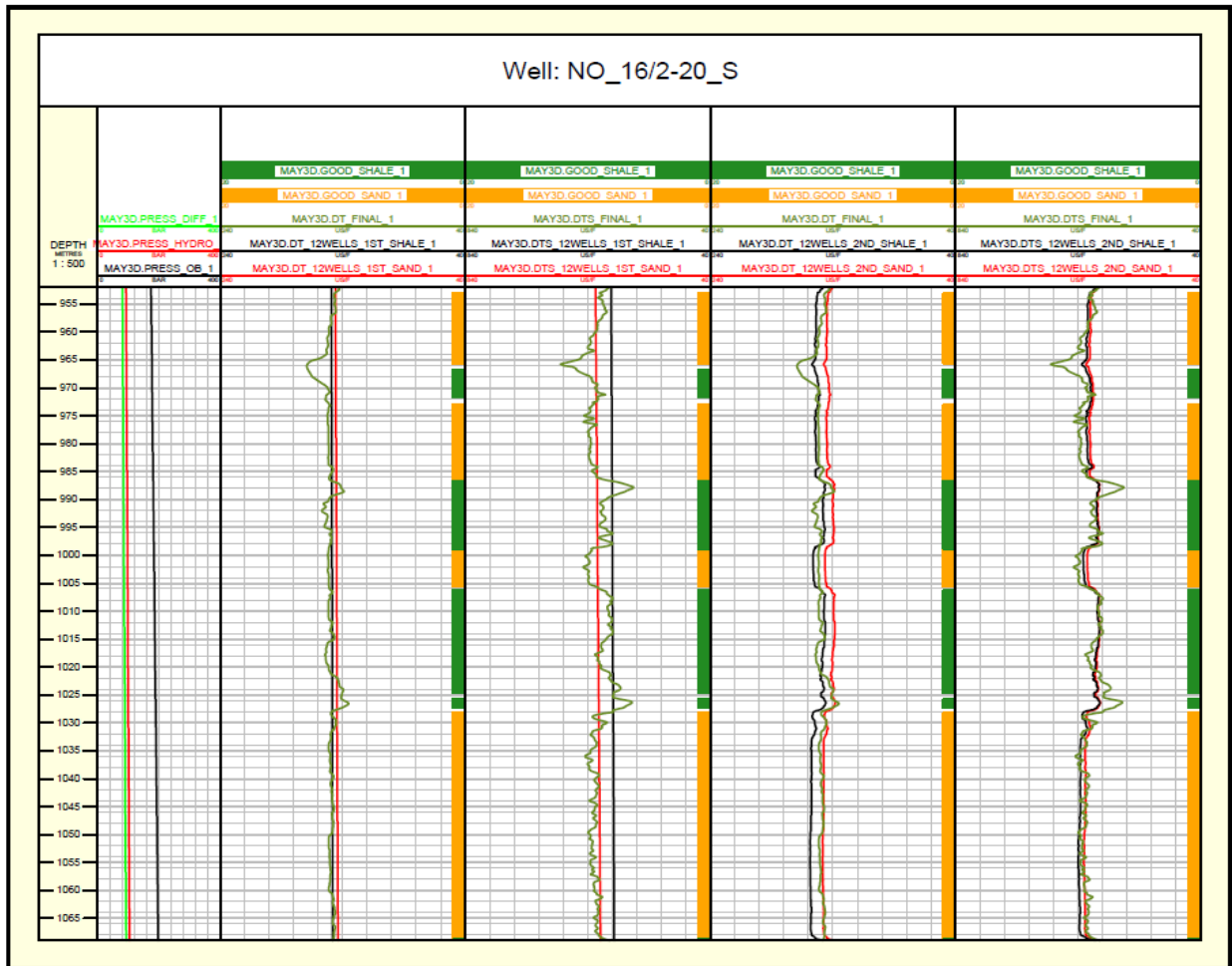


Figure D10. DT and DTS calculated based on the first and second sonic models for the Skade formation in the well 16/2-20 S. The optimization was based on all wells together.

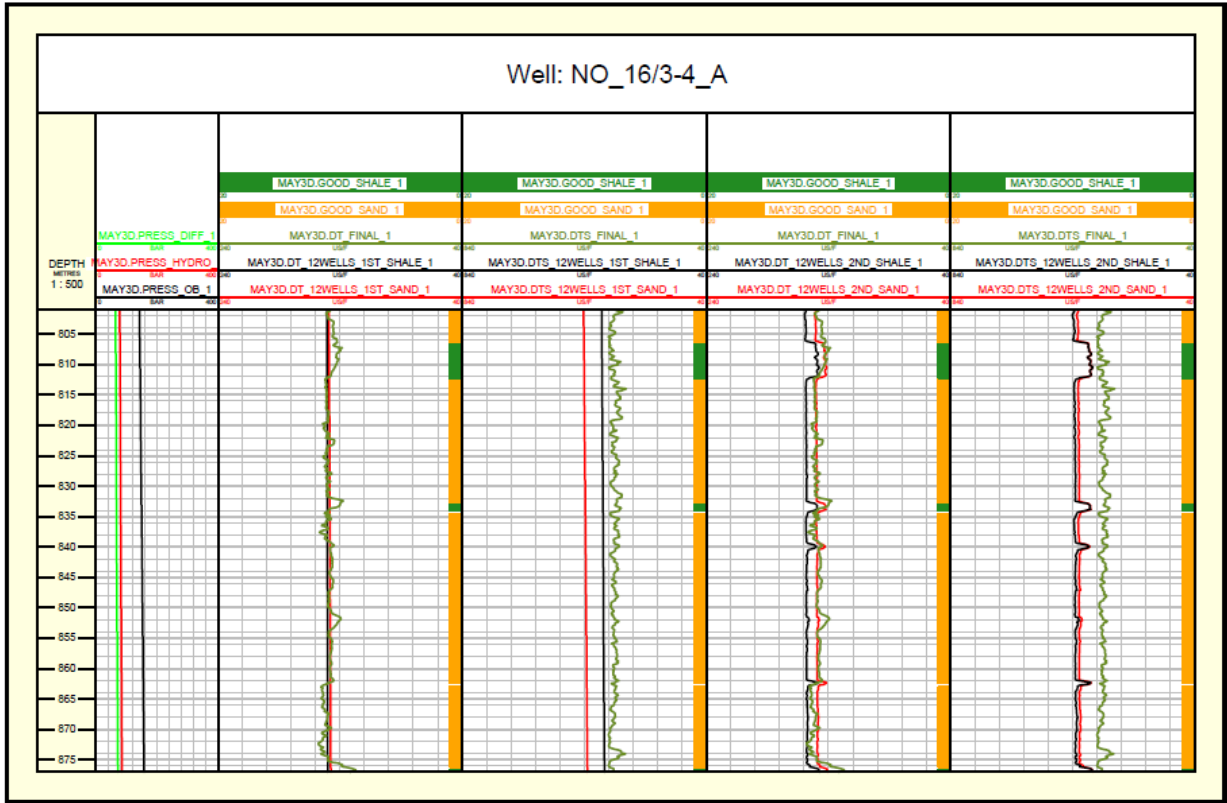


Figure D11. DT and DTS calculated based on the first and second sonic models for the Utsira formation in the well 16/3-4 A. The optimization was based on all wells together.

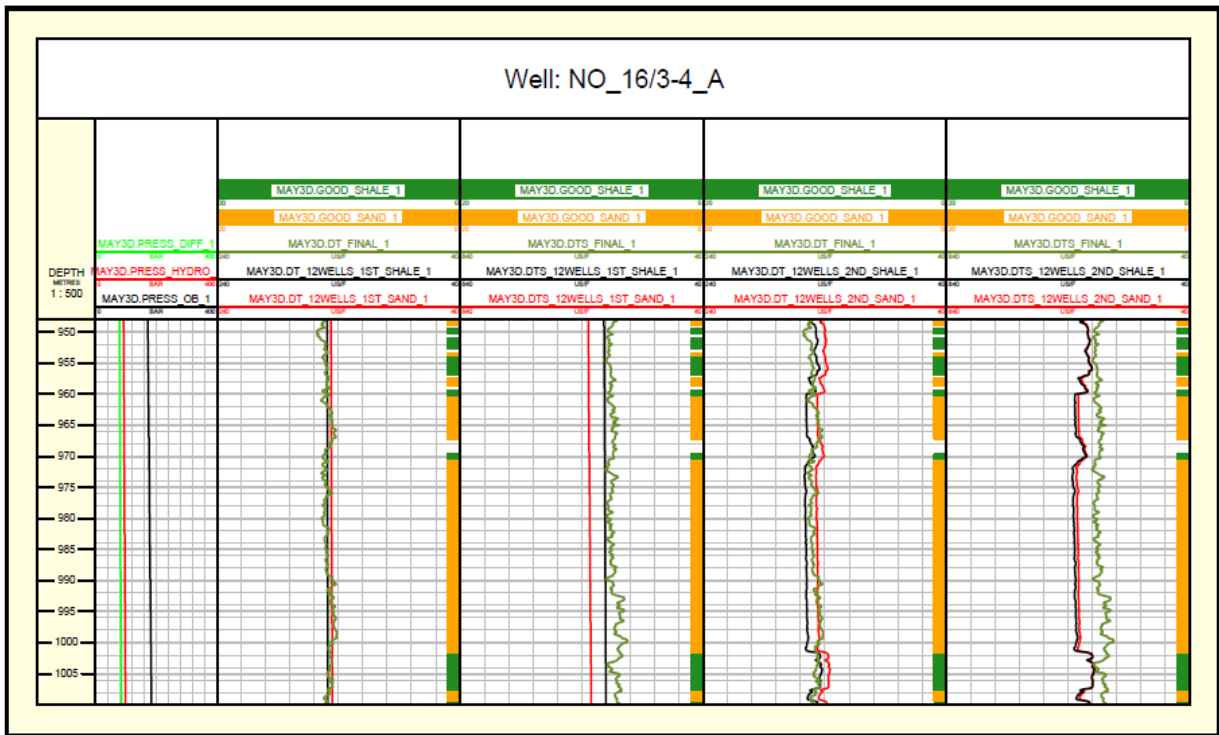


Figure D12. DT and DTS calculated based on the first and second sonic models for the Skade formation in the well 16/3-4 A. The optimization was based on all wells together.

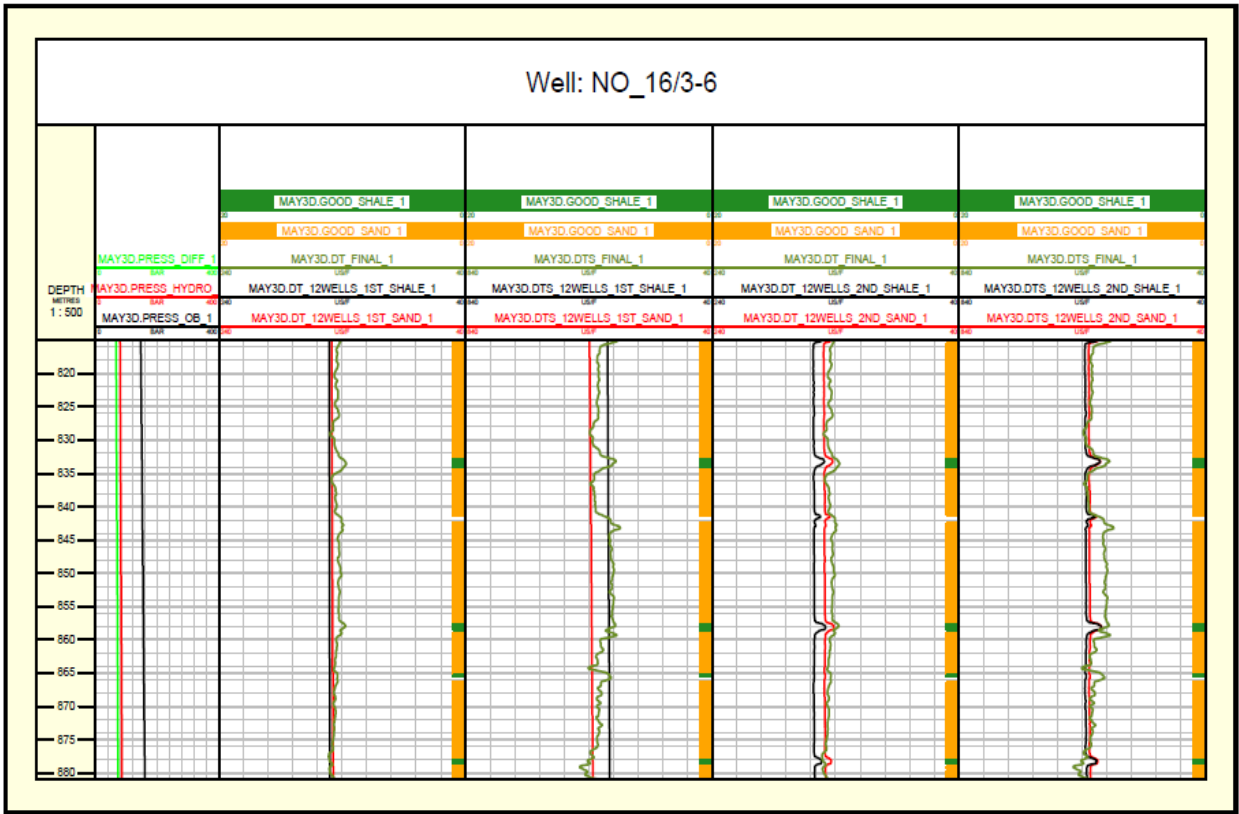


Figure D13. DT and DTS calculated based on the first and second sonic models t for the Utsira formation in the well 16/3-6. The optimization was based on wells together.

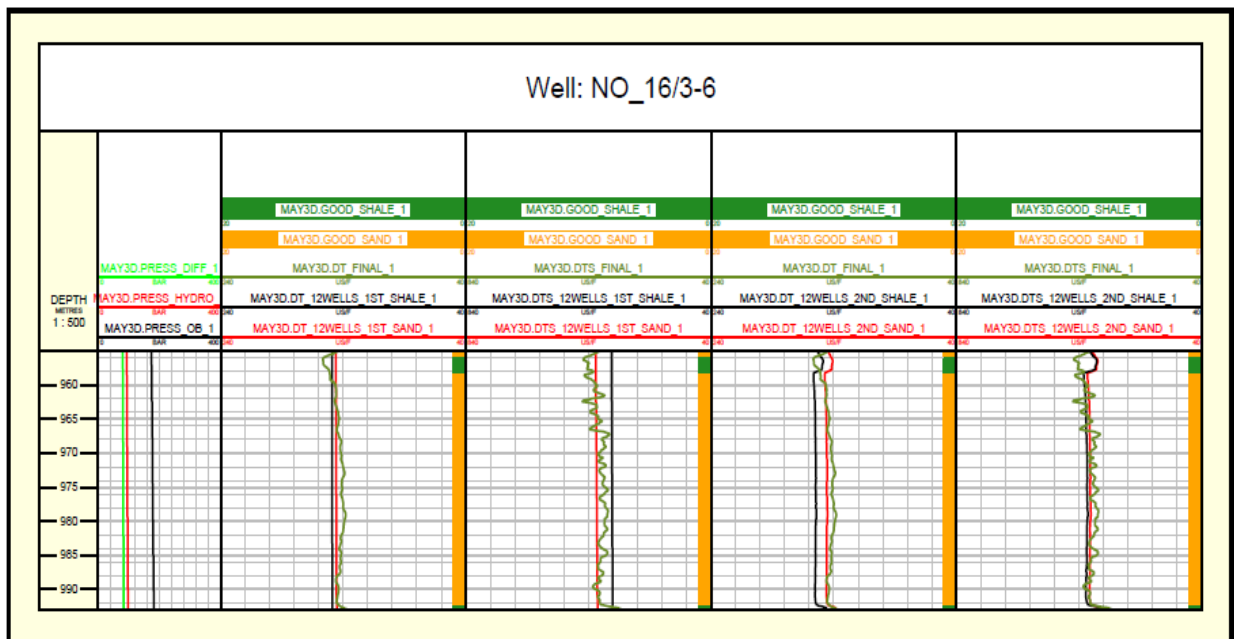


Figure D14. DT and DTS calculated based on the first and second sonic models for the Skade formation in the well 16/3-6. The optimization was based on all wells together.

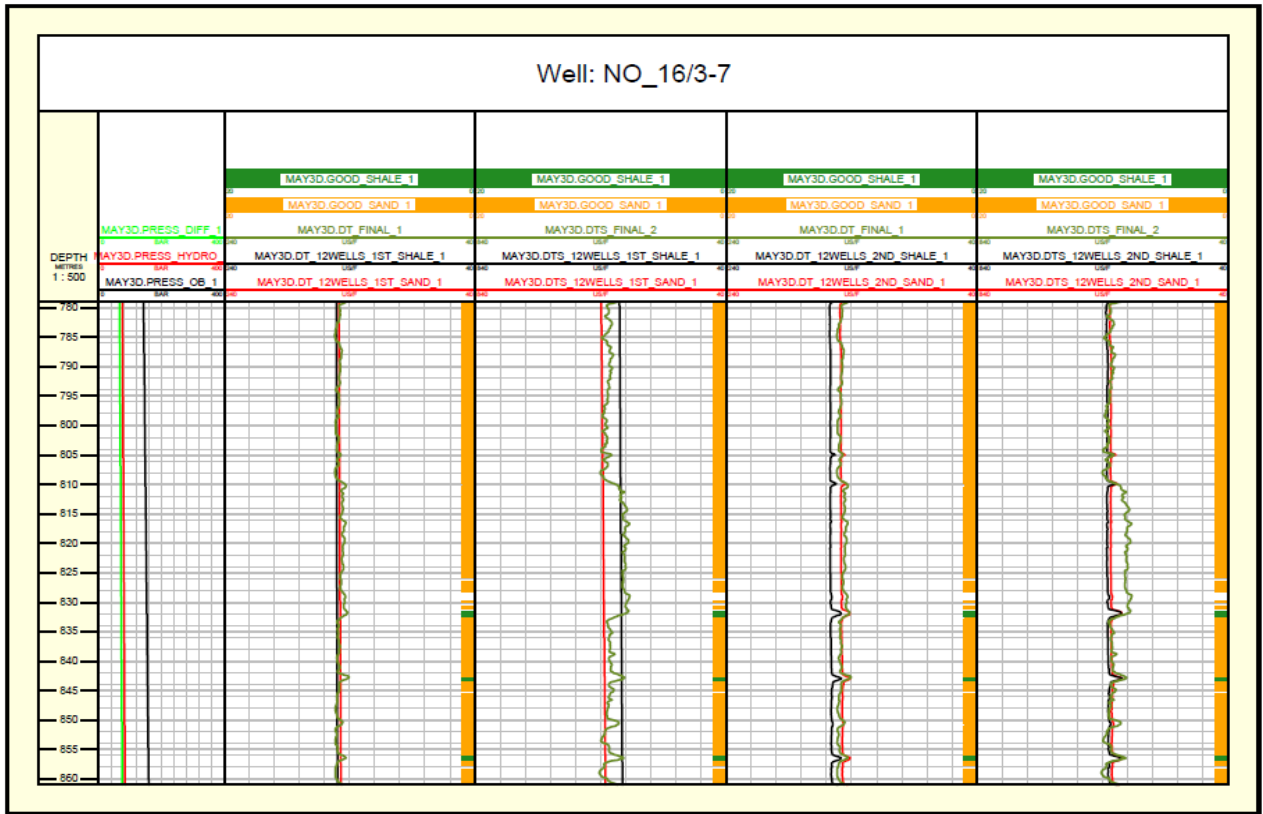


Figure D15. DT and DTS calculated based on the first and second sonic models for the Utsira formation in the well 16/3-7. The optimization was based on all wells together.

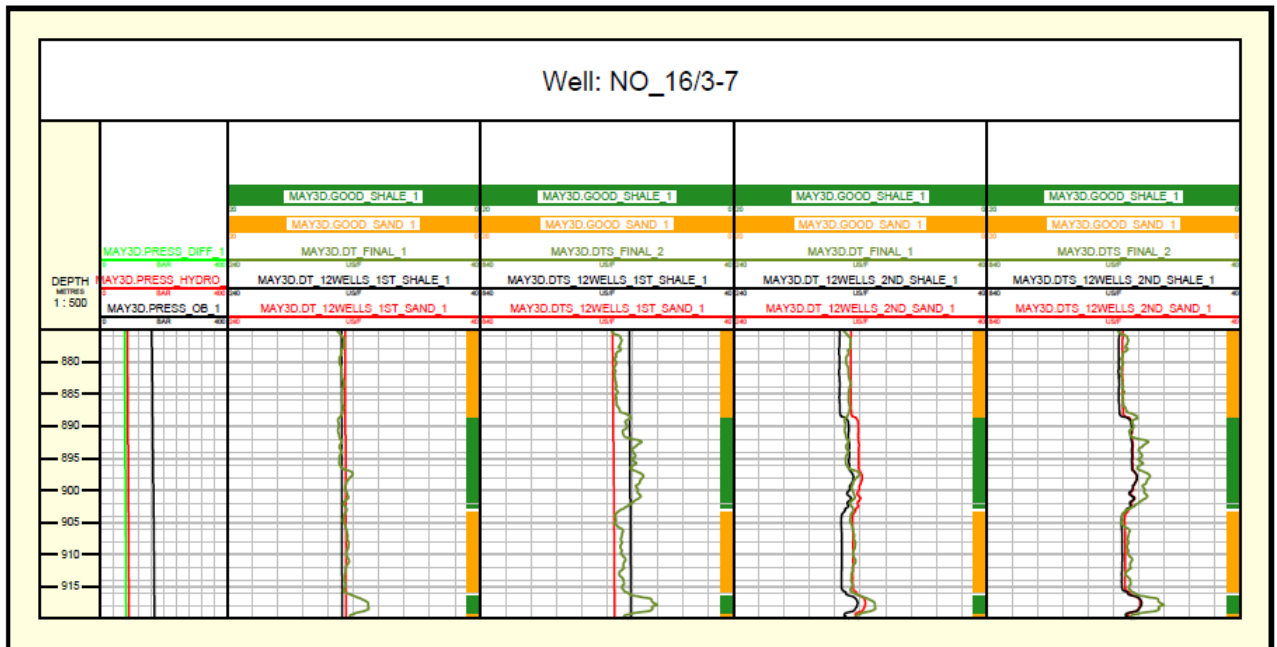


Figure D16. DT and DTS calculated based on the first and second sonic models for the Skade formation in the well 16/3-7. The optimization was based on all wells together.

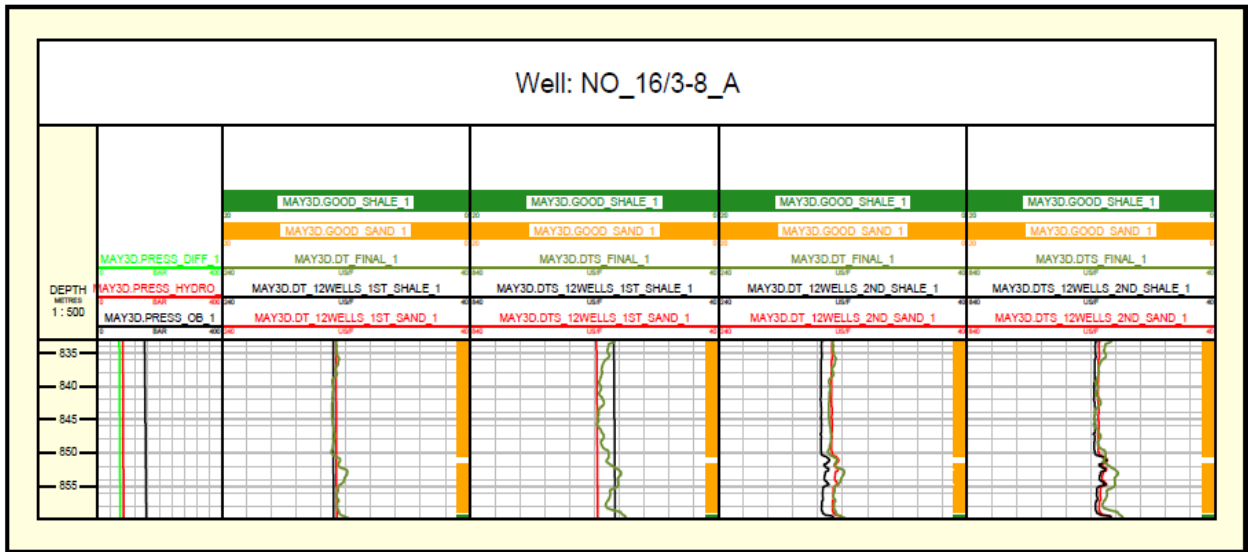


Figure D17. DT and DTS calculated based on the first and second sonic models for the Utsira formation in the well 16/3-8 A. The optimization was based on all wells together.

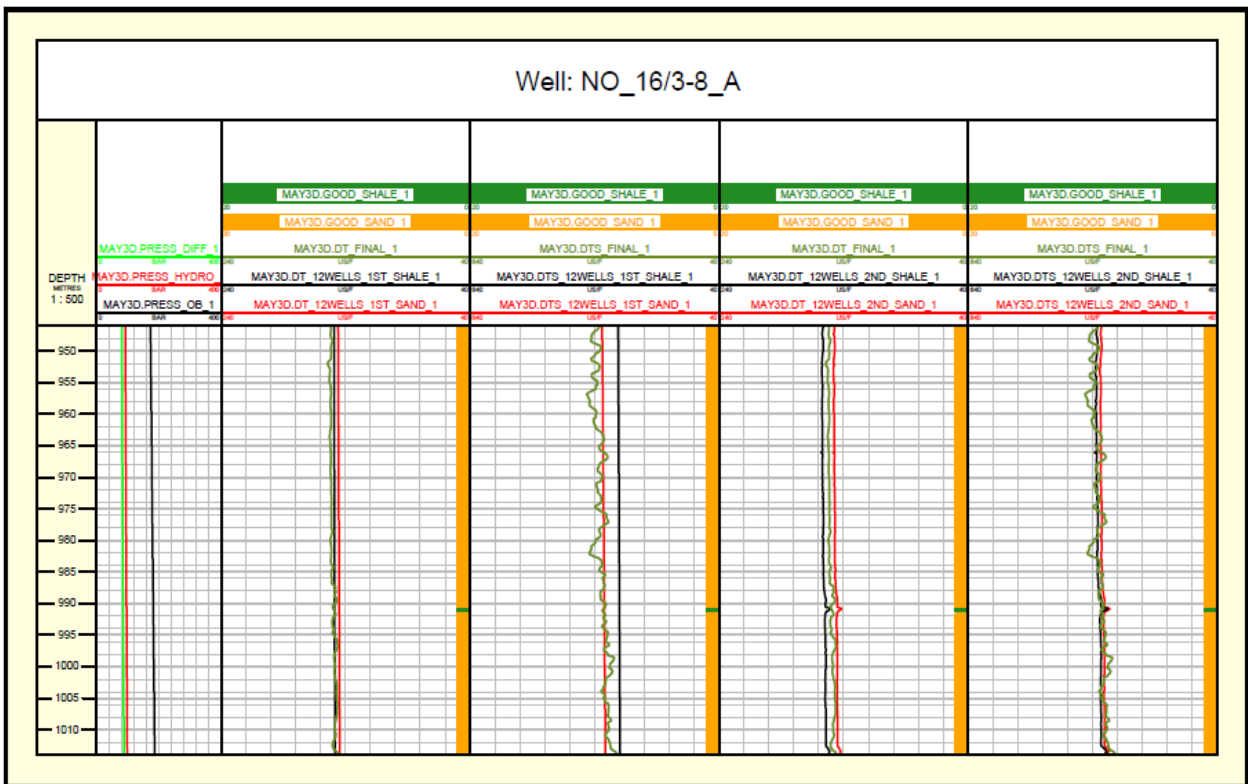


Figure D18. DT and DTS calculated based on the first and second sonic models for the Skade formation in the well 16/3-8 A. The optimization was based on all wells together.

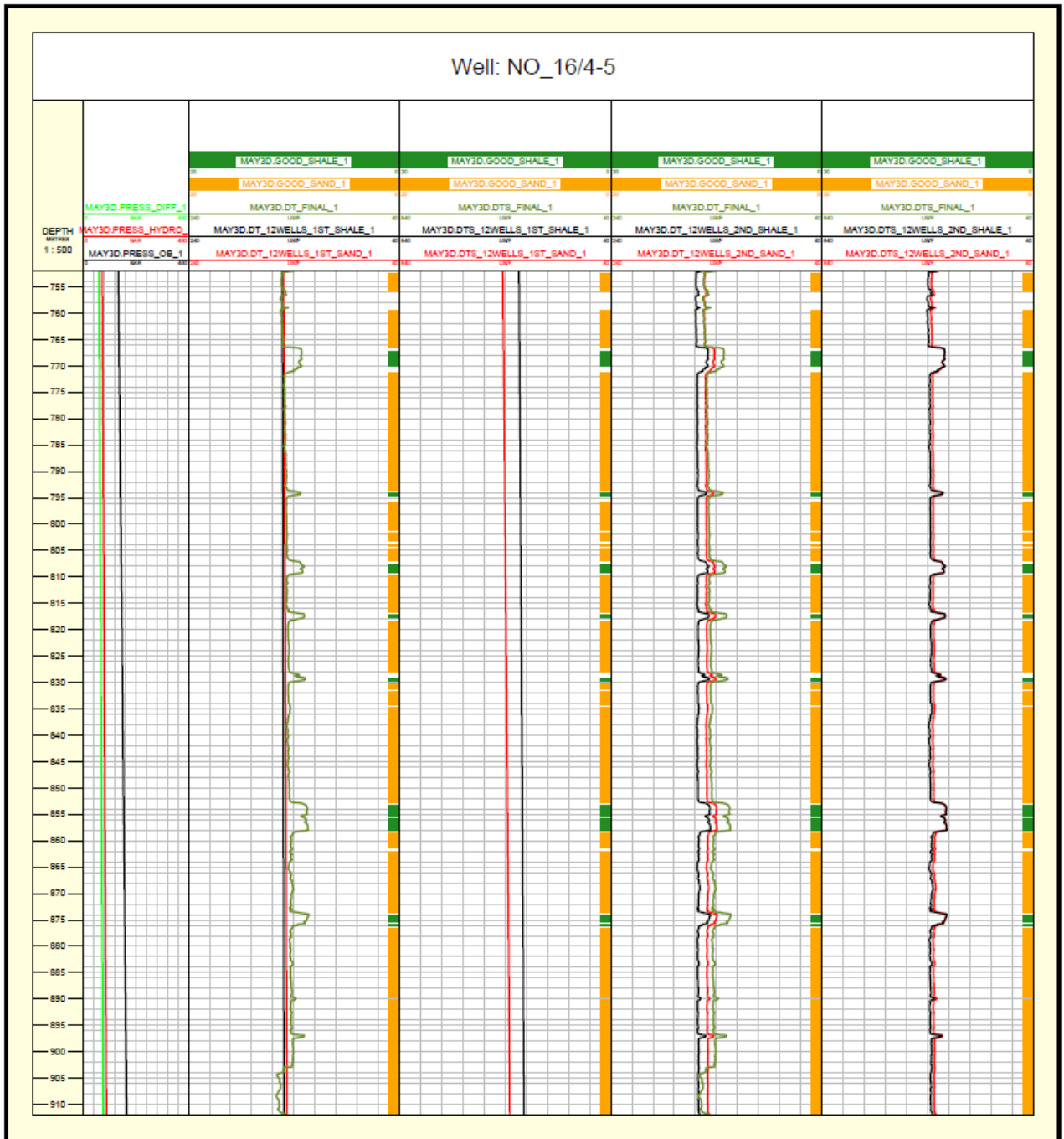


Figure D19. DT and DTS calculated based on the first and second sonic models for the Utsira formation in the well 16/4-5. The optimization was based on wells together.

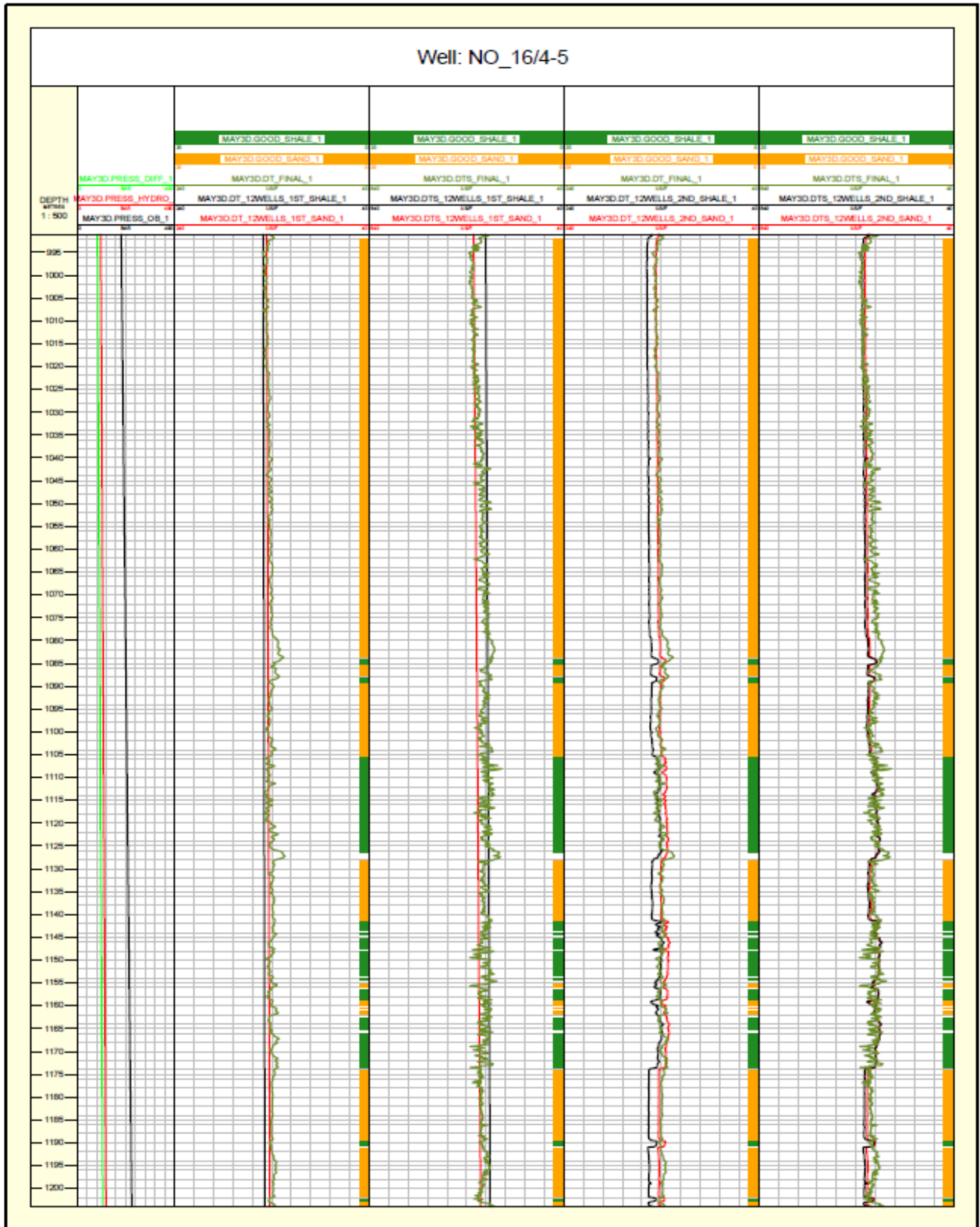


Figure D20. DT and DTS calculated based on the first and second sonic models for the Skade formation in the well 16/4-5. The optimization was based on all wells together.

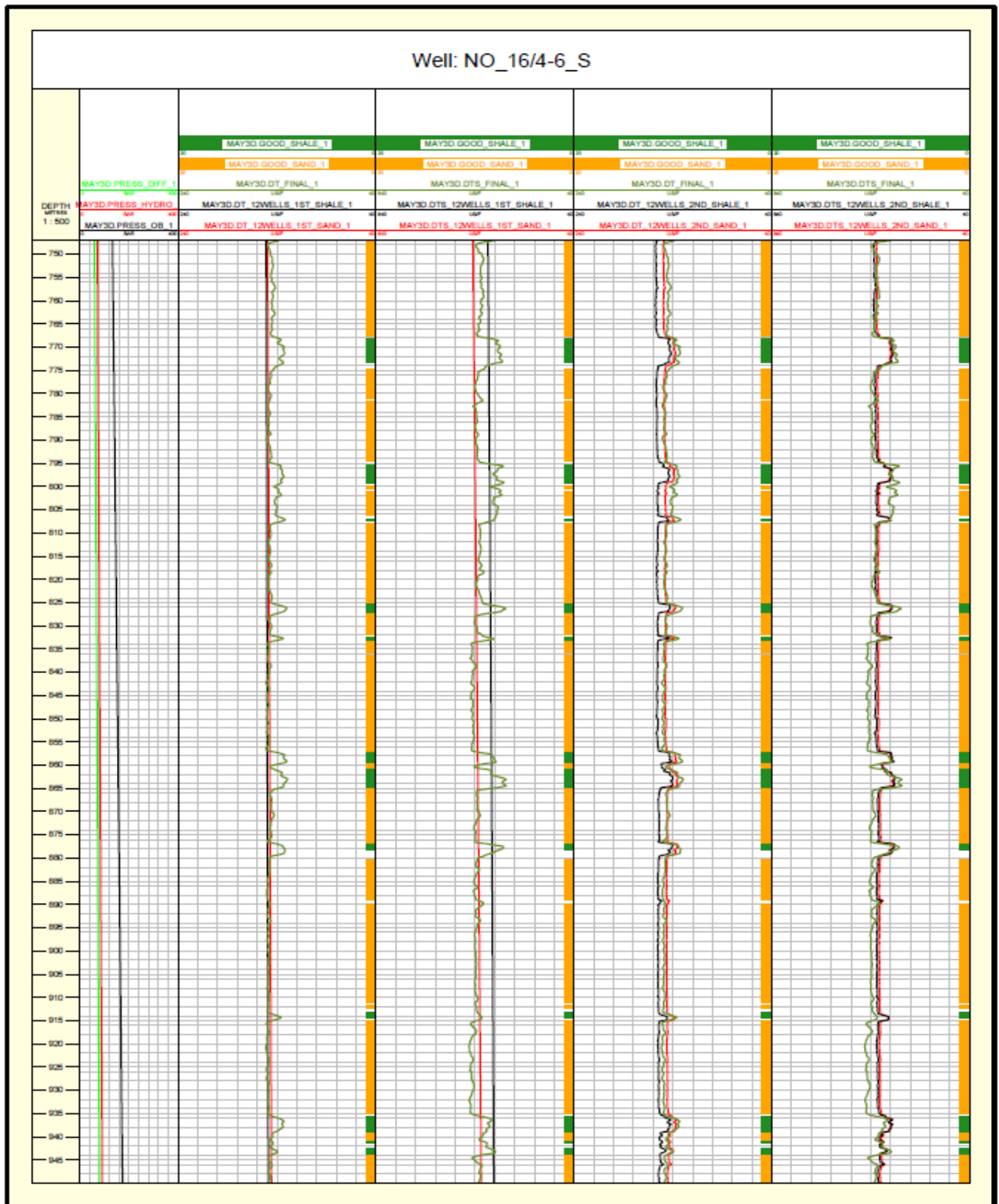


Figure D21. DT and DTS calculated based on the first and second sonic models for the Utsira formation in the well 16/4-6 S. The optimization was based on all wells together.

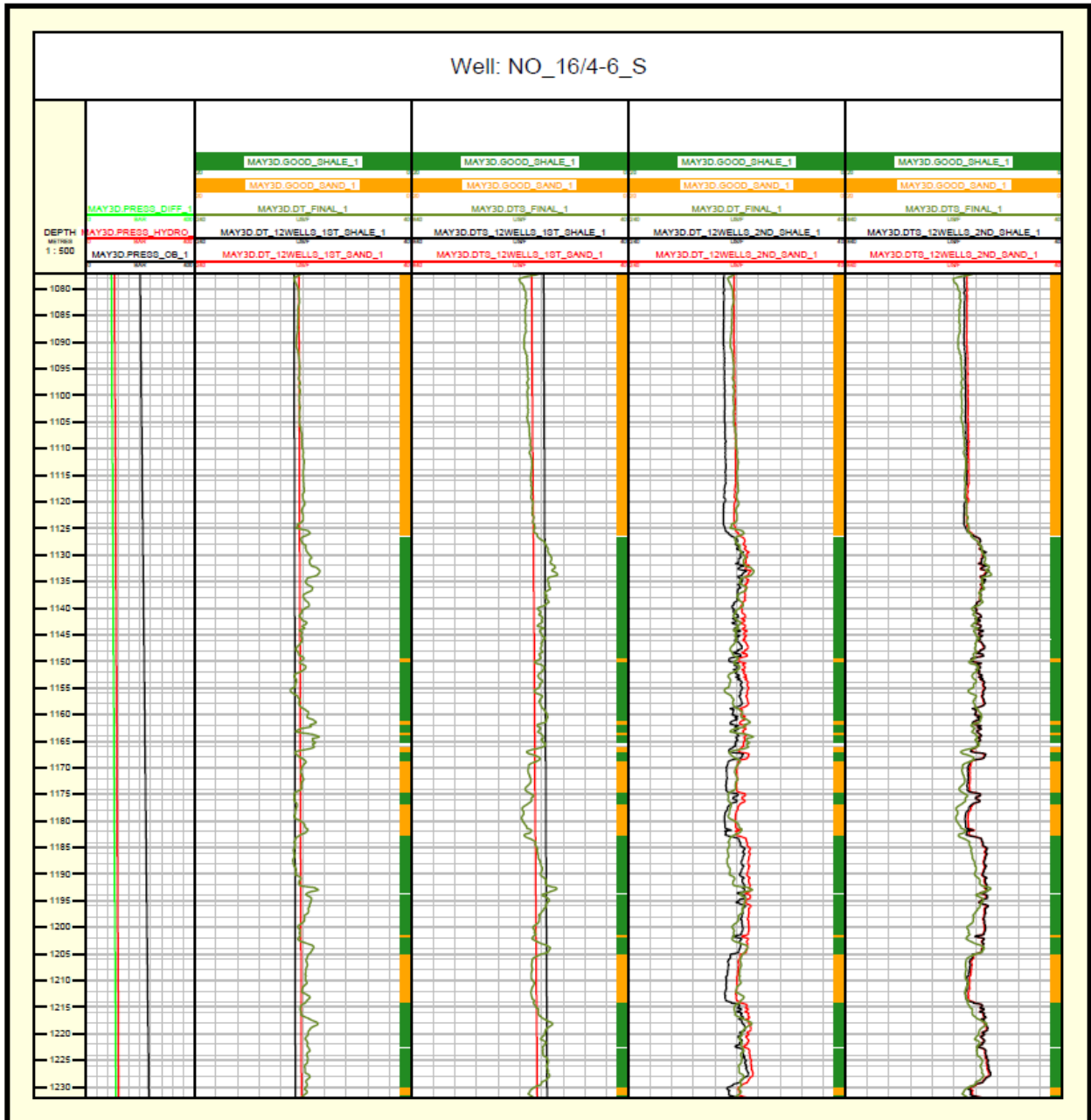


Figure D22. DT and DTS calculated based on the first and second sonic models for the Skade formation in the well 16/4-6 S. The optimization was based on all wells together.

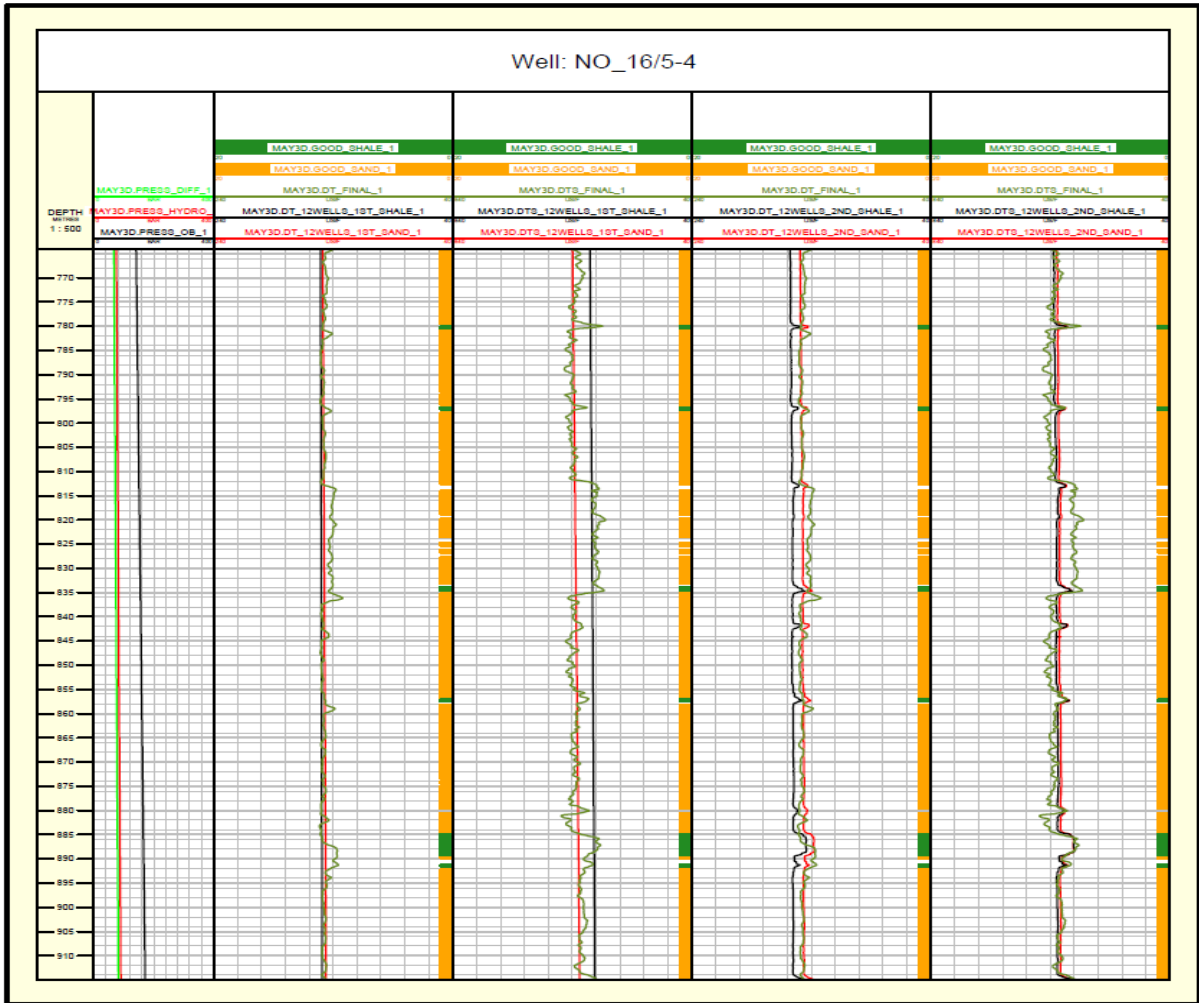


Figure D23. DT and DTS calculated based on the first and second sonic models for the Utsira formation in the well 16/5-4. The optimization was based on all wells together.

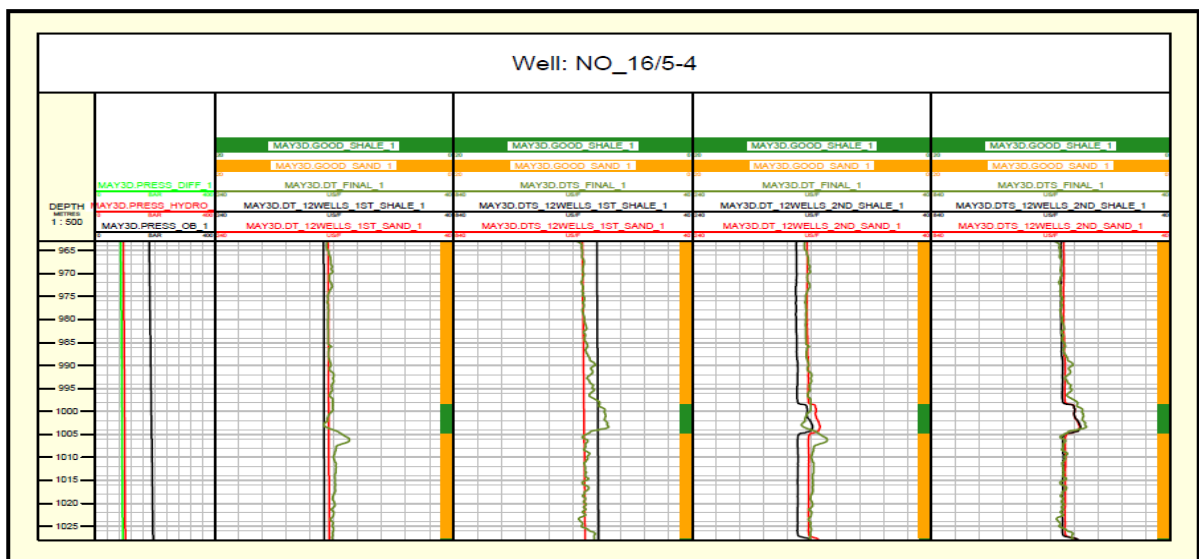


Figure D24. DT and DTS calculated based on the first and second sonic models for the Skade formation in the well 16/5-4. The optimization was based on all wells together.

Appendix E. CPI plots showing DT and DTS calculated based on the first and second sonic models for the Utsira, Skade and Grid formations – optimization is based on every well

Here we showed CPI plots displaying DT and DTS calculated using the first and second sonic models for the Utsira, Skade and Grid formations optimized for every well separately. We presented CPIs for the 10 final wells, since we excluded wells 16/3-4A and 16/4-5 due to bad raw data of DT and DTS which have influence to the final results of the models. We should mention that Grid formation was found only in wells 16/2-4 and 16/2-5. Hence, only for these certain wells we presented CPIs for all three sand formations.

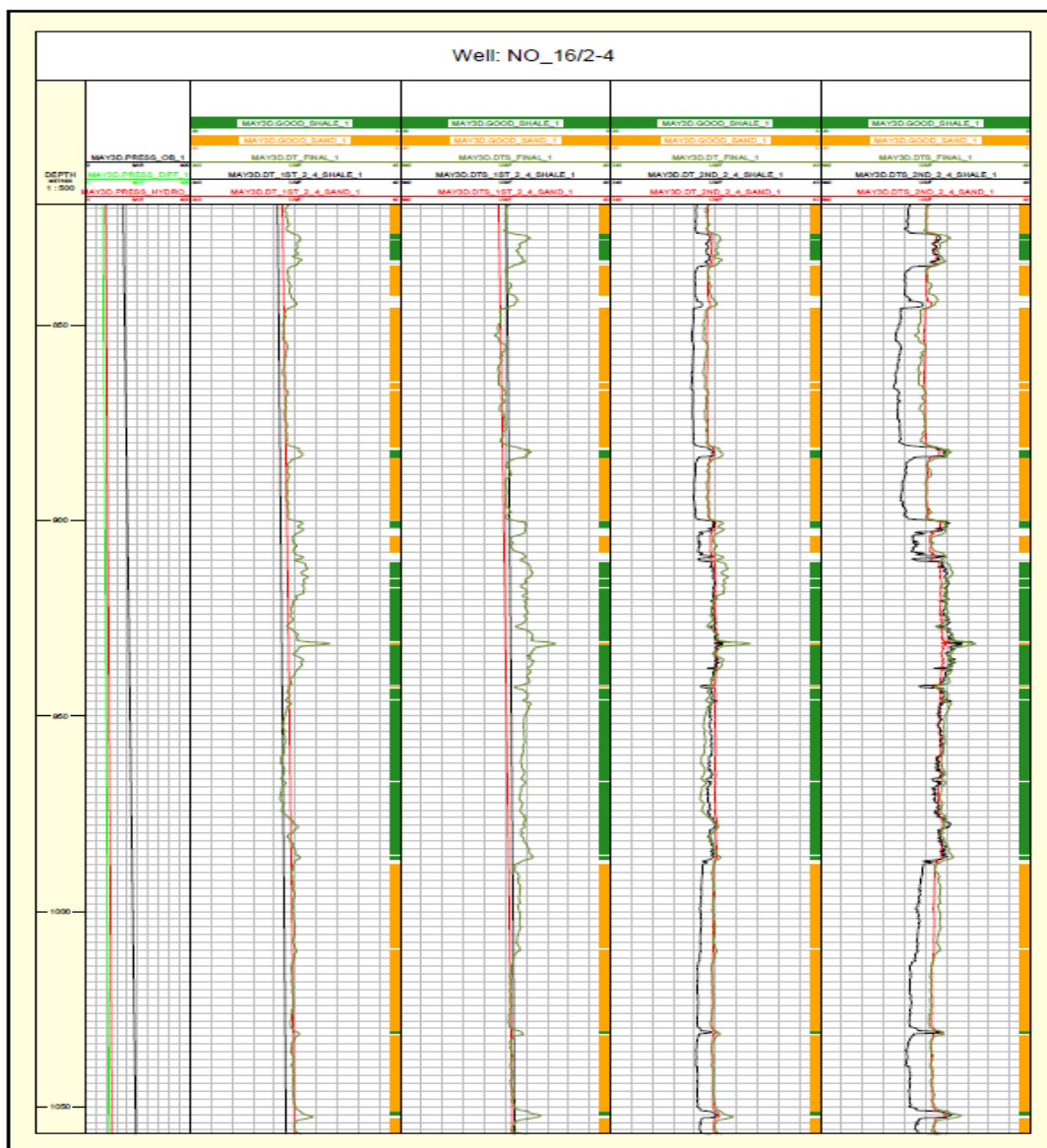


Figure E1. DT and DTS calculated based on the first and second sonic models for the Utsira formation in the well 16/2-4. The optimization was based on only this well.

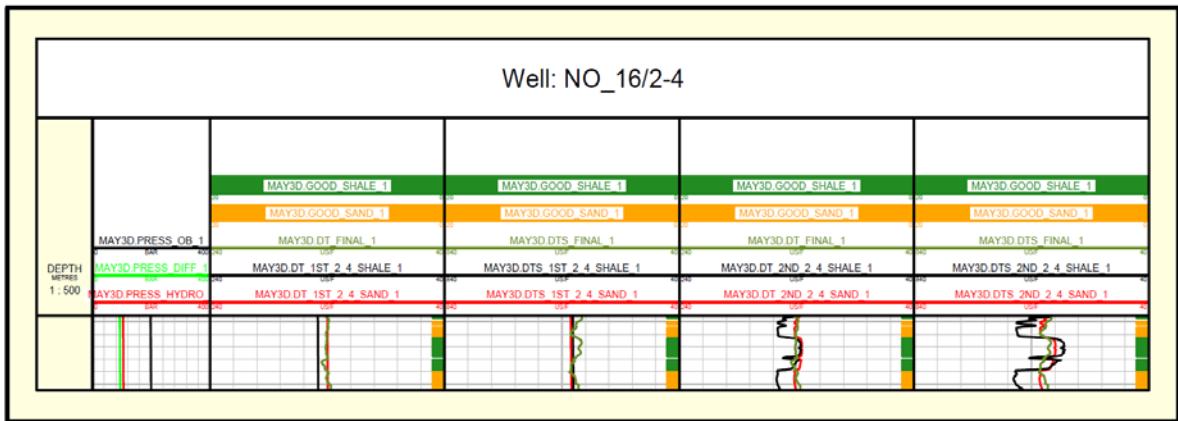


Figure E2. DT and DTS calculated based on the first and second sonic models for the Skade formation in the well 16/2-4. The optimization was based on only this well.

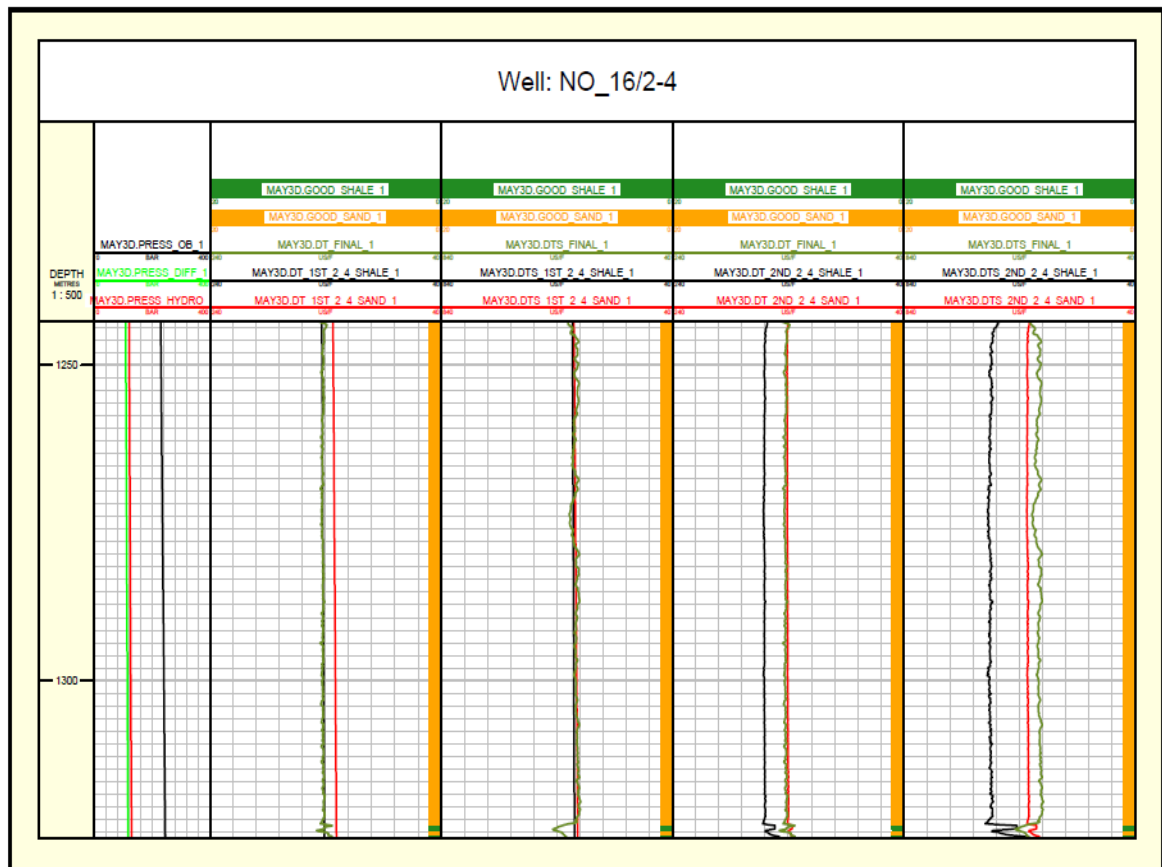


Figure E3. DT and DTS calculated based on the first and second sonic models for the Grid formation in the well 16/2-4. The optimization was based on only this well.

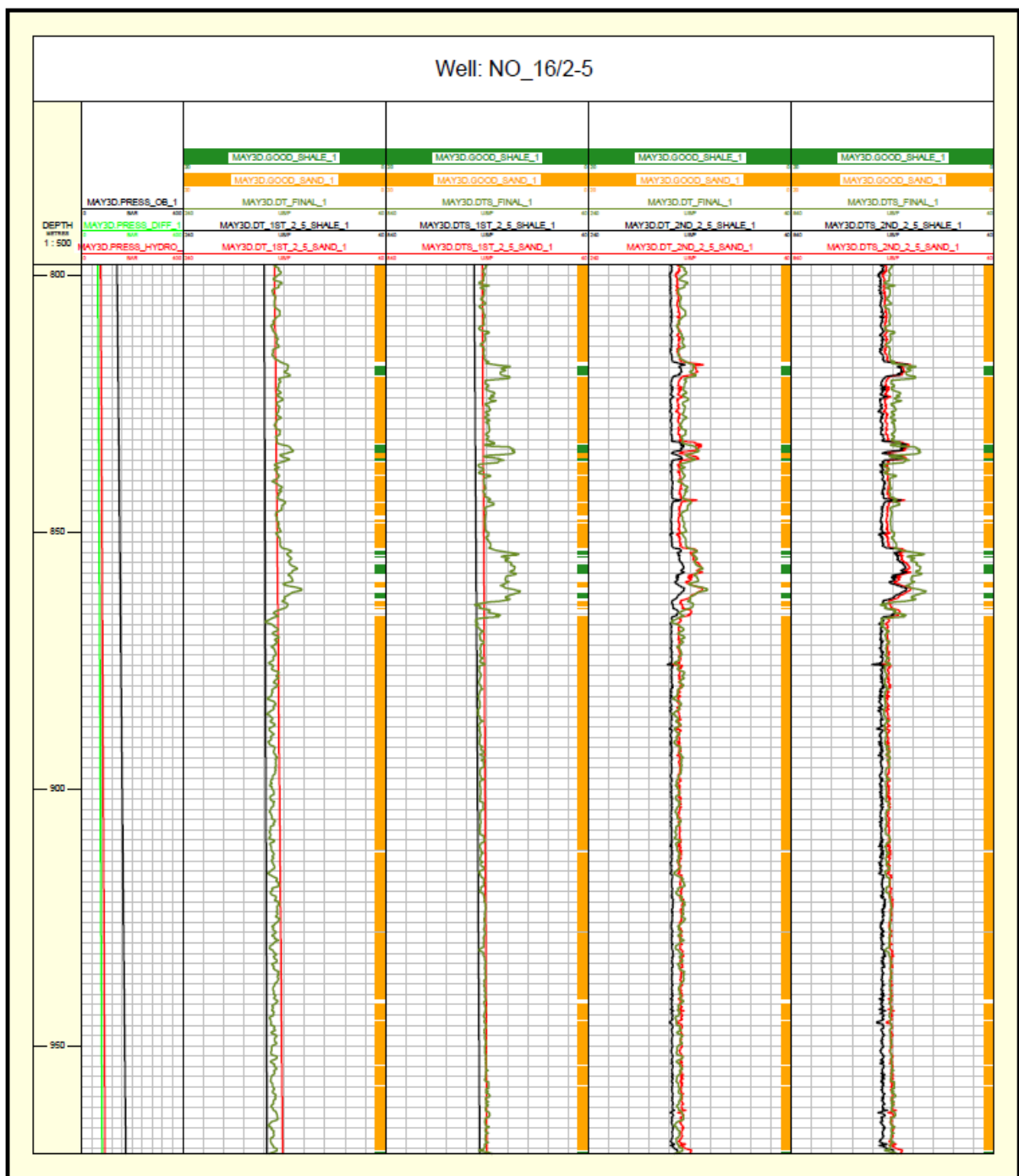


Figure E4. DT and DTS calculated based on the first and second sonic models for the Utsira formation for the well 16/2-5. The optimization was based on only this well.

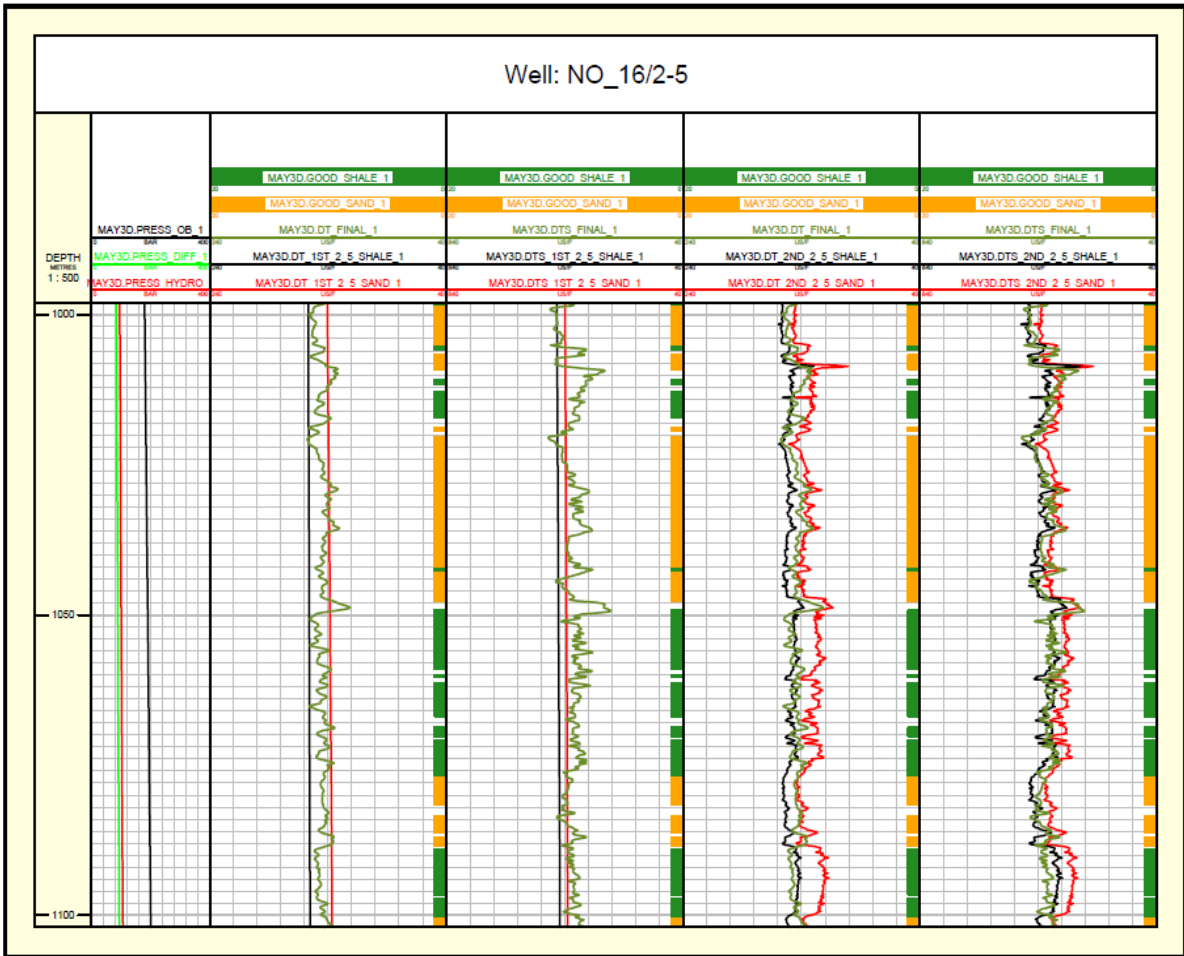


Figure E5. DT and DTS calculated based on the first and second sonic models for the Skade formation in the well 16/2-5. The optimization was based on only this well.

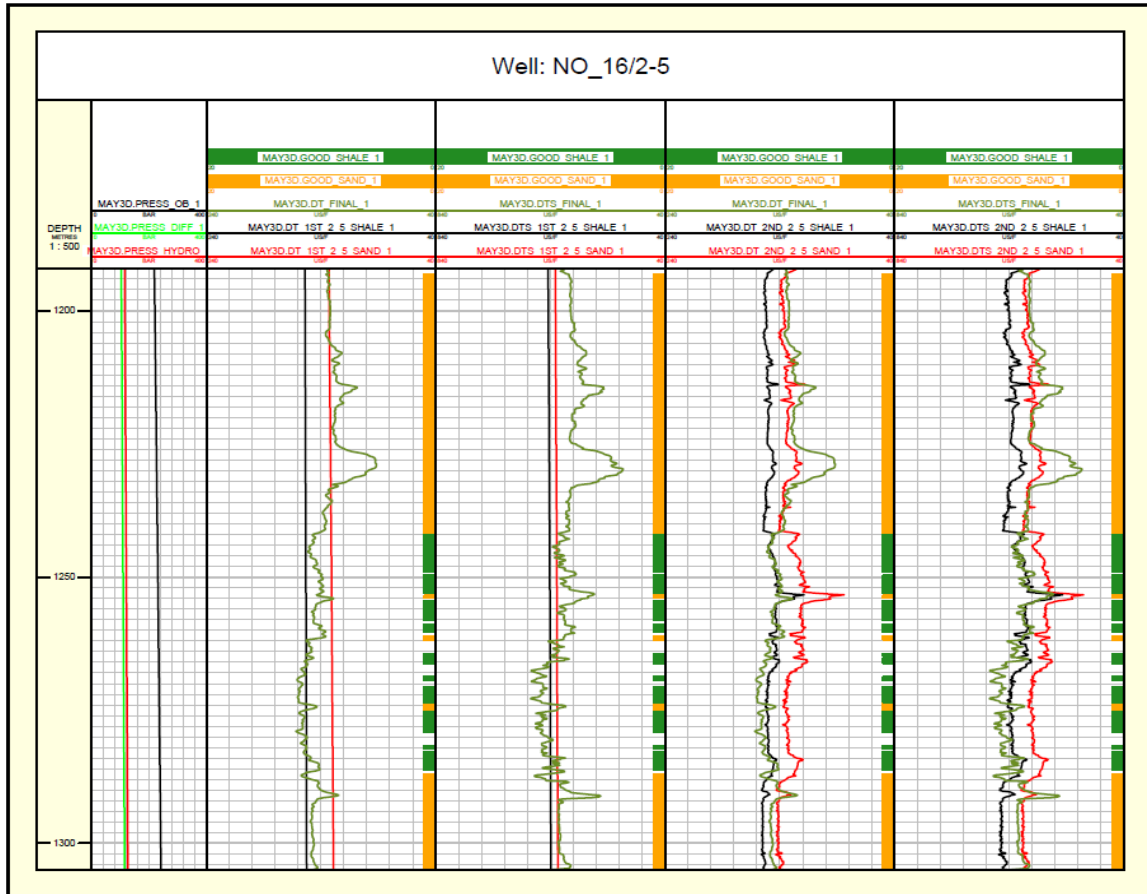


Figure E6. DT and DTS calculated based on the first and second sonic models for the Grid formation in the well 16/2-5. The optimization was based on only this well.

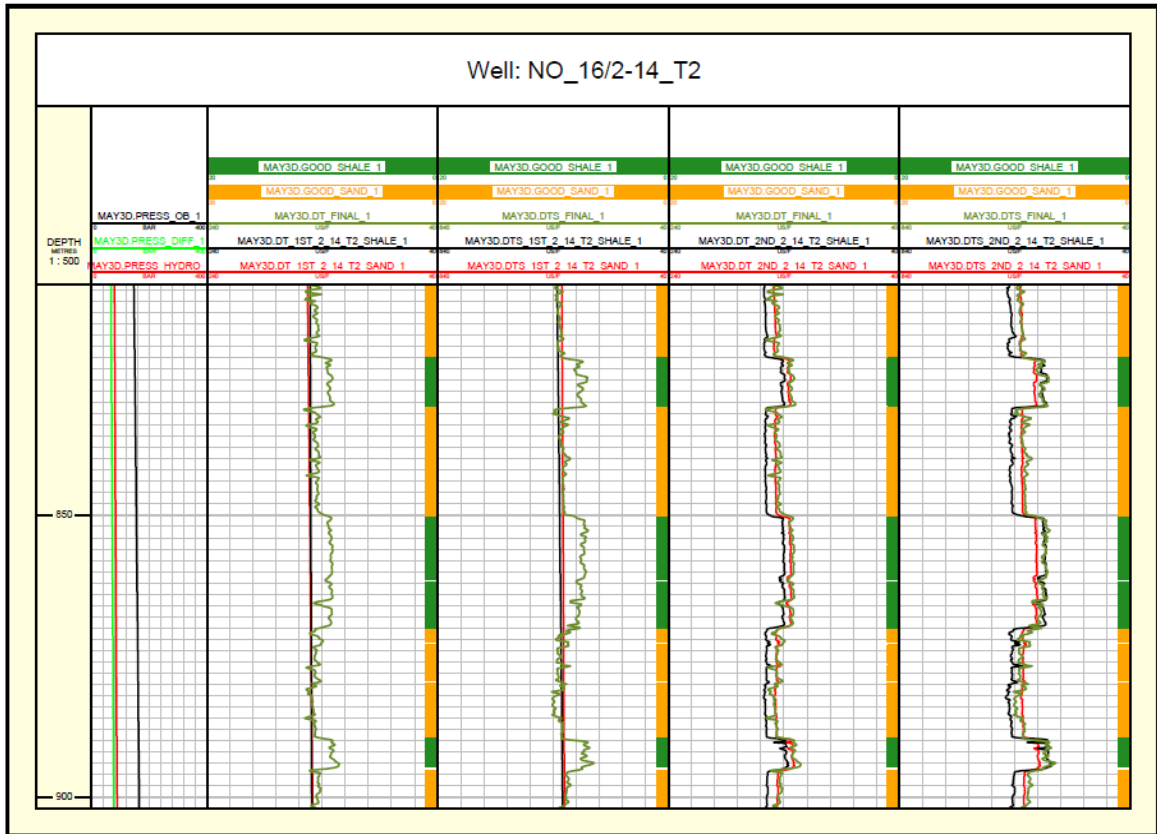


Figure E7. DT and DTS calculated based on the first and second sonic models for the Utsira formation in the well 16/2-14 T2. The optimization was based on only this well.

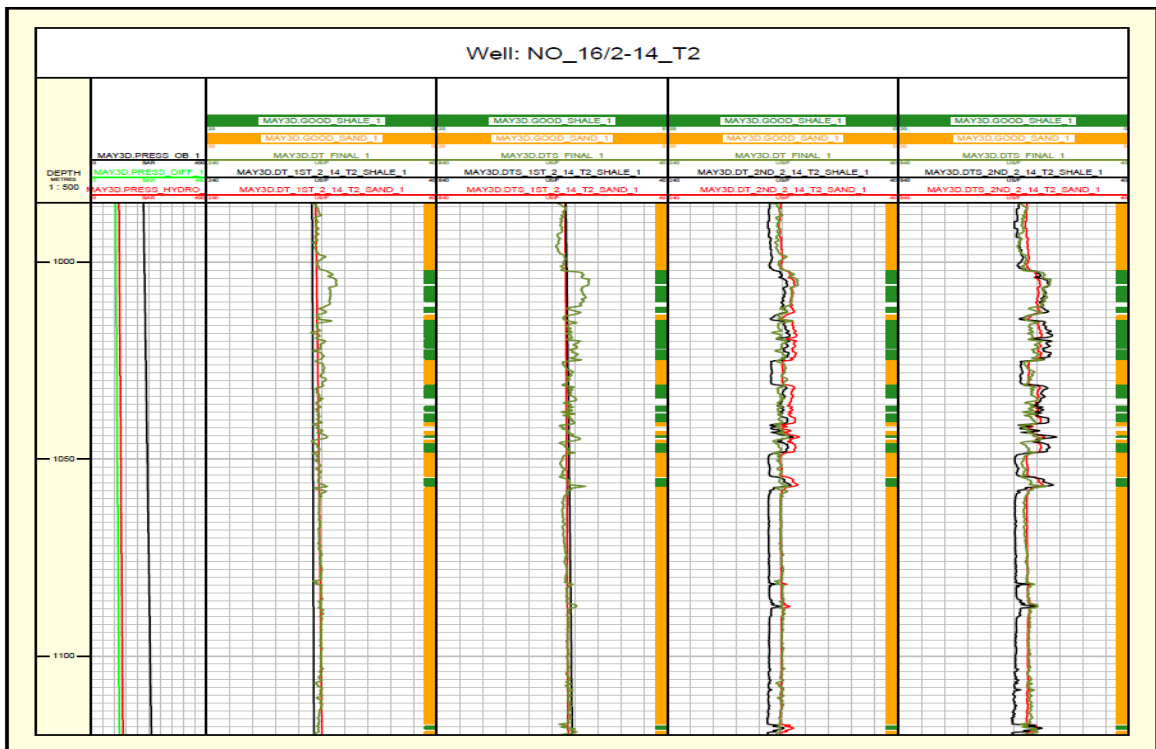


Figure E8. DT and DTS calculated based on the first and second sonic models for the Skade formation in the well 16/2-14 T2. The optimization was based on only this well.

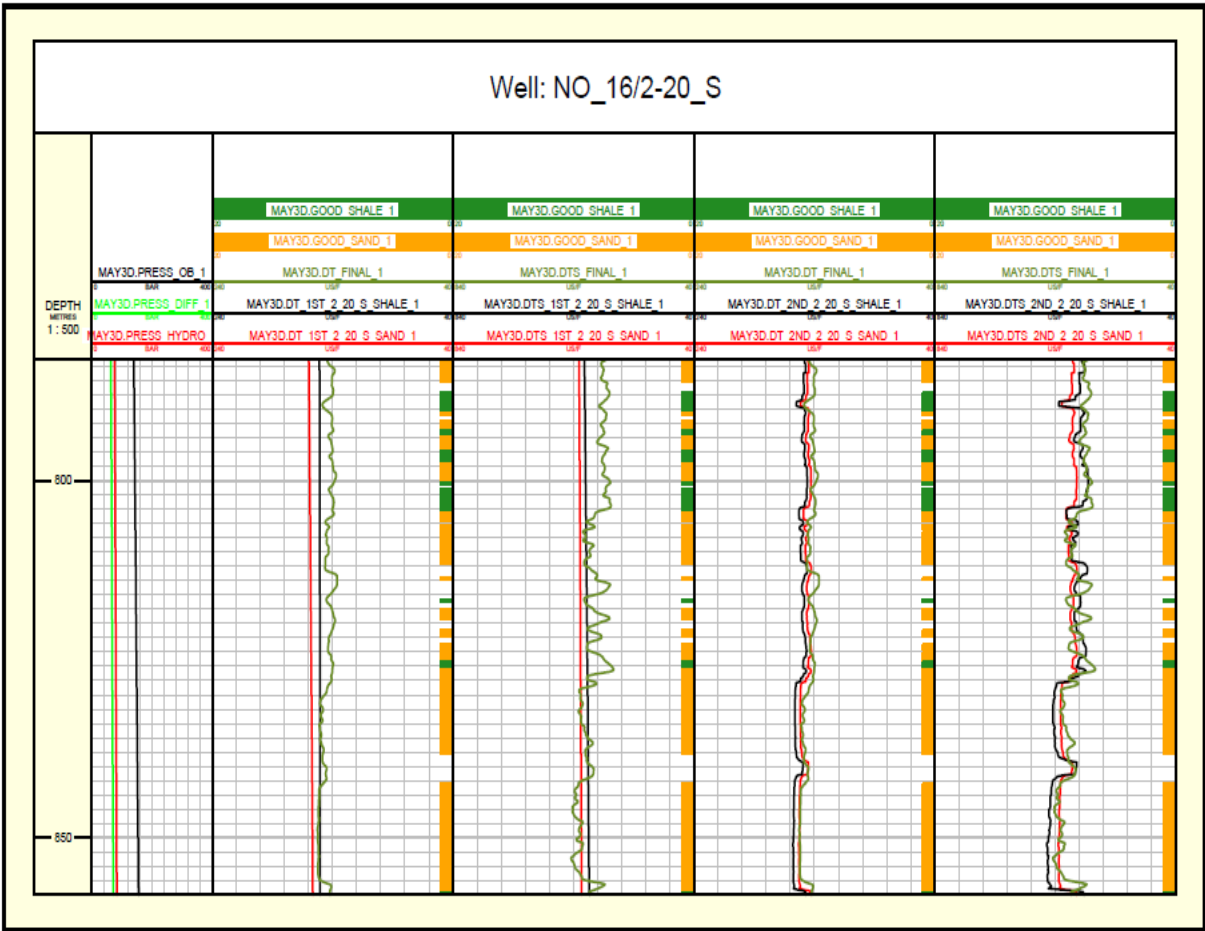


Figure E9. DT and DTS calculated based on the first and second sonic models separately for the Utsira formation in the well 16/2-20 S. The optimization was based on only this well.

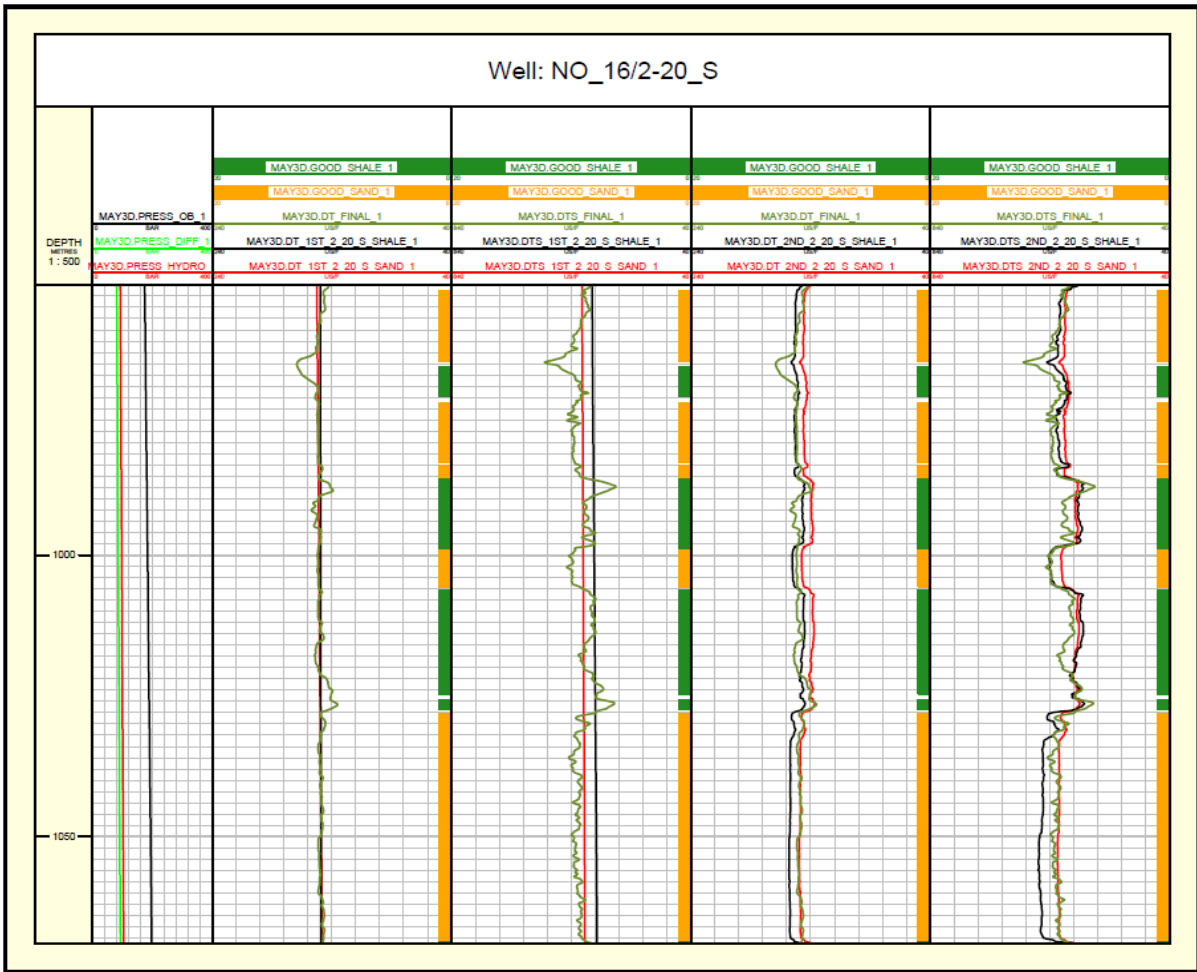


Figure E10. DT and DTS calculated based on the first and second sonic models for the Skade formation in the well 16/2-20 S. The optimization was based on only this well.

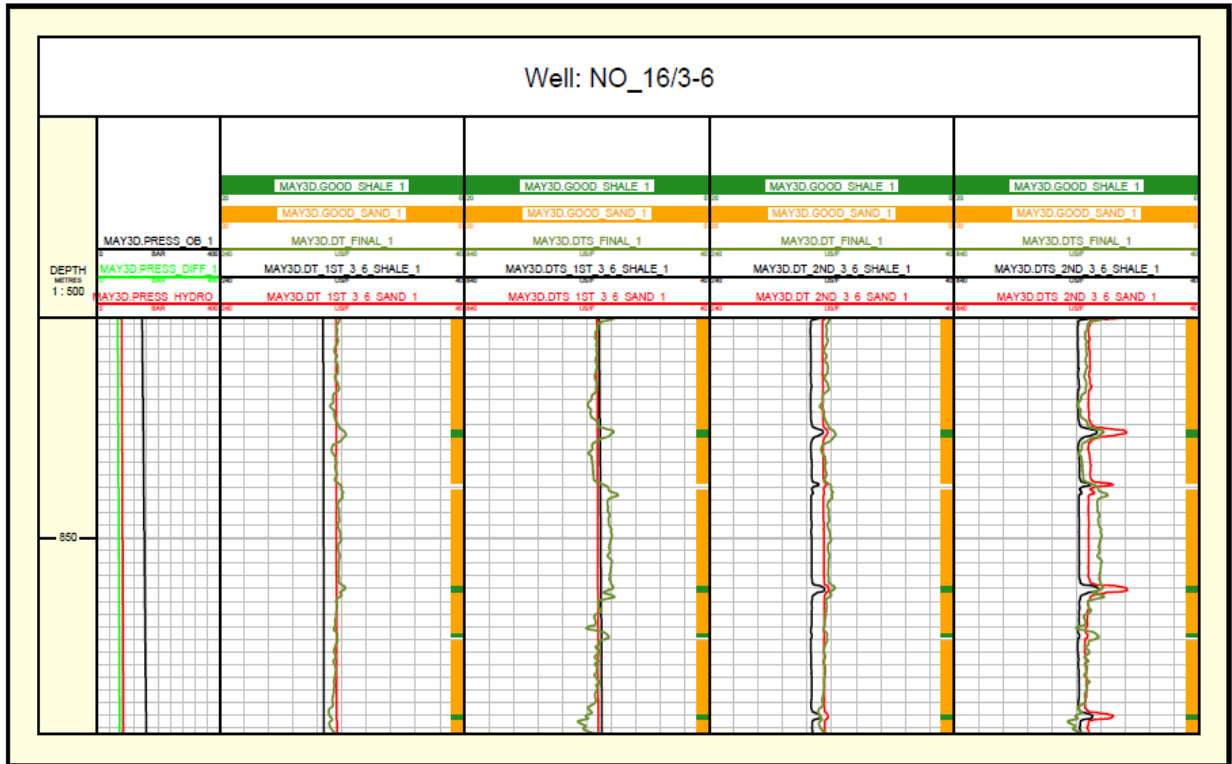


Figure E11. DT and DTS calculated based on the first and second sonic models for the Utsira formation in the well 16/3-6. The optimization was based on only this well.

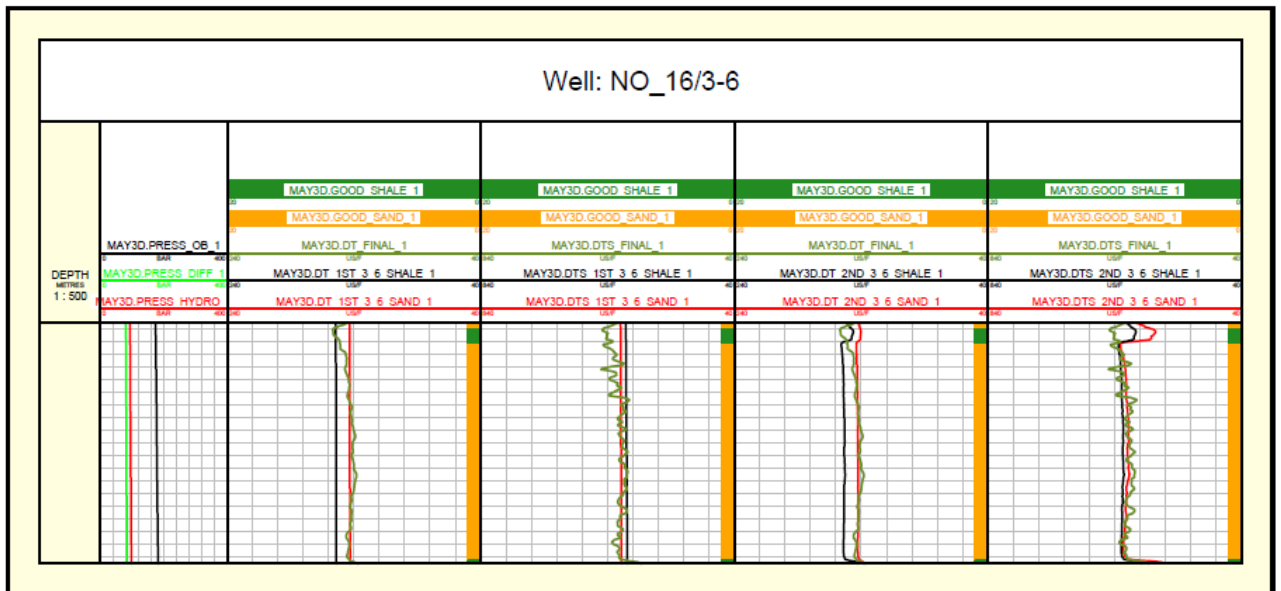


Figure E12. DT and DTS calculated based on the first and second sonic models for the Skade formation in the well 16/3-6. The optimization was based on only this well.

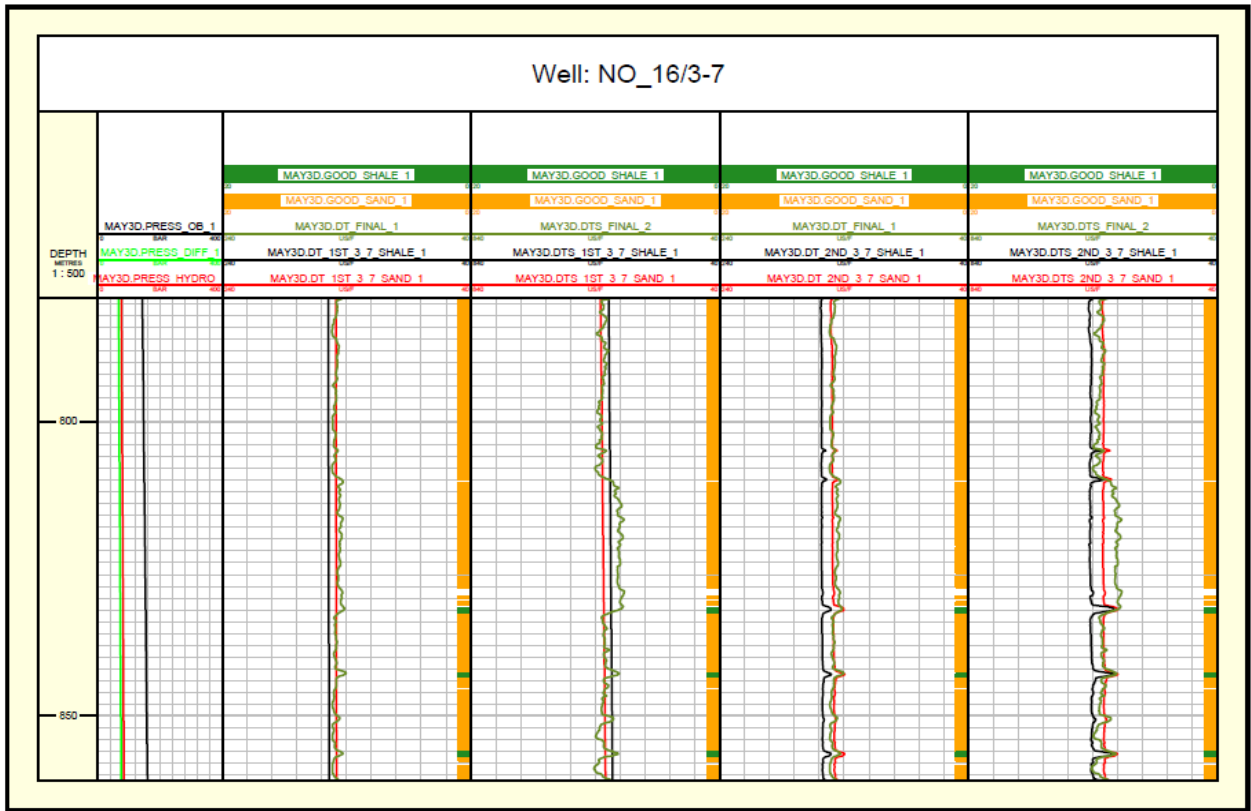


Figure E13. DT and DTS calculated based on the first and second sonic models for the Utsira formation in the well 16/3-7. The optimization was based on only this well.

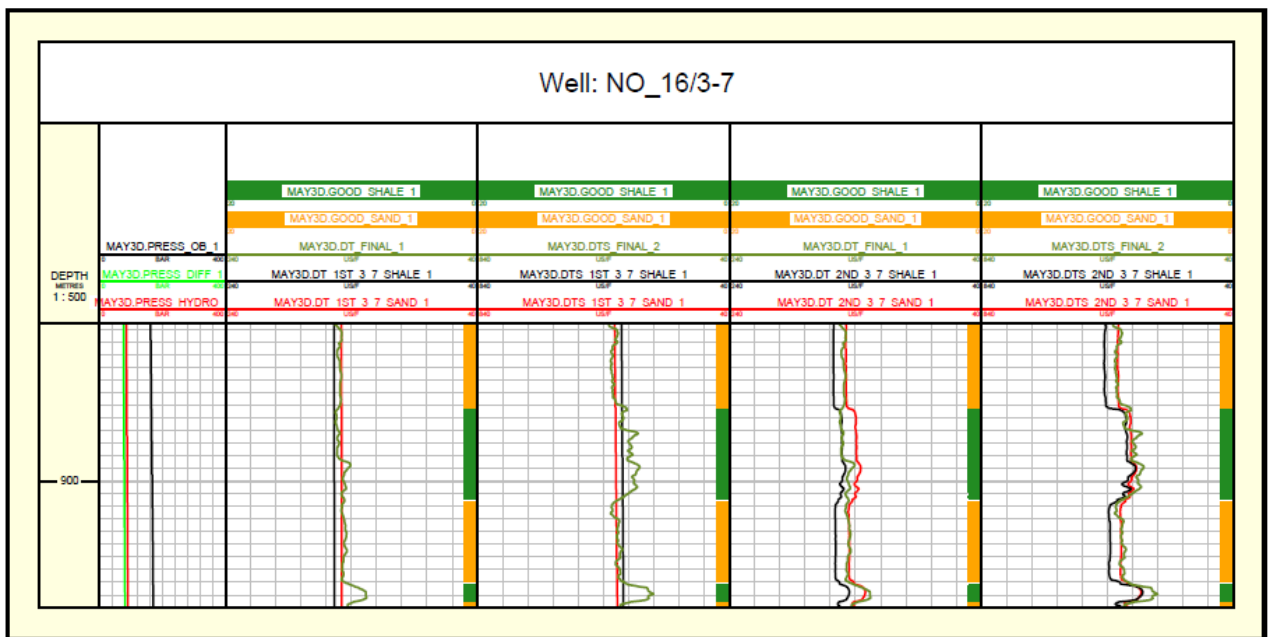


Figure E14. DT and DTS calculated based on the first and second sonic models for the Skade formation in the well 16/3-7. The optimization was based on only this well.

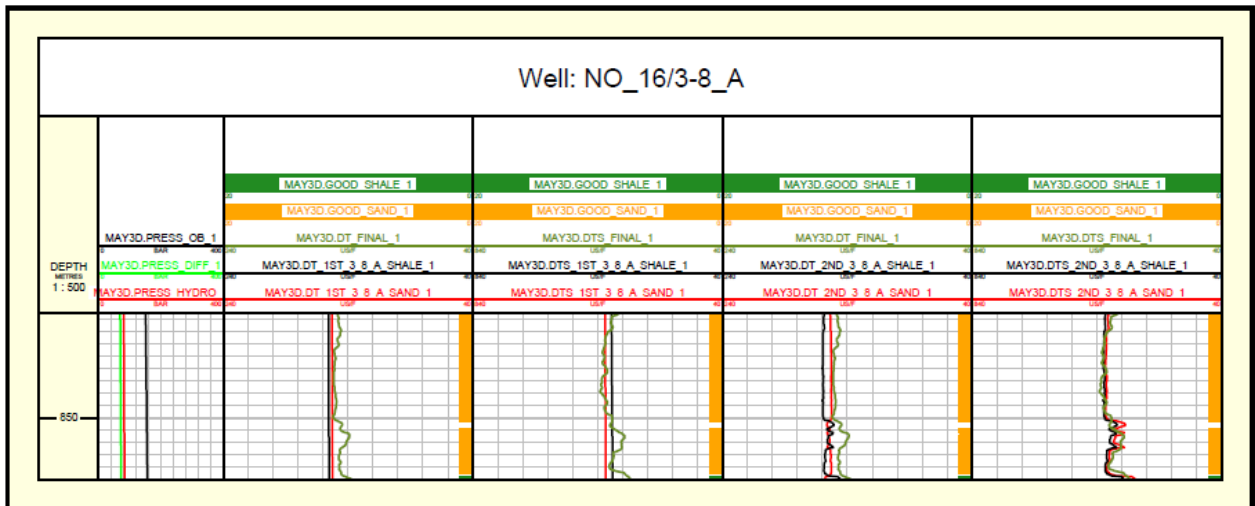


Figure E15. DT and DTS calculated based on the first and second sonic models for the Utsira formation in the well 16/3-8 A. The optimization was based on only this well.

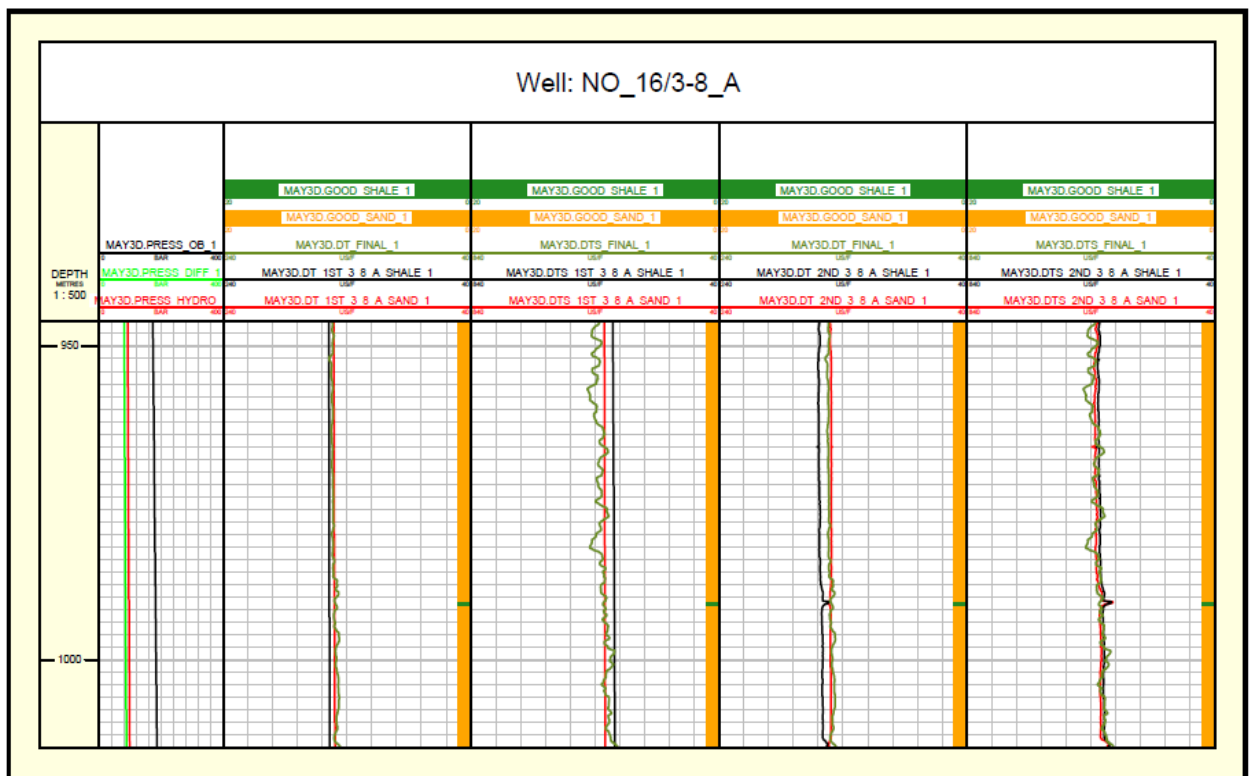


Figure E16. DT and DTS calculated based on the first and second sonic models for the Skade formation in the well 16/3-8 A. The optimization was based on only this well.

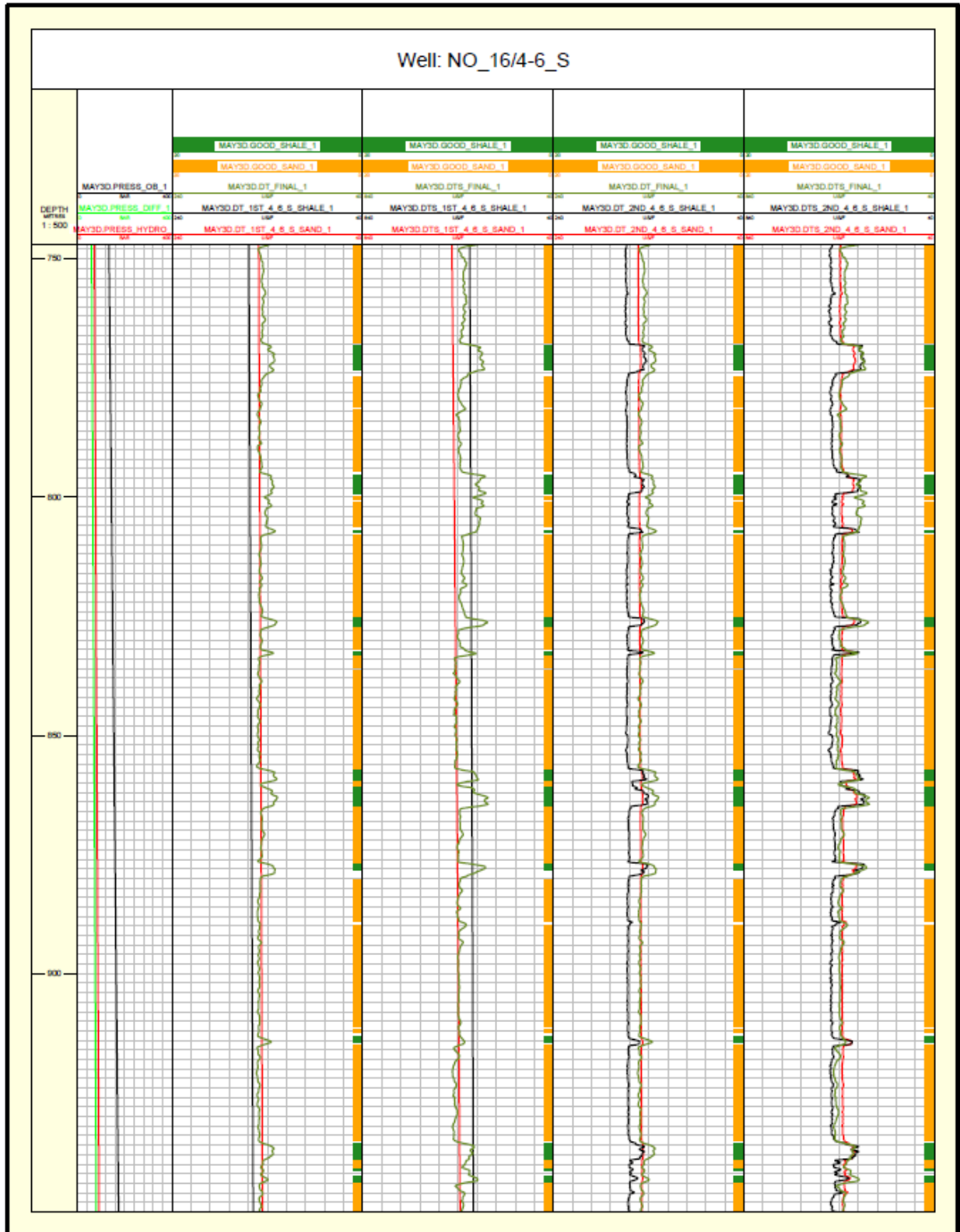


Figure E17. DT and DTS calculated based on the first and second sonic models for the Utsira formation in the well 16/4-6 S. The optimization was based on only this well.

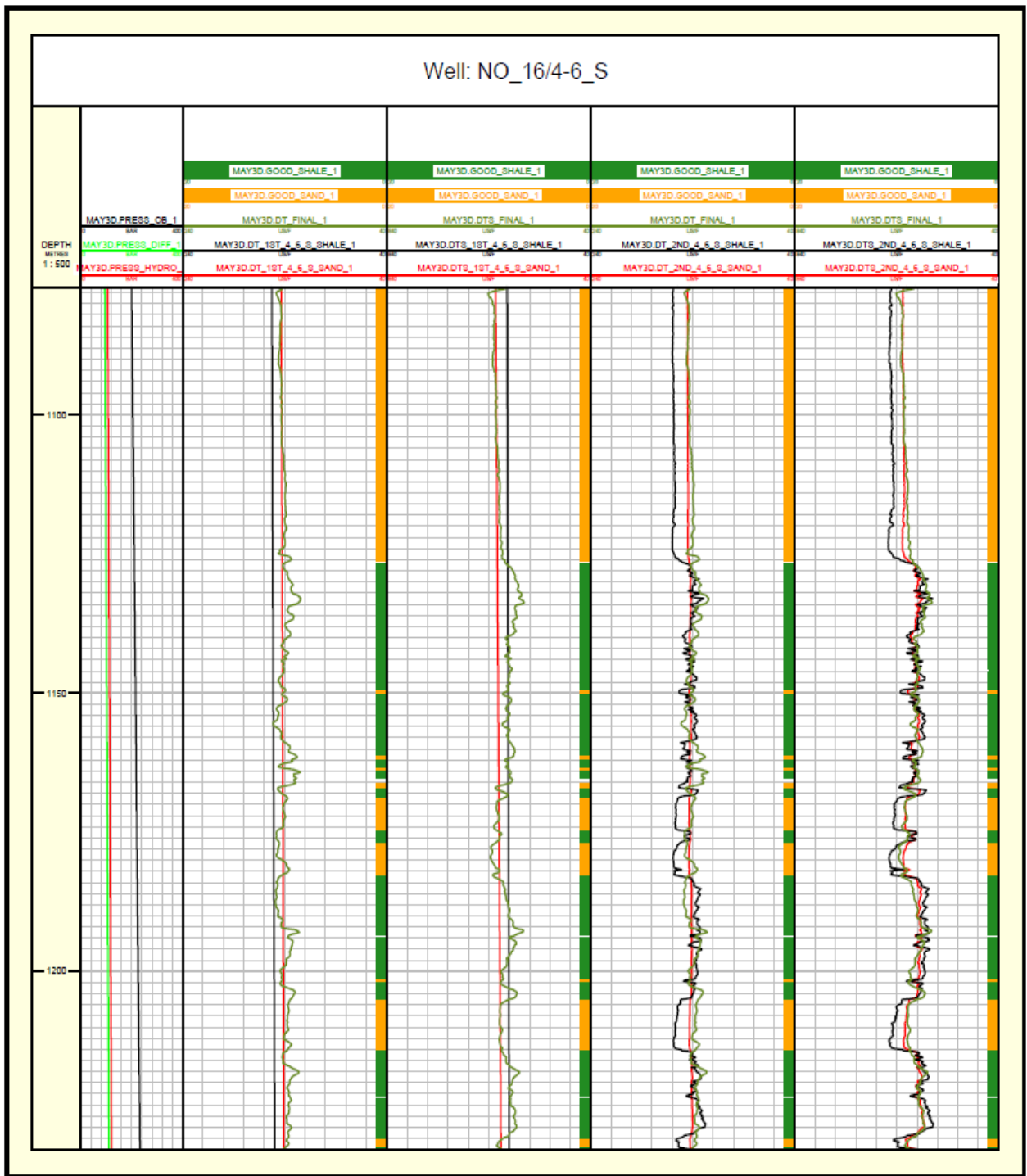


Figure E18. DT and DTS calculated based on the first and second sonic models for the Skade formation in the well 16/4-6 S. The optimization was based on only this well.

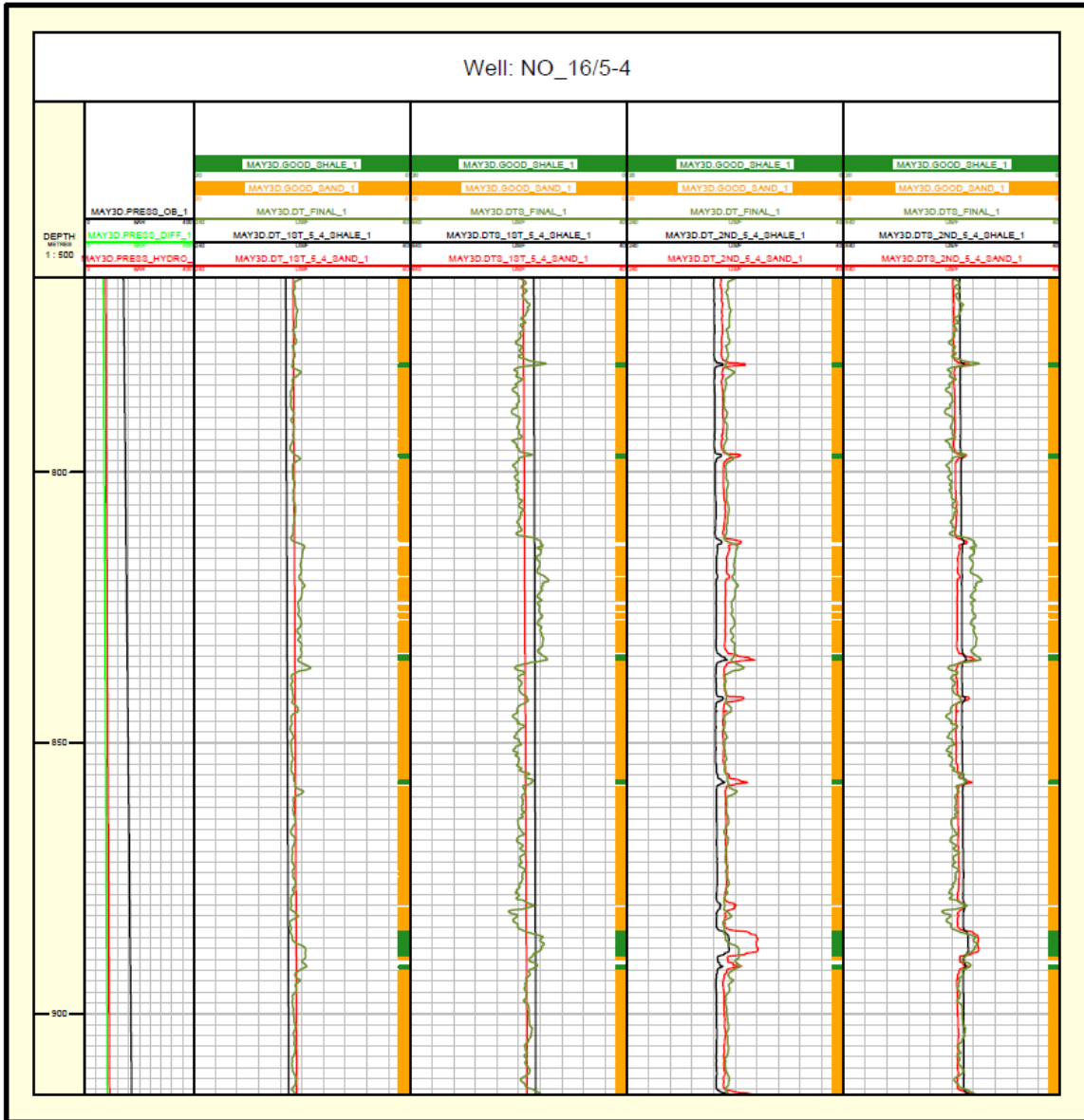


Figure E19. DT and DTS calculated based on the first and second sonic models for the Utsira formation in the well 16/5-4. The optimization was based on only this well.

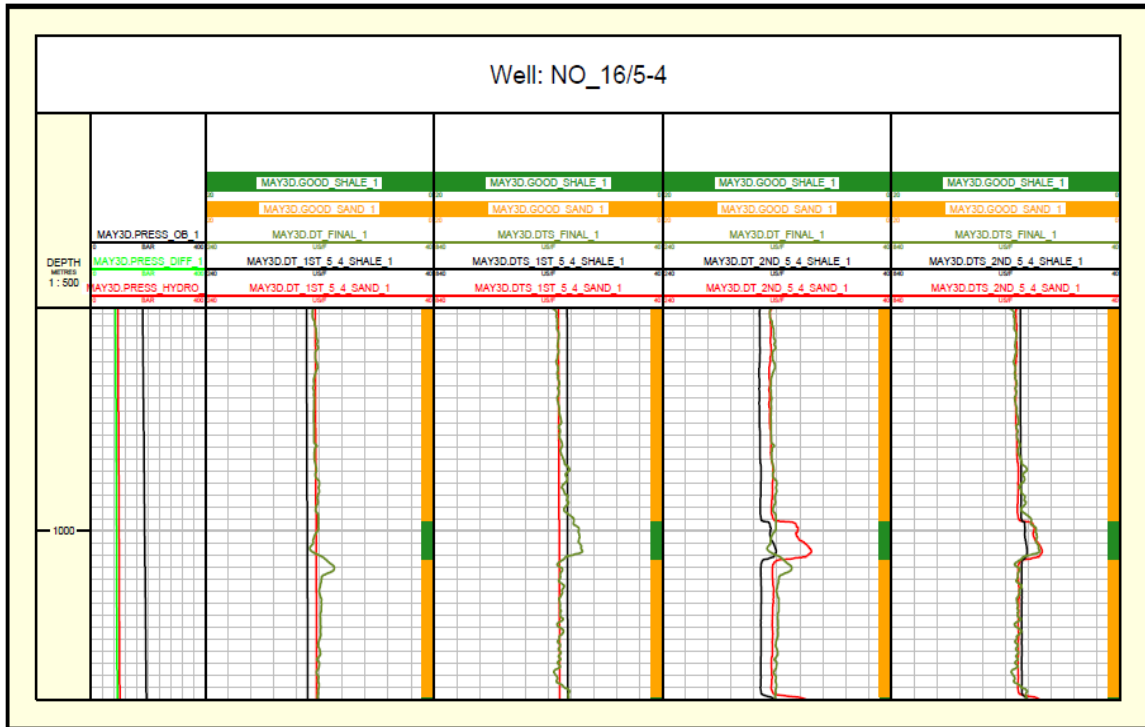


Figure E20. DT and DTS calculated based on the first and second sonic models for the Skade formation in the well 16/5-4. The optimization was based on only this well.